# Optimisation of PBG-Waveguides for THz-Driven Electron Acceleration

**Andrew W. Vint**

A thesis presented for the degree of
Doctor of Philosophy

Department of Engineering
University of Lancaster
United Kingdom
November 2020

# Declaration

I herewith formally declare that I, Andrew William Vint, have written the submitted thesis independently in accordance with §PR2.6.2 of MARP 2020-21 Postgraduate Research Regulations. This thesis has not been handed in or published before in the same or similar form to any university or institution. I certify to the best of my knowledge that this thesis does not infringe upon anyone's copyright and all major sources of information are properly referenced. The work was completed under the guidance of Doctor Rosa Letizia, at Lancaster University, UK.

Signed Andrew Vint 2021.05.20
16:12:28 +01'00'

Andrew W. Vint

30th November, 2020.

Engineering Dept., Lancaster University, Lancaster, UK, LA1 4YW

lancaster.ac.uk/engineering/

# Contents

# List of Tables

# List of Figures

# Glossary

## List of Acronyms

| Acronym | Definition |
|---|---|
| BBU | Beam Breakup |
| BWO | Backward Wave Oscillator |
| BDWPA | Beam-Driven Wakefield Plasma Acceleration |
| CCR | Coherent Cherenkov Radiation |
| CST | Publisher of Microwave Studio Software |
| DLA | Dielectric Laser Acceleration |
| DLW | Dielectric-Lined Waveguide |
| DR | Deflection Ratio |
| EDWPA | Electromagnetically-Driven Wakefield Plasma Acceleration |
| FIT | Finite Integral Technique |
| HOM | Higher Order Mode |
| ISM | Industrial, Scientific, and Medical |
| IP | Ionisation potential of a gas in a plasma |
| LIGA | *Lithographie, Galvanoformung, Abformung*, A manufacturing process |
| LSE | Longitudinal-Section Electric mode, a hybrid propagating mode which has electric field vector in the axis of propagation |
| LSM | Longitudinal-Section Magnetic mode, a hybrid propagating mode which has magnetic field vector in the axis of propagation |
| MAP | Micro-Accelerator Platform |
| MPB | MIT Photonic Bands Software |
| PBC | Periodic Boundary Condition |
| PBG | Photonic Bandgap |
| PBG-W | Photonic Bandgap Waveguide |
| PEC | Perfect Electrical Conductor |
| PhC | Photonic Crystal |
| PhC-W | Photonic-Crystal Waveguide |
| PIC | Particle-in-Cell |
| RF | Radio Frequency |
| RMS | Root Mean Square |

| Acronym | Definition |
|---|---|
| TD | Time Domain Solver |
| $TE$ | Transverse-Electric mode, a propagating electromagnetic mode in which the electric field vector is always perpendicular to the direction of propagation. |
| $TEM$ | Transverse-Electromagnetic mode, a propagating electromagnetic mode in which the electric and magnetic field vectors are always perpendicular to the direction of propagation. |
| $TM$ | Transverse-Magnetic mode, a propagating electromagnetic mode in which the magnetic field vector is always perpendicular to the direction of propagation. |
| TWT | Travelling Wave Tube |

# List of Symbols

| Symbol | Definition |
|---|---|
| $\mathbf{a}$ | Unit Vector |
| $\alpha$ | Twiss Alpha |
| $\mathbf{b}$ | Reciprocal Unit Vector |
| $B_\perp$ | Beam Brightness |
| $\mathbf{B}$ | Magnetic Flux Density |
| $\beta$ | $v/c$, Normalised Velocity; Twiss Beta |
| $c$ | Speed of Light, $299\,792\,458\,m/s$ (exact) |
| $C$ | Separation of Dielectric |
| $\gamma$ | Lorentz (Relativistic) Factor; Twiss Gamma |
| $\mathbf{D}$ | Displacement Field |
| $\nabla$ | Vector Differential Operator |
| $\mathbf{E}$ | Electric Field |
| $E_{acc}$ | Longitudinal electric field on axis |
| $E_{max}$ | Maximum electric field in structure |
| $\epsilon$ | Emittance |
| $\varepsilon$ | $\varepsilon_r\varepsilon_0$, Material Permittivity |
| $\varepsilon_r$ | Relative Permittivity |
| $\varepsilon_0$ | Permittivity of Free Space, $8.8541878128 \times 10^{-12}\,F/m$ |
| $f_0$ | Central Frequency |
| $\mathbf{F}$ | Force |
| $\mathbf{G}$ | Reciprocal Lattice Vector |
| $h$ | Planck's Constant, $6.62607015 \times 10^{-34}\,J\cdot s$ |
| $\mathbf{H}$ | Magnetic Field |
| $\hat{\mathbf{\Theta}}$ | Eigenvalue Operator |
| $i$ | $\sqrt{-1}$, Imaginary Unit |
| $I$ | Current |
| $\mathbf{J}$ | Current Density |
| $\mathbf{k}$ | Wave Vector |
| $\lambda$ | Wavelength |
| $\lambda_0$ | Free-Space Wavelength |
| $\mathbf{M}$ | Magnetisation |
| $\mu$ | $\mu_r\mu_0$, Material Permeability |

| Symbol | Definition |
|---|---|
| $\mu_r$ | Relative Permeability |
| $\mu_0$ | Permeability of Free Space, $1.2566370621 \times 10^{-6}\, H/m$ |
| $\mathbf{p}$ | Momentum |
| $\mathbf{P}$ | Polarisation |
| $q$ | Charge of particle |
| $Q$ | Total Charge |
| $\mathbf{r}$ | Position Vector |
| $\mathbf{R}$ | Lattice Vector |
| $\rho$ | Charge Density |
| $\rho_c$ | Electrical Resistivity |
| $\mathbf{S}$ | Poynting Vector |
| $\sigma_c$ | Electrical Conductivity |
| $\sigma$ | Standard Deviation |
| $t$ | Time |
| $T$ | Thickness of Dielectric |
| $\mathbf{v}$ | Velocity |
| $\underline{\mathbf{v}}$ | Complex Reluctivity |
| $v_g$ | Group Velocity |
| $v_p$ | Phase Velocity |
| $\omega$ | Angular Frequency |
| $\omega_0$ | Central Angular Frequency |
| $Z$ | Impedance |
| $Z_0$ | Impedance of Free Space, $\sqrt{\mu_0/\varepsilon_0} \approx 377\,\Omega$ |

# Acknowledgements

The completion of this undertaking was only possible thanks to the many brilliant colleagues, friends, and mentors I have had the utmost fortune in being surrounded by.

First and foremost, I would like to thank my supervisor Dr Rosa Letizia. You gave me the chance in the first place where others may have not, guided me, and allowed me to grow as both a scientist and a person.

I would also like to thank Prof. Graeme Burt for your patience and insight into problems that were not always obvious or transparent, and for stepping up without hesitation when you were needed.

To my colleagues and friends across Daresbury, it is safe to say that you made my worst days bearable, and my best days the best. Tom, I thank you for your patience and calm explanations of complex ideas, and for showing me just what a PhD was. Alisa, you taught me the subtleties of terahertz. Paolo, Kay, Roland, Lina, Taylor, Taaj, Billy, Joe, Alex, Ruta, Jacinda, Kristina, Marta, and many others—our games, lunches, and random chats made it all worthwhile.

And to my parents, Aileen and Bill, thank you for your support and encouragement from start to end. For being either a phone-call away, or a quiet cheerleader when each were needed.

Finally, it is no stretch of the imagination to say that none of this could have happened without the unwavering support of my partner, Tammy. You pushed me across the starting line, you kept me going even through the darkest moments, and you made sure I didn't stop until the end. From the bottom of my heart, thank you.

This work was funded by the Cockcroft Studentship grant ST/N504129/1.

# Abstract

**Andrew William Vint, MSc High Power Radio Frequency Science and Engineering, MSci Physics**
**Doctor of Philosophy**
**Optimisation of PBG-Waveguides for THz-Driven Electron Acceleration**
**November 2020**

Particle acceleration in dielectric structures driven by laser sources has been demonstrated as a viable approach to overcome the limitations of conventional accelerator technology and achieve unprecedented levels of electric field gradients. Among the dielectric laser acceleration schemes possible, the use of THz high energy pulses has gained increasing attention in recent years to provide a solution to the challenging whole bunch acceleration problem typical of the optical frequency regime. Most of the experimental work performed so far in THz driven acceleration is based on dielectric lined waveguides. This thesis investigates the use of photonic crystal technology to assess their potential in supporting THz acceleration. Photonic crystals have already been extensively investigated as optical scale accelerating structures. The use of photonic crystals over conventional dielectric lined metal walls allows for higher breakdown resistance which in turn offers the potential of higher accelerating gradients. For this reason, photonic crystals are a potential future technology for high-gradient, low-footprint particle accelerators. Here, their properties are exploited in novel metal/dielectric structures to provide efficient acceleration at THz. In particular, a methodology for the design and optimisation of photonic crystal-based waveguides, also known as photonic bandgap waveguides (PBG-Ws), for THz electron acceleration is presented. The effects of broad and narrow pulse bandwidths on the effective accelerating voltage are considered, with particular attention on providing a design methodology to tune central frequency of operation. The effects of tunability, coupling, wall-fields, and beam-driven excitation are numerically investigated and compared to the dielectric lined waveguide. Advantages and limitations of two main geometries of PBG-based waveguides are provided. It was found that 1D PBG-based waveguides lead to better accelerating voltage overall, while 2D PBG-based waveguides are interesting for very narrowband coherent Cherenkov source applications. In addition, the design methodology here presented is not limited to photonic crystal-based waveguides as shown by results obtained for the dielectric lined waveguide and can contribute to the design of future THz acceleration dielectric structures.

*What has been hitherto done, however, has by no means exhausted the field of electrical research. It has rather opened up that field, by pointing out subjects of enquiry, and furnishing us with means of investigation.*

— James Clark Maxwell, *A Treatise on Electricity and Magnetism*

# 1

# Introduction

## 1.1 Particle Acceleration

To the untrained eye—a microwave oven, an antique television, and the x-ray in a dentist's office bear little in common. Under the surface though they all share one common trait: Their operation is based on that of the particle accelerator. Particle accelerators are devices which accelerate streams of charged particles via electric and magnetic fields to high energies to either extract the energy from the particles in the form of electromagnetic radiation, or use the high energy particles themselves as a tool. The high energy electromagnetic radiation or particles emitted from

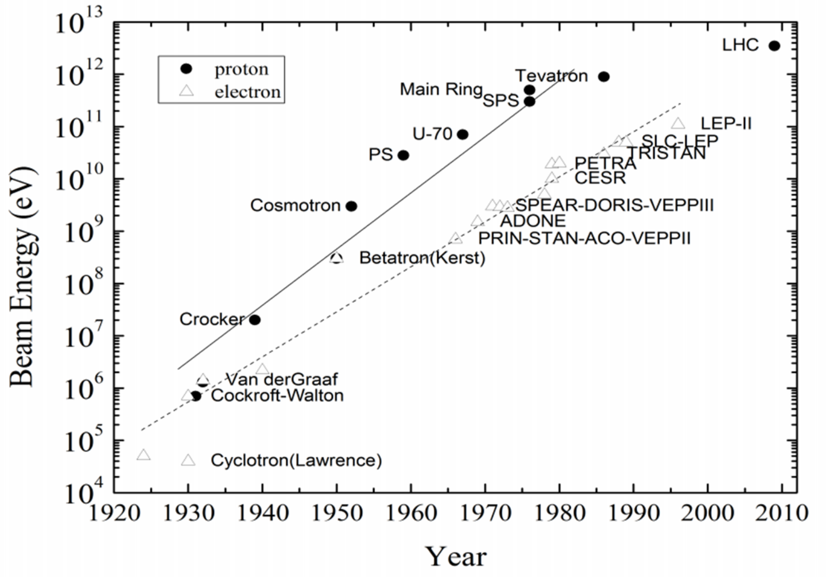

Figure 1.1: Energy of particle accelerators by construction year, where circles are proton accelerators, and triangles are electron accelerators [1].

these devices is used in many disciplines of industrial, scientific, and medical (ISM) fields.

With the growth of ubiquity of these devices, so too has the energy capability of these devices grown. Similar to Moore's law for processor evolution [2], Livingston noted that the energy frontier of particle accelerators grows by a factor of 10 every six years [3] [1]. The eponymous "Livingston Plot", shown in Fig. 1.1, shows that whilst generally holding true, as of 2010 the energy capability of accelerators is plateauing—and to overcome this limit novel technologies are required.

## 1.2 Conventional Particle Accelerators

A particle accelerator is a device which uses electric and magnetic fields to increase the kinetic energy of streams of charged particles. The earliest devices used static electric fields generated via either the charging of capacitor banks such as the Cockcroft-Walton generator [4, 5] or generated via the charging of static electricity such as the Van de Graaff accelerator. The gradient in these devices was however limited by the size of their construction as effects such as corona and discharge become problematic. This limit led to the use of high-frequency electromagnetic radiation instead. Several methods were developed to make use of the alternating voltages that high-frequency supplies. The Wideroe accelerator uses an alternating electric field with drift tubes to shield the charged particle beam from the decelerating phases of the fields. A schematic for this can be seen in Fig. 1.2.

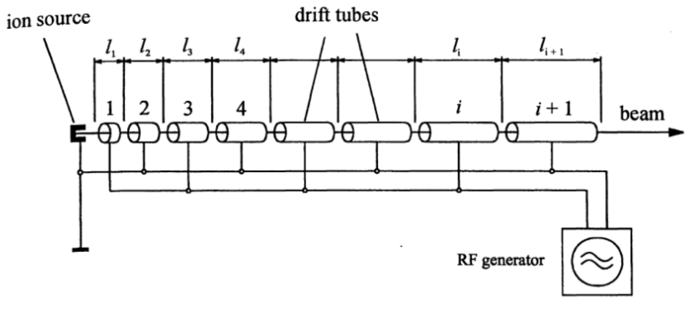

Figure 1.2: Schematic of the Wideroe Particle accelerator as shown in [5].

With devices being single-pass such as the Wideroe accelerator, final energy is contingent on length and thus monetary cost. Circular devices however can use the same accelerating structures repeatedly. The earliest device to make use of a circular beam path is the cyclotron—a crossed field device in which two D-shaped electrodes are positioned between the poles of a magnet. Radio-frequency (RF) is applied to the electrodes, and as the particles transition the gap between the electrodes they are accelerated. As their momentum increases, so does their gyroradius and as such the same gap can accelerate the same bunch repeatedly. The beam is then extracted at the edge. A schematic can be seen in Fig 1.3.

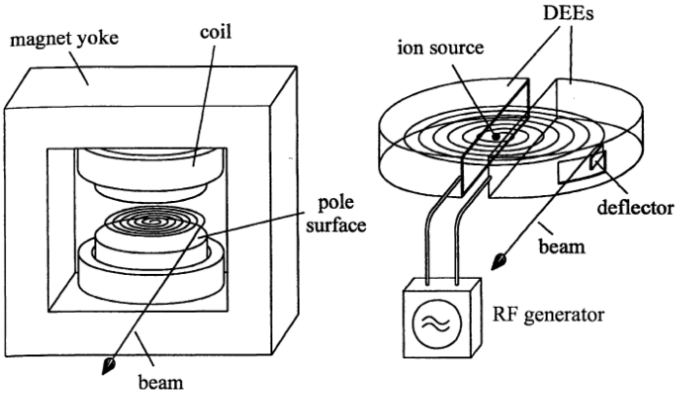

Figure 1.3: Schematic of the Cyclotron Particle accelerator as shown in [5].

The synchrotron is another device which allows the same beam to make multiple passes of the same accelerating structures. This device, which unlike the cyclotron features a fixed beam radius, features multiple bending magnets which only have field in the region of the beam. The name "synchrotron" coming from the fact that as the radius is fixed, the ratio of beam energy to magnetic field must be constant and thus magnetic field must grow synchronously with the beam energy. A schematic for the synchrotron can be seen in Fig. 1.4.

Synchrotrons use metallic cavities as the acceleration structures with geometry designed such that they are resonant at a desired frequency. The effectiveness of these cavities however decreases as the confined energy increases however due to a combination of surface heating and field emission. The former of these two effects can be combatted by transitioning from conventional metallic cavities to super-

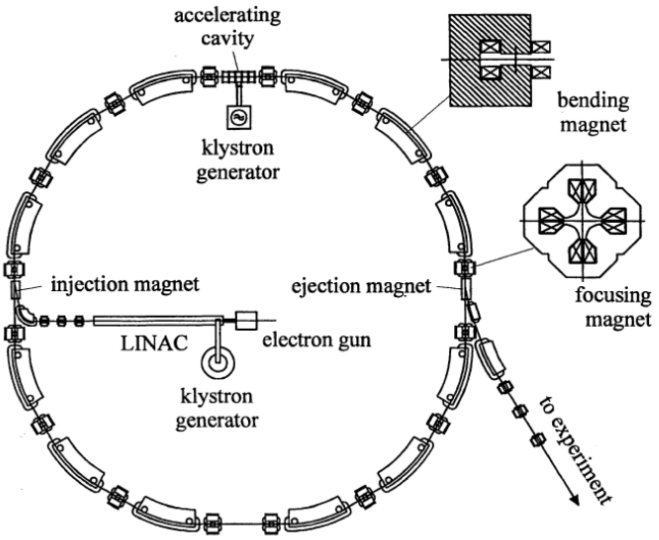

Figure 1.4: Schematic of the Synchrotron Particle accelerator as shown in [5].

conducting cavities. When a material becomes a superconductor, its resistance drops effectively to zero and as such the surface heating by driven currents will also effectively drop to zero. This allows the cavity to store much higher energies, and thus supply higher gradients to the accelerated particles for each pass.

This superconducting effect is relevant not only to high-gradient cavities, but to the array of steering magnets employed in a conventional accelerator. High magnetic fields are generated by high currents in wire coiled round a magnetic core. To achieve higher magnetic fields, higher currents and more windings are required. If copper wire is used, even with effective water cooling, the highest nondestructive current density is approx. $100\,A/mm^2$. Using superconducting wires however, fine wires with extremely high currents are achievable and thus much higher magnetic fields can be obtained.

The steering magnets mentioned previously play a critical role in particle accelerators. The simplest of which is the dipole, shown in (a) of Fig. 1.5 which serves to bend the beam along the desired path curvature. A quadrupole magnet, shown in (b) of Fig. 1.5 acts as a focusing structure in one of the two transverse planes to the beam propagation. They will however defocus in the other plane in accordance with Earnshaw's Theorem [6] and thus often come in a focusing-defocusing pair known as a "FODO" lattice. A more complex magnet is the sextupole magnet, shown in (c) of Fig. 1.5, and compensates for energy spread in the beam. Higher order magnets may also be used however these are more specialised and not “typical” magnets in an accelerator.

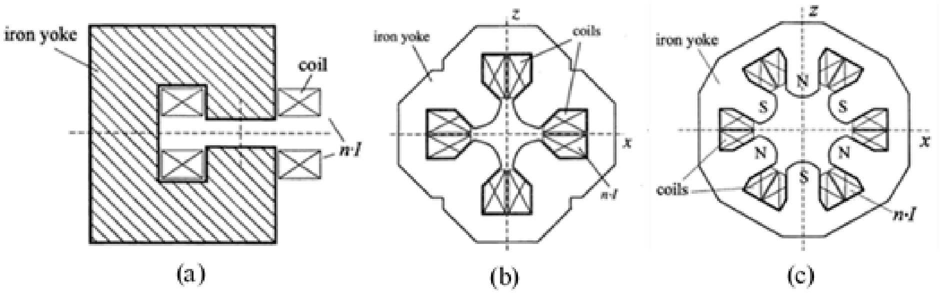

Figure 1.5: Schematic of steering magnets in accelerators as shown in [5]. (a) is the dipole bending magnet, (b) is the quadrupole focusing magnet, and (c) is the chromatic aberration correcting sextupole magnet.

With the devices to accelerate and steer the beam, it is also essential to know both where the beam is, properties of it, and if it even exists or has decayed. With this requirement, the field of beam diagnostics developed. One of the simplest methods for location and current measurement is the fluorescent screen. The beam, impingent on the screen, will excite the phosphors which is then recorded by a CCD camera. The brightness of the dot created by the beam on the fluorescent screen indicates the beam current, and the positioning indicates whether the beam is off-axis. To measure the beam current, a Faraday cup can be employed, which captures the entire beam and the change in charge is recorded. As both of these methods are destructive, they are often not desirable if the lifetime of the beam is to be maintained. For non-destructive testing, using the field of the beam can also be employed for diagnostics. A beam propagating near a metal wall will induce an eddy current in the wall and thus a voltage will be generated longitudinally. This voltage can be exploited as a wall-current monitor. If instead of a solid metal pipe, the beam propagates through a coil of wire, this will act as a transformer and thus a pulse will be generated as the beam passes.

There are also device designs which make use of novel technologies such as terahertz, dielectrics, plasma, and photonics to create the accelerating gradients.

These are reviewed in detail in chapter 2 and thus will not be discussed here.

## 1.3 Motivation for Dielectric Based Accelerators

While the footprints of many particle accelerators are small, their operational energies and/or beam currents are also limited. This is due to the dual complication of structures being constructed at the scale of the accelerating fields wavelength, and the gradient in conventional metallic structures having an empirical upper gradient of $< 100\,MV/m$ with many cavities operating in the region of $50\,MV/m$ [7]; this being due to a combination of pulse duration, frequency, and acceptable breakdown rate (BDR) with BDR $\propto E^{30}t^{5}$ where $E$ is the electric field and $t$ is pulse length.

To address the issue of the growing footprint accelerators, the accelerating gradient must be increased. As the two main limits on accelerating gradient are wavelength and field strength, and with the metallic cavities currently employed already operating near their empirical field strength ceiling, the frequency must be varied. In scaling structures to the range of terahertz and beyond, the wavelength problem is overcome but the field strength has not. Restricting the frequency to terahertz instead of continuing to optical frequencies offers the benefit of improved coupling between the particle-beam, and the desired accelerating phase of an electromagnetic wave, also known as beam-wave coupling; as since these devices require a beam, the aperture and dimensions of THz-frequency geometries allow beams with larger charges to propagate. Additionally the use of THz allows the beam to be localised within a single half/quarter of an accelerating wavelength. Optical frequency devices however result in the beam spanning several wavelengths longitudinally, leading to discontinuous acceleration.

Skin depth $\delta$—or the depth at which field intensity drops to $1/e$ where $e$ is the natural base—at THz frequencies for most metals becomes so small that surface heating and deformation is difficult to prevent with cooling, and the field emission problem is unaddressed. This can be illustrated from the skin depth equations, where for when $\varepsilon\omega \ll \sigma_c$ such as in metal:

$$\delta = \sqrt{\frac{2}{\omega\mu\sigma_c}} \tag{1.1}$$

and cases where $\varepsilon\omega \gg \sigma_c$ such as dielectric:

$$\delta = \frac{2}{\sigma_c}\sqrt{\frac{\varepsilon}{\mu}} \tag{1.2}$$

where $\varepsilon$ and $\mu$ are the materials permittivity and permeability respectively, $\sigma_c$ is its electrical conductivity, and $\omega$ is the electromagnetic radiation's frequency. Due to this inability to scale to high frequencies, conventional RF devices are difficult to realise with the combined skin depth problem and small physical dimensions. Due to dielectrics being insulators and having a large energy gap between the conduction and valence bands of their electronic structure, they can withstand high electric fields before the electrons are elevated to the conduction band. Constructing the accelerating cavity from this insulating dielectric can offer the ability to tolerate higher field strengths and lower surface heating, leading to the field of dielectric laser acceleration (DLA). This use of dielectric makes synchronism possible without complex periodic geometries in the vacuum channel, as the dielectric itself acts as a slow wave structure. The high breakdown limit of dielectrics is exploited to push acceleration gradients higher than possible in metal based devices. These structures can also be used as a radiation source when coupled with a highly relativistic beam.

## 1.4 Research Objective

The issue with implementing dielectrics as acceleration devices is that they often transmit electromagnetic radiation rather than reflect it as is required for confinement and therefore the more conventional dielectric waveguides designs in literature do not employ a hollow core. Photonic crystals, made from dielectric with an engineered geometric periodicity, have been investigated intensively by the DLA community as a method for overcoming the transmissive nature of dielectrics, with the use of the photonic bandgap to create a quasi-waveguide (PBG-W) for particle accelerators. PBG-W based linear accelerators offer a unique method of accelerating particles without metal cavities. The objective of this thesis is to investigate photonic crystal technology for THz driven electron acceleration. In particular, for the first time—a combined design approach employing simple 1D and 2D PBG-Ws clad by metal plates is proposed for THz driven acceleration. A methodology for optimising these structures, as well as other waveguide designs, to the available THz pulse bandwidth is presented.

The investigation into the PBG-W will study the flexibility of this solution in comparison with alternatives such as the dielectric-lined waveguide (DLW), with focus paid on accelerating voltages obtained for both broadband and narrowband excitation pulses. Whilst photonic crystal waveguides for acceleration have been investigated for DLA at optical wavelengths, the study presented in this thesis will examine their properties at THz frequencies.

The analysis will investigate external laser excitation of the PBG-Ws with a study of coupling the laser pulses into the PBG-W for acceleration. The dispersive nature of the waveguides and how the accelerating voltage varies with THz pulse bandwidth in relation to that is investigated. Additionally, the wakefields generated via beam excitation of the structures will be studied, and the suitability of PBG-Ws will be discussed as beam driven devices such as coherent Cherenkov radiation (CCR) sources, dielectric wakefield accelerators (DWAs), and potential other beam-driven applications.

Some of the main parameters used in this work are briefly defined here. Characteristic impedance, or interaction impedance, is a common metric used in this thesis and the DLA field as a whole. It is a figure defined as the product of the accelerating field over power flow in the structure. A related figure is the $R/Q$ which is a product of power loss on the walls, to energy propagating in the structure.

Phase and group velocities are discussed which are the velocities of a phase-point in an electromagnetic wave, and the envelope of the wave respectively. Permittivity is a measure of a materials polarisability, and represents the materials ability to store energy under the influence of an electric field. Other figures used in this work are defined when used.

## 1.5 Layout of Thesis

This thesis begins with a literature review in the second chapter, which will report on the current state of the art in the study of novel high-frequency acceleration. It will examine THz acceleration, novel acceleration designs such as the use of dielectric and plasma, and it will also examine relevant publications in the field of photonic crystal based particle acceleration. It will examine structures which are laser-driven and beam-driven in their operation.

The third chapter examines the theory underpinning photonic crystal based accelerators. It begins with first principles, evaluating Maxwell's equations for dielectric media and analysis of periodic dielectric media. It then moves onto discussing some figures of merit for quantifying the acceleration capability of photonic crystal waveguides. It will also examine the technologies of THz sources and micro-fabrication which make this work possible.

As the third chapter examines externally driven photonic crystal waveguides, the fourth chapter examines beam driven structures. It begins with a fundamental description of what a charged particle beam is, then moves onto methods for extracting energy from highly relativistic beams. The chapter closes by examining the fundamentals of wakefield generation and information that can be derived from wakefields.

The fifth chapter encompasses the bulk of work undertaken during this PhD programme and examines the acceleration capabilities of laser driven photonic crystal waveguides. The chapter starts with the 1D Bragg based waveguide. It begins with the unit cell analysis, studies waveguides with both periodic and metal clad boundaries, and examines the acceleration voltage bandwidth with a $100\,mJ$ pulse. This study is then undertaken for the triangular lattice 2D photonic crystal. In addition, the amplitude of electric and magnetic fields on the metallic walls are investigated, coupling into the waveguide, and the mesh analysis for simulation was undertaken.

The sixth chapter of this thesis examines the alternate approach of driving the PBG-W with a highly relativistic electron beam to excite the structure. The PBG-Ws are simulated in the wakefield solver with the beam in four positions to obtain the wakefield impedance for each. Metal clad, and parallel plate geometries are considered. The energy loss for the beam as it propagates through the structure is measured and provided as a figure of merit. The DLW is also considered as a comparison for the PBG waveguides.

## 2

# Novel Particle Acceleration: Current State of the Art

Metallic acceleration structures are vast and varied with a rich century-plus history of development [8] [9] [10]. These can cover everything from the standing-wave synchrotrons and linacs used in places like CERN, Fermilab, or KEK, to cyclotrons employed in proton treatment centres such as the Christie [11]. Even the magnetron used in the microwave oven is a metallic-based acceleration structure [12]. The focus of this section however is to provide an overview of the novel approaches to acceleration in which the context of this research is for smaller footprint, higher gradient, and stronger field resistance.

This chapter begins by examining the setups employed for THz acceleration some novel techniques which are being investigated around the world such as plasma-based methodologies. It will then move into dielectric-employing structures not utilising a photonic bandgap, and finally then discuss the definition of photonic crystals/photonic bandgaps and their current state of the art (SOA) in proposed photonic bandgap based structures for high frequency acceleration.

## 2.1 Terahertz Acceleration

A commonly accepted frequency range for an electromagnetic regime is $0.4 - 400$ units—where this unit may be Hz (AC), kHz (low-frequency), MHz (RF), GHz (Microwave); indeed visible light begins at 400 THz—or 700 nm. Between these regimes exists the thermal-emission band. Development of high-power devices which are able to operate in various frequency bands of AC-Microwave and of IR-Visible has existed with technical maturity for decades. The region between these two regimes however, at approx 400 GHz-40 THz, where the radiation has a wavelength similar to room-temperature IR emission, has long been problematic. This is known as the “Terahertz Gap”, where high power sources are difficult to create. And while there has been an exponential growth in the study of the subject [13], there is typically no available off-the-shelf equipment. And while one can mention the sun, or cosmic background radiation, or the act of peeling tape as technically THz sources, none are particularly useful in the field of particle accelerators. Furthermore, much of the work undertaken in the THz field is more closely related with spectroscopy and imaging than high power sources or acceleration [14]. Thus whilst difficult to generate, THz acceleration is of interest over optical frequency due to the combination of larger geometry and single-wavelength acceleration. THz geometries allow transversely larger beams to be coupled into the structure, whilst also ensuring the beams are longitudinally short enough to be accelerated by a single wavelength “bucket”. This, combined with the high gradients offered by the short THz wavelengths means the potential for high-gradient, small-footprint acceleration is achievable.

Conventional high-power RF sources are typically free-electron based devices. Klystrons, travelling wave tubes (TWTs), backward wave oscillators (BWOs), and gyrotrons are common and comprehensively studied devices. These devices, whilst off-the-shelf and well established components for generating high powers at RF and microwave frequencies, scale poorly to higher frequencies. This is due to the skin-depth resistive wall losses, beam effects, apertures, and the concentration of high electric and magnetic fields required for their operation at high-frequencies and powers in the watt-range and higher. Studies have been undertaken however at pushing the frequency limits of these devices. With the advent of superconducting magnets allowing for very high magnetic fields, gyrotrons show promise at being an off-the-shelf high-power THz source in the future [15, 16, 17].

The method of generating pulsed THz at Daresbury [18, 19] is through the use of optical down-conversion [20]. A nonlinear crystal such as lithium niobate, which features a large second-order susceptibility [21]—in which its optical properties can be largely and non-linearly changed with an intense light pulse—is illuminated by TW laser pulses. The combination of wavelengths with nonlinear response causes photomixing in the nonlinear crystal; which is the process of generating radiation from two identical polarisation laser pulses. The two laser pulses with differing frequencies illuminate the photomixer which generates radiation with frequency which is the difference between the two illuminating pulses. The result is pulsed THz emission from the crystal and the efficiency of the conversion is proportional to the effective non-linearity squared [22]. The typical power output of these processes is sub-microwatt however in the future it is expected for this to increase by orders of magnitude [23]. A schematic for the full THz acceleration setup can be seen in Fig. 2.1. This setup has also been investigated as use as a beam dechirper for the CLARA free-electron laser (FEL) [24]. In this setup, a 250 $MeV$ electron beam has the RMS energy spread reduced from 0.24% to 0.08% whilst preserving emittance. The dechirping resulted in a calculated pulsed power increase from the FEL of 30%.

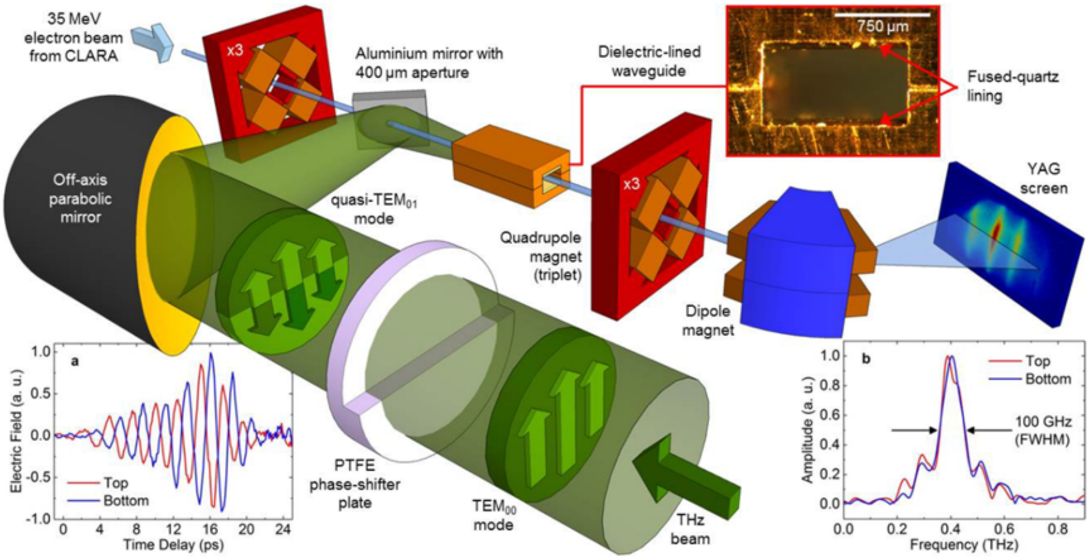

Figure 2.1: Schematic of the THz acceleration setup at Daresbury using a dielectric lined waveguide, as proposed in [18].

The Segmented Terahertz Electron Accelerator and Manipulator (STEAM)

Table 2.1: Experimental measurements for state of the art THz acceleration

| Parameter | Value | Source |
|---|---|---|
| Highest Gradient Achieved | $100\,MV/m$ | [26] |
| Largest Energy Gain | $7\,keV$ | [29] |
| Longest Accelerating Length | $4.3\,mm$ | [18] |
| Largest Charge Accelerated | $60\,pC$ | [18] |
| Highest Repetition Rate | $1\,kHz$ | [25] |

facility [25] is a terahertz-driven electron accelerator which offers $pC$ bunch charges with $kHz$ repetition rates. It has the ability to accelerate, streak, focus or compress the bunch depending on the mode of operation. As the ubiquity of these sort of devices increases, the gradients and energies achievable from the bunch will further improve. Further THz acceleration work in [26] has investigated longer accelerating lengths to increase the acceleration to multi-MeV energy gains by using alumina-lined DLW in combination with the STEAM streaker to increase the energy gain of the bunch by an order of magnitude.

The SINBAD (Short INnovative Bunches and Accelerators) facility at DESY is one other installation investigating THz acceleration [27]. The facility houses a THz laser and the electron bunches produced are $fs$ in duration, allowing them to be uniformly accelerated by the THz source. The “AXSIS” accelerator is a fully-THz driven accelerator, and as of 2019 [28] the construction is nearing completion.

Work investigating linear THz acceleration at MIT [29] obtained a maximum energy gain of $7\,keV$ from a $3\,mm$ length dielectric lined waveguide driven by $0.45\,THz$; giving an accelerating gradient of $2.3\,MeV/m$ for a $25\,fC$ bunch.

Summary of some experimentally measured state of the art THz acceleration figures is shown in table 2.1.

## 2.2 Plasma-Based Accelerating Structures

Plasma acceleration is a method under investigation for generating large accelerating gradients without risk of field emission or surface heating. The fundamental nature of plasma lends itself well to generation of high electric fields. These high

Table 2.2: Experimental measurements for state of the art in EDPWA

| Parameter | Value | Source |
|---|---|---|
| Highest Electric Field | $100\,GV/m$ | [33] |
| Highest Gradient Achieved | $100\,GV/m$ | [33] |
| Largest Energy Gain | $7.8\,GeV$ | [34] |
| Longest Accelerating Length | $20\,cm$ | [32] |
| Largest Charge Accelerated | $1\,nC$ | [35] |
| Highest Repetition Rate | $20\,Hz$ | [35] |

fields are excited in the plasma when the quasi-neutral state of the plasma is disrupted by charge separation; which can be triggered either by high-energy electromagnetic fields, or high-energy particle beams. As such, they can loosely be defined as wakefield structures and are so in literature.

### 2.2.1 Electromagnetically-Driven Plasma Wakefield Acceleration (EDPWA)

The concept of using a plasma being capable of accelerating charged particles was first suggested in 1949 [30] when discussing cosmic rays. Expanding on this idea, the concept of applying this to terrestrial particle acceleration was proposed in 1979 [31]. The principle of this method of acceleration is a high power electromagnetic pulse incident on the plasma causes charge expulsion as it propagates into the plasma. This charge-separated "bubble" in the wake of the pulse, in which the light electrons have been expelled but the heavy ions have not, contains a large electric field in which an injected particle beam could use for acceleration.; an example of which can be seen in Fig. 2.2.

Extremely high accelerating gradients for this method, on the order of $> 100\,GV/m$ and energies of $> 100\,MeV$ with bunch charges $> 1\,nC$ have been demonstrated as early as 1995 however the quality of the beam was poor [33]. As this field has evolved, labs such as LBNL have reported achieving beam energies of $4.2\,GeV$ with 6% energy spread in accelerating lengths of $9\,cm$ in 2014 [32]; and up to $7.8\,GeV$ in $20\,cm$ in 2019 [36, 34]

Work at the Centre for Relativistic Science at IBS in Korea have pushed the

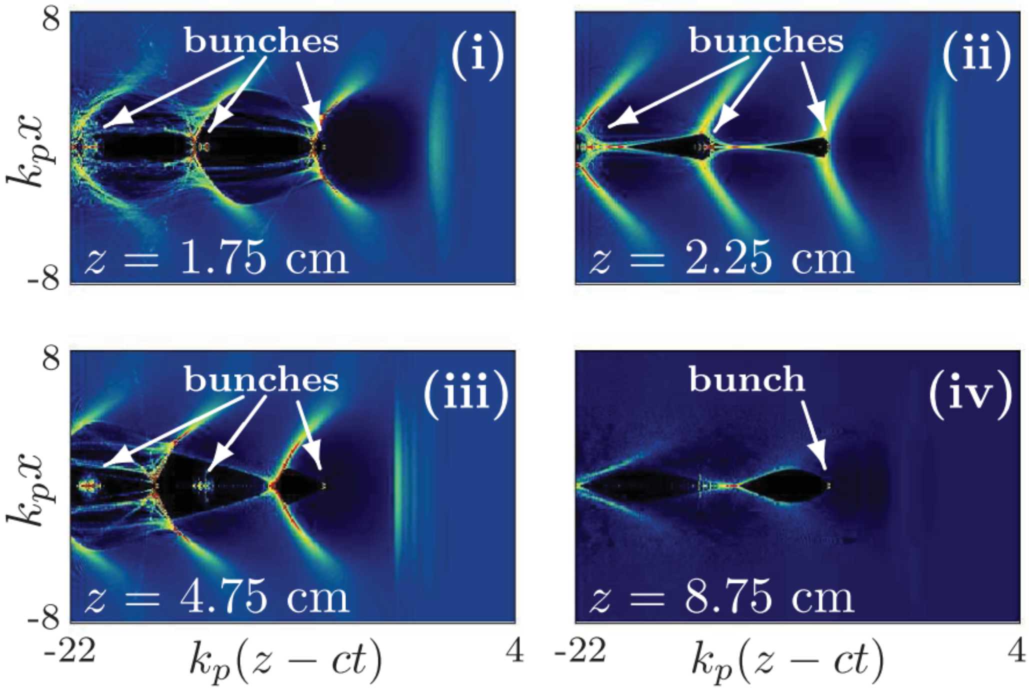

Figure 2.2: Simulated EDPWA as proposed in [32].

largest accelerated charge in EDPWA to $70\,pC$ with a peak energy of $2.3\,GeV$ [37], and up to $1\,nC$ with much lower accelerated energies $> 500\,keV$ in [35]. The repetition rate in EDWPA has been pushed from $10\,Hz$ with up to $1\,GeV$ beam energy in 2011 [38] to $20\,Hz$ with a lower beam energy of $12\,MeV$ in 2018 [35].

A summary of some experimentally measured state of the art THz acceleration figures is shown in table 2.2.

### 2.2.2 Beam-Driven Plasma Wakefield Acceleration

The “bubble” formed in a plasma cell does not need to be generated with a laser. Using a beam of high-energy electrons, the Coulomb repulsion force will similarly expel electrons and generate a region of ions with a large electric field which can be used for acceleration. First proposed in 1985 [39], SLAC have achieved several milestones in this field. Using a lithium vapour plasma; a $1.3\,m$ interaction length was produced. The peak energy obtained from the structure was $5.3\,GeV$ on a $120\,pC$ bunch [40], with the record for largest gradient and bunch size being

Table 2.3: Experimental measurements for state of the art in BDPWA

| Parameter | Value | Source |
|---|---|---|
| Highest Electric Field | $52\,GV/m$ | [42] |
| Highest Gradient Achieved | $52\,GV/m$ | [42] |
| Largest Energy Gain | $43\,GeV$ | [42] |
| Longest Accelerating Length | $10\,m$ | [44] |
| Largest Charge Accelerated | $200\,pC$ | [41] |
| Highest Repetition Rate | $10\,Hz$ | [46] |

achieved two years previously [41]. Their beam-driven plasma has also achieved extreme gradients of $52\,GV/m$ [42] and energy gains of approx. $43\,GeV$ at repetition rates of $10\,Hz$. The hurdle still faced is emittance growth, with current work aiming to reduce this to push for $TeV$-energy electron bunches [43].

The advanced wakefield experiment (AWAKE) experiment at CERN uses proton beams instead of electrons for the drive bunch in a $10\,m$ long rubidium plasma [44]. Run 1 of this experiment ran from 2016-2018 achieving self-modulation of the drive proton bunch, and acceleration of an injected electron bunch achieving energy gains of approx. $2\,GeV$. Run 2 of the AWAKE experiment will investigate scalability, high gradients, and beam quality [45].

The work discussed here is summarised in table 2.3

## 2.3 Dielectric-Based Accelerating Structures

Starting with the review of dielectric-based accelerating structures which was undertaken in 2014 [47] and discussing the latest developments in the field, this section gives a brief overview of the latest developments for dielectric-based accelerating structures. Whilst the focus of this is on dielectric laser acceleration at optical frequencies, due to the scalability of Maxwell's equations, the structures themselves can be designed wavelength agnostic, and it is other factors such as beam-size, manufacturability, and even molecular size which put the absolute limit on them.

Not all dielectric-based structures make use of photonic crystals. With examples shown in Fig. 2.3, work undertaken by Leedle et al. [48] makes use of dual rows of dielectric cylinders surrounding a vacuum beam channel which serve to modulate the phase of the incoming accelerating wave, known as phase reset, and thus produce a uniform accelerating gradient. This structure, tested in 2015, was designed for sub-relativistic acceleration. It showed accelerating gradients of $370\,MeV/m$.

To achieve this phase modulation, the structure does not need to be pillars. It can be as simple a dielectric slab with surface corrugation. This structure first proposed by Plettner in 2006 [49] and then later expanded upon by Peralta in 2012 [50] and even at Daresbury by Wei in 2015 [51]. The device proposed by Peralta was tested in 2013 [52], the device was found to provide an energy gain of $69.2\,MeV$ with gradient of $191.1\,MeV/m$.

A summary of some experimentally measured state of the art THz acceleration figures is shown in table 2.4.

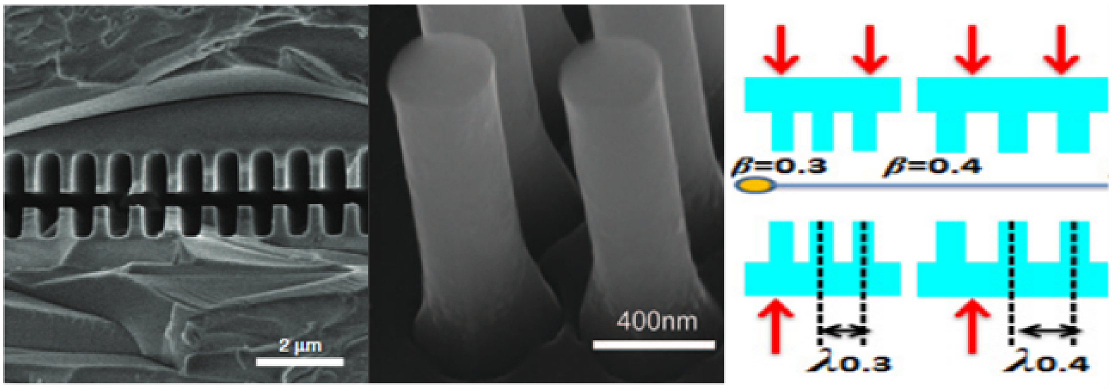

(a) (b) (c)

Figure 2.3: Images of the dielectric-based sub-relativistic "phase-reset" acceleration structures in which use dielectric to modulate the phase of an accelerating wave so the phase-shift relative to the beam is 0; as proposed by (a) Peralta [50] (b) Leedle [48] (c) Wei [51].

Table 2.4: Experimental measurements for state of the art in dielectric-based accelerators

| Parameter | Value | Source |
|---|---|---|
| Highest Electric Field | $370\,MV/m$ | [48] |
| Highest Gradient Achieved | $370\,MV/m$ | [48] |
| Largest Energy Gain | $69.2keV$ | [52] |
| Longest Accelerating Length | $450\,\mu m$ | [52] |
| Largest Charge Accelerated | $0.5\,pC$ | [52] |
| Highest Repetition Rate | $76\,MHz$ | [48] |

## 2.4 Photonic Crystal Based Accelerators

### 2.4.1 Bragg Structures for High Frequency Laser Acceleration

Photonic crystals are an engineered periodic media in which, due to interference, the periodicity leads to a "forbidden" band or bands of electromagnetic frequencies. The forbidden bands disallow the propagation of electromagnetic radiation. The periodicity of these devices has length scales on a similar length scale to the wavelengths they are engineered for; in contrast with metamaterials which have the length scales of engineering much smaller than the wavelength engineered for. The fundamental property PhCs are engineered by is the permittivity/refractive index as it is the ratio between permittivities which creates the bandgap. These devices can be conceptually simple layers of alternating materials with dissimilar permittivites, also known as a one-dimensional photonic crystal as it is only periodic in one dimension. They can also extend up to three-dimensional periodic crystals in which there is a periodicity in all three axes.

The size of the bandgap created is in proportion to the ratio of the dielectrics used. A smaller bandgap will be created from a low ratio of dielectrics, and thus has the property of only excluding a narrow range of frequencies. A broader bandgap is created by a higher ratio of dielectrics but to get a large bandgap, high permittivity materials must be used which by consequence will cause a larger percentage of the field incident to couple into the material and thus be more sensitive to breakdown limit of the material, and machining defects. The selection of materials for the work in this thesis is discussed in chapter 5.

The bandgap created by photonic crystals allows them to be engineered for specific frequencies to be used as reflectors. This effect can be exploited to confine electromagnetic states in a vacuum channel as a quasi-waveguide. The expected advantage of using photonic crystal as the slow-wave structure is twofold: first that it can be tuned so that it preferentially confines a desired wavelength, but radiates the undesired wavelengths excited by HOMs; and secondly high fields on walls, and wall losses should be lower than conventional metallic waveguides which experience field emission and surface resistance. This is thanks to the skin depth property of materials, or the thickness of which for current density is $1/e$ of the surface current; where $e$ is the natural base. In dielectrics, the skin depth is much greater than in metals, thus ensuring energy deposited by the radiation per unit volume is lower.

The Bragg-based photonic crystal, being only periodic in one dimension, has attracted attention due to its simplicity. Due to scalability, fabrication of these structures requires only layer stacking or controlled deposition depending on which technology would be more applicable to the design frequency [53] and [47].

The micro-accelerator platform (MAP) structure shown in Fig. 2.4, was developed at UCLA and is a $1\,mm$ length optical-frequency Bragg stack consisting of layers of hafnia and zirconia. Hafnia, with a permittivity of $\varepsilon_r = 3.54$ at 800 nm; and zirconia, with $\varepsilon_r = 4.71$ [54] [55] [56] gives a dielectric ratio of 1.33 which was deemed sufficient for the MAP structure. This ratio, combined with the PhC geometry, determines the width of the photonic bandgap created. Testing of this structure [57, 58] however revealed that while accelerating gradients were $0.5\,GeV/m$, energy gain for the $60\,MeV$, $10\,pC$ beam was poor at $0.5\,keV$ with low uniformity. Additionally, the beam was launched with a repetition rate of $10\,Hz$ and the highest electric field to accelerating gradient in the structure was stated as being 2:1. The use of a beam longer than the wavelength of the laser used for excitation, combined with the aperture being smaller than the transverse size of the beam—whilst not the only properties which dictate beam losses—are compounding factors in this result. The values obtained are summarised in table 2.5.

Methods for coupling radiation into Bragg structures has also been studied. The use of a grating structure which offers side coupling with selective mode excitation was investigated [59, 60]. This uses a grating structure on the side of the vacuum channel to increase propagation into the Bragg waveguide with a selected number of layers with resulting output of a quasi-plane wave. A similar method for coupling into the MAP structure is also illustrated in Fig. 2.4

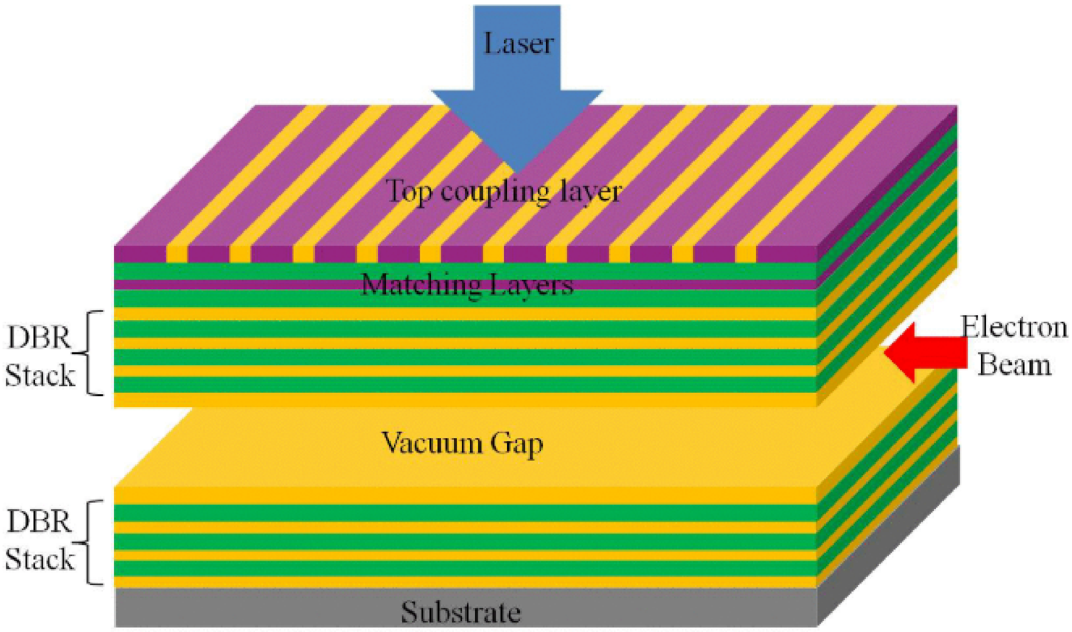

Figure 2.4: Micro-accelerator platform (MAP) structure as proposed and fabricated in [55].

Table 2.5: Experimental measurements for state of the art in Bragg Accelerator Structure

| Parameter | Value | Source |
|---|---|---|
| Highest Electric Field | $1\,GV/m$ | [58] |
| Highest Gradient Achieved | $0.5\,GeV/m$ | [58] |
| Largest Energy Gain | $0.5\,keV$ | [58] |
| Longest Accelerating Length | $1\,mm$ | [58] |
| Largest Charge Accelerated | $10\,pC$ | [57] |
| Highest Repetition Rate | $10\,Hz$ | [58] |

Bragg structures have been investigated for lower frequency devices such as free-electron maser at Strathclyde [61] [62] [63]. Using a cylindrical topology with internal corrugation, a Ka-band ($26.5-40\,GHz$) narrow-band source using $100\,A$, $200-300\,keV$ beam can be used to generate $1.5-2.0\,MW$, $200\,ns$ pulses giving a 5% conversion efficiency.

A summary of some experimentally measured state of the art THz acceleration figures is shown in table 2.5.

### 2.4.2 2D Photonic Crystals for High Frequency Laser Acceleration

As the dimensions of periodicity in a photonic crystal increase, so too does their ability to strongly confine the accelerating electromagnetic mode within the beam channel and therefore their characteristic impedance [47]. To maintain the dielectric ratio required for the bandgap, this can result in either high-$\varepsilon_r$ inclusions in a low-$\varepsilon_r$ background, or vice versa. While dielectric pillars offer some benefits in regards to dielectric acceleration as mentioned previously, a photonic-crystal based on pillars does not provide a $TM_z$ bandgap, only $TE_z$ and as such cannot be used for accelerating structures.

One geometry investigated in 2003 proposes a slab dielectric featuring circular holes and a triangular unit cell [64]. This work only focused on the characteristic impedance, with a calculated accelerating voltage of $190\,MV/m$. It was further investigated in [65] where it featured an internal corrugation which itself has a longitudinal periodicity and spatial amplitude modulation. This structure, seen in Fig. 2.5, has been proposed to simultaneously accelerate a particle bunch, and focus the beam. Published theoretical results put the expected accelerating gradient at $1-2.5\,GeV/m$ for $\gamma = 6-1000$, at the time of this thesis being written there are no published experimental results for this structure.

Another proposed 2D-periodic PBG-W structure is the longitudinal fibre as discussed in [66] and then investigated for accelerator applications in [67], [68]. The device, seen in Fig. 2.6 was calculated to have a characteristic impedance of $19\,\Omega$ and an accelerating field-max field ratio of $E_{acc}/E_{Max} = 0.48$. Experimental

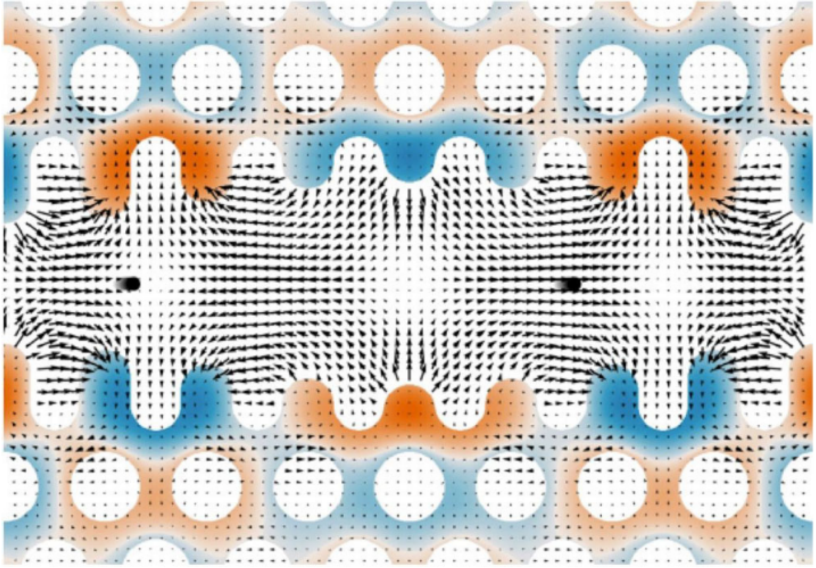

Figure 2.5: Schematic of the bi-periodic photonic-crystal waveguide as proposed in [65]

beam tests have not been published at time of writing.

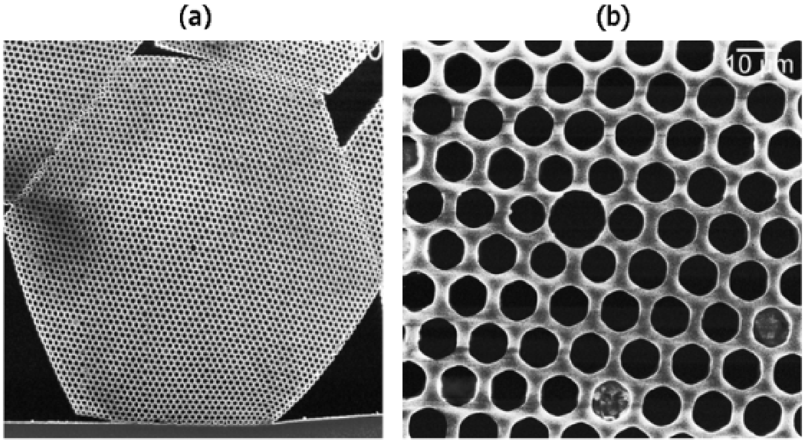

Figure 2.6: Photographs of the 2D-periodic PBG-W where (a) 700 $\mu m$ wide structure, and (b) 12 $\mu m$ diameter central defect as shown in [67].

### 2.4.3 3D Photonic Crystals for High Frequency Laser Acceleration

A 3D photonic crystal based waveguide is another geometry studied in literature. Opal, a well known gemstone [69], is a photonic crystal which features spheres of silica with diameter of similar order to the wavelength of visible light. it does

Table 2.6: Experimental measurements for state of the art in Woodpile Structure

| Parameter | Value | Source |
|---|---|---|
| Highest Electric Field | 2 GV/m | [75] |
| Highest Gradient Achieved | 530 MV/m | [73] |
| Longest Accelerating Length | 10.5 mm | [75] |
| Largest Charge Accelerated | 235 pC | [75] |

not however offer a bandgap which confines $TM_z$ modes. Additionally, “inverse opal” structure exists, but gives a small bandgap for the complexity [70]. Thus a different structure which must be both simple enough to manufacture, and offer a geometry which confines the correct accelerating modes. This resulted in the woodpile structure [71], an example of which is shown in Fig. 2.7. Simulated results for the woodpile, designed for bandgap of $4.26\,\mu m$ ($70.38\,THz$) gave expected accelerating voltages in excess of $1\,GV/m$ without damage [72]. These values are summarised in table 2.6

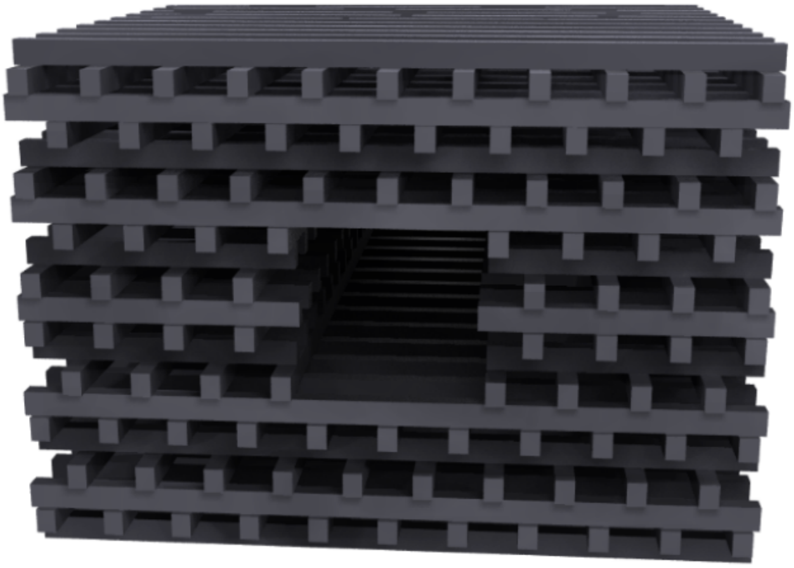

Figure 2.7: Schematic of the woodpile photonic-crystal waveguide as proposed in [73]

The woodpile structure promises some of the highest characteristic impedance (defined in chapter 3) of any photonic crystal structure [47] and has been experimentally investigated having been manufactured in silicon [74] [73] and alumina [75].

## 2.5 Hybrid Technologies

As with any technology, an approach to a problem rarely exists in isolation. Designs which incorporate multiple technologies mentioned in this section are also being investigated.

The first of these technologies that will be mentioned is the combination plasma-photonic crystal approach. The plasma photonic-crystal woodpile as tested in [76] uses an array of discharge tubes in the arrangement of the woodpile structure. While this technology closely resembles a metal-based artificial dielectric structure, it offers the additional benefits of switchable conductors without reconstruction. Whilst this design falls under the remit of photonic crystals, it has been investigated in work more closely related to metamaterials [77, 78]. Additionally, physical characterisation is at early stages and has not been investigated for accelerator applications.

Other hybrid plasma technologies are however at a more advanced readiness level. The "trojan horse" plasma wakefield acceleration, discussed in detail in [79]. Fundamentally, this technology uses both EDPWA and BDPWA in a multi-species plasma with the ratio of ionisation potentials (IP) being $\gg 1$. A bunch with a large charge density drives the low IP gas as a BDPWA but not the high IP gas which remains unionised. A laser pulse ionises the high IP gas which releases electrons into the BDPWA bubble

Hybrid designs for photonic crystal structures as proposed in [80] uses deformed photonic crystal walls or additional photonic crystal boundaries to act as a full 3D waveguide. Whilst this design focused on fibre optics, the acceleration capability of these hybrid waveguides has not been determined and may prove to be a contemporary to other all-dielectric designs.

## 2.6 Beam-Driven Accelerators

Many of the previous structures examined have required an external source of electromagnetic radiation for operation. As shown with the BDPWA technology, the energy to drive a structure does not need to come from an electromagnetic wave but can instead be supplied by a particle beam depositing its energy into the structure. In this section, two applications of this beam/structure interaction will be investigated: Wakefield acceleration, and Cherenkov sources. The former uses a high-charge (drive) bunch to interact with a slow-wave structure to create an accelerating mode in the structure. A low-charge (witness) bunch coupled in at the correct phase will be accelerated by the excited mode. The latter uses the slow-wave structure to instead excite the mode for other applications such as a radiation source.

As many structures discussed in this thesis are sub-millimetre in scale, applicable electron beams are required. Brookhaven National Lab is capable of producing quasi-rectangular $100\,pC$ electron bunches with $60\,MeV$ of energy focused into a $100\,\mu m$ diameter and $300\,\mu m$ length [81]. Work at Daresbury has utilised a beam of Gaussian $100\,pC$ electron bunches with $35\,MeV$ of energy and a Gaussian RMS value (i.e. standard deviation $\sigma_r$) between $70 - 100\,\mu m$; with a length of $\sigma_z = 2\,ps$ and $\sigma_z = 0.3\,ps$ after bunch compression, giving a spatial length of $\sigma_z \approx 90\,\mu m$ [82]. Attosecond-length electron bunches have also been achieved at SLAC, offering bunches with length of $\sigma_z = 410\,as$ $(123\,nm)$ with $\sigma_r = 100\,\mu m$, $60\,MeV$ energy and $1\,pC$ bunch charge [83].

For CCR, the beam must be longitudinally much smaller than the wavelength whilst simultaneously being small enough to propagate in a structure without serious edge effects or alignment issues. Aperture size to transverse beam size of $10 : 1$ or greater being preferable [84] however $2 : 1$ being adequate for preliminary work as more than 70% of the beam can be transported in a $40\,mm$ long DLW structure as shown in [85]. Longitudinal size of the beam for CCR emission shows a requirement of $\sigma_z/\lambda \lessapprox 1/4$ [86].

### 2.6.1 Dielectric-Lined Waveguides for High Frequency Acceleration

In linear acceleration, slow wave structures are required to reduce the phase velocity of a propagating mode to match the velocity of the particles to be accelerated. To achieve this the structure can be as simple as applying a dielectric lining to a rectangular waveguide (DLW). As conventional RF technology does not scale to THz and beyond, this DLW provides an alternative methodology, and also offers simplicity in both construction and available analytic approach to construction; coupled with the high fields that dielectrics can support.

A silica-based DLW has been investigated at Daresbury for use in both acceleration [18] and deflection [87] driven by an external pulsed-laser source; and for novel wakefield applications [85]. Laser-driven acceleration work made use of a $35\,MeV$ electron beam which was accelerated at a gradient of $2\,MV/m$. The experiments were based at CLARA which has a $70 - 100\,pC$, $35\,MeV$ electron beam at $0.3 - 2\,ps$ length and a designed minimum RMS transverse size of $100\,\mu m$ however lower has been achieved experimentally [88, 89]. A CCR source investigated based on the DLW with the CLARA beam was investigated [82]. A DLW in which the aperture could be varied between $300 - 910\,\mu m$ in a parallel-plate geometry was found to provide $0.55 - 0.95\,THz$.

Work in [90] uses a cylindrical alumina-lined DLW as a microbuncher. It achieves this by injecting an energy-chirped electron beam and the short-range wake, or wake within the region of the bunch that excites it, and the structure effectively converts the energy-chirp to spatial chirp—with the frequency tuning of the structure affecting the spatial period of the microbunches. For this work, a $130\,pC$ bunch was used at $57\,MeV$ and $1\,MeV$ energy chirp.

### 2.6.2 Photonic Crystal Based Wakefield Structures

As with the CCR work discussed previously, dielectric can be used as a slow wave structure for a high frequency Cherenkov source. Photonic crystals, being pure dielectric, offer this benefit with the additional capability of confinement without requiring metal walls. The Bragg structure was used as a CCR source in [91] being driven by a $1\,ps$, $100\,pC$ bunch. It produced a narrowband $210\,GHz$ excitation. It also offered reduced energy spread of the bunch reducing the energy spread from $120\,keV$ to $60\,keV$ and reduced mean central energy by $70\,keV$. One further key point of this work is that the excitation and beam properties are consistent with simulations.

When a laser pulse is counter-propagated in the Bragg structure to an electron bunch, the Compton-scattering effect leads to an efficient X-ray source [92] [93]. Work at Brookhaven published that the scattering between their $60\,MeV$ beam and $10.6\,\mu m$ carbon dioxide laser produced $6.5\,keV$ $(0.2\,nm)$ photons; and at the PLEIADES facility in Lawrence Livermore lab produced $78\,keV$ $(0.015\,nm)$ from a $57\,MeV$ beam and a $820\,nm$ Ti-Sapphire laser pulse. Furthermore, using a single laser with pulses to both accelerate the electrons, and to counter-propagate allowed them to produce $0.4 - 2\,keV$ $(3 - 0.6\,nm)$ photons.

Coherent Cherenkov radiation has also been proposed for higher-dimension 2D-periodicity photonic crystals [94] and experimentally investigated in the 3D-periodic woodpile using elliptical beams to mitigate higher-order and spurious modes [75]. The woodpile structure with a vertical aperture of $250\,\mu m$ produced CCR at $0.10 - 0.15\,THz$ with the elliptical beam reducing the higher-order mode at $0.25 - 0.30\,THz$ to negligible amplitude.

# 3

# Overview of Electromagnetic Theory for PBG-W Particle Accelerators

This chapter presents an overview of the fundamental theory of photonic crystal technology and how this can be used for the design of electromagnetic wave confinement. Then, the design methodology developed in this thesis for the analysis and comparison of PBG waveguides in the context of broadband THz acceleration is provided. Following, considerations on the available manufacturing techniques for the realisation of the proposed designs are given. Finally, the computational methods used in this work with their advantages and limitations are briefly defined.

## 3.1 Maxwell equations in periodic media

As with any study of electromagnetic phenomena, one must begin at the start. In 1865, James Clark Maxwell published "A Dynamical Theory of the Electromagnetic Field", in which he derived the electromagnetic wave equation and developed a series of twenty equations. Eighteen of these twenty equations were vectorised, by Oliver Heaviside and Willard Gibbs in 1884, into six. These combined eight being rewritten as the famous four—common in all modern electromagnetic study—two constitutive equations, and the continuity of charge. In differential form, these equations are:

Gauss' Law:

$$\nabla \cdot \mathbf{D} = \rho \tag{3.1}$$

Where $\mathbf{D}$ is the displacement field, and $\rho$ is the charge density. Gauss' Law for Magnetism:

$$\nabla \cdot \mathbf{B} = 0 \tag{3.2}$$

Where $\mathbf{B}$ is the magnetic flux density. Faraday's Law:

$$\nabla \times \mathbf{E} = -\frac{\partial \mathbf{B}}{\partial t} \tag{3.3}$$

Where $\mathbf{E}$ is the electric field and $t$ is time. Ampère's law with Maxwell's correction:

$$\nabla \times \mathbf{H} = \mathbf{J} + \frac{\partial \mathbf{D}}{\partial t} \tag{3.4}$$

Where $\mathbf{H}$ is the magnetic field and $\mathbf{J}$ is the current density. Additionally the constitutive relationships:

$$\mathbf{B} = \mu \mathbf{H} = \mu_0 \mathbf{H} + \mathbf{M} \tag{3.5}$$

$$\mathbf{D} = \varepsilon \mathbf{E} = \varepsilon_0 \mathbf{E} + \mathbf{P} \tag{3.6}$$

Where $\mu$ and $\varepsilon$ are the permeability and permittivity of the material, $\mu_0$ and $\varepsilon_0$ are the permeability and permittivity of free space, $\mathbf{P}$ is polarisation of the material, and $\mathbf{M}$ is the magnetisation. And the continuity of charge:

$$\nabla \cdot \mathbf{J} = -\frac{\partial \rho}{\partial t} \tag{3.7}$$

For completeness, Ohm's law should also be mentioned:

$$\mathbf{J} = \sigma_c \mathbf{E} \tag{3.8}$$

where $\sigma_c$ is the electrical conductivity of the material.

From these equations the wave equation can be derived. Taking the curl of each Faraday's Law and Ampère's law with Maxwell's correction yields:

$$\nabla \times \nabla \times \mathbf{E} = -\frac{\partial}{\partial t}[\nabla \times \mathbf{B}] \tag{3.9}$$

$$\nabla \times \nabla \times \mathbf{B} = \nabla \times \mathbf{J} + \frac{\partial}{\partial t}[\nabla \times \mathbf{D}] \tag{3.10}$$

Using the known vector identity:

$$\nabla \times [\nabla \times \mathbf{X}] = \nabla(\nabla \cdot \mathbf{X}) - \nabla^2 \mathbf{X} \tag{3.11}$$

where $\mathbf{X}$ is an arbitrary spatial vector function. For vacuum propagation of waves, there are no free charges or current, and it is neither polarisable nor magnetisable, thus $\rho = \mathbf{J} = \mathbf{M} = \mathbf{P} = 0$; additionally, $\varepsilon = \varepsilon_0$ and $\mu = \mu_0$. This yields the pair of equations:

$$\nabla^2 \mathbf{E} = \frac{1}{c^2}\frac{\partial^2 \mathbf{E}}{\partial t^2} \tag{3.12}$$

$$\nabla^2 \mathbf{B} = \frac{1}{c^2}\frac{\partial^2 \mathbf{B}}{\partial t^2} \tag{3.13}$$

Where $c$ is the speed of light, and:

$$c = \frac{1}{\sqrt{\mu_0 \varepsilon_0}} \tag{3.14}$$

Expanding this analysis into dielectrics, some assumptions hold true for many dielectric materials and will be used. Firstly we assume that the field strengths present in said dielectrics will remain within the region in which linear behaviour is observed and that the material is macroscopic and isotropic compared to the wavelengths of interest. Secondly it is assumed that the dielectric materials will exhibit negligible magnetisation; and polarisation is negligible without a driving field (i.e. the dielectrics are not ferroelectric). Additionally it is assumed the dielectric at Cartesian position vector $\mathbf{r}$ does not vary with time $t$ and that the materials are transparent thus the relative permittivity and permeability $\varepsilon_r$ and $\mu_r$ are real and positive. Finally for many dielectric materials, the relative permeability is close to the vacuum permeability and as such for analysis $\mu_r = 1$. Thus equations 3.5 and 3.6 become:

$$\mathbf{B}(\mathbf{r}, t) = \mu_0 \mathbf{H}(\mathbf{r}, t) \tag{3.15}$$

$$\mathbf{D}(\mathbf{r},t) = \varepsilon_0\varepsilon_r(\mathbf{r})\mathbf{E}(\mathbf{r},t) = \varepsilon(\mathbf{r})\mathbf{E}(\mathbf{r},t) \tag{3.16}$$

Which in turn, when applied to Maxwell's equations (Eqns. 3.1–3.4), these become:

$$\nabla \cdot [\varepsilon(\mathbf{r})\mathbf{E}(\mathbf{r},t)] = 0 \tag{3.17}$$

$$\nabla \cdot \mathbf{H}(\mathbf{r},t) = 0 \tag{3.18}$$

$$\nabla \times \mathbf{E}(\mathbf{r},t) = -\mu_0 \frac{\partial \mathbf{H}(\mathbf{r},t)}{\partial t} \tag{3.19}$$

$$\nabla \times \mathbf{H}(\mathbf{r},t) = \varepsilon(\mathbf{r}) \frac{\partial \mathbf{E}(\mathbf{r},t)}{\partial t} \tag{3.20}$$

Now defining the propagating fields as a complex-valued field we can define:

$$\begin{aligned} \mathbf{H}(\mathbf{r},t) &= \mathbf{H}(\mathbf{r}) \exp[-i\omega t] \\ \mathbf{E}(\mathbf{r},t) &= \mathbf{E}(\mathbf{r}) \exp[-i\omega t] \end{aligned} \tag{3.21}$$

where $i$ is the imaginary unit, $\omega$ is the angular frequency. Inserting Eqns. 3.21 into 3.17 and 3.18 we get:

$$\nabla \cdot [\varepsilon(\mathbf{r})\mathbf{E}(\mathbf{r})] = 0 \tag{3.22}$$

$$\nabla \cdot \mathbf{H}(\mathbf{r}) = 0 \tag{3.23}$$

Since these equations are now time independent, the propagating wave can be defined spatially. Thus assuming the wave is a transverse plane wave, it can be defined in terms of wave vector $\mathbf{k}$:

$$\mathbf{H}(\mathbf{r}) = \mathbf{a} \exp[i\mathbf{k} \cdot \mathbf{r}] \tag{3.24}$$

where **a** is the amplitude vector of the plane wave, with requirement $\mathbf{a} \cdot \mathbf{k} = 0$. With this, Eqns. 3.19 and 3.20 become:

$$\nabla \times \mathbf{E}(\mathbf{r}) - i\omega\mu_0\mathbf{H}(\mathbf{r}) = 0 \tag{3.25}$$

$$\nabla \times \mathbf{H}(\mathbf{r}) + i\omega\varepsilon(\mathbf{r})\mathbf{E}(\mathbf{r}) = 0 \tag{3.26}$$

The magnetic and electric fields can then be decoupled. Dividing 3.26 by $\varepsilon_r(\mathbf{r})$, and taking the curl, we get the magnetic master equation:

$$\nabla \times \left( \frac{\nabla \times \mathbf{H}(\mathbf{r})}{\varepsilon_r(\mathbf{r})} \right) = \left( \frac{\omega}{c} \right)^2 \mathbf{H}(\mathbf{r}) \tag{3.27}$$

from equation 3.14 and $\nabla \times \mathbf{E}$ is given in Eqn. 3.25. This eigenvalue problem is the basis for calculating modes in dielectric media. From this, the electric fields can be extracted by:

$$\mathbf{E}(\mathbf{r}) = \frac{i}{\omega\varepsilon(\mathbf{r})} \nabla \times \mathbf{H}(\mathbf{r}) \tag{3.28}$$

and from Eqn. 3.27 we can define the master equation as a Hermitian operator eigenvalue problem:

$$\hat{\mathbf{\Theta}}\mathbf{H}(\mathbf{r}) = \left( \frac{\omega}{c} \right)^2 \mathbf{H}(\mathbf{r}) \tag{3.29}$$

Where:

$$\hat{\mathbf{\Theta}}\mathbf{H}(\mathbf{r}) \triangleq \nabla \times \left( \frac{\nabla \times \mathbf{H}(\mathbf{r})}{\varepsilon_r(\mathbf{r})} \right) \tag{3.30}$$

## 3.2 Lattice Geometry

Now that we have Maxwell's equations defined for dielectric structures, the definitions can be refined for periodic dielectric structures. When structures exhibit periodicity, they also begin to exhibit collective bulk behaviour. The more defined and consistent the periodic structure, the stronger the bulk behaviour. In this thesis, most work has focused on structures which exhibit two dimensions of periodicity, with the third dimension being either infinitely non-periodic, or non-periodic with the perfect electrical conductor (PEC) boundary condition in which transverse electric fields $E_t = 0$. This section will examine the effects of constructing these 2D-periodic structures with respect to geometry, materials, and propagating modes.

To proceed with the analysis of the photonic crystal based structures examined in this thesis, examining the physics of 1D-periodic structures allows for the simplest explanation of the fundamental property required in these structures - the photonic bandgap. In photonic crystal media, the smallest repeating zone that can be defined on the photonic crystal vectors is known as the "Brillouin zone". To define this zone, a Fourier analysis on the structure determines the spatial harmonics and the lowest one is taken. A more comprehensive analysis of this can be found in [95]. Once the Fourier series is known, the periodicity function of the photonic crystal can be defined using the primitive lattice vectors, or the smallest vector which can point from one point in the PhC lattice to another. Thus defining a lattice vector in terms of primitive lattice vectors as:

$$f(\mathbf{r}) = f(\mathbf{r} + \mathbf{R}) \tag{3.31}$$

where $f$ is a function periodic on the lattice, thus $\mathbf{R}$ is the lattice vector. thus reciprocal lattice vector $\mathbf{G}$ can be defined as:

$$\mathbf{R} \cdot \mathbf{G} = N2\pi \tag{3.32}$$

for any value of $\mathbf{R}$, where $N$ is an integer. $\mathbf{R}$ and $\mathbf{G}$ are of the form:

$$\mathbf{R} = l\mathbf{a}_1\hat{\imath} + m\mathbf{a}_2\hat{\jmath} + n\mathbf{a}_3\hat{k} \tag{3.33}$$

and

$$\mathbf{G} = l'\mathbf{b}_1\hat{\imath} + m'\mathbf{b}_2\hat{\jmath} + n'\mathbf{b}_3\hat{k} \tag{3.34}$$

where $(l, m, n)$ and $(l', m', n')$ are integers. For one-dimensional PhCs such as in Fig. 3.1, which is periodic in only one dimension, we can define, $\mathbf{a}_i \cdot \mathbf{b}_j = 2\pi\delta_{ij}$ and thus reciprocal lattice vectors can be written in terms of lattice vectors:

$$\mathbf{b}_1 = \frac{2\pi(\mathbf{a}_2 \times \mathbf{a}_3)}{\mathbf{a}_1 \cdot (\mathbf{a}_2 \times \mathbf{a}_3)},\ \mathbf{b}_2 = \frac{2\pi(\mathbf{a}_3 \times \mathbf{a}_1)}{\mathbf{a}_1 \cdot (\mathbf{a}_2 \times \mathbf{a}_3)},\ \mathbf{b}_3 = \frac{2\pi(\mathbf{a}_1 \times \mathbf{a}_2)}{\mathbf{a}_1 \cdot (\mathbf{a}_2 \times \mathbf{a}_3)} \tag{3.35}$$

From this, we can define the Bloch wave vector in any photonic media as:

$$\mathbf{k} = k_1\mathbf{b}_1 + k_2\mathbf{b}_2 + k_3\mathbf{b}_3 \tag{3.36}$$

where $\mathbf{k}$ lies inside the Brillouin zone. Thus we can now define the general eigenvector equation for photonic crystals:

$$\mathbf{H}_{\mathbf{k}}\left(\mathbf{r}\right) = e^{i\mathbf{k}\cdot\mathbf{r}}\mathbf{u}_{\mathbf{k}}\left(\mathbf{r}\right) \tag{3.37}$$

where $\mathbf{u}$ is a periodic function. Now since we know Eqn. 3.37, we can define the photonic bands in a periodic structure as an eigenvalue via Eqn. 3.29.

$$\begin{gathered}
\hat{\boldsymbol{\Theta}}\mathbf{H}_{\mathbf{k}} = \left(\frac{\omega(\mathbf{k})}{c}\right)^2 \mathbf{H}_{\mathbf{k}} \\
\nabla \times \frac{1}{\varepsilon_r(\mathbf{r})}\nabla \times e^{i\mathbf{k}\cdot\mathbf{r}}\mathbf{u}_{\mathbf{k}}(\mathbf{r}) = \left(\frac{\omega(\mathbf{k})}{c}\right)^2 e^{i\mathbf{k}\cdot\mathbf{r}}\mathbf{u}_{\mathbf{k}}(\mathbf{r}) \\
(i\mathbf{k} + \nabla) \times \frac{1}{\varepsilon_r(\mathbf{r})}(i\mathbf{k} + \nabla) \times \mathbf{u}_{\mathbf{k}}\left(\mathbf{r}\right) = \left(\frac{\omega(\mathbf{k})}{c}\right)^2 \mathbf{u}_{\mathbf{k}}(\mathbf{r})
\end{gathered} \tag{3.38}$$

and thus the Hermitian operator for photonic-crystal modes can be defined as:

$$\hat{\boldsymbol{\Theta}}_{\mathbf{k}}\mathbf{u}_{\mathbf{k}}(\mathbf{r}) \triangleq (i\mathbf{k} + \nabla) \times \frac{1}{\varepsilon_r(\mathbf{r})}(i\mathbf{k} + \nabla) \times \mathbf{u}_{\mathbf{k}}(\mathbf{r}) \tag{3.39}$$

Since the functions within the Brillouin zone still feature symmetry, those which vary by symmetry alone can be discounted. Thus we define within the Brillouin zone, the “irreducible Brillouin zone” within which all functions are unique. Therefore when the periodicity of a photonic crystal is known, solving over all wave-vectors in the irreducible Brillouin zone allows us to calculate the band diagram. This is the basis of the software MPB [96] which is detailed later in the chapter.

### 3.2.1 1D-Periodic Multilayer Film

The 1D-Periodic multilayer film, also known as a Bragg stack and shown in Fig. 3.1, uses alternating materials of juxtaposed permittivity, in which the ratio and layer thickness is tuned to allow the stack to function as a mirror. Exploiting the symmetry of the structure, the modes which can propagate in the structure can be described in terms of the wave-vector $\mathbf{k}$, the propagation vector $\mathbf{r}$, and band number $n$. Since the structure is only periodic in the y-direction, we can separate $\mathbf{k}$ into the xz plane $\mathbf{k}_{||}$ and $k_y$, and equivalently for $\mathbf{r}$ into $\mathbf{r}_{||}$ and $y$. Since we know the wave vectors describe how the mode is affected by translation operators, and the band number is proportional to frequency, the modes in Bloch form can be written as:

$$\mathbf{H}_{n,k_y,\mathbf{k}_{||}}(\mathbf{r}) = e^{i\mathbf{k}_{||}\cdot\mathbf{r}_{||}} e^{ik_y y} \mathbf{u}_{n,k_y,\mathbf{k}_{||}}(y) \tag{3.40}$$

Where $\mathbf{u}(y) = \mathbf{u}(y+R) \Rightarrow |R \mod a| = 0$. Examining $\mathbf{k}$ as it’s constituents $k_x, k_y, k_z$, as the structure is infinite in the x-z plane, $-\infty < k_x, k_z < \infty$. Due to the discrete translational symmetry the structure exhibits in $y$ however, we can restrict $k_y$ to a finite length, the 1D-Periodic Brillouin zone:

$$-\pi/a < k_y < \pi/a \tag{3.41}$$

Now if we consider a wave propagating purely in $y$ and thus $\mathbf{k} = k_y$. Knowing the dispersion relationship:

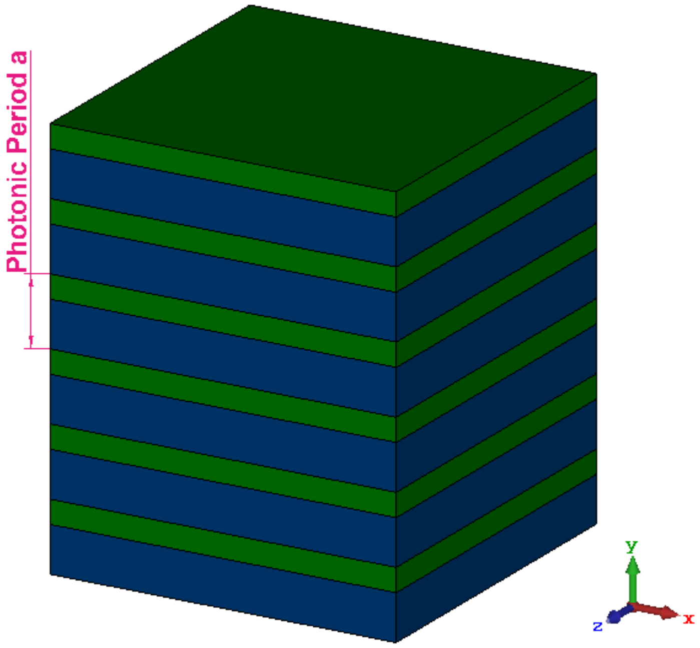

Figure 3.1: A 1D-periodic multilayer film, or Bragg stack. Each layer is a quarter wavelength thick, with green $\varepsilon_r = 12$ and blue $\varepsilon_r = 3$, giving a dielectric ratio of 4. The photonic period $a$ in this scenario the sum of the thicknesses of both layers.

$$\omega(k) = \frac{ck}{n} \tag{3.42}$$

And from Eqn. 3.41 we can see that $k_y$ will repeat as the structure repeats, thus the dispersion of the mode must also repeat and to preserve symmetry it must fold back on itself. The gap between bands $n$ occurs at the edge of the Brillouin zone, where $k_y = \pi/a$. From this, the lattice vectors are trivial and can be written as:

$$\mathbf{a}_1 = a\hat{j} \tag{3.43}$$

Where $\mathbf{a}_2$ and $\mathbf{a}_3$ can assume any value due to homogeneity in that axis. Thus we can write the reciprocal lattice vector:

$$\mathbf{b}_1 = \frac{2\pi}{a}\hat{j} \tag{3.44}$$

### 3.2.2 2D-Periodic Photonic Structure

Continuing from the 1D Bragg structure proposed, we can expand this definition to a 2D structure based on a triangular lattice, which will be extensively investigated in this thesis.

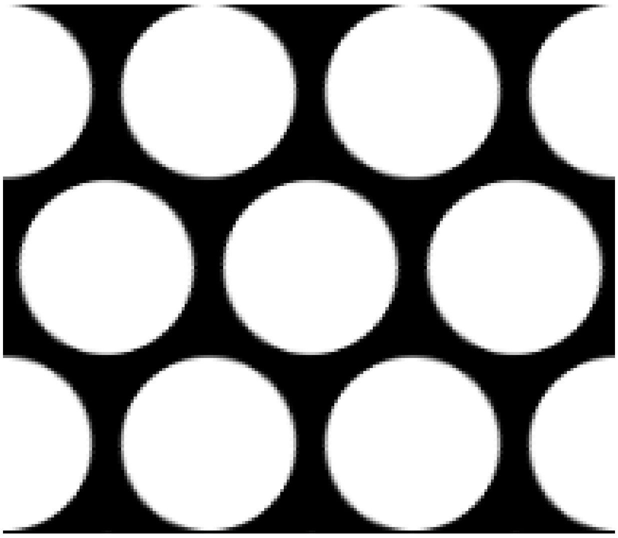

Figure 3.2: Triangular lattice photonic crystal, with black as dielectric, and white as vacuum.

Examining Fig. 3.2 we can identify the lattice vectors $\mathbf{a}_1$ and $\mathbf{a}_2$, and primitive lattice vectors $\mathbf{b}_1$ and $\mathbf{b}_2$ as follows:

$$\mathbf{a}_1 = a\frac{\left(\hat{k}+\hat{\jmath}\sqrt{3}\right)}{2},\ \mathbf{a}_2 = a\frac{\left(\hat{k}-\hat{\jmath}\sqrt{3}\right)}{2} \tag{3.45}$$

$$\mathbf{b}_1 = \frac{2\pi}{a}\frac{\left(\hat{k}+\hat{\jmath}\right)}{\sqrt{3}},\ \mathbf{b}_2 = \frac{2\pi}{a}\frac{\left(\hat{k}-\hat{\jmath}\right)}{\sqrt{3}} \tag{3.46}$$

where $\mathbf{a}_3$ can assume any value due to homogeneity in that axis.

As with all photonic crystals, the ratio of permittivities determines the bandgap. Thus while this structure could be a composite of multiple materials, the simplest would be a solid slab of dielectric, with vacuum holes through it. The bandgap therefore purely depends on the choice of primary dielectric to manufacture. For 2D-PBG-based structures, the bandgap is typically not valid for every polarisation of the electromagnetic wave propagation. For structures which are isolated islands of dielectric perpendicular to the direction of electromagnetic propagation, such as discrete pillars, the bandgap will be predominantly for transverse-electric electromagnetic states—or states in which the electric field vector is perpendicular to the axis of propagation. Similarly, for thin interconnected “veins” the bandgap will be for transverse-magnetic electromagnetic states. A combination of these two structures can be found in a triangular-hole array where the 2D periodic structure can be seen as localised islands connected by thin dielectric veins. This combination potentially allows the design of a TE/TM bandgap that overlap in a similar frequency range leading to a complete bandgap.

## 3.3 Photonic Crystal Structures for High Frequency Accelerators

As in previous sections discussed, the fundamental property of photonic crystals is to provide a bandgap. This forbidden band disallows electromagnetic radiation at certain frequencies to propagate. This property is exploited in photonic crystal technology to design different functionalities whose building blocks are typically resonant cavities and waveguides. The design principle is based on the so-called ”defect strategy”. Disrupting the periodicity of the photonic crystal introduces a a defect and thus a discontinuity in the forbidden region. This discontinuity can be used for confinement in a similar way to a conventional metallic waveguide and the propagating modes feature similarities with slow-wave metal structures.

In hollow smooth-walled metal waveguides—propagating modes are typically propagate with a component of the magnetic field in the axis of propagation, also known as transverse-electric (TE) modes, or similarly with electric field in the axis of propagation known as transverse-magnetic (TM) modes. For particle acceleration, the aim would be to use the TM mode. A slow wave structure is required to control the phase velocity—or velocity of the wave sinusoid—of the accelerating radiation in the waveguide. Without this, the phase velocity of the accelerating TM modes never becomes subluminal and thus cannot be coupled with a propagating particle beam. When the waveguides feature a slow-wave structure, the effect is to distort the pure TE/TM distinction of the modes and they become hybrid. The group velocity—or velocity of the wave packet—determines how long the accelerating wave will co-propagate with the particles to be accelerated. For free space propagation $v_p = v_g = c$ and thus the accelerating structure is required not only for confinement but synchronism.

To obtain some details on the scaling of the structures relative to properties such as group velocity, surface fields, and accelerating fields, we can start with the assumption of a speed-of-light TM mode [47] in which $\mathbf{E} = [0\,0\,E_z]^T$, and $H_z = 0$. From this, Maxwell's equations can be reduced to a transverse form:

$$\nabla_\perp \times \mathbf{E}_\perp = 0 \tag{3.47}$$

$$\nabla_\perp \times \mathbf{H}_\perp = i\omega E_z \hat{k} \tag{3.48}$$

$$\nabla_\perp \times E_z \hat{k} = 0 \tag{3.49}$$

$$\mathbf{E}_\perp = -Z_0 \hat{k} \times \mathbf{H}_\perp \tag{3.50}$$

From Eqn. 3.49, We can also rewrite Eqn. 3.47 as a scalar potential function $-\nabla^2\Phi$. Using this and Eqn. 3.50 we can solve Eqn. 3.48:

$$\nabla^2\Phi = -\frac{i\omega E_z}{c} \tag{3.51}$$

From the assumption that the value of $E_z$ has a constant value in the plane perpendicular to the direction of propagation, Eqn. 3.51 has the solution:

$$\Phi = -\frac{A\left(x^2 + \alpha_e y^2\right)}{2} \tag{3.52}$$

And thus the field components of the TM mode are:

$$\mathbf{E}_\perp = A\left(x\hat{i} + \alpha_e y\hat{j}\right) \tag{3.53}$$

$$\mathbf{H}_\perp = \frac{A}{Z_0}\left(x\hat{i} - \alpha_e y\hat{j}\right) \tag{3.54}$$

$$E_z = \frac{ic}{\omega}A\left(1+\alpha_e\right) \tag{3.55}$$

where $A$ is a constant, and $\alpha_e = 1 - e_e$ and $e_e$ is the elliptic eccentricity of the waveguide. From this, we can get the ratio of accelerating to deflecting field at the walls for a fundamental harmonic TM mode as:

$$\frac{E_z}{\mathbf{E}_\perp} = \frac{\lambda_0\left(1+\alpha_e\right)}{\pi D} \tag{3.56}$$

where D is the semi-minor axis of the channel. With this, if we assume all energy stored in the photonic crystal is in magnetic fields, we can write the group velocity of the above accelerating mode as:

$$v_g \leqslant \frac{c}{1 + 2\left(E_z/|\mathbf{E}_\perp|\right)^2} \tag{3.57}$$

While these equations can give an approximation of the modal behaviour in a PhC based waveguide accelerator, the boundary conditions are not metallic. The modes propagating are typically hybrid modes and are more closely aligned with the mode structure in dielectric-lined waveguides. These hybrid modes propagate as a superposition of both TE and TM modes and have a different definition: if the mode has no electric field perpendicular to the dielectric—is known as longitudinal section electric (LSE); similarly for magnetic fields known as LSM [97]. We can write the dispersion for the LSE$_{mn}$ as:

$$\begin{aligned} k^{(0)}_{ymn}\sin\left[k^{(1)}_{ymn}(b-a)\right]\sin\left[k^{(0)}_{ymn}a\right]... \\ -k^{(1)}_{ymn}\cos\left[k^{(0)}_{ymn}a\right]\cos\left[k^{(1)}_{ymn}(b-a)\right] = 0 \end{aligned} \tag{3.58}$$

The dispersion for the LSM$_{mn}$ mode can also be written:

$$\begin{aligned} &k_{ymn}^{(1)} \sin\left[k_{ymn}^{(1)}(b-a)\right] \sin\left[k_{ymn}^{(0)} a\right] ... \\ &\qquad -\varepsilon_r k_{ymn}^{(0)} \cos\left[k_{ymn}^{(0)} a\right] \cos\left[k_{ymn}^{(1)}(b-a)\right] = 0 \end{aligned} \tag{3.59}$$

When assuming a perfectly conducting boundary [98], the potential function $\psi$ for the LSE can be written as:

$$\psi_{hmn} = \begin{cases} A_{mn} \dfrac{1}{i\omega\mu_0} \cos\left[\dfrac{m\pi}{w}\left(x+\dfrac{w}{2}\right)\right] \cos\left[k_{ymn}^{(0)} y\right] e^{-i\beta_{mn} z} & 0<y<a \\ B_{mn} \dfrac{1}{i\omega\mu_0} \cos\left[\dfrac{m\pi}{w}\left(x+\dfrac{w}{2}\right)\right] \sin\left[k_{ymn}^{(1)}(b-y)\right] e^{-i\beta_{mn} z} & a<y<b \end{cases} \tag{3.60}$$

and similarly the LSM mode:

$$\psi_{emn} = \begin{cases} C_{mn} \sin\left[\dfrac{m\pi}{w}\left(x+\dfrac{w}{2}\right)\right] \sin\left[k_{ymn}^{(0)} y\right] e^{-i\beta_{mn} z} & 0<y<a \\ D_{mn} \sin\left[\dfrac{m\pi}{w}\left(x+\dfrac{w}{2}\right)\right] \cos\left[k_{ymn}^{(1)}(b-y)\right] e^{-i\beta_{mn} z} & a<y<b \end{cases} \tag{3.61}$$

which provide the basis to extract the mode field components. These modes provide a good approximation to the modes that can be found in a PhC-waveguide. The assumption of a perfectly conducting electric boundary however no longer applies. Instead, the boundary condition is of evanescent decay, where the modes have the form:

$$\mathbf{H}(\mathbf{r}) = e^{iky}\mathbf{u}(y)\, e^{-\kappa y} \tag{3.62}$$

where the wave vector is complex $k + i\kappa$ and the imaginary component causes the wave to decay over length $1/\kappa$ [95]. Thus while the dielectric-lined metallic waveguides have a concise analytic solution, the photonic-bandgap based waveguides are highly dependent on photonic crystal geometry.

## 3.4 Broadband Acceleration

Conventional RF devices often operate with a bandwidth of a few percent [99, 100]. These narrowband sources have negligible non-synchronous components of the pulse and figures of merit can be evaluated at only the frequency of interest. For lasers to achieve high powers at THz frequencies however, the use of few-cycle pulses [87] generates bandwidths of many 10's of percent. In this broadband regime, the asynchronous propagating frequency components of the acceleration pulse will also have a transient effect on the accelerating voltage. This can be illustrated as the consequence of a Fourier transform of the pulse having a broadband energy spectral distribution (ESD). Narrowband ESD pulses can be approximated as a pure Gaussian distribution:

$$\widetilde{U}(\omega) = U_{max} \exp\left[-\frac{(\omega-\omega_0)^2}{2\sigma^2}\right] \; (J/Hz) \tag{3.63}$$

Where $\omega_0$ is the centre frequency, $U_{max}$ is the spectral energy at the centre-frequency, and $\sigma$ is the standard deviation of the curve. Broadband ESD pulses can however show a skew in the distribution. To incorporate a skew in a Gaussian, it can be modified with an arbitrarily chosen fit term which allows it to fit the pulse distribution thus:

$$\widetilde{U}(\omega) = U_{max} \exp\left[-\left(\frac{(\omega-\omega_0)}{\sqrt{2}\sigma}\right)^2 \left(\frac{\omega_0}{\omega}\right)^x\right] \; (J/Hz) \tag{3.64}$$

Where $x$ is the source-dependent frequency-decay coefficient. Thus equations 3.63 and 3.64 are consistent when $x = 0$. This gives the expected exponential decay profile at frequencies higher than $\omega_0$ while preserving the Gaussian distribution below. This can be seen in Fig. 3.3. This method was used to represent the data for an experimentally obtained THz pulse at Daresbury.

The pulse used for analysis has a peak at $\omega_0$ with $E_{max}$ for each $\sigma$ calculated to provide $\int_0^\infty \widetilde{U}(\omega)\, d\omega = 100\, mJ$. The $100\, mJ$ figure was chosen as while current

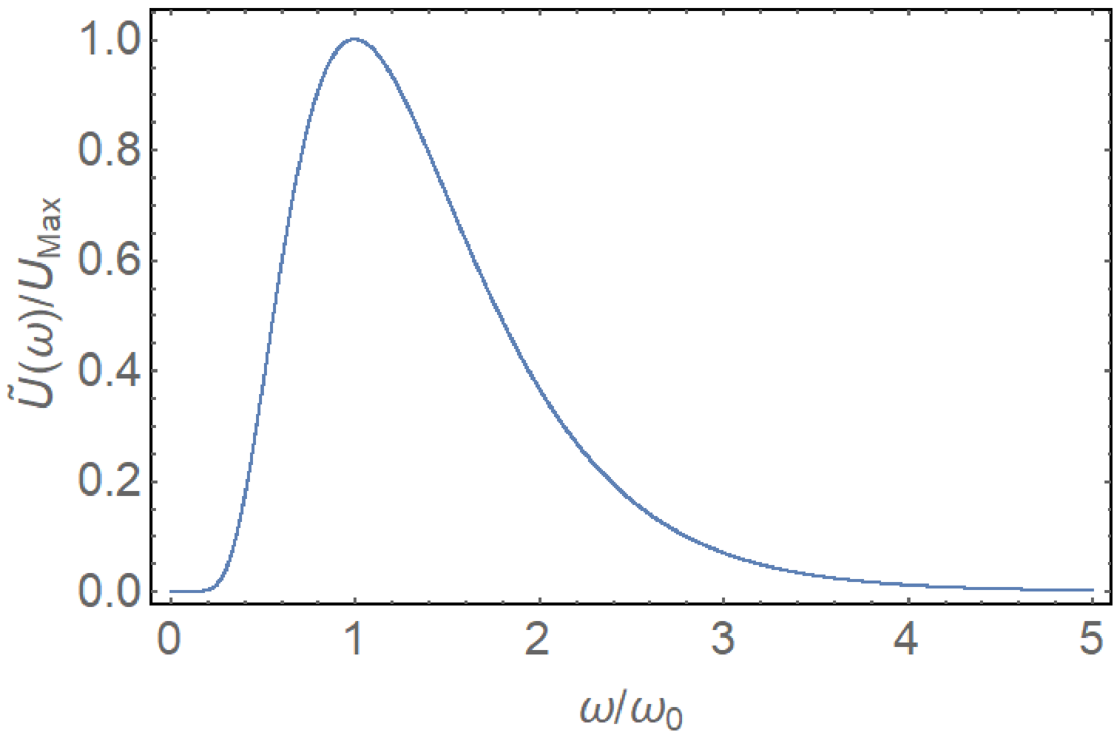

Figure 3.3: Normalised spectral energy distribution curve for broadband $\sigma = 0.5\omega_0$ THz, $x = 1$ pulse.

sources cannot reach these energy figures, it is expected to become commonly feasible in the next few years [23].

In addition, the frequency-decay coefficient $x = 1$ for simplicity in analysis. To calculate the accelerating bandwidth, the spectral voltage profile for the accelerating mode was required to be calculated. This was obtained via:

$$\widetilde{V}(\omega) = \mathbb{R}\left[T(\omega)\right]\sqrt{\widetilde{U}(\omega)Z_c(\omega)}\;(V/Hz) \tag{3.65}$$

Where $Z_c(\omega)$ is the spectral characteristic impedance and $T(\omega)$ is the spectral transit time factor, calculated by:

$$T(\omega) = \frac{1}{L}\int_0^L \exp\left[i\omega z\left(\frac{1}{v_p(\omega)} - \frac{1}{v_b(\omega)}\right)\right]\,dz \tag{3.66}$$

Where $L$ is the length of the structure, $v_p(\omega)$ is the spectral phase velocity of the accelerating mode, and $v_b(\omega)$ is the spectral particle velocity. In a structure of length $L$, some asynchronous frequencies will propagate with a net accelerating effect, others will propagate with a net decelerating effect. An example of the resultant spectral voltage profile is shown in Fig. 3.5

Integrating over all frequencies as in Eqn. 3.67 gives the total accelerating voltage. Calculating Eqn. 3.64 for increasing $\sigma$ allowed Eqn. 3.67 to be plotted against $\sigma$ which illustrated the optimal source bandwidth for acceleration in the structure, an example of which can be seen in Fig. 3.4.

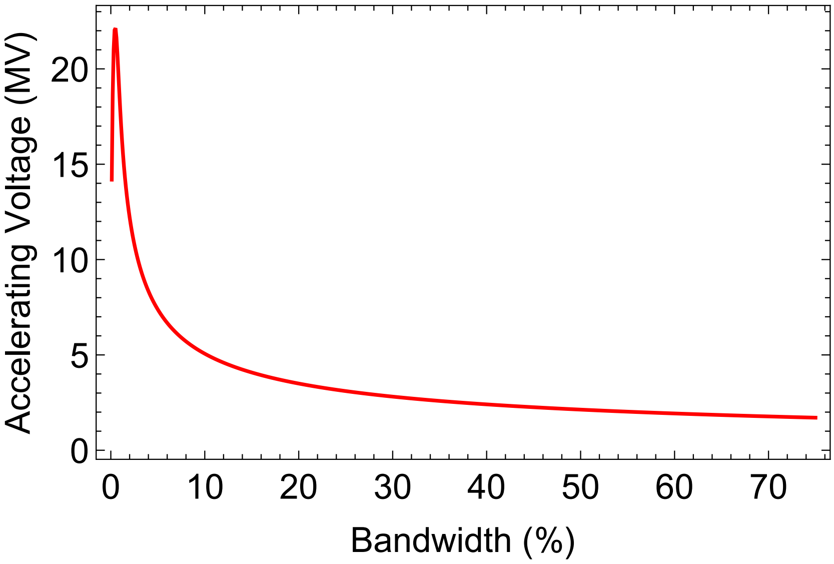

Figure 3.4: Example of spectral voltage profile obtained from Eqn. 3.65.

$$V_{acc} = \int_0^\infty \widetilde{V}(\omega)\, d\omega \ (V) \tag{3.67}$$

## 3.5 Figures of merit

One of the main figures of merit (FoM) in conventional RF accelerators is the shunt impedance $r_s$. This is defined, as in Eqn. 3.68 as the ratio of the accelerating field $E_{acc}$ squared to the power dissipated on the walls of the cavity $P_{loss}$ per unit length. [101]

$$r_{s(def)} \equiv \frac{E_{acc}^2}{\dfrac{\delta P_{loss}}{\delta z}} \quad (\Omega) \tag{3.68}$$

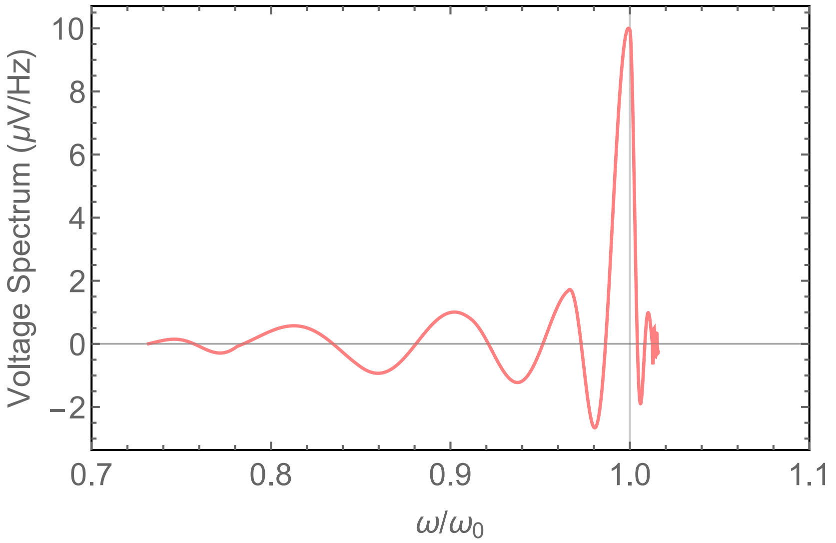

Figure 3.5: Example of spectral voltage profile obtained from Eqn. 3.65.

Thus in a known length of cavity $L$, assuming the field is not varying longitudinally, Eqn. 3.68 becomes Eqn. 3.69:

$$r_s = \frac{E_{acc}^2 LT}{P_{loss}} = \frac{(VT)^2}{P_{loss}} \quad (\Omega) \tag{3.69}$$

where $T$ is the *transit-time factor*, or the voltage seen by a particle under the influence of amplitude-variation of the accelerating field. This FoM is typically not used for PBG-W structures however due to the wall-losses being a small component of the total power figure in the structure. The characteristic impedance $Z_c$ is instead typically used [47] in the context of dielectric laser accelerators. This is defined as the product of the accelerating field $E_{acc}$ with the integrated Poynting vector **S** giving average power flow in the direction of acceleration in the structure via Eqn. 3.70.

$$Z_{c(def)} \triangleq \frac{E^2}{\int \mathbf{S}\,\delta A} = \frac{E^2}{P_{flow}} \quad (\Omega/m^2) \tag{3.70}$$

Thus to ensure Eqn. 3.70 has the correct units of $\Omega$, the value is calculated for a structure of one accelerating wavelength $\lambda$ long which allows scalability between structures designed for different wavelengths. Thus instead of $Z_{c(def)}$ in Eqn. 3.70 we use $Z_c$:

$$Z_c = \frac{E^2\lambda^2}{P_{flow}} = \frac{V_\lambda^2}{P_{flow}} \quad (\Omega) \tag{3.71}$$

Where $V_\lambda$ is the per-wavelength accelerating voltage in the structure. Due to the structure being dispersive, $\lambda$ is not constant with $\omega$ and is extracted from the wave-vector $k_z$ as $\lambda(\omega)$. When $Z_c$ for one wavelength is known, $Z_c$ for structures of length $L$ can be calculated via:

$$Z_c = \frac{V_\lambda^2}{P_{flow}} \frac{L}{\lambda(\omega)} \quad (\Omega) \tag{3.72}$$

While $Z_c$ is often used in literature [47] and provides a good first look at the behaviour of the structure allowing for a quick evaluation of the dimensions of interest, a more detailed analysis was required to incorporate the broadband nature of the excitation pulse.

To determine the effect of group velocity $\beta_g = v_g/c$ on the accelerating voltage, another figure is required. Combining $Z_c$ with the group velocity as in Eqn. 3.73 gives the $R/Q$ value—which relates losses as the electromagnetic wave propagates, with the energy confinement of the structure.

$$\frac{R}{Q} = \frac{Z_c\beta_g}{2\pi\lambda} \quad (\Omega/m) \tag{3.73}$$

Similarly to $Z_c$, the $R/Q$ is an adequate FoM for analysis of single-frequency excitation structures. The final accelerating voltage of a structure excited by a broad-bandwidth pulse however depends on both $R/Q$, and the synchronism of the pulse through the structure: both pulse-envelope and phase-angle synchronism. Examining the process of calculating the voltage in section 3.4, the calculation for the accelerating voltage in Eqn. 3.65 and Eqn. 3.67 relates the co-propagation of the field and bunch. Consequently, both phase synchronism and pulse-envelope synchronism are required to calculate the accelerating voltage as once the particle bunch has passed the accelerating pulse, it will receive no more acceleration. From this it can be inferred the voltage is proportional to the group velocity:

$$T(\omega) \propto v_g \tag{3.74}$$

thus from Eqns. 3.65 and 3.74 it can be seen:

$$V(\omega) \propto v_g \sqrt{Z_c} \tag{3.75}$$

Also from Eqn. 3.73 we can see that:

$$\frac{R}{Q} \propto v_g Z_c \tag{3.76}$$

thus:

$$V \propto \sqrt{v_g \frac{R}{Q}} \tag{3.77}$$

Therefore from this a new figure of merit was introduced, the velocity-modified R/Q coefficient $\zeta_v$:

$$\zeta_v = v_g \frac{R}{Q} \tag{3.78}$$

Maximising of this factor in structures at the interaction point is a single-parameter method for optimising maximum accelerating voltage across the total frequency bandwidth, as low group velocity will provide short interaction time, and low $R/Q$ provides low interaction between the pulse and beam.

## 3.6 Fabrication techniques

The photonic-crystal based devices investigated in this thesis have a high aspect ratio i.e. the ratio of the longest side to the shortest is large. An example of this is the 2D photonic crystal which requires holes many times deeper than the diameter of the hole. The production of these structures consequently requires specialised manufacturing techniques. These can broadly be grouped into two methodologies:

Subtractive and additive. The former are conceptually more conventional techniques, which include precision milling and plasma/reactive gas etching. The latter are more novel 3D-printing based processes. Finally there are certain processes which straddle both definitions, such as *LIGA* (A German acronym for Lithographie, Galvanoformung, Abformung—described in section 3.6.3). The most mature technology for the designs in this thesis is the deep reactive ion etching technique, which is detailed in 3.6.1.

### 3.6.1 Subtractive Methods

Subtractive manufacturing methods involve beginning with a solid block, and removing material according to a pattern. The simplest of these is precision machining: cutting, grinding, and drilling using mechanical means. For the structures in this thesis, hole depths are typically $\lessapprox 2\,mm$ and diameter $\lessapprox 0.3\,mm$, requiring a tolerance of $\lessapprox 0.01\,mm$. A micromachining [102] aspect ratio of $9 - 10$ would provide sufficient headroom for production. For these structures, precision milling may also be an option [103]. Some options may require double-sided drilling, but augmenting the cylindrical hole into a double-conic shape may be beneficial. Other subtractive methods are often also referred to as machining or milling—however unlike the first, are more often chemical or reactive processes than physical. Pure chemical etching, while common in fields like PCB manufacture, performs poorly with high aspect ratio structures due to the isotropic nature of the etch compared to the anisotropic requirement of the cut.

Deep reactive ion etching (DRIE) [104, 105] is a reactive ion etching method for high aspect-ratio silicon structures which can produce fine detail on the length scale of structures investigated in this thesis. With silicon slabs up to $600\,\mu m$ thick and several square-millimetre surface area, it can produce details on the scale of a few microns. Recent advances in DRIE [106] reveal etching capabilities of over $1\,mm$ slab thickness with etching angle $\theta \approx 90^\circ$ allowing for aspect ratios $> 40$; with the addition of much research for this process being specific to silicon. An example of DRIE in 1 $mm$ thick silicon slab [106] is shown in Fig. 3.6. This method is likely the method of choice for the 2D photonic crystal structures investigated in this thesis as it has the advantage of being a mature technology, with likely the main disadvantage being tooling costs for a one-off structure.

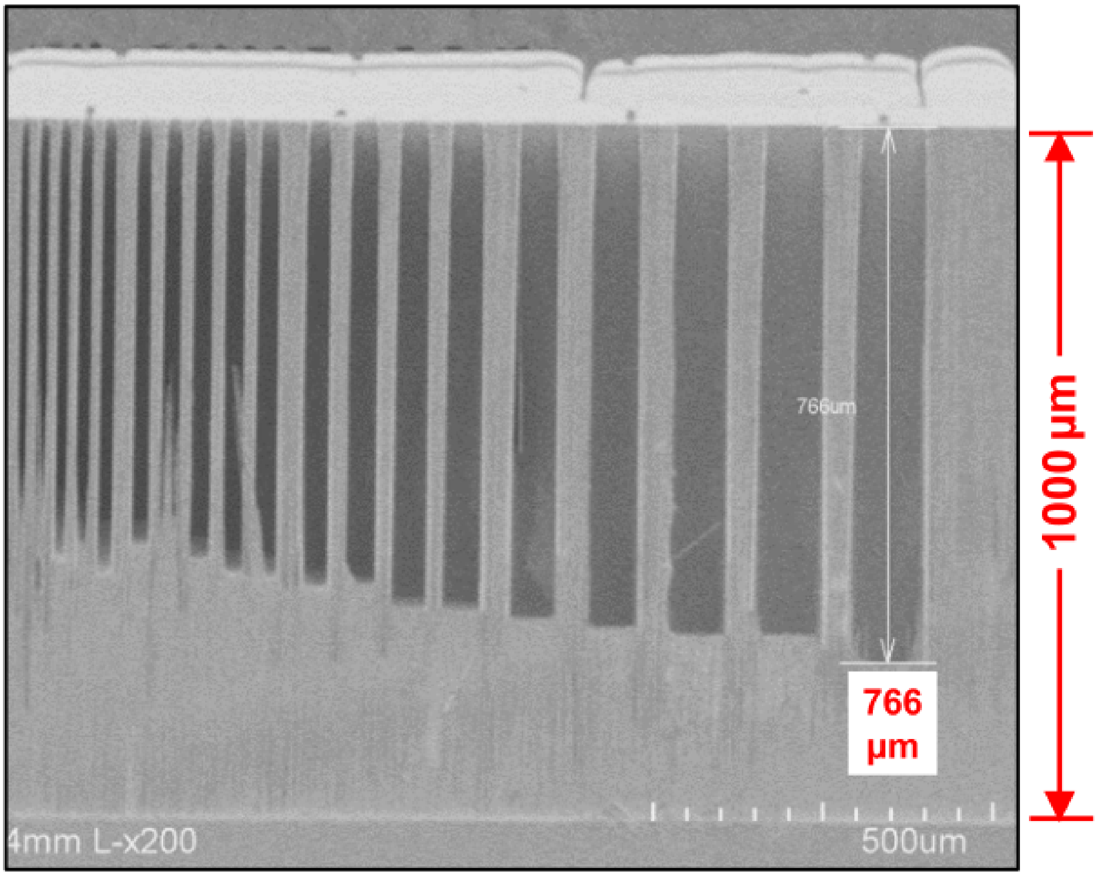

Figure 3.6: An example of DRIE in 1 $mm$ thick silicon slab as shown in [106].

Spark erosion, or electrical-discharge machining (EDM) will use a similar setup to mechanical machining but instead of mechanical material removal, uses a high-current spark to vaporise the surface. While conventionally applied to metal surfaces, ceramics and silicon can also be machined in this way [107, 108]. The precision and tolerance required from EDM to produce the silicon structures this thesis investigates was first documented by Sato in 1985 [109, 110] and with the advances in machining over more than three decades overcoming many of the inherent difficulties of high-aspect-ratio micromachining [111], it is expected this would be a viable option to produce the structures to exacting dimensions. The advantage of this method is that it has decades of research behind it and is likely a viable method to etch silicon. The disadvantage is this method is predominantly used for metals, with ceramic etching being less mature and thus leading to a high cost for potentially poor product.

Other methods of subtractive manufacturing include combination chemical-EDM etching [112], plasma ablation [113], and laser cutting [114]. Each of these methods, and others not mentioned feature their own advantages and disadvantages in the materials they can machine, the maximum aspect ratios they can machine, the size limits, speed, and repeatability. Every subtractive method available will not be covered in this thesis.

### 3.6.2 Additive Methods

The more recent developments in additive production methods are occurring in 3D printing. While originally restricted to polymers and metals, the ability to 3D print complex non-extrudable 3D pieces out of ceramic is growing [115]. For 3D printing of ceramics, the expected method is selective-laser sintering. A layer of ceramic powder is laid flat, and selectively sintered by a laser according to the desired pattern. The layers are built up and the laser sintering is repeated [116]. At micron-scale, there are still inherent difficulties with the process. The material has a requirement to be flowable however this requires the use of coarse particles and as such limits the achievable resolution even with smaller spot-size lasers. The high thermal gradients can also cause cracking in the structure and lead to other deformities [117]. As such, while this method may be viable for some structures, it is less preferable to pursue this over other methods.

One of the conceptually simpler additive methods is known as electroforming. While this process usually cannot grow dielectrics, it can be the precursor in the LIGA process, discussed later. With this process, complex-shaped metal parts can be grown on a substrate with high accuracy for large aspect ratios. A metal substrate has a photo-resist coating deposited, which is then exposed to UV light which hardens the mask. The mask itself can either be screened from the UV light, or the UV light applicator itself is a small-dot UV laser. The mask is then washed, which removes the unhardened mask, leaving bare-metal substrate. This substrate has the metal electro-deposited to form the component which can then be harvested from the substrate [118].

Overall, the disadvantages of additive methods outweigh the advantages for the structures investigated in this thesis. In the next few years, as methods continue to advance, they may become more cost effective with the reduced tooling costs and quick production they could offer.

### 3.6.3 Further Methods

The further methods mentioned in this section are unlikely to be applicable to the work undertaken in this thesis at the time of printing, however they are relevant to other photonic crystal designs and as such are mentioned for completeness. LIGA—a German acronym for Lithographie, Galvanoformung, Abformung—is a 3 stage process of lithography, electroplating, and moulding to create high-aspect-ratio microstructures out of polymer, ceramic, or metal [119]. The fundamentals of this process, as captured in the name, initially begins with the creation of a mask with low-Z carrier and high-Z patterned absorber. These are created through various methods such as electron beam lithography and can provide sub-micron resolutions for thinner masks. These masks absorb X-rays while the structure is exposed in a high-field region such as created by a synchrotron. The exposed regions can then be etched away. The remaining regions can then be electroplated with metal to provide a mould for replication through methods such as injection moulding, with sol-gel processes being a promising future step for ceramic structures [120].

A common method for creating extrudable structures is the stack-and-draw method. Much like fairground rock, this method involves the creation of a large primary and drawing it through a funnelled nozzle until it is the desired diameter. Typically this requires materials that are either compressible, or can be heated until malleable. Additionally, whilst it preserves its radial structures aspect ratio, the longitudinal structures are deformed by the degree of compression. As such, while useful for longitudinal photonic-crystal structures, the transverse PhC structures investigated in this thesis could not be produced this way.

## 3.7 Numerical Methods for Computational Electromagnetics

The package which most of the work in this thesis was carried out in is CST (Computer Simulation Technology) Studio by Dassault Systemes [121]. This is a combined CAD/electromagnetic modelling software using a range of different solvers. The fundamentals of the mathematics behind the required solvers will be discussed in this section. CST at its core is a combination of finite-element and finite-integral techniques.

### 3.7.1 Eigenmode Solver

The fundamental solver used at the heart of the work in this thesis is the eigenmode solver. This solver uses metallic boundary conditions to calculate resonant mode patterns and their corresponding frequencies when no excitation is applied. This calculation is similar to calculating the resonant frequencies of a guitar string with the boundary conditions of a node at each end. The eigenmodes and frequencies are solutions to the eigenvalue equation:

$$\left(\nabla \times \underline{\mathbf{v}}\right)\left(\nabla \times \mathbf{E}\right) = \underline{\omega}^2 \underline{\varepsilon} \mathbf{E} \tag{3.79}$$

Where $\underline{\mathbf{v}}$ is the complex reluctivity:

$$\underline{\mathbf{v}} = \frac{1}{\underline{\mu}} = \mathbf{v}'\left(\omega_0\right) - i\mathbf{v}''\left(\omega_0\right) \tag{3.80}$$

and $\underline{\varepsilon}$ is the complex permittivity of the material:

$$\underline{\varepsilon} = \varepsilon'(\omega_0) - i\varepsilon''(\omega_0) \tag{3.81}$$

and $\underline{\omega}$ is the complex angular frequency, related to the real angular frequency and the Q-factor [122] via:

$$\underline{\omega} = \omega \left(1 + \frac{i}{2Q}\right) \tag{3.82}$$

CST documentation is ambiguous about what method is implemented in the tetrahedral meshing setup and is likely to be at least partially proprietary. For hexahedral mesh setups, two methods are employed: The Advanced Krylov Subspace model, and the Jabobi-Davidson Method (JDM). The mathematics itself behind these techniques is not the subject of this thesis and will not be dissected in detail, however an understanding of how they operate is desired.

The Advanced Krylov Subspace (AKS) model is an efficient tool for finding eigenvalues of large sparse matrices. If we define a large sparse matrix $A$, and we want to find the solution $Ax = b \rightarrow x = A^{-1}b$, we can define a Krylov subspace $K_m$, for $A$ and non-zero vector $v$ as:

$$K_m(A, v) \equiv span\left\{v, Av, A^2v, ...A^mv\right\} \tag{3.83}$$

Since for large values of $m$, $K_m$ is an invariant subspace of vector space $V$ w.r.t. $A$, we can write $K_m(A, b)$ which contains solution to $Ax = b$. This method gains efficiency due to the ability to reduce order of solver if eigenvalues are close together and while solutions will not be exact, they will be a good approximation. Thus for photonic crystal structures if we define matrix $A$ as the permittivity and conductivity, we can define vector $v$ as wave vector $k$ and find eigenmodes for the structure. A more in-depth analysis of this method can be found in [123, 124].

The JDM is a combination of two principles for finding the eigenvalue of a matrix. The first part—The Davidson principle—is to apply a Ritz-Galerkin approach, and the second is Jacobi orthogonal component correction. It is an iterative method beginning with an initial estimate of the solution. Given a sparse square matrix $A$, and target $\tau$, eigenvalues of $A$ are found closest to $\tau$.

Let $v_1, v_2, ..., v_m$ be a set of orthonormal vectors in the space $R$, where $V_m = [v_1, v_2, ..., v_m]$ and we can write $\mathbf{u}$ as a linear combination of these basis vectors $\mathbf{u} = V_m\mathbf{s}$. For the Ritz-Galerkin approach, we are looking for vectors $\mathbf{s} \in F^m$ such that the Galerkin condition holds:

$$AV_m\mathbf{s} - \theta V_m\mathbf{s} \perp v_1, v_2, ..., v_m \tag{3.84}$$

Which is true only if $(\theta, \mathbf{s})$ is a solution to eigenvalue problem

$$V_m^* A V_m \mathbf{s} = \theta \mathbf{s} \tag{3.85}$$

Using the harmonic Rayleigh-Ritz method, eigenvalues which are closest to target $\tau$ are eigenvalues of largest magnitude from $(A - \tau I)^{-1}$ thus imposing the condition for test space $\mathcal{V}$:

$$(A - \tau I)^{-1}\tilde{\mathbf{u}} - (\tilde{\theta} - \tau)^{-1}\tilde{\mathbf{u}} \perp \mathcal{V} \tag{3.86}$$

To avoid the requirement of inverting the large sparse matrix $A$, we choose $\mathcal{V} = (A - \tau I)^*(A - \tau I)V_m$, where $\tilde{\mathbf{u}} = V_m\tilde{\mathbf{s}}$, allowing us to write the generalised eigenvalue problem:

$$V_m^*(A - \tau I)^*(A - \tau I)V_m\tilde{\mathbf{s}} = (\tilde{\theta} - \tau)V_m^*(A - \tau I)^* V_m\tilde{\mathbf{s}} \tag{3.87}$$

And thus iteratively minimising $|\tilde{\theta} - \tau|$ allows us to calculate the eigenvalues. This is a brief overview of the process, further reading can be found in [125, 126].

### 3.7.2 Time-Domain Solver

CST offers two time-domain solvers. The first, the Transmission Line Matrix (TLM) solver is useful for evaluation of the electromagnetic emissions of circuit boards in electromagnetic compatibility and interference (EMC/EMI) testing. As such, it is not applicable to the work in this thesis and is mentioned only for completeness.

The second, the Transient solver is a finite-integration technique (FIT) based solver which calculates electromagnetic propagation over a hexahedral mesh, incorporating the Perfect Boundary Approximation, and the Thin Sheet Technique. The FIT, first proposed by Weiland in 1977 [127], is a type of finite-difference time domain (FDTD) calculation which discretises integral-form Maxwell's equations. Starting with the integral form:

$$\oint_{\partial A} \mathbf{E} \cdot ds = -\oiint_{A} \frac{\partial \mathbf{B}}{\partial t} \cdot d\mathbf{A} \tag{3.88}$$

$$\oint_{\partial V} \mathbf{B} \cdot d\mathbf{A} = 0 \tag{3.89}$$

$$\oint_{\partial A} \mathbf{H} \cdot ds = \oiint_{A} \left( \frac{\partial \mathbf{D}}{\partial t} + \mathbf{J} \right) \cdot d\mathbf{A} \tag{3.90}$$

$$\oint_{\partial V} \mathbf{D} \cdot d\mathbf{A} = \iiint_{V} \rho dV \tag{3.91}$$

Defining area $\Omega$ as the area of interest for solving, which is a simply connected, bounded region of space where $\Omega \in \mathbb{R}^3$. We then divide $\Omega$ into a finite number of cells $V_i$ such that they are either hexahedral or tetrahedral and they fit exactly with their neighbouring cells, thus they will either share a point, an edge, or a 2D polygon. This division results in computational grid $G$. If we now assume $\Omega$ is hexahedral, we can write:

$$\begin{gathered} G \triangleq \{V_{i,j,k} \in \mathbb{R}^3 |\, V_{i,j,k} \triangleq [x_i, x_{i+1}] \times [y_i, y_{i+1}] \times [z_i, z_{i+1}]\,, \\ i = 1, ..., I-1,\ j = 1, ..., J-1,\ k = 1, ..., K-1\} \end{gathered} \tag{3.92}$$

Restricting $G$ to single cell volume $V_n$, Faraday's law—Eqn. 3.88—can be rewritten for facet $A_z\,(i, j, k)$ of $V_n$ as ODE:

$$\begin{aligned}\hat{e}_x\left(i,j,k\right)+\hat{e}_y x\left(i+1,j,k\right)-\hat{e}_x\left(i,j+1,k\right)...&\\ -\hat{e}_y\left(i,j,k\right)=-\frac{d}{dt}\hat{b}_z\left(i,j,k\right)&\end{aligned}\tag{3.93}$$

where $e_x$ is the voltage on one edge of surface $A_z\left(i,j,k\right)$:

$$\hat{e}_x=\int_{x_i,y_j,z_k}^{x_{i+1},y_j,z_k}\mathbf{E}\cdot d\mathbf{s}\tag{3.94}$$

and similarly $\hat{b}_z$ is the integrated magnetic flux through a facet of $A_z\left(i,j,k\right)$:

$$\hat{b}_z\left(i,j,k\right)=\oiint_{A_z(i,j,k)}\mathbf{B}\cdot d\mathbf{A}\tag{3.95}$$

Thus these discretised values of the electric and magnetic fields can be summed over for overall field profiles, or expressed as matrices for further processing. A more in-depth analysis of FIT can be found in [128]. Coupled with the PBA, which deforms hexahedral mesh cells to more closely fit a metallic boundary at the expense of computation efficiency, this method provides a robust method for calculating time-domain electromagnetics.

### 3.7.3 Frequency-Domain Solver

The frequency-domain solver assumes a time-harmonic dependence of the calculated fields, and as such can be described as phasors $\mathbf{E}(t)=\mathfrak{Re}\left[\mathbf{E}(\omega)e^{i\omega t}\right]$ to calculate S-parameters. While useful in many electromagnetic problems, is less applicable to photonic crystal simulations due to their non-trivial mode structures, and non-applicability of S-parameters at short THz pulse lengths, it is only mentioned for completeness.

### 3.7.4 Wakefield Solver

The CST wakefield solver is a method for computing wake potentials with a simplified input charge to improve computational economy. The electromagnetic fields are computed in a standard time-domain solver, with the effects of bunch-charge calculated in post-processing. Beam effects are neglected and instead is an infinitely thin line with appropriate current to excite the structure. As such, it cannot be used to study the beam itself, and instead is only used for examining the effect the beam has on the structure.

### 3.7.5 Particle-in-Cell Solver

The full particle-in-cell (PIC) solver is one of the more complex solvers CST employs. This solver combines a time domain solver calculating propagating fields, with a quantised ballistic solver and particle interaction Monte Carlo simulation. As expected, this demands a high computational power and significant time investment for each simulation run. There are multiple computational methods developed for PIC, each applying differently to different aspects of the calculation. The CST particle studio suite is based on algorithms developed in MAFIA-4 [129] and uses the “leap frog” method of integration, however the exact methods are proprietary. Due to approaches in other solvers with the PBA, it is expected the PIC solver will follow a conformal EM-PIC model [130].

Many particle-emission models will involve an extremely large number of particles, with number densities in the range of $10^{11} - 10^{12}$ per bunch not being unrealistic [131]. This presents a challenge to even the most powerful computers and as such require methods to improve efficiency. As Lorentz force calculations can be simplified to only be dependent on charge-to-mass ratio—the use of so-called “super particles”, or macroparticles, is used. These particles are where emission points are grouped into emission regions of a single larger particle. While some detail is lost in this, the emission grid can be chosen such that it still represents sufficient collisional and interactive properties. Two methods of macroparticle design are commonly used are fixed weight and variable weight. Fixed weight macroparticles each have the same charge-mass ratio and a non-uniform emission surface. These macroparticles are used by programs such as ASTRA [132]. CST uses variable-weight macroparticles, where the emission surface is uniform and the charge-mass ratios are varied. While both methods are viable, care must be taken in transporting numerical results between the two as it can lead to artefact effects such as "grid heating" [133], where the bunch space-charge effects are misinterpreted by the solver and leads to spurious high fields. Furthermore, mesh must be carefully controlled to ensure that neither collision effects nor mesh effects introduce spurious noise [134].

To conserve computational power, the particle momentum is calculated using the "leap frog" method of integration. The fundamental aspect of this numerical integration method is calculating the value, such as velocity or position of a particle at interleaved points in time so that the full dynamics evolve as the system evolves. CST performs this calculation on a 4-stage cycle of calculating the current distribution from particle motion → updating the electric and magnetic fields → interpolating the fields at particle positions → updating particle positions and momentums [122].

### 3.7.6 MIT Photonic Bands (MPB)

CST Microwave Studio operates on a Cartesian coordinate system for analysis. While this is fine for investigation of operation of general electromagnetic devices, analysing the bandgap of structures often requires arbitrary coordinate systems to be defined. MIT Photonic Bandgap software (MPB) [96, 135] is a Linux-based GNU GPL free and open-source program designed to calculate the band structures of photonic crystals in arbitrary coordinate systems. It can also calculate dispersion relations and the electromagnetic modes of PhCs and can perform calculations in parallel distributed MPI computing if required.

It solves Maxwell's equations in periodic dielectric structures for arbitrary wave vectors to calculate definite-frequency eigenstates. It can perform these calculations in either 1D, 2D, or 3D depending on the photonic crystal of interest.

## 3.8 Conclusion

This chapter has focused on the underpinning theory of photonic crystals with their application to particle acceleration. Starting with first principles as originally put forward by Maxwell, these were applied to periodic dielectric media. The physical description of photonic crystals and the electromagnetic behaviour in them was examined. The application to acceleration was studied, with the definition of several figures of merit including accelerating voltage, impedance, and the $\zeta_v$ parameter was created. The chapter then investigated methods for fabrication of these sub-millimetre devices in both additive and subtractive regimes. The chapter closed with an examination of the computational electromagnetics which underpin the simulation work in this thesis.

# 4

# The Physics of Beam-Based Radiation: An Overview

This chapter provides an overview of the highly relativistic beams for acceleration, and how the energy can be extracted. Beginning with the Vlasov equation description for a bunch, the emittance is defined. Methods for extracting energy through Bremsstrahlung, transition, diffraction, and Cherenkov radiation are examined, and these are combined into the fundamental theorem of wakefields. The wakefield potential and impedance are examined with respect to relativistic bunches. Finally, the subject of beam break up and by extension the Panofsky-Wenzel theorem is briefly examined.

## 4.1 Charged Particles in Bunches

The study of beam radiation and dynamics is a broad field with much work dedicated to it; the majority of which is outside the scope of this thesis. A basic understanding of beam-structure interaction however is required to underpin the work investigated here. The beam in regards to accelerator physics is a flow of charged particles either continually or discretised in time with duty cycle, whilst following a designated path. In the latter—the time discretised packets are known as bunches. The interest for this thesis will be upon electron bunches. The fundamental aspect of particle accelerators is that particle motion is affected by both electric and magnetic fields. This is captured in the Lorentz force equation.

$$\mathbf{F} = q(\mathbf{E} + \mathbf{v} \times \mathbf{B}) \tag{4.1}$$

Accelerators typically do not deal with single particles however, and instead they are considered in either a continuous stream or discretised bunch. When we have a collection of particles with distribution function $f(\mathbf{r}, \mathbf{p}, t)$ with position $\mathbf{r}$ and momentum $\mathbf{p}$, we can write the evolution of the collection as the Vlasov equation:

$$\frac{\partial f(\mathbf{r}, \mathbf{p}, t)}{\partial t} + \frac{d\mathbf{r}}{dt} \cdot \nabla f(\mathbf{r}, \mathbf{p}, t) + \frac{d\mathbf{p}}{dt} \cdot \nabla_p f(\mathbf{r}, \mathbf{p}, t) = 0 \tag{4.2}$$

where $\nabla_p = \hat{i}\frac{\partial}{\partial p_x} + \hat{j}\frac{\partial}{\partial p_y} + \hat{k}\frac{\partial}{\partial p_z}$. For cases in which intra-bunch collisions can be neglected, we can instead assume a self-consistent bunch field, and we know $\mathbf{F} = \frac{d\mathbf{p}}{dt}$ and $\mathbf{v} = \frac{d\mathbf{r}}{dt}$, we can rewrite 4.2 as the Vlasov-Maxwell equation:

$$\frac{\partial f(\mathbf{r}, \mathbf{p}, t)}{\partial t} + \mathbf{v} \cdot \nabla f(\mathbf{r}, \mathbf{p}, t) + \mathbf{F} \cdot \nabla_p f(\mathbf{r}, \mathbf{p}, t) = 0 \tag{4.3}$$

where $\mathbf{F}$ is the Lorentz force defined in Eqn. 4.1. [136]. This description, whilst fully encompasses the physics of a particle beam, is cumbersome and computationally intense in practice. As such, a more computationally economic method must be used for general analysis of beams.

## 4.2 Beam Emittance

One common macroscopic measurement of a particle beam is known as the emittance. Linked to the particle distribution discussed in section 4.1, this is a measure of the average spread of the particles in position-momentum phase space. Assuming no energy lost via radiative mechanisms (such as mechanisms discussed in section 4.3), the propagation can be classed as harmonically oscillating and will occupy a constant-area ellipse in 6D phase space. Furthermore if it can be assumed that the motions in Cartesian coordinates are separable, such that:

$$f(\mathbf{r}, \mathbf{p}, t) = f_x(x, p_x, t) f_y(y, p_y, t) f_z(z, p_z, t) \tag{4.4}$$

so that at any point in time $t$, then a 2D phase-space volume can be used to describe the beam and thus three orthogonal planes of $x, p_x$, $y, p_y$ and $z, p_z$ are studied. The choice of bounding ellipse often depends on application, for the work here it will be restricted to $e^{-1}$ of the peak particle density. Additionally since it is often preferred to measure the divergence angle than the momentum directly [137], the transverse phase-spaces can be combined into the trace-spaces where the identities $x' = p_x/p_z$ and $y' = p_y/p_z$ are used for the $x, x'$ and $y, y'$ planes [138].

If the beam can be approximated by a Gaussian distribution, assuming no focusing, the initial distribution function can be written as:

$$f(x, x') = \frac{1}{2\pi\sigma_x\sigma_{x'}} \exp\left(-\frac{x^2}{2\sigma_x^2}\right) \exp\left(-\frac{x'^2}{2\sigma_{x'}^2}\right) \tag{4.5}$$

where $\sigma_x$ and $\sigma_{x'}$ are the standard deviations in position and momentum respectively. On this plot, when we take the $e^{-1}$ curve, the ellipse following standard form is written as $x^2/\sigma_x^2 + x'^2/\sigma_{x'}^2 = 1$ and the area of this ellipse is defined as $A = \pi\sigma_x\sigma_{x'}$; and from this we can extract the definition of emittance:

$$\epsilon_x = \sigma_x\sigma_{x'} \tag{4.6}$$

Emittance is a conserved area of phase space which obeys Liouville's theorem [139], which for a system in which $f\left(x, p_x, t\right)$, can be written as:

$$\frac{df}{dt} = \frac{\partial f}{\partial t} + \left(\frac{\partial f}{\partial x}\frac{dx}{dt} + \frac{\partial f}{\partial p_x}\frac{dp_x}{dt}\right) = 0 \tag{4.7}$$

Assuming the canonical equations of motion are obeyed by the particles, each element of a volume of phase space is constant in time. Employing the general ellipse equation $ax^2 + 2bxy + cy^2 = d$ and area $A = \pi d/\sqrt{ac - b^2}$ we can see that additional parameters are required. These in accelerator physics are known as the Twiss (or Courant-Snyder) parameters and are written as $\alpha_x$, $\beta_x$, and $\gamma_x$ however should not be confused with loss factor $\alpha$, wavenumber or phase velocity $\beta$, or Lorentz factor $\gamma$. Writing the emittance in terms of Twiss parameters we get:

$$\epsilon_x = \gamma_x x^2 + 2\alpha_x x x' + \beta_x x'^2 \tag{4.8}$$

With the parameters being related as only the major and minor axes, and angle of tilt are required to define an ellipse since the $\epsilon$ is constant. This leads to the requirement of $A = \pi\epsilon/\sqrt{\gamma_x\beta_x - \alpha_x^2}$ and therefore the constant area requirement gives the relationship between the parameters:

$$\gamma_x\beta_x - \alpha_x^2 = 1 \tag{4.9}$$

The relationship between the Twiss parameters and the area of the emittance ellipse is illustrated in Fig. 4.1:

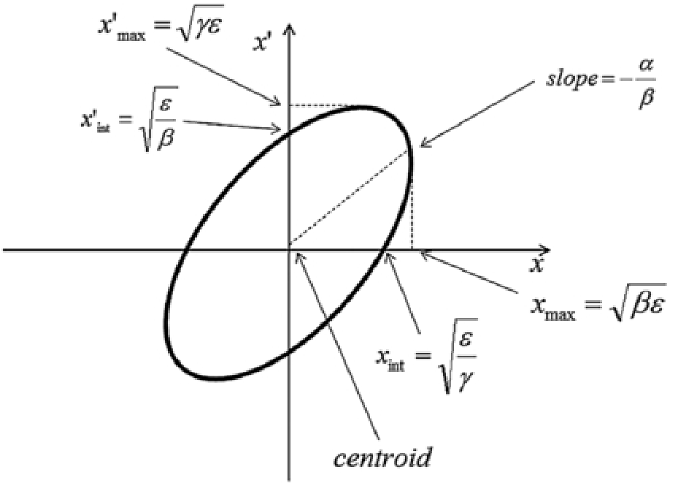

Figure 4.1: An Emittance Ellipse, indicating the relation between geometry and Twiss parameters indicated [140].

The act of accelerating or decelerating the beam leads to the emittance changing, as increasing the longitudinal momentum will lead to a shrinking of the emittance ellipse area, and vice versa. This effect is known as adiabatic damping. In comparison with the emittance discussed, also known as *geometric emittance*, we instead can define a *normalised* emittance by $\epsilon_{nx} = \beta\gamma\epsilon_x$ where $\beta\gamma$ is the Lorentz factor. From this, an alternative measure of beam divergence, the beam brightness can also be defined:

$$B_{\perp} = \frac{I}{\epsilon_{nx}\epsilon_{ny}} \tag{4.10}$$

where $I$ is the average current of the bunch.

## 4.3 Extracting Energy from Relativistic Beams

Effective high-power electromagnetic sources across the frequency spectrum operate by coupling particle beams with resonant cavities at the appropriate wavelength. From domestic 1 kW 2.45 GHz magnetrons inside a domestic microwave, operating in a crossed-field regime, to the 20 MW 1 GHz CLIC klystron utilising accelerated electron bunches to amplify an input signal and radiate coherently in tuned cavities. As the frequency increases however, so too does the efficiency drop—driven by limits in space-charge, confinement, and ohmic losses. At THz frequencies, these problems are difficult to solve and consequently there is a sparsity of high-power sources in this range, colloquially known as the THz-gap.

The mechanics of how these devices operate all rely the fundamental principle of particle-wave coupling thus using a beam to excite a structure to extract energy. As per Newton's first law and the law of conservation of energy, the only way to extract energy from a charged particle/beam is to cause it to experience some form of deceleration, impedance change, or external force.

### 4.3.1 Bremsstrahlung Radiation

Conceptually the simplest method of extracting energy from a high-energy beam is to slow it down. This can either be from deflection via field or charged particle, or via collision. The lost kinetic energy of the particles is converted into radiation over a continuous spectrum. As the $\Delta E$ increases, so does the peak frequency of the emission spectrum, where $hf = \Delta E$. Bremsstrahlung emission is the dominant effect in technologies such as synchrotron radiation, cyclotron radiation, and free-electron lasers; however some literature defines Bremsstrahlung as a specific type of radiation emitted from deceleration of a charged particle interacting with the nucleus of an atom in matter [9].

### 4.3.2 Transition and Diffraction Radiation

When a charged particle/beam experiences a change in impedance by transitioning from one homogeneous medium with defined permittivity and permeability, into a homogeneous medium with differing permittivity and/or permeability, transition radiation (TR) is released. First discovered in 1945 by Ginzburg and Frank, then expanded upon for x-ray emission in 1959 by Garibian, transition radiation has been useful in high energy physics with applications such as beam monitoring. While TR is prescribed to occur when a beam transitions between any two materials with different properties, we shall here focus on one transition—from vacuum to zero-resistivity metal (or perfect electrical conductor—PEC) where without the additional effects of Cherenkov or bremsstrahlung, the radiation emitted is purely to the annihilation of the charge/image-charge dipole on the surface.

If we assume an electron travelling each with charge $q$ and velocity $\mathbf{v}$ normal to the surface of the metal, the energy emitted by the particle within a solid angle $d\Omega$ at an angle $\theta$ to the beam longitudinal axis is given by:

$$dW = \frac{q^2|\mathbf{v}|^2 \sin^2\theta}{\pi^2 c^3} d\omega d\Omega \tag{4.11}$$

where $d\omega$ is the frequency range of interest. Thus total radiation in the $2\pi$ sr solid angle is given by:

$$dW_T = \frac{4q^2|\mathbf{v}|^2}{3\pi c^3} d\omega \tag{4.12}$$

This can be rewritten to calculate the position and trajectory of particles impinging on a metal surface and thus is useful for beam diagnostics. A more detailed analysis was performed in [141].

As shown, transition radiation occurs when charged particles pass through a medium with differing electromagnetic properties. Diffraction radiation on a similar note occurs when charged particles pass near a material with differing EM properties. The inhomogeneous combination of media experienced by the particles field causes emission of radiation if the DR condition is met:

$$h < \frac{\gamma\lambda}{2\pi} \tag{4.13}$$

where h is the height from the surface. Thus when a beam is passed through a known aperture size, the spectrum emitted can be used for non-invasive beam diagnostics [142]. If we again assume PEC material, with aperture $a$

$$I_D\left(a,\omega,\theta\right) = W_T\left(\omega,\theta\right) A^2\left(a,\omega,\theta\right) \tag{4.14}$$

Where the aperture correction term $A$ is defined as:

$$A\left(a,\omega,\theta\right) = \frac{\omega a}{\beta\gamma c} J_0\left[\frac{\omega a \sin\theta}{c}\right] K_1\left[\frac{\omega a}{\beta\gamma c}\right] \tag{4.15}$$

and $J_0$ and $K_1$ are Bessel function and modified Bessel function of the zeroth and first kind respectively [143]. Using $c = f\lambda$ it can be seen from Eqn. 4.15 that the energy in the radiation is proportional to the ratio between wavelength and aperture showing as $a \to \infty$, $I_D \to 0$.

### 4.3.3 Cherenkov Radiation

Cherenkov radiation, which is the cause of the blue glow in water-moderated nuclear reactors, is closer to Bremsstrahlung radiation than the TD/DR in that it does not require inhomogeneous disruption of the beam field. The mechanism this radiates by is the beam self-field passing through a media with dielectric $\varepsilon_r$ faster than the speed of light in that medium, $v_p = c/\sqrt{\varepsilon_r}$. Consequently, similar to a body moving faster in air than the speed of sound, this creates an electromagnetic "shock" as asymmetric polarisation occurs due to a field imparting a polarisation on the media faster than the media can respond.

When the charged particle is moving at speed $\beta c$ through the medium with energy $E = mc^2(\gamma - 1)$, the threshold condition of $\beta = 1/n$—where $n$ is the refractive index—and $\theta = 0$ is imposed, where if not met then no radiation is emitted. Thus the Cherenkov angle for the radiation can be defined as:

$$\cos\theta = \frac{1}{\beta n} \tag{4.16}$$

Thus we can see for Cherenkov radiation to be emitted, $\beta n \geq 1$ and the maximum angle when $\beta \to 1$, $\theta_{max} = \cos^{-1}(1/n)$ [144]. Following the derivation in [145], if we assume the material is dielectric and thus $\mu_r = 1$, the total energy emitted per unit length $dz$ if the Cherenkov condition is met has the relationship:

$$\frac{dE}{dz} \propto \int \omega \left(1 - \frac{c^2}{v^2 n^2(\omega)}\right) d\omega \tag{4.17}$$

### 4.3.4 Coherent Radiation

A charged particle bunch can emit temporally coherent radiation when the length of the bunch is shorter than the wavelength of the radiation. This coherence effect can increase the radiative field $E$ as $E \propto N^2$ compared to $E \propto N$ of incoherent radiation, where $N$ is the number of particles per bunch.

Given a single propagating particle in structure which gives radiation envelope $A(t)$, we can state that the electric field emitted is $E(t) = A(t)e^{i\omega_0 t}$ and consequently Fourier transform of $E(t)$ is $\tilde{E}(\omega) = \int A(t)e^{i\omega_0 t}e^{-i\omega t}dt$. Using the superposition principle, the collective field of the electrons in the bunch can be given by:

$$E_{\Sigma}(t) = \sum_{j=1}^{N} E(t - t_j) \tag{4.18}$$

where $t_j$ is the relative time delay between particles in the bunch. Again taking the Fourier transform of the total field $\tilde{E}_{\Sigma}(\omega) = \int E_{\Sigma}(t)e^{-i\omega t}dt$ where we know the Fourier time-shift identity $\mathcal{F}[x(t \pm t_0)] = X(i\omega)e^{\pm i\omega t_0}$, we can write:

$$\tilde{E}_{\Sigma}(\omega) = \tilde{E}(\omega) \sum_{j=1}^{N} e^{i\omega t_j} \tag{4.19}$$

From this, we can then write the intensity of the radiation as:

$$I_{\Sigma} = |\tilde{E}_{\Sigma}(\omega)^2| \tag{4.20}$$

The intensity can be split into two sections: the incoherent contribution when $j = k$, and the coherent contribution when $j \neq k$. We can then write the intensity as:

$$I_{\Sigma} = I(\omega) \sum_{j=1}^{N} \sum_{k=1}^{N} e^{i\omega t_j} e^{-i\omega t_k} \tag{4.21}$$

For the incoherent radiation intensity, the energy from each particle just adds cumulatively and thus is a multiple of intensity and particle number $N$. This leaves the coherent contribution which we can then write as:

$$I_{\Sigma} = I(\omega) \left( N + \sum_{j \neq k}^{N} e^{i\omega(t_j - t_k)} \right) \tag{4.22}$$

where $i\omega(t_j - t_k)$ takes account for the correlation between any two particles.

## 4.4 Beam Loading, The Fundamental Theorem of Wakefields

In the previous sections we have discussed various methods of extracting energy from a particle beam. The concept of beam loading combines all of these mechanisms for accelerating cavities into the fundamental theorem of wakefields. In conventional accelerators, wakefields are often little more than a nuisance effect to mitigate and decouple from the structures. In terms of novel acceleration however they offer a different mechanism to generate high-gradients for acceleration. Deliberate engineering of the structures to extract a wakefield which is desirable for acceleration is the basis of fields such as dielectric wakefield acceleration (DWA)

[146]. As we know, when a charged particle is moving relativistically, length contraction causes its field lines to compress. For wakefields from a single highly relativistic particle, we can say $v \approx c$ and thus the wakefield must only be present behind the particle. As such, ahead of the particle there will be zero wakefield. Additionally, a wakefield only exists when the particle's own Coulomb field is in some way slowed or deflected so that it can no longer keep up with the particle. Thus when a $\beta \approx 1$ charged particle traverses a wakefield structure in $z$, it excites longitudinal wake $W_{||}(z)$. For this single particle, when the charge itself is at $W_{||}(0)$, and small distance $\Delta z$ behind the charge, the fundamental theorem of wakefields as derived in [147] states:

$$W_{||}(0 - \Delta z) = 2W_{||}(0) \tag{4.23}$$

where the 2 is arrived at as a driving charge will see half the voltage it induces. As previously stated, $W_{||}(0 + \Delta z) \equiv 0$ for all $\Delta z$ as wakefields must trail the particle; additionally, space charge effects are neglected. One important aspect of designing structures specifically for wakefield excitation however is the near-field/short-range wakes, or the effect the bunch has on itself which has important aspects for beam stability and emittance.

The analytic method for solving the wakefields in a given structure is to use the Green's functions calculated for a point charge. This can then be convoluted for an arbitrary beam shape to calculate the wakefield potentials. When a cylindrically symmetric simple geometry is not observed however, this method is both abstruse and highly non-trivial. The Greens functions for a comparatively-simple dielectric-lined waveguide were only analytically derived in 2013 [148], of which the design has relatively few degrees of freedom. For a design such as a photonic crystal based waveguide, which has many geometries and the degrees of freedom which accompany each geometry—the derivation a 3D analytic Green's function would be a large undertaking. As such, while this may be an avenue of future work in the study of PBG-Ws, the wakefield study in this thesis focused on numerical calculation.

### 4.4.1 Relativistic Charges

When a point charge is at rest, the field lines are uniformly spaced around the charge. For the observer, as the particle's velocity increases and tends towards the speed of light, the field lines compress longitudinally to the direction of propagation by a factor of Lorentz factor $\gamma$ due to the effects of length contraction, where:

$$\gamma = \frac{1}{\sqrt{1-\beta^2}} \tag{4.24}$$

In the case of ultra relativistic particles, where $\gamma \gg 1$, the fields form a "pancake" around the equator of the particle and the field lines at $\theta = 0, \pi$ tend to 0. Assuming no transverse variation in the velocity, we can write the distribution of the electric field lines as:

$$\mathbf{E} = \frac{q}{r^2\gamma^2\left(1-\beta^2\sin^2\theta\right)^{3/2}}\mathbf{r} \tag{4.25}$$

where $\theta$ is the angle between the direction of propagation, and the angle to the observer [149].

### 4.4.2 Wakefield Potential

As the wakefield is only ever behind a drive charge in a structure, if it enters the wakefield structure $t = 0$ with velocity $\beta = 1$ then coordinate $z_d = ct$. The charge may also be offset from the longitudinal centre-axis of the structure $\mathbf{r}_d$. A witness charge trailing the drive by longitudinal distance $s$ with offset $\mathbf{r}_w$ with longitudinal coordinate $z_w = z_d - s = ct - s$. The wake potential, in volts/coulomb, as seen by the witness particle is then:

$$\begin{aligned} w_{||}\left(\mathbf{r}_d, \mathbf{r}_w, z_w\right) &= -\frac{1}{q_d}\int_0^L E_{||}\left(\mathbf{r}_w, z_w, t\right) dz\bigg|_{t=(z_w+s)/c} \\ w_{\perp}\left(\mathbf{r}_d, \mathbf{r}_w, z_w\right) &= \frac{1}{q_d}\int_0^L E_{\perp} + c\left(\hat{z}\times\mathbf{B}\right) dz\bigg|_{t=(z_w+s)/c} \end{aligned} \tag{4.26}$$

Thus can be seen the wake potentials are a function not only of the position of the driving charge, but of the offset and trailing time behind the charge. With the wakefield potential defined, the transformer ratio ($T_R$) can be defined as the ratio of maximum decelerating field in the drive bunch $W_M^-$, with the maximum accelerating field seen by the witness bunch $W_M^+$. Writing this in terms of wake potentials we then get:

$$T_R = \left|\frac{W_M^+}{W_M^-}\right| \tag{4.27}$$

The efficiency of this transfer can be defined as the energy the drive bunch deposits into the witness bunch relative to the total energy contained in the drive bunch. Examining a drive bunch, with $n_d$ particles with energy $q_d V_i$ which would be brought to rest in distance L, we can state $V_i = -V_M^-$ Thus:

$$\eta = \frac{U}{n_d q_d V_i} = \frac{\int_0^T I\left(t\right) V^-\left(t\right) dt}{n_d q_d V_M^-} \tag{4.28}$$

and we can also state the charge required to provide accelerating gradient $E_a$ as:

$$Q = \frac{L E_a T_R}{4\eta k} \tag{4.29}$$

where $k$ is the loss factor. A more detailed analysis can be found in [150].

In the use of a symmetric beam which is much shorter than the wakefield mode wavelength, the limit of $T_R \leq 2$ will be approached when $W_M^- = W^-\left(0\right)$. It is possible to build multimoded structures and use tailored bunch shapes in which the field amplitude of the modes add constructively to produce $T_R > 2$ however these are specifically engineered special cases. Furthermore the injection of a witness bunch will create its own wakes which will add in superposition with the driving wake. Consequently in general one must ensure $n_d q_d > n_w q_w$ to maintain $T_R > 1$ [151].

### 4.4.3 Wakefield Impedance

As with any electromagnetically resonant structure—when it is excited, the fields will form modes. These modes will form relative to the longitudinal and transverse fields from the beam driving the structure. To calculate the modes generated from a beam, taking the Fourier transform of the wake potential we get the expression:

$$W\left(z_w\right) = \frac{1}{n_d q_d} \int_{-\infty}^{\infty} \tilde{w}\left(\omega\right) \tilde{\rho}\left(\omega\right) \exp\left[i \omega z_w\right] d\omega \tag{4.30}$$

While it may seem counter-intuitive, wakefield impedance and transformer ratio are inversely related such that a strong wakefield impedance leads to a poor $T_R$. This is seen as a consequence of the $T_R$ and accelerating gradient additionally being inversely related as shown in [152].

### 4.4.4 Beam Current Limits and Beam Instability

By the repulsive nature of the charged particles in a particle beam, and at rest without external forces upon them will break up. "Collective effects" (CE) is a broad umbrella term which covers many physical phenomena present in beam instabilities. Some instabilities are fairly obvious such as charge repulsion, and some others have more complex and subtle properties such as the ponderomotive force. In a wakefield structure however one of the more dominant beam breakup events is the beam exciting transverse wakefield modes which give a lateral kick to the beam. This can either be a large singular effect over a single pass, or a small cascading effect which affects the beam over multiple passes. For the purpose of this thesis, the main BBUs examined will be that of the effects of short range wakes on the bunch that excited them, and high-order modes which may lead to divergence and/or emittance growth.

For the first CE mentioned, the case of beam instability arising due to short range wakefields can also be called single-bunch beam breakup (SBBU). This can be excited by a beam propagating with an offset to the centroid of the accelerating structure. When excited, the leading particles of the bunch will experience zero deflecting forces however the trailing particles which may or may not also be offset will feel the deflecting fields excited by the leading particles.

The Panofsky-Wenzel theorem is a useful relationship in wakefield studies. Fundamentally if, for an accelerating system that has a defined boundary beyond which there is no beam-wave interaction, we know the transverse variation of the longitudinal fields—we can know the longitudinal variation of the transverse fields. Considering the momentum of particles in a bunch, we can write the PWT as:

$$\nabla \times \Delta \mathbf{p} = 0 \tag{4.31}$$

Or more intuitively as a function of transverse and longitudinal components:

$$\nabla_{\perp} \Delta p_z = \frac{\partial}{\partial z} \Delta p_{\perp} \tag{4.32}$$

The derivation and proofs of this theorem can be found in literature and as such will not be repeated here. General proofs which do not assume any particular beam or structure shapes can be found by Panofsky and Wenzel in [153] or additionally [154].

## 4.5 Conclusion

This chapter examined the fundamentals of particle beams and their interaction with structures. It begins with a description of what a bunch is with the Vlasov equation. The emittance is then defined as a common parameter used to characterise propagating beams. Some methods of extracting energy from highly-relativistic particle beams are then examined and the concept of coherence discussed. These methods of energy extraction are then combined into the fundamental theorem of wakefields, and wakefield potential and impedance are discussed. The chapter closes by addressing the concept of collective effects on the beam.

## 5

# Externally-Driven Photonic Crystal Based Waveguides

This chapter presents numerical studies of photonic crystal based waveguides for THz driven particle acceleration. The focus is the methodology of designing for a specific centre-frequency in the photonic-bandgap, and impedance calculations to compute the expected accelerating voltage from a provided pulse. A 1D and a 2D PhC-based waveguide are investigated to identify modal dispersion characteristics and accelerating voltage. The chapter closes with an investigation into the ability to couple electromagnetic radiation into these structures. Some work has been undertaken for acceleration at 1 THz and later work undertaken at 500 GHz, due to scope-shift. The scalability of these structures however mean that results are applicable at both frequencies when appropriate scaling is used.

## 5.1 1D-Periodic PBG-W: Bragg Stack Based Waveguide

As shown in section 3.3, photonic crystals exist in dimensions of periodicity. As such, THz waveguides in which construction was based on photonic-crystal with a single dimension of periodicity were considered first.

To design a Bragg stack with maximum confinement, each layer must be one quarter transverse wavelength thick [155]. For this we assume there is no transverse wavenumber perpendicular to the Bragg stack. Thus for a PBG-W based on the photonic crystal in Fig. 5.1, the wavenumber in the Cartesian $y$-axis $k_y = 0$ in:

$$k = \sqrt{k_x^2 + k_y^2 + k_z^2} \tag{5.1}$$

Where $k$ is the wavenumber, with $k_x$, $k_y$, and $k_z$ as the wavenumber components in the $x$, $y$, and $z$ axes respectively. Knowing the phase velocity:

$$v_p = \frac{\omega}{k} \tag{5.2}$$

where $\omega$ is the angular frequency. When $v_p = c$, and $c$ is the speed of light, we can write:

$$\omega = ck \tag{5.3}$$

In dielectric of refractive index $n = \sqrt{\varepsilon_r}$, with $\varepsilon_r$ is the relative permittivity of the material:

$$k = \frac{n\omega}{c} \tag{5.4}$$

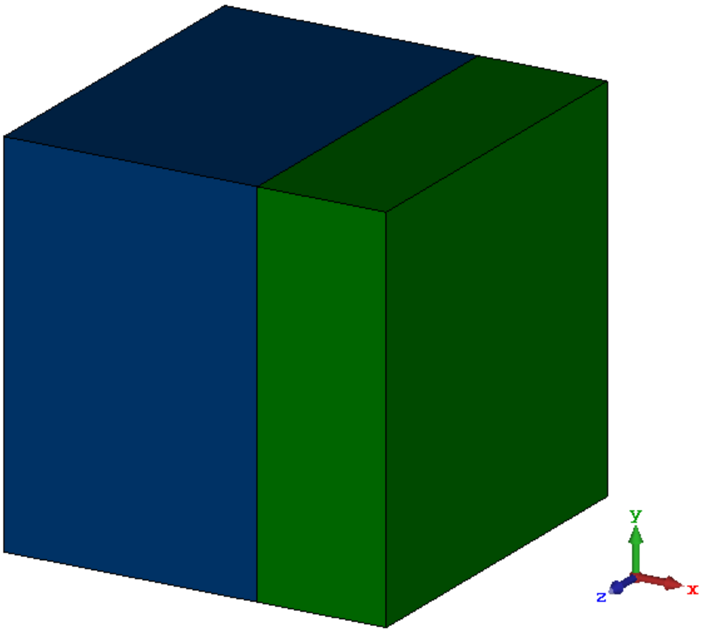

Figure 5.1: Unit cell of quarter-wave thickness layers Bragg stack, with alternating layers of dielectrics with $\varepsilon_r = 11.66$ and $\varepsilon_r = 3.75$.

thus we can write:

$$k_x^2 = k^2 - k_z^2 = \left(\frac{n\omega}{c}\right)^2 - k_z^2 \tag{5.5}$$

As we approach $c$ in the $z$-axis, $k_z$ becomes:

$$k_z = \frac{\omega}{c} \tag{5.6}$$

and now we can write:

$$k_x^2 = \left(\frac{n\omega}{c}\right)^2 - \left(\frac{\omega}{c}\right)^2 = \left(\frac{\omega}{c}\right)^2 \left(n^2 - 1\right) \tag{5.7}$$

Using the definition $k = \frac{2\pi}{\lambda}$:

$$\left(\frac{2\pi}{\lambda_x}\right)^2 = \left(\frac{\omega}{c}\right)^2 \left(n^2 - 1\right) \tag{5.8}$$

where $\lambda_x$ is the transverse $x$-axis wavelength, thus:

$$\lambda_x = \frac{2\pi c}{\omega} \frac{1}{\sqrt{n^2 - 1}} \tag{5.9}$$

where we know from the outset that the design is for a quarter-wavelength layer thickness $\lambda_x = 4D$, where $D$ is the layer thickness, thus:

$$D = \frac{\lambda_0}{4\sqrt{n^2 - 1}} = \frac{\lambda_0}{4\sqrt{\varepsilon_r - 1}} \tag{5.10}$$

where $\lambda_0$ is the free-space wavelength. The materials chosen for a Bragg stack must be selected in such a way to provide a sufficient dielectric ratio to create a photonic bandgap capable of confining a broad bandwidth pulse. For this structure, alternating layers of silicon and quartz ($SiO_2$) in quarter-wave thickness was chosen with $\varepsilon_r = 11.66$ [156] and $\varepsilon_r = 3.75$ [157] respectively, giving a dielectric ratio of 3.12. The unit cell for modal analysis in CST eigenmode simulation is shown in Fig. 5.1. The boundaries are fully periodic within $x$, $y$, and $z$; and the resultant dispersion of the photonic bands shown in Fig. 5.2.

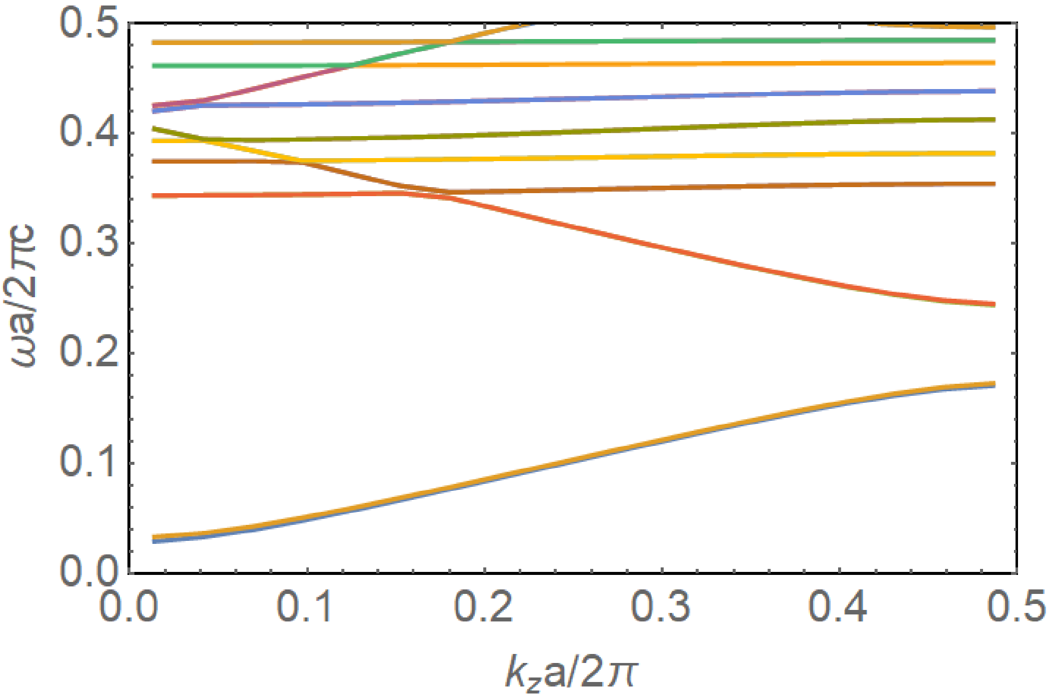

Figure 5.2: Band diagram for Bragg structure shown in Fig. 5.1, with total bandgap visible between 0.17 and 0.24

The band diagram in Fig. 5.2 illustrates the dispersion for each mode supported by the photonic crystal, with each line doubled as an artefact from calculating a one-dimensional structure in two-dimensions. The gap between the first and second mode shows a region in which no mode is supported by the photonic crystal i.e. the photonic bandgap. It is shown to be a sufficient bandgap for confinement of a broadband accelerating pulse, a 1D-periodic PBG-W was designed for initial examination, the unit cell of which is shown in Fig. 5.3. The PBG-W is a stack of the unit cells shown in Fig. 5.1, with each dielectric slab of dielectric in the unit cell known as a "layer". The vacuum channel has a width of $0.6\lambda_0$ and the inner layer of the Bragg stack, or "pad layer", was adjusted in thickness to ensure synchronism of $v_p/c = 1$ at the frequency of interest [158]. The adjustment is dependent on the channel width and whether the low or high permittivity dielectric is closer to the centre as defined in the equations:

$$\Delta_1 = \begin{cases} \dfrac{1}{k_1}\arctan\left[\left(\dfrac{Z_1}{Z_0}\dfrac{\omega_0}{c}C\right)^{-1}\right] & Z_1 > Z_2 \\ \dfrac{1}{k_1}\arctan\left[\left(-\dfrac{Z_1}{Z_0}\dfrac{\omega_0}{c}C\right)\right] & Z_1 < Z_2 \end{cases} \tag{5.11}$$

when:

$$k_1 = \frac{\omega_0}{c}\sqrt{\varepsilon_r - 1} \tag{5.12}$$

and:

$$Z_1 = \frac{k_1}{\omega_0 \varepsilon_0 \varepsilon_r} \tag{5.13}$$

where $\Delta_1$ is the first layer thickness multiplier, $k_1$ is the transverse wavenumber of the first layer, $Z_1$ & $Z_2$ are the impedances of the first and second layers respectively, the impedance of free space $Z_0 = \sqrt{\mu_0/\varepsilon_0} \approx 377\,\Omega$, $\omega_0$ is the frequency of interest, and $C$ is the width of the vacuum channel. For the $1\,THz$ Bragg based waveguide investigated here, $\Delta_1 = 0.557612$.

The Bragg-based PBG-W is infinite in the $y$-direction and is implemented in CST via a periodic boundary condition (PBC). Additionally the PBG-W is periodic in the $z$-direction, with variation in the phase-shift to plot the propagating mode dispersion. The extremities of the $x$-direction are bound by a perfectly electrically conducting (PEC) metal as open boundaries are disallowed in the CST eigenmode solver; where 10 layers of each dielectric are used to ensure a sufficient number to minimise the effect of the metal boundary.

The resultant accelerating $v_p/c = 1$ mode for the structure, showing good confinement and the evanescent decay of the field into the photonic crystal is shown in Fig. 5.4. The dispersion for this mode is shown in Fig 5.5. The figure also shows the top of PhC band 1, and the bottom of PhC band 2, the limits of the total bandgap, the frequency of interest, and the speed of light line. The intersection of the speed of light line and the frequency line illustrates where $v_p/c = 1$ and thus

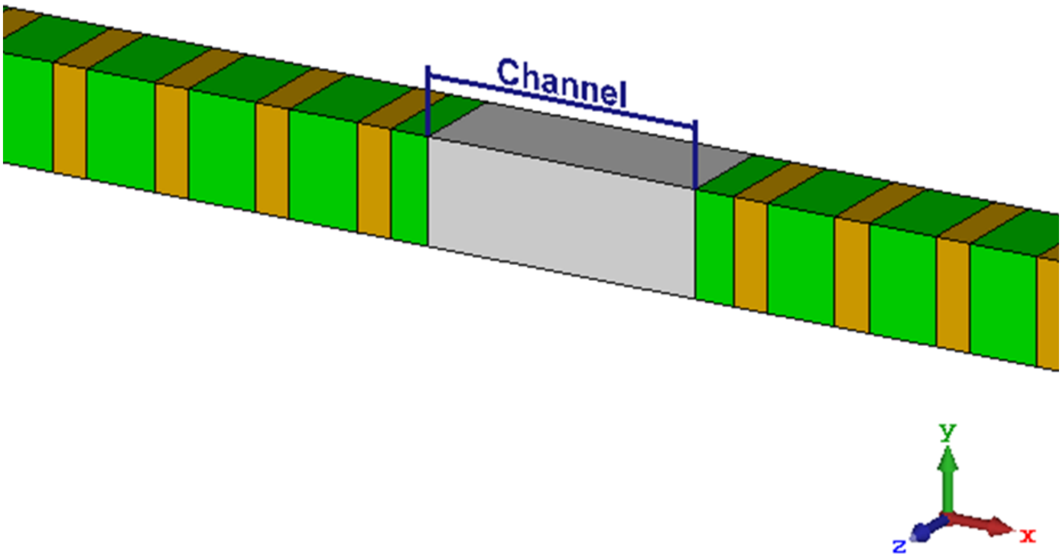

Figure 5.3: Quarter-wave Bragg stack with first layer modified to a pad layer according to equations 5.11.

the ideal point of synchronism between accelerating mode and highly relativistic particle beam.

For each frequency point on the dispersion curve, the characteristic impedance $Z_c$ is also recorded. This $Z_c$ is zero-padded at all frequencies outside the dispersion curve. From this, using the method illustrated in Eqns. 3.65–3.67, the accelerating voltage for a $5\,mm$ length structure can be calculated. This resulting voltage, shown in Fig. 5.6, reveals that the structure has a low peak bandwidth at $\sigma = 0.5\%$ giving an accelerating voltage of $22\,MV$, or gradient of $4.4\,GV/m$. At higher

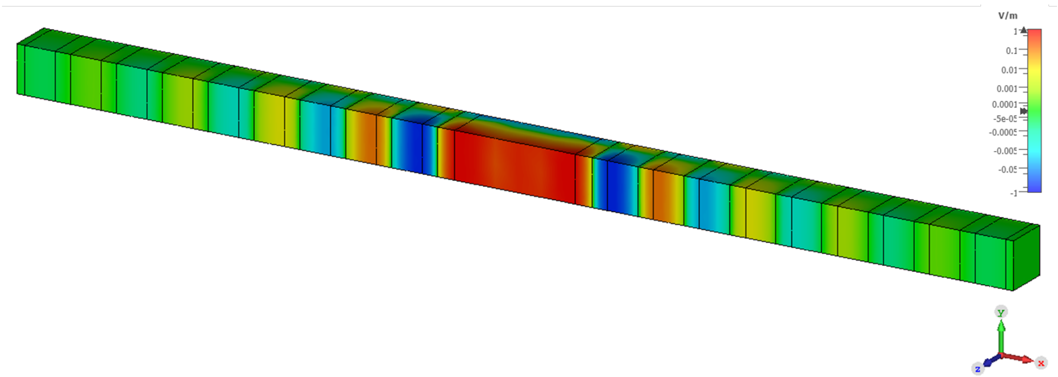

Figure 5.4: Longitudinal E-field component profile of the accelerating mode in quarter-wave Bragg stack with modified pad-layer of $\Delta_1 = 0.557612$

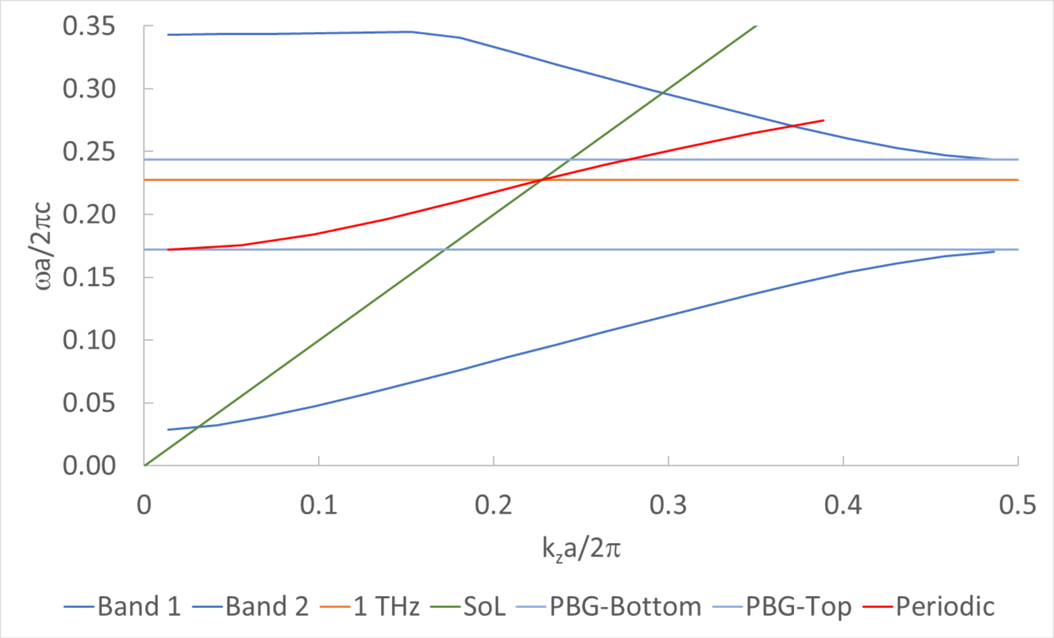

Figure 5.5: Dispersion of accelerating mode in a quarter-wave Bragg stack with modified pad-layer. This particular structure was designed to operate at $1\,THz$.

bandwidths, the accelerating voltage for a $\sigma = 10\%$ pulse gives $5\,MV$ $(1\,GV/m)$; and $3\,MV$ $(600\,MV/m)$ for a $\sigma = 25\%$ bandwidth. For a PhC-based acceleration structure, these acceleration voltages would be sufficient for acceleration of highly-relativistic electrons.

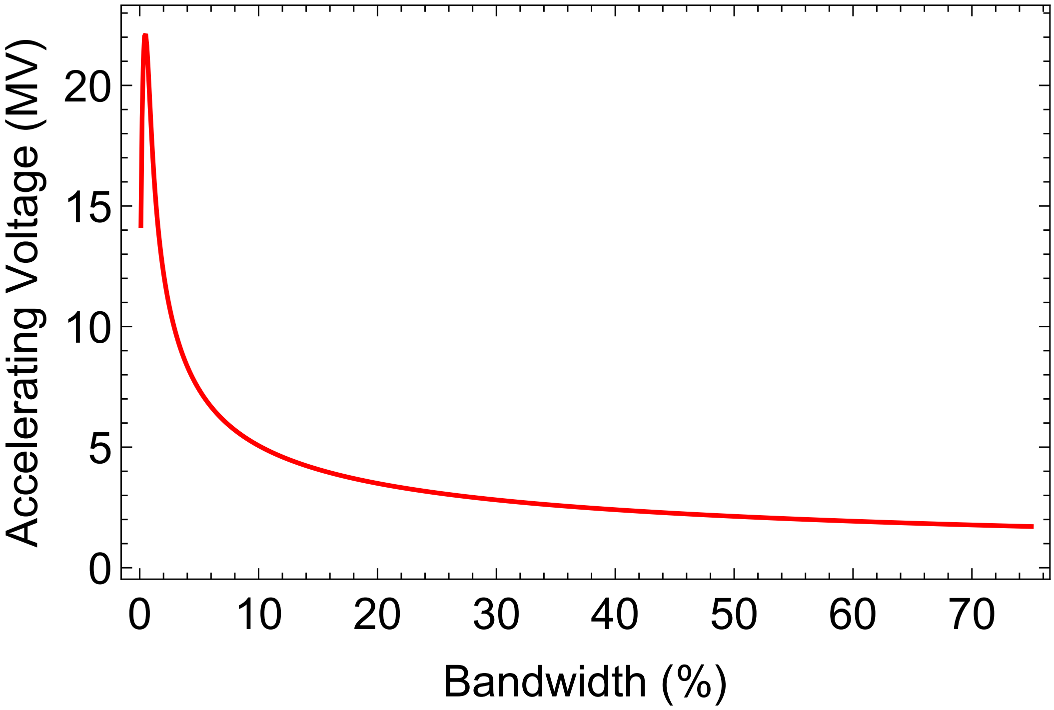

Figure 5.6: Accelerating voltage for input pulse bandwidth in quarter-wave Bragg stack with modified pad-layer.

### 5.1.1 Metal-Clad Boundaries

The periodic boundary conditions of the previous section were a good first look at the behaviour of photonic crystal based waveguides for acceleration. A periodic boundary is however not a true representation of a real structure and in order to design a waveguide which is capable of confining modes in all three dimensions, a modification of the planar Bragg-based waveguide to provide confinement in the $y$-axis was required. Of the many forms of waveguide that exist, two topographies lend themselves to desirable construction designs: rectangular, and parallel plate. With these designs, one fully confines the central channel in metal, and the other is infinite in the minor transverse plane, respectively. As the closed-type (metal-clad) designs were expected to give higher interaction impedances, the structure was truncated with parallel metal-plates in the $y$-axis.

Three vacuum gap $T/C$ aspect ratios of 1.2, 1.5, and 2.0 were considered. The accelerating mode excited in the $T/C = 2.0$ Bragg-based waveguide can be seen in Fig. 5.7 with the field profile shown in Fig. 5.8. Examining the dispersion for the mode excited in these $T/C$ ratios in Fig. 5.9, as the width of the structure increases it tends towards the infinite structure, which in itself is an approximation of a parallel plate waveguide. The synchronism point was also seen to have shifted and is no longer the desired interaction frequency and consequently the acceleration voltage is poor in comparison as shown in Figs. 5.10 and 5.11. As the synchronism condition in Eqn. 5.11 no longer holds, the pad layer was modified such that $\Delta_1 = 0.899059$ and $\Delta_1 = 0.675358$ for the $T/C = 1.2$ and $T/C = 2.0$ ratios respectively. The dispersion was again calculated and can be seen in Fig. 5.12, with comparison of $T/C = 1.2$ and $T/C = 2.0$ accelerating voltage bandwidths shown in Fig. 5.13.

Comparison across structures in Fig. 5.14 shows that the parallel plate structure still presents the highest acceleration voltage of the Bragg structures, however due to the limitations of the eigenmode solver, a true parallel plate waveguide cannot be modelled however in practise this structure is worth investigation. Further models with time domain and PIC solvers would further illustrate its acceleration capability.

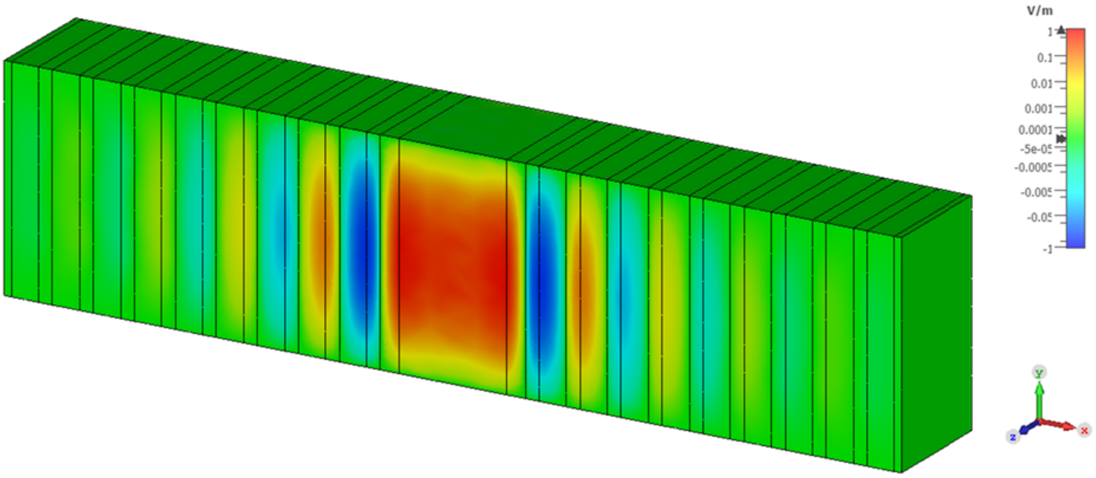

Figure 5.7: Accelerating mode in metal-clad Bragg accelerating structure

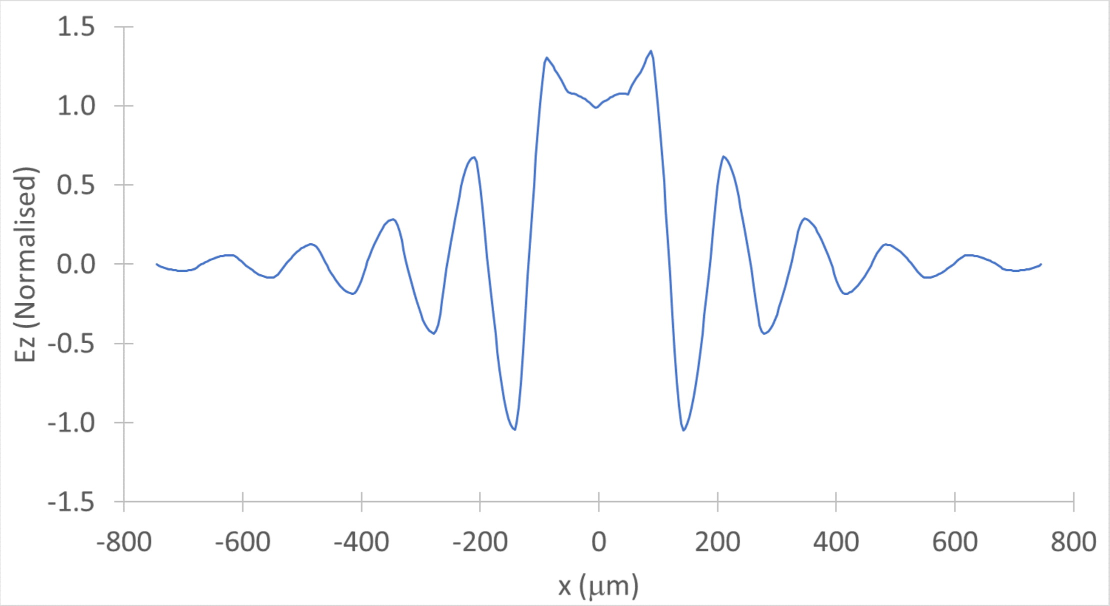

Figure 5.8: $E_z$ component of the accelerating mode in the Bragg-based metal-clad waveguide on $x$-axis, normalised to field at $x = 0$.

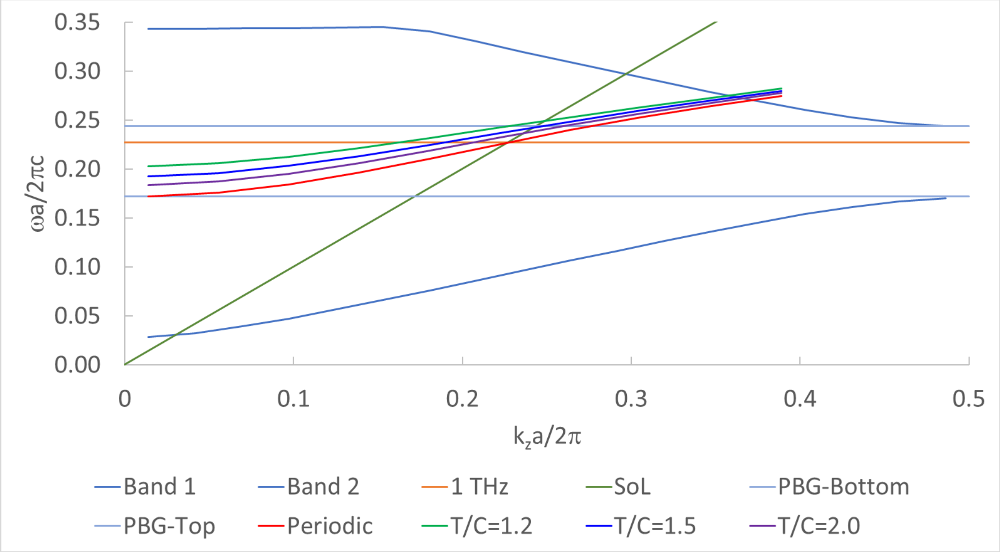

Figure 5.9: Dispersion of accelerating mode in the metal-clad Bragg-based waveguide with modified pad-layer in $T/C = 1.2$, $1.5$, $2.0$ and periodic structure. This particular structure was designed to operate at $f_0 = 1\,THz$.

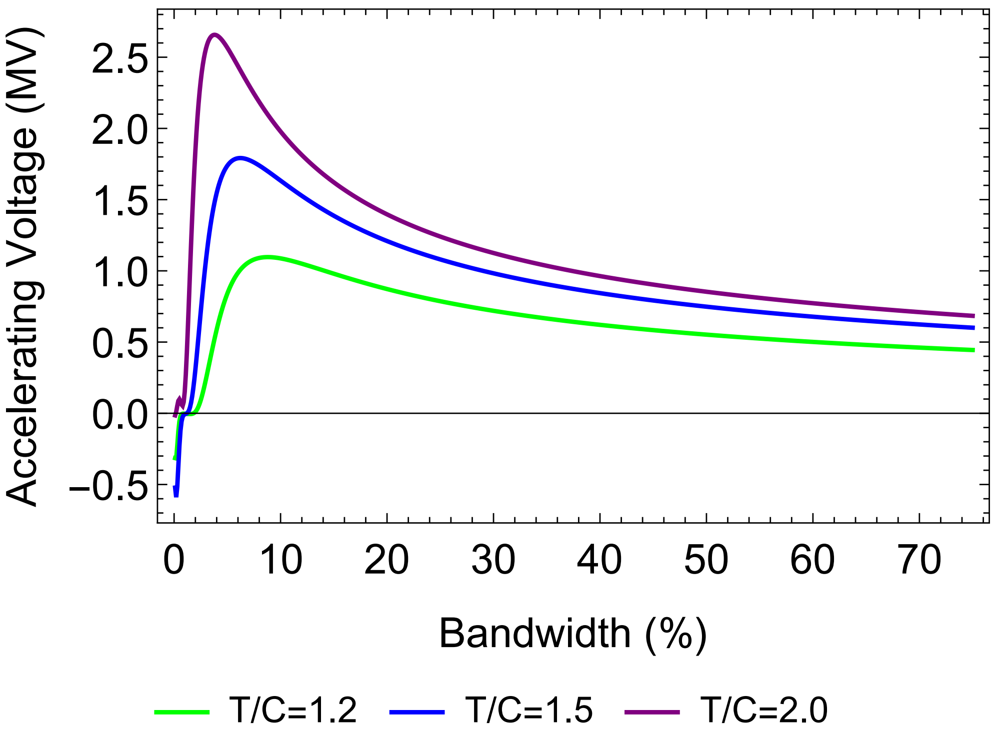

Figure 5.10: Comparison of accelerating voltage for $T/C = 1.2$, 1.5, 2.0 metal-clad Bragg structures. Pad layer utilised matching condition in Eqns. 5.11.

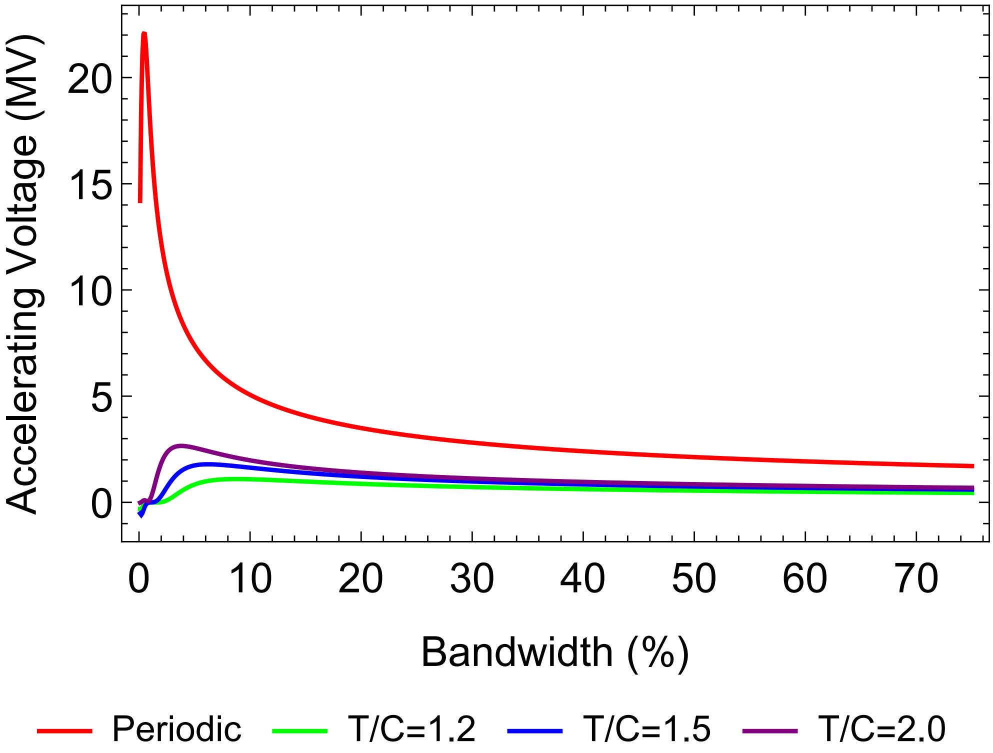

Figure 5.11: Comparison of accelerating voltage bandwidth for $T/C = 1.2$, 1.5, 2.0 metal-clad Bragg-based waveguide with periodic boundary Bragg-based waveguide.

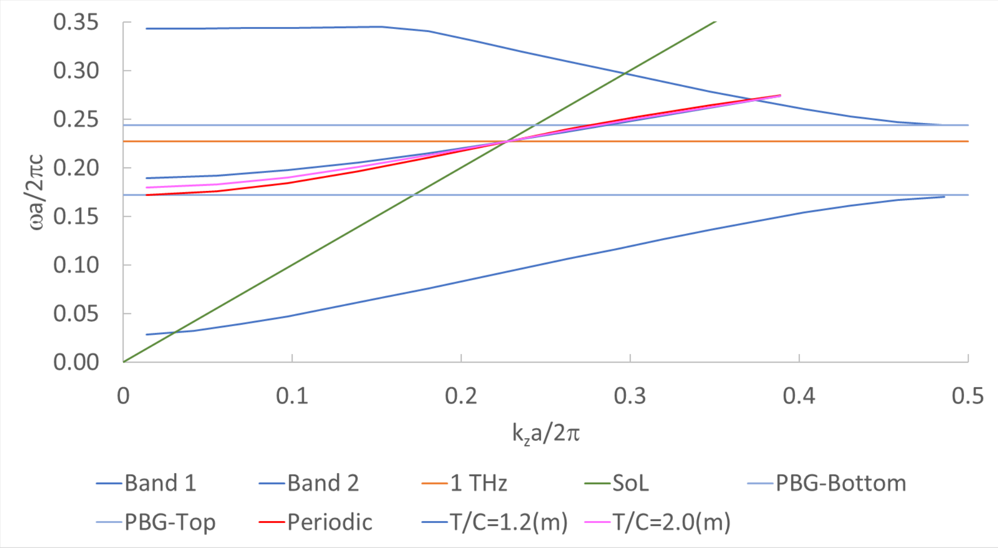

Figure 5.12: Accelerating mode dispersion in Bragg waveguide structure with $T/C$ ratios of 1.2, 1.5, and 2.0. Pad layer was modified such that $v_p/c = 1$ for desired frequency $f = 1\,THz$ with $\Delta_1 = 0.899059$ and $\Delta_1 = 0.675358$ for $T/C = 1.2$ and $T/C = 2.0$ respectively.

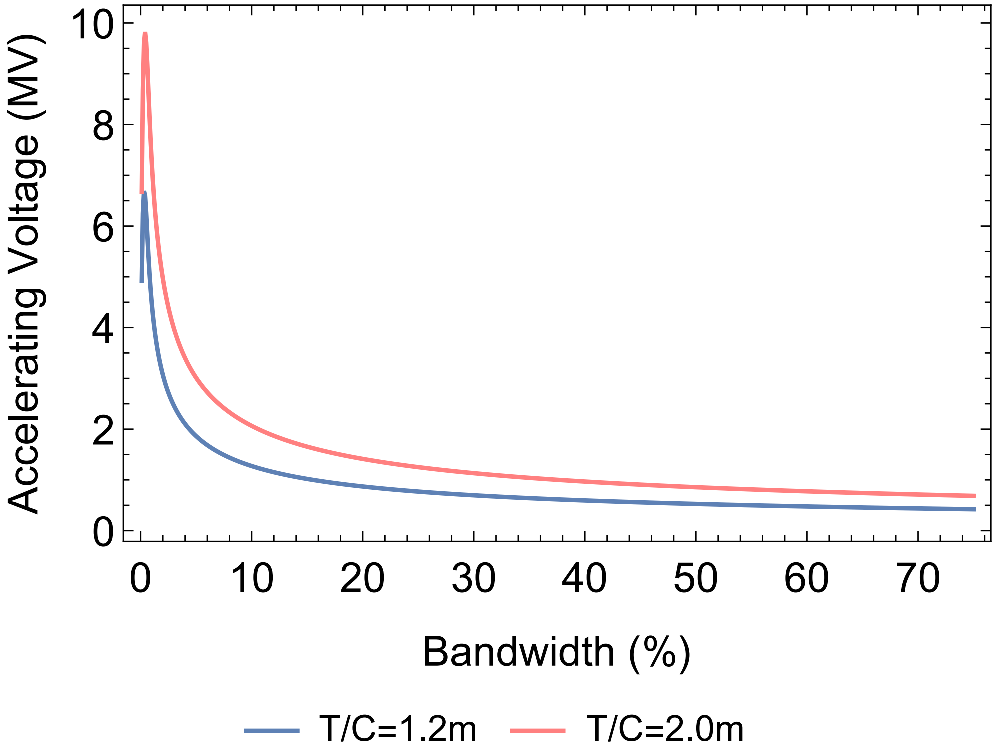

Figure 5.13: Acceleration voltage for $T/C = 1.2$, 2.0 with pad layer modified for $v_p/c = 1$ synchronism at $f_0$. The “m” in the legend indicates these ratios have a pad layer modified to ensure the $v_p/c = 1$ condition.

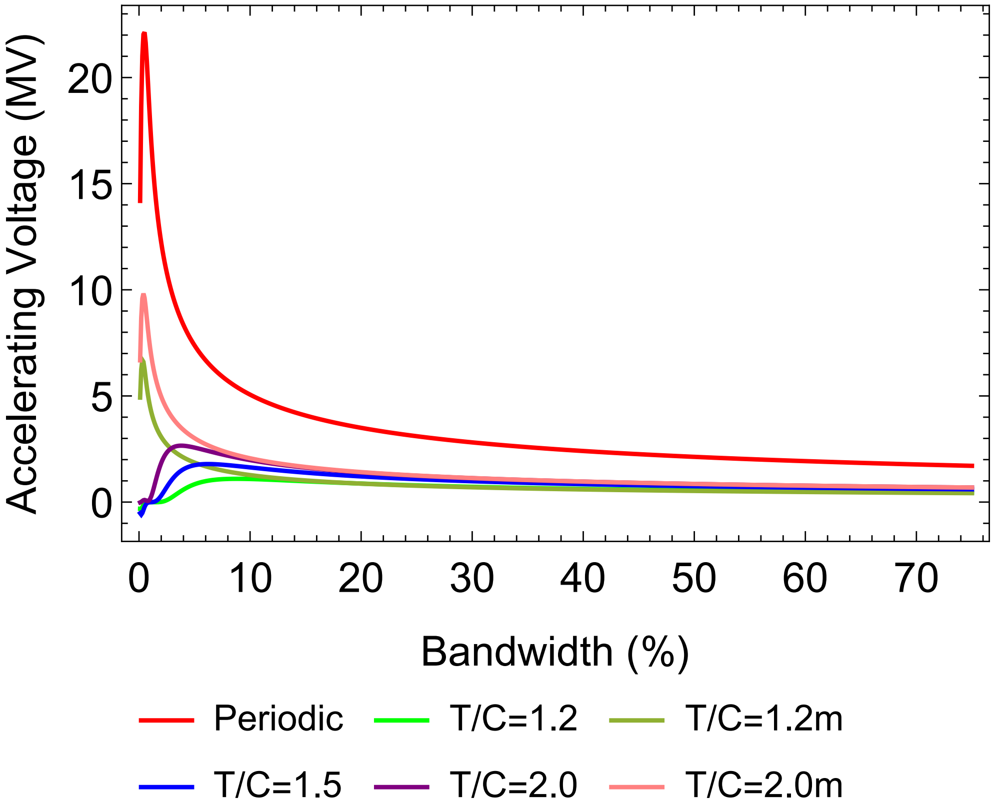

Figure 5.14: Comparison of all accelerating voltage bandwidth figures obtained for the Bragg-based waveguide. The "m" in the legend indicates these ratios have a pad layer modified to ensure the $v_p/c = 1$ condition.

## 5.2 2D-Periodic PBG-W: Triangular Lattice Based Waveguide

So far, analysis has focused on 1D-periodic Bragg-based waveguides for acceleration. As shown in [47], waveguides based on 2D-periodic photonic crystals can offer increased impedances over 1D-periodic structures. Slab-based 2D-periodic structures have the advantage of being relatively easy to manufacture especially when based on lattices of holes in a dielectric material. In comparison with the precision layer deposition required for Bragg structures or the 3D-printing requirements of 3D-periodic structures, this could be conceptually easier to realise. This section explores the accelerating performance of 2D-periodic photonic crystal based waveguides and compares the results with the 1D-periodic Bragg-based waveguide investigated previously. A triangular lattice of holes in a dielectric slab is considered for the design of the 2D-periodic PBG-W.

### 5.2.1 Material Selection

For a PBG-W to be useable in accelerator applications beyond proof-of-concept, it not only needs to perform well in relation to high-gradient acceleration characteristics. Certain characteristics such as those detailed in chapter 3 can be used as figures-of-merit (FoMs) for comparing structures without requiring the undertaking of full particle dynamics calculations. Many of these FoMs are related to the physical structure of the accelerator, which for dielectric-based waveguides—is dictated by the dielectric itself. As the photonic bandgap is proportional to the dielectric ratio of the constituent media in the PhC, and this photonic crystal design utilises the periodic spacing of vacuum holes in a solid dielectric slab, a higher relative permittivity $\varepsilon_r$ of the dielectric slab leads to a broader bandgap.

Higher $\varepsilon_r$ however has the opposing effect of both increasing the manufacturing precision required near the vacuum channel due to smaller regions having a greater effect on the field. Additionally, the group velocity of a propagating mode is reduced through the dielectric-based waveguide as defining the refractive index in the dielectric:

$$n\left(\omega\right) = \sqrt{\varepsilon_r\left(\omega\right)\mu_r\left(\omega\right)} \tag{5.14}$$

where the relative permeability of most dielectrics is $\mu_r = 1$ allowing the phase velocity $v_p$ to be given as:

$$v_p\left(\omega\right) = \frac{c}{n\left(\omega\right)}\left(m/s\right) \tag{5.15}$$

The group index $n_g$ details the change in group velocity in dielectric media. From the definition of $v_p$, $n_g$ can be defined as:

$$n_g\left(\omega\right) = \frac{c}{v_g\left(\omega\right)} = c\left(\frac{d\omega}{dk}\right)^{-1} = \frac{d}{d\omega}\left[\omega n\left(\omega\right)\right] \tag{5.16}$$

And thus applying the chain rule we get:

$$n_g\left(\omega\right) = n\left(\omega\right) + \omega\frac{dn\left(\omega\right)}{d\omega} \tag{5.17}$$

A common material used in photonic structures is quartz (silica, $SiO_2$) which has a permittivity of between $\varepsilon_r = 3.95$ [159] and $\varepsilon_r = 4.4$ [160] at THz frequencies. Whilst this allows for an expected group velocity of $v_g = 0.48c - 0.63c$ at $v_p/c = 1$, the maximum bandgap for this structure was found to be $16 - 23\%$ which is not suitable for confining a broadband THz pulse.

With the desire of both a high permittivity, and a mature fabrication process, silicon has a permittivity of $\varepsilon_r = 11.7$ and loss tangent $\tan\delta < 10^{-3}$ [156] [161]. This combination of manufacturing data available for silicon, high permittivity with maximum photonic bandgap of 52% which is wide enough to encompass the majority of a broadband THz pulse, meant this was an acceptable fabrication material to select for investigation into 2D-periodic PBG-Ws.

### 5.2.2 Unit Cell Analysis

For analysis of the 1D-periodic Bragg unit cell, this was constructed in CST and evaluated in the eigenmode solver. This was possible as the unit-cell had a square unit cell. For investigation of 2D-periodic photonic-crystal structure in this chapter, the unit cell was triangular and thus could not be fully evaluated in the same solver. The program MPB, discussed in chapter 3, was used to calculate the photonic bands. A triangular lattice was chosen as analysis of the "gap-map", or location of photonic bandgaps as a function of hole radius, in [95] indicates that a rectangular grid of holes will not provide a bandgap capable of confining both $TE_z$ and $TM_z$ modes. A triangular grid of holes in a dielectric slab however will confine both types of modes simultaneously. MPB was set up to output the gap configuration for a range of hole radii.

MPB was set up with lattice vectors defined as in Eqn. 5.18, where $\Gamma$, $M$, and $K$ are points on the reduced Brillouin zone, and an example of the 2D lattice can be seen in Fig. 5.15. The corresponding gap-map of hole-radius versus bandgap in Fig. 5.16. The gap-map illustrates a bandgap of approx 50% is obtainable between $0.40 - 0.45\, r/a$. Plotting the bands for the case of $r = 0.445a$ in Fig. 5.17, the $TM_z$ bandgap can be seen between $0.30 - 0.48$; the $TE_z$ bandgap is not shown.

$$\Gamma = 0,\, M = \frac{\pi}{a}\hat{j},\, K = \frac{\pi}{a}(\hat{j} + \hat{k}) \tag{5.18}$$

### 5.2.3 2D PBG-W Analysis

The PBG structures modelled in MPB provided an indication of how 2D-periodic triangular lattice based PBG-Ws performed as acceleration structures. The first step is to construct a quasi-2D waveguide using periodic boundaries in CST. The periodic boundary in the direction of propagation was parametrically swept, while the transverse non-PhC boundary was set to a phase-shift of 0. Using the bandgap plots produced, the normalised centre-frequency of the bandgap was obtained, and thus choosing the centre-frequency, the photonic-crystal period was calculated. To

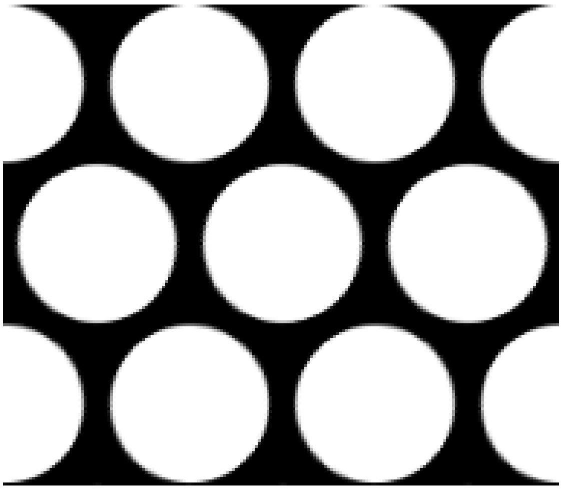

Figure 5.15: The triangular irreducible-Brillouin-zone structure as output by MPB and used in the calculation of the bandgaps for this structure

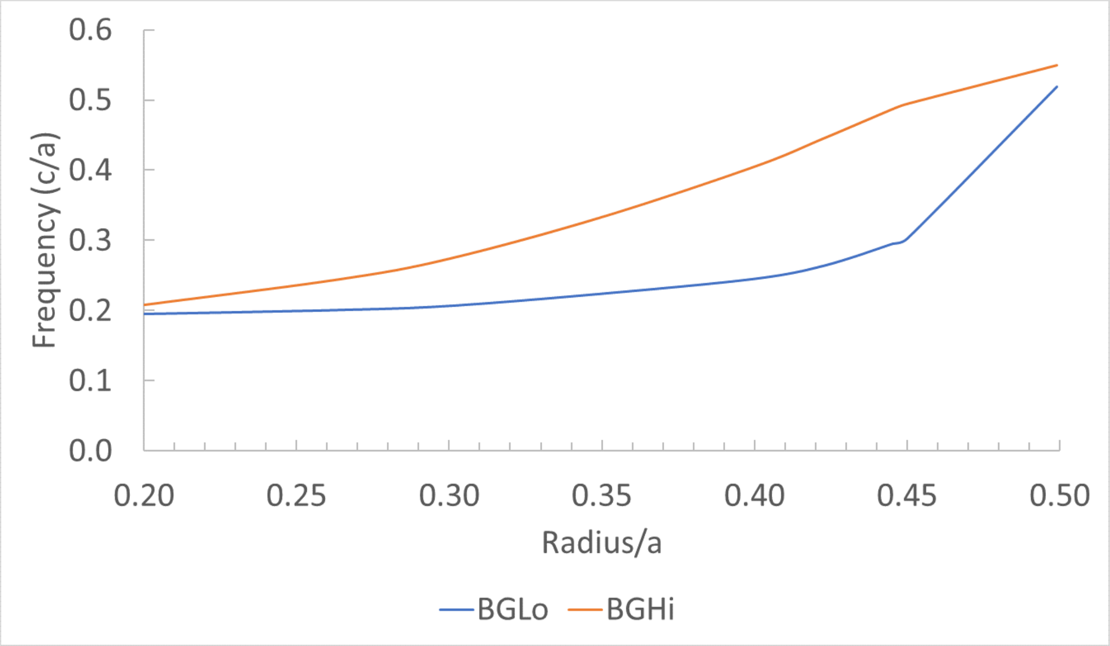

Figure 5.16: “Gap Map” of the bandgap for triangular lattice of holes in silicon $\varepsilon_r = 11.66$, indicating the bottom and top of the main bandgap BGLo and BGHi respectively.

investigate the effect of the location of the bandgap on the accelerating voltage, two radii were investigated. For a $1\,THz$ centre-frequency PBG-W with hole radius 0.423a and 0.445a, the photonic-period was calculated at $a = 106.3514\,\mu m$ and $a = 117.0390\,\mu m$. This gives a phase of interaction of 127.71° and 140.54° respectively.

Using the definitions shown in Fig. 5.18, the length in z-axis and the thickness

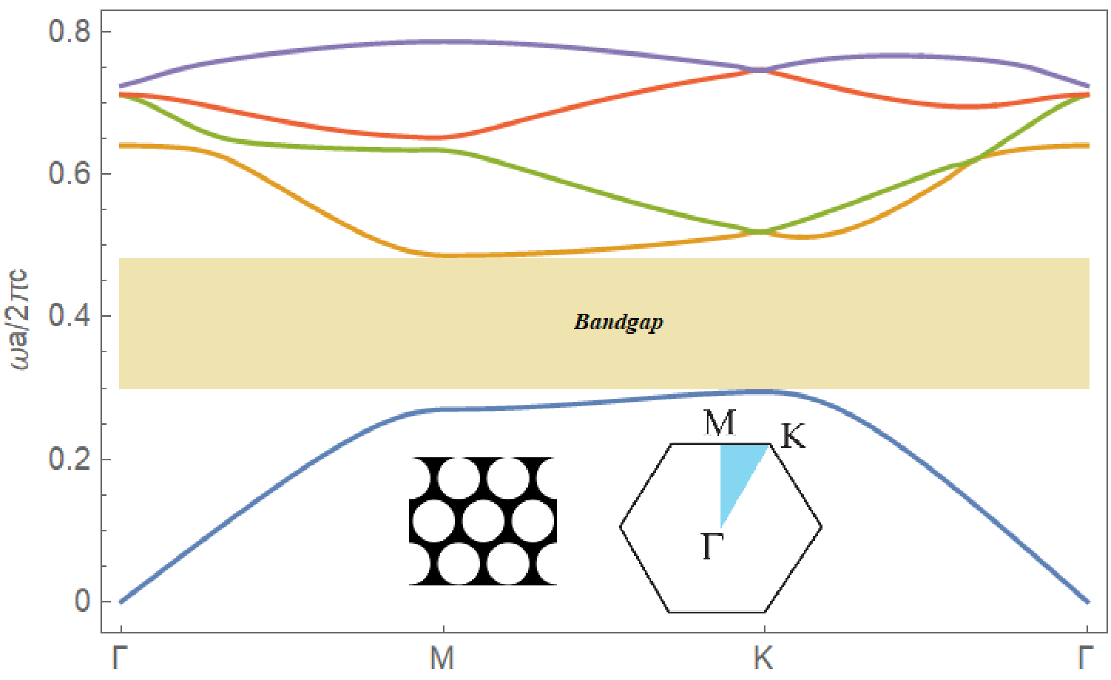

Figure 5.17: Band diagram for the 2D-PBG structure of $r = 0.445a$ and $\varepsilon_r = 11.66$ TM polarisation showing bandgap centred on $\omega a/2\pi c \approx 0.4$ corresponding to $1THz$ for $a = 117\mu m$. The PBG structure—where black is dielectric and white is vacuum, and irreducible Brillouin zone are shown in inset to the left and right respectively.

in x-axis were set to the size of the photonic period $a$. The channel width was set to $C = 0.6\lambda_0$ and the pad layer was adjusted so that the phase velocity at the centre-frequency was $v_p/c = 1$. For $r = 0.423a$ and $r = 0.445a$, the pad layer

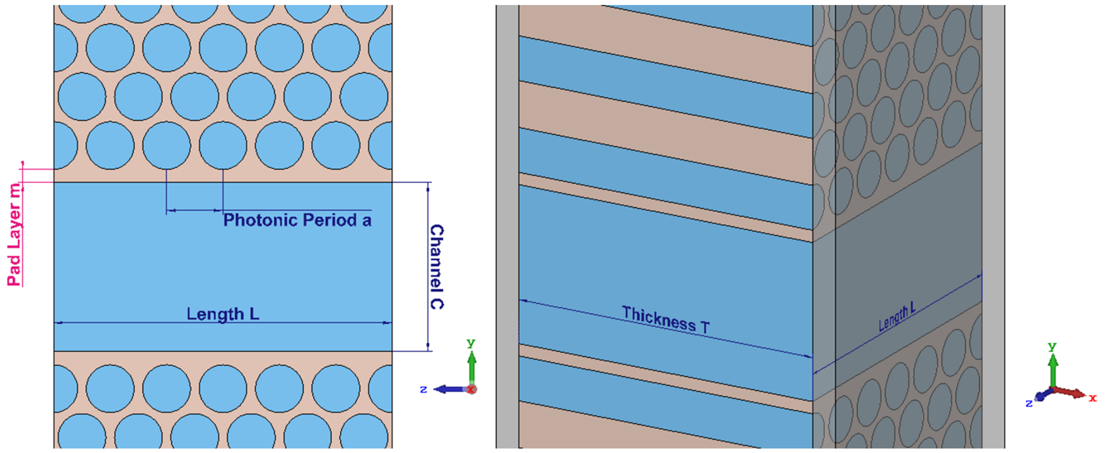

Figure 5.18: Schematic of the full 3D PBG-W using the 2D-periodic triangular lattice photonic crystal with the elevation view on the left, and the isometric view on the right. Orange is silicon, blue is vacuum, and transparent grey is the metallic cladding of the PBG-W.

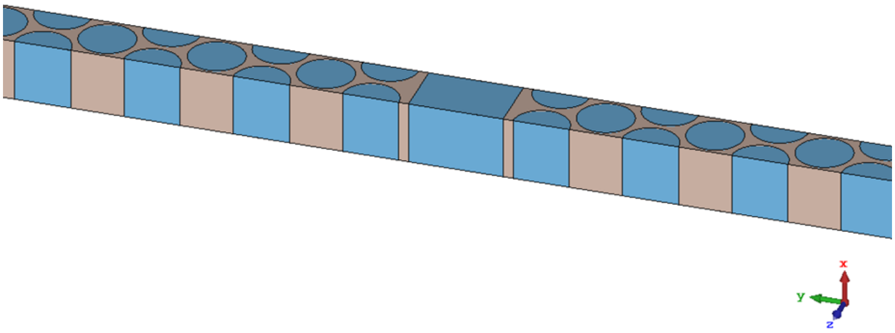

Figure 5.19: Example of 2D-Periodic triangular lattice based PBG-W with periodic $x$ and $y$ boundaries. Design parameters for each investigated case can be found in table 5.1.

was $m = 0.2326a$ and $m = 0.1799a$ respectively. The number of photonic periods of PhC used was 10.5. The unit cell of the resulting PBG-W is shown in in Fig. 5.19. Eigenmode simulations of this structure provide the field patterns of the fundamental accelerating mode. The $E_z$ component of the accelerating mode is shown in Fig. 5.20, with a 2D plot of $E_z$ on the $y$-axis at x=0 shown in Fig. 5.21. The list of design parameters in the design of these PBG-Ws can be found in table 5.1.

Table 5.1: Design Parameters in 2D-Periodic Triangular Lattice Based PBG-W with periodic boundary conditions (PBC).

| Parameter | Design 1 | Design 2 | Design 3 | Design 4 |
|---:|---|---|---|---|
| Hole Radius | $0.350a$ | $0.423a$ | $0.445a$ | $0.445a$ |
| Channel Width | $3.5a$ | $1.5a$ | $1.5a$ | $3.0a$ |
| PBG Width | 39.2% | 51.2% | 49.1% | 49.1% |
| Photonic Period $a$ | $83.4322\,\mu m$ | $106.3514\,\mu m$ | $117.0390\,\mu m$ | $117.0390\,\mu m$ |
| Interaction Angle | 83.43° | 127.71° | 140.49° | 140.49° |
| Pad Layer | $0.352983a$ | $0.232604a$ | $0.179900a$ | $0.155600a$ |

The resultant dispersion for both structures can be seen below in Fig. 5.22. It shows that while the bandgap for the structure is roughly the same size as per Fig. 5.16, the actual point of interaction varies. The negative group velocity region in the $r = 0.423a$ situation likely having a retarding effect on the voltage.

The accelerating voltage obtained from these two designs is calculated for varying THz pulse bandwidths and compared in Fig. 5.23. In comparison to the earlier Bragg-based waveguides, the accelerating voltage for this structure is poor. Exam-

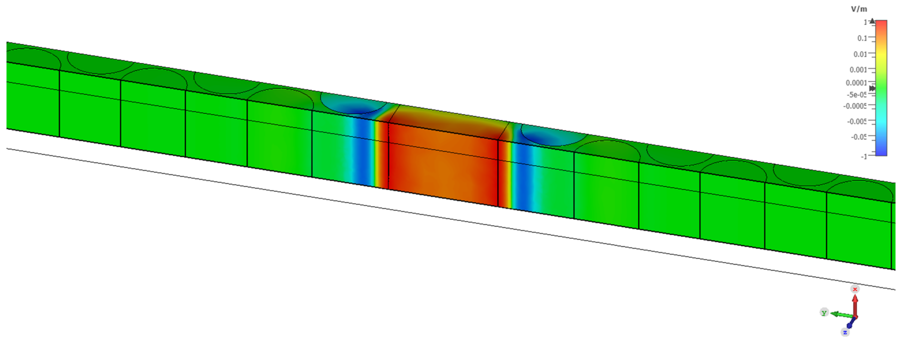

Figure 5.20: Accelerating mode in a triangular-lattice PBG-W with $C = 1.5a$, $r = 0.0.445a$. Full list of parameters given in table 5.1.

ining the dispersion for the accelerating mode in Fig. 5.22, the interaction point between with the particle beam is in a low group velocity region of the curve. This implies a low value of power flow resulting in a low accelerating voltage even though the interaction impedance is generally high in this region of the dispersion. To shift the interaction point into a region of the dispersion in which the group velocity is higher, the channel must be made wider. The previous simulations used a channel width of $C = 0.6\lambda_0$ which corresponds to approximately $1.5a$. As the $r = 0.445a$ PBG-W design had a higher accelerating voltage, further investigation was carried out considering this radius. Doubling the channel width to $C = 3a$,

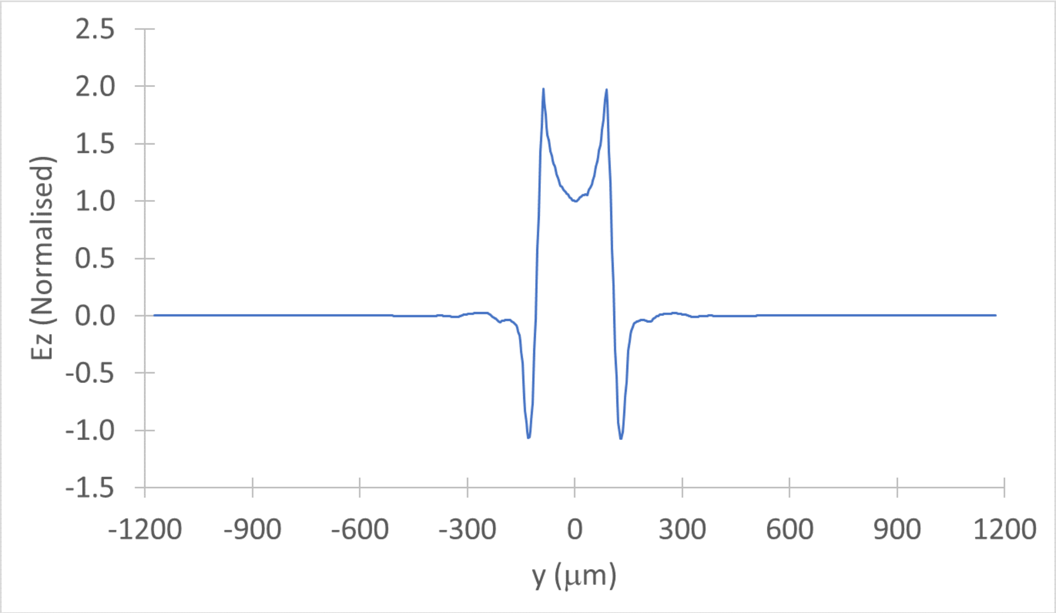

Figure 5.21: $E_z$ component of the accelerating mode in the 2D-Periodic triangular lattice based periodic boundary waveguide on $y$-axis, normalised to field at $y = 0$.

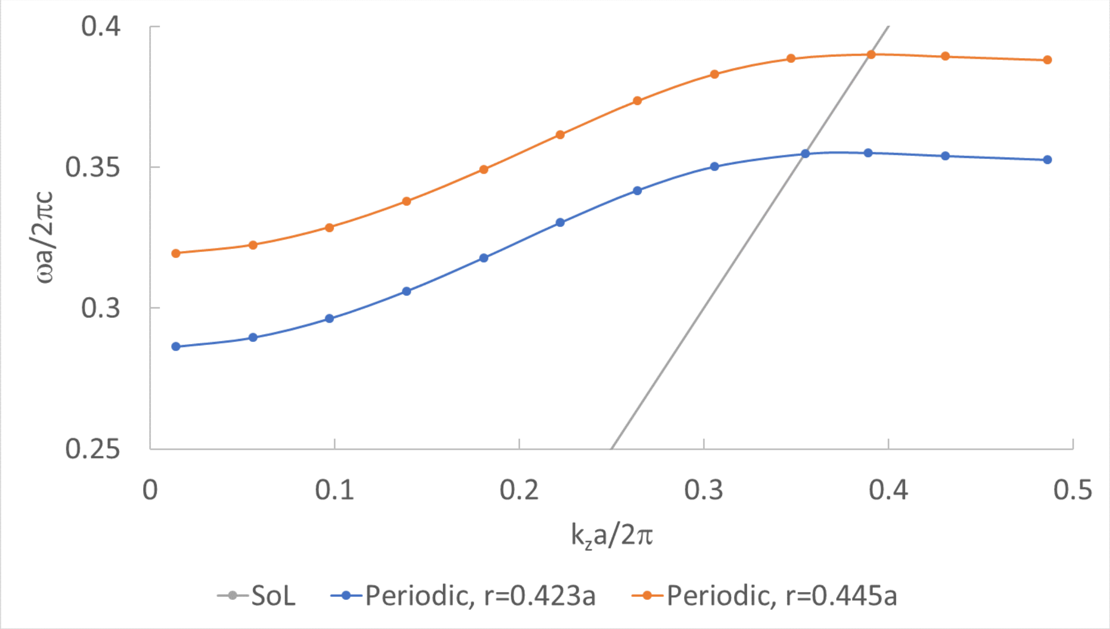

Figure 5.22: Comparison of accelerating mode dispersion for triangular lattice based PBG-Ws with $r = 0.423a$ and $r = 0.445a$.

the structure was again matched for $v_p/c = 1$ at $\omega_0$. The variation of the pad layer thickness required to tune the central frequency to the desired value of $1\,THz$ is

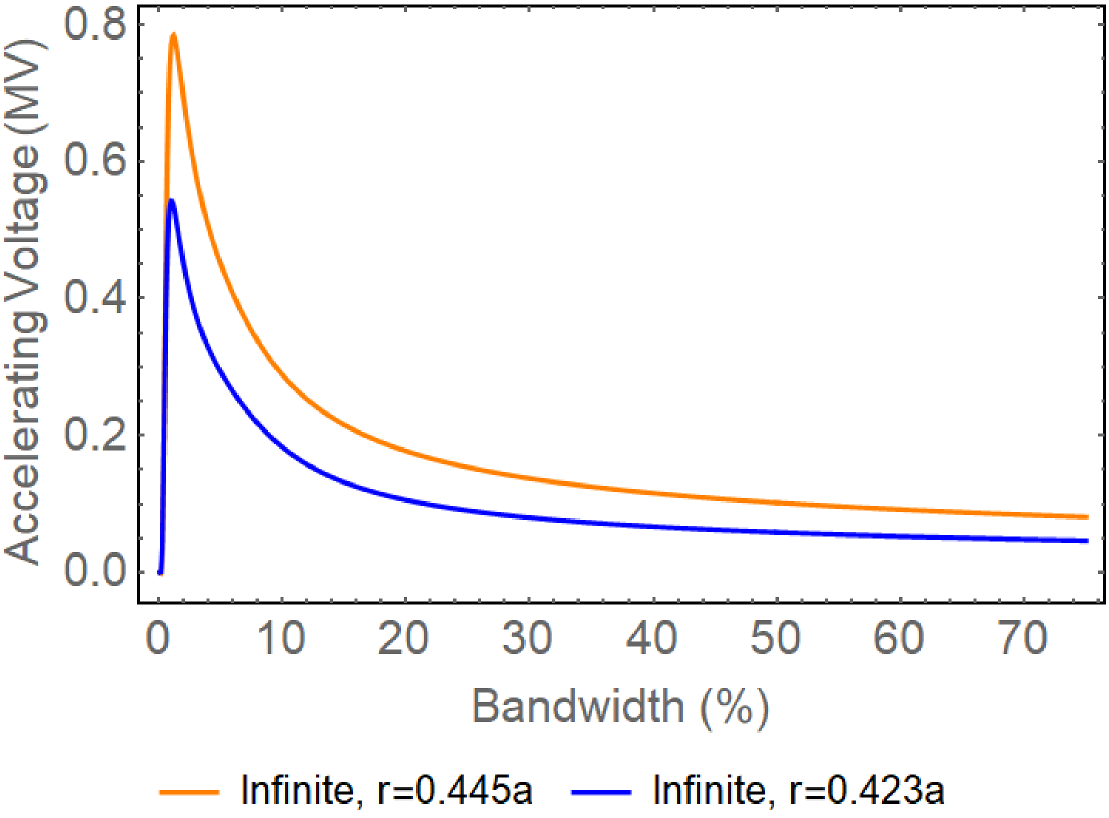

Figure 5.23: Accelerating voltage in $r = 0.423a$ and $r = 0.445a$ structures.

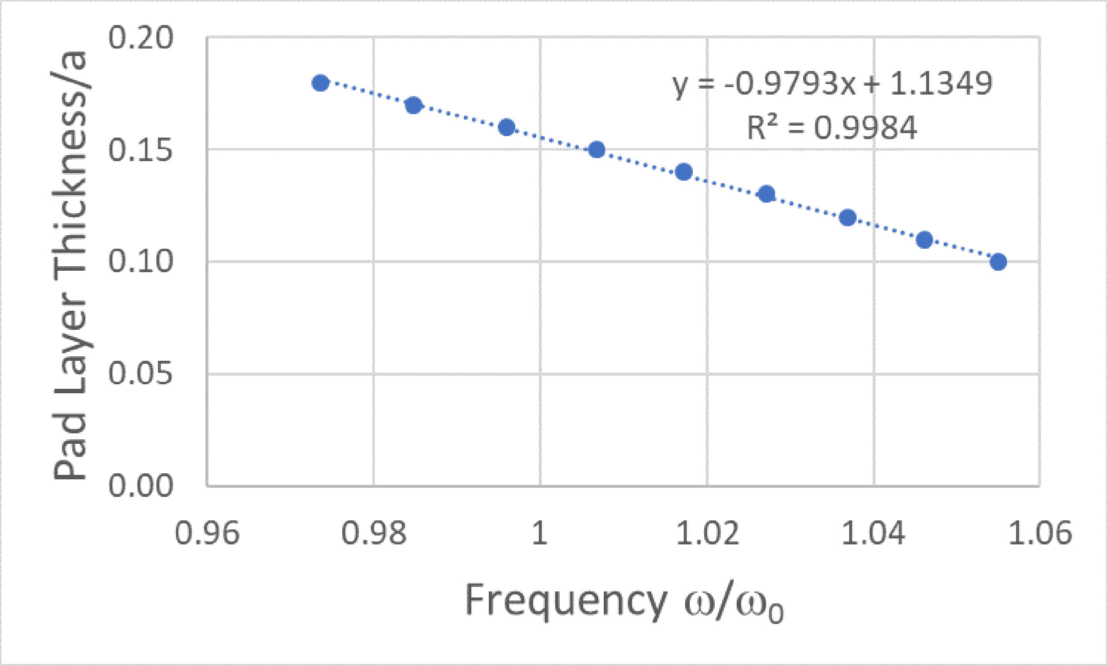

Figure 5.24: Pad layer tuning for desired frequency $\omega_0$ in PBG-W with hole radius $r = 0.445a$ and channel width $C = 3a$.

given in Fig. 5.24.

The dispersion for the accelerating mode in the $C = 3a$ is shown in Fig. 5.25. While the group velocity is higher at the interaction point, it is still close to the poor power flow region. Additionally, above this, there is a large portion of the bandgap which has no accelerating mode and as such does not contribute to acceleration. The dispersion's group velocity is always positive however so does not fold back on itself and reduce overall interaction. The characteristic impedance comparison between the two $r = 0.445a$ is shown in Fig. 5.26. As can be seen from this figure, to achieve higher accelerating voltage, simply designing for high $Z_c$ is insufficient and can even be disadvantageous. The voltage spectrum comparison for a pulse bandwidth of $\sigma = 10\%$ is calculated and shown in Fig. 5.27. It can be noted that while both structures were designed to be synchronous with $\omega/\omega_0 = 1$, the $C = 1.5a$ structure ($C = 0.6\lambda_0$) has been detuned, likely by the negative group velocity region of the mode's dispersion. The resultant voltage bandwidth for the increased channel width case as compared to the previous cases is shown in Fig. 5.28. The results show an increase of $600 - 700\%$ accelerating voltage for identical pulses in the increased channel width and reinforces the requirement of more than just $Z_c$ at the interaction point as a reference figure of merit. Group velocity also plays an important role in beam-wave coupling and thus the $\zeta_v$ parameter presented in chapter 3, Eqn. 3.78 is a more applicable parameter. Investigating greater channel widths may have presented further improvements in the accelerating voltage. This was investigated further in section 5.3.

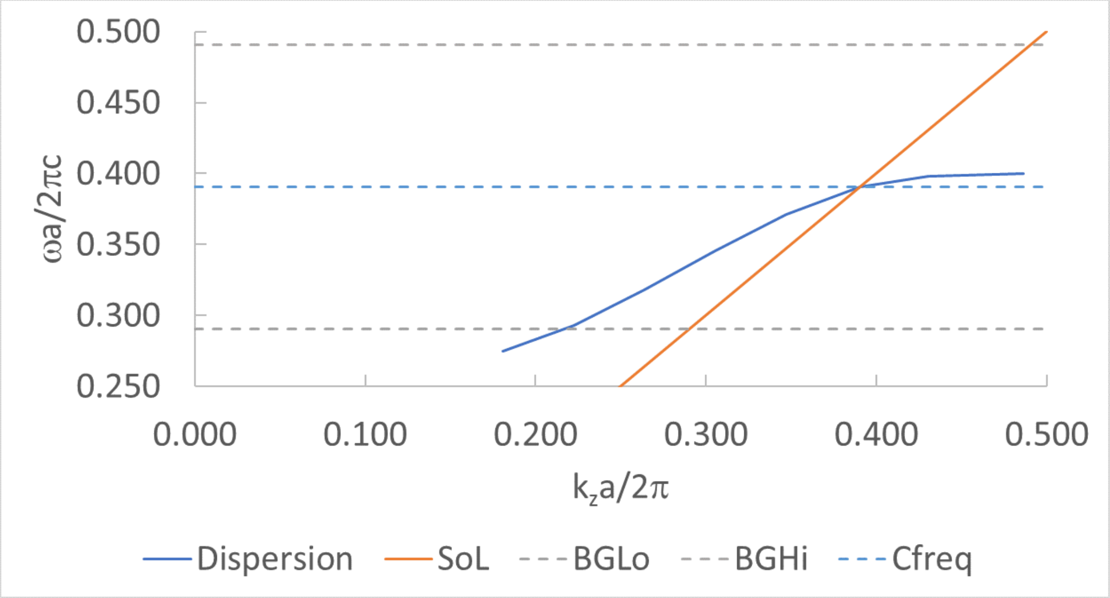

Figure 5.25: Pad layer required for desired frequency $\omega_0$ in PBG-W with hole radius $r = 0.445a$ and channel width $C = 3a$.

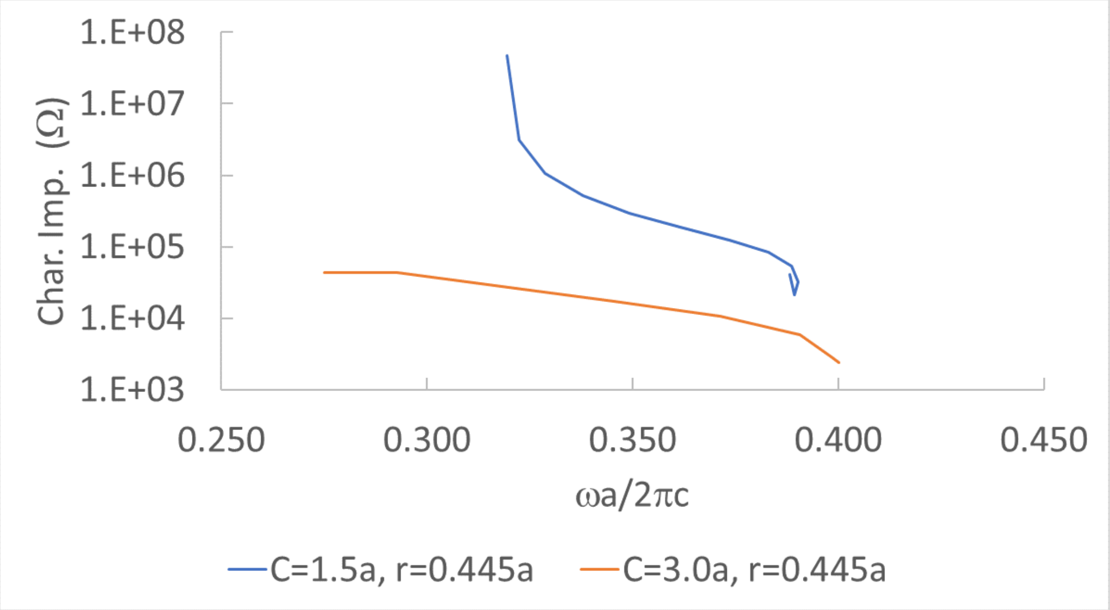

Figure 5.26: Comparison of characteristic impedance against frequency in $r = 0.445a$ structures with $C = 1.5a$ and $C = 3.0a$.

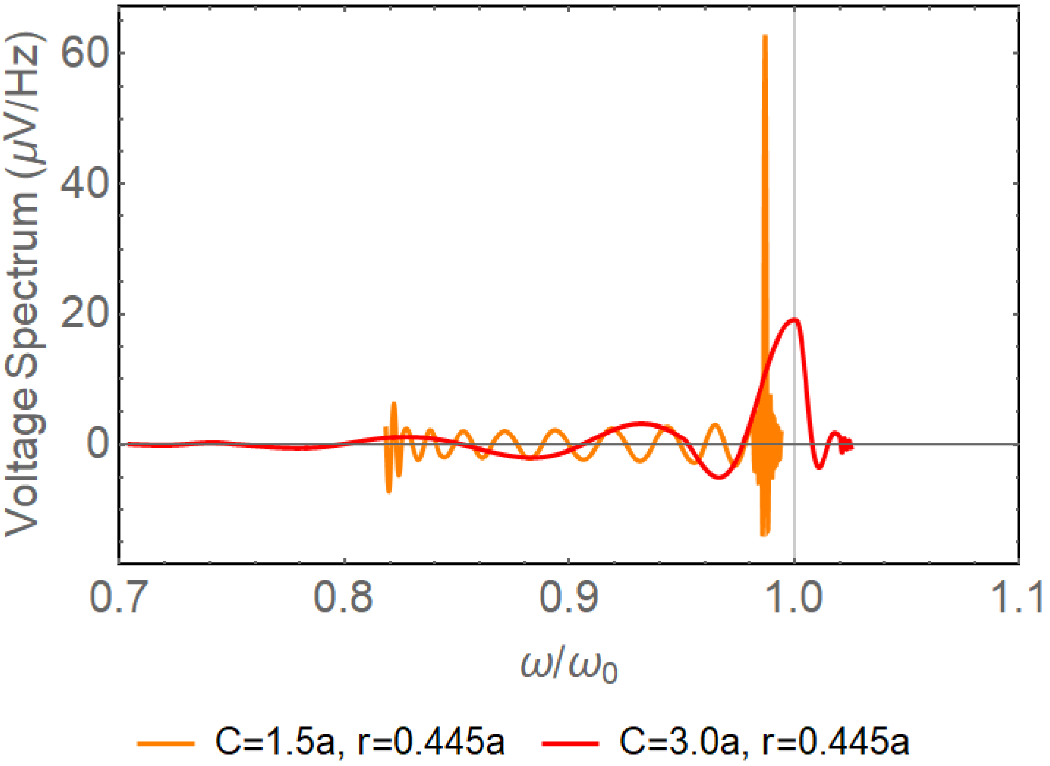

Figure 5.27: Comparison of voltage spectrum for a 10% bandwidth pulse for $C = 1.5a$, $3.0a$ showing the detuning from $\omega_0$ experienced in the $C = 1.5a$ structure.

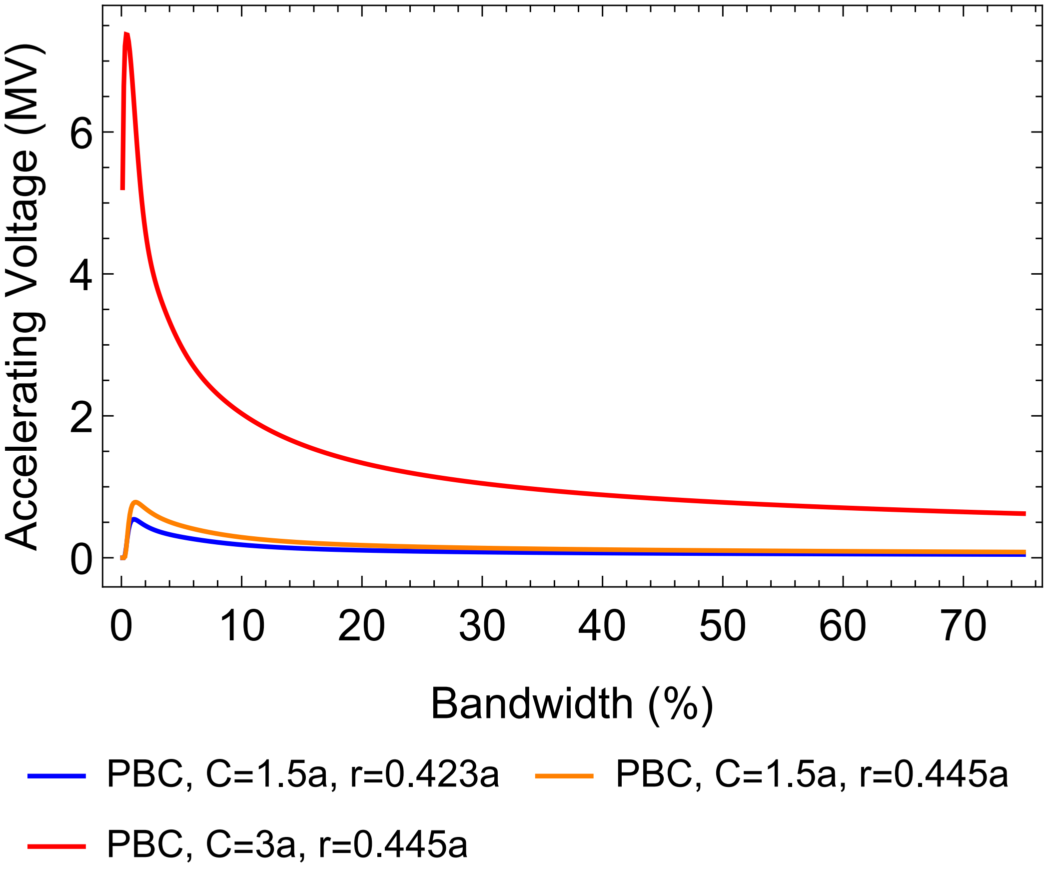

Figure 5.28: Comparison of accelerating voltage in the $C = 3.0a$ case with the two $C = 1.5a$ cases, showing all round increased voltage for a wider channel.

## 5.3 3D PBG-Waveguide Analysis

### 5.3.1 Metal plate boundaries

As with the Bragg structure, while the infinite height model can give an indication of performance of the PBG-W, a full 3D structure is required to investigate the physical implementation. As before, the slab (Fig. 5.18) is made of a finite thickness and clad externally with parallel metal plates. The schematic, shown in Fig. 5.29, illustrates the triangular lattice of vacuum holes in silicon PBG-W clad with metal plates on all sides. To determine the ideal $T/C$ ratio, $\zeta_v$ is swept across channel width and thickness for $r = 0.445a$. Fig. 5.30 shows that $\zeta_v$ is maximised when the channel width is low and the ratio is $T/C = 1.5$. Repeating the study in Fig. 5.24 for a range of channel widths, the relationship between channel width $C$ vs pad layer thickness $m$ for an accelerating mode at $\omega/\omega_0$ can be calculated and is shown in Fig. 5.31.

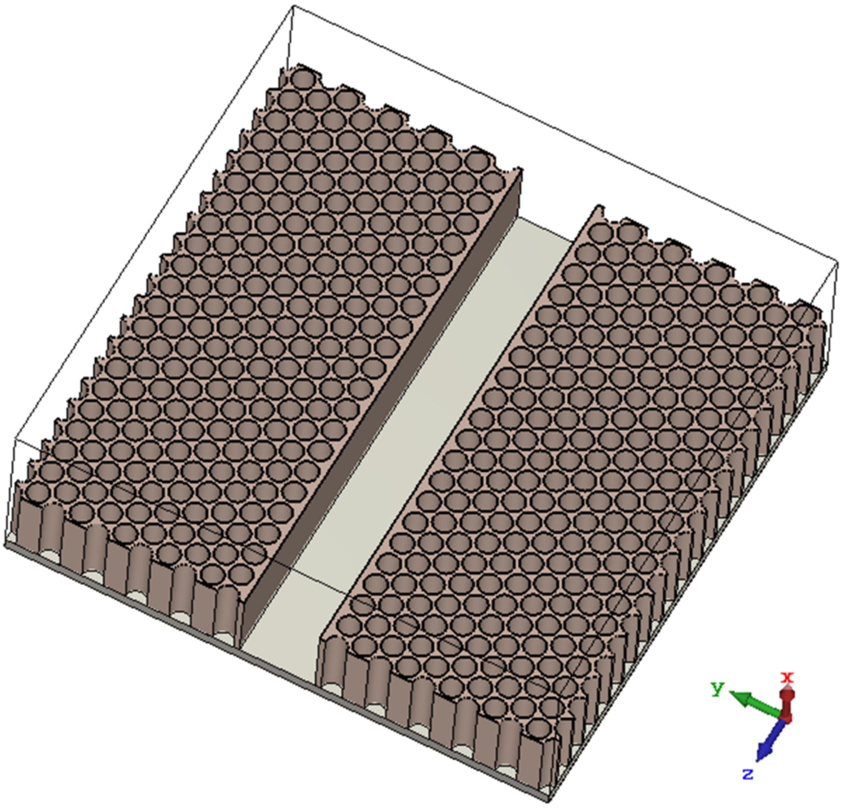

Figure 5.29: Schematic of the triangular lattice 3D PBG-W. Brown is silicon, and grey is the metal cladding. The schematic shows the internals on a cut-plane, with the full size illustrated as a wireframe.

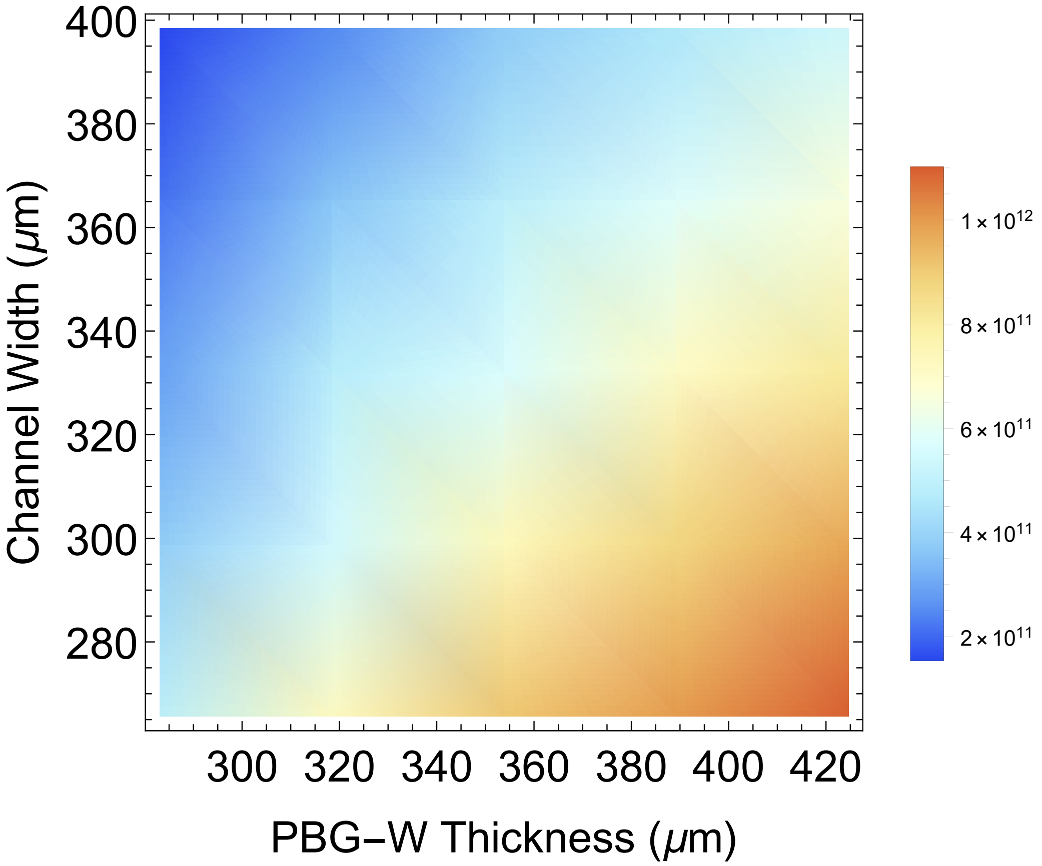

Figure 5.30: $\zeta_v$ map of channel width C vs thickness T shows that it is maximised between $T/C = 1.5$ and $T/C = 2$.

Knowing the relationship in Fig. 5.31, $\zeta_v$ as a function of channel width can be calculated. Fig. 5.32 illustrates that the optimal channel width is in the region of $C = 3a$ for slab thickness $T/C = 1.5$ and hole radius $r = 0.445a$ based PBG-W. The resultant accelerating mode can be seen in Fig. 5.33, with field plots shown in Figs. 5.34–5.36. The spectral voltage can be seen in Figs. 5.37, with the accelerating bandwidth plot compared with other investigated structures in Fig. 5.38; as well as the preliminary design investigated in [162] for comparison.

It can be seen that while a higher voltage is produced than in the preliminary design—likely due to a more rigorous $\zeta_v$ investigation, and not treating the thickness $T$ as a free variable for all investigation—this metal-clad structure does not produce as high an accelerating voltage as the previously investigated PBG-Ws. One of the expected reasons this compared to the Bragg-based waveguide or DLW, discussed later in section 5.3.2, is due to the dispersion of the accelerating

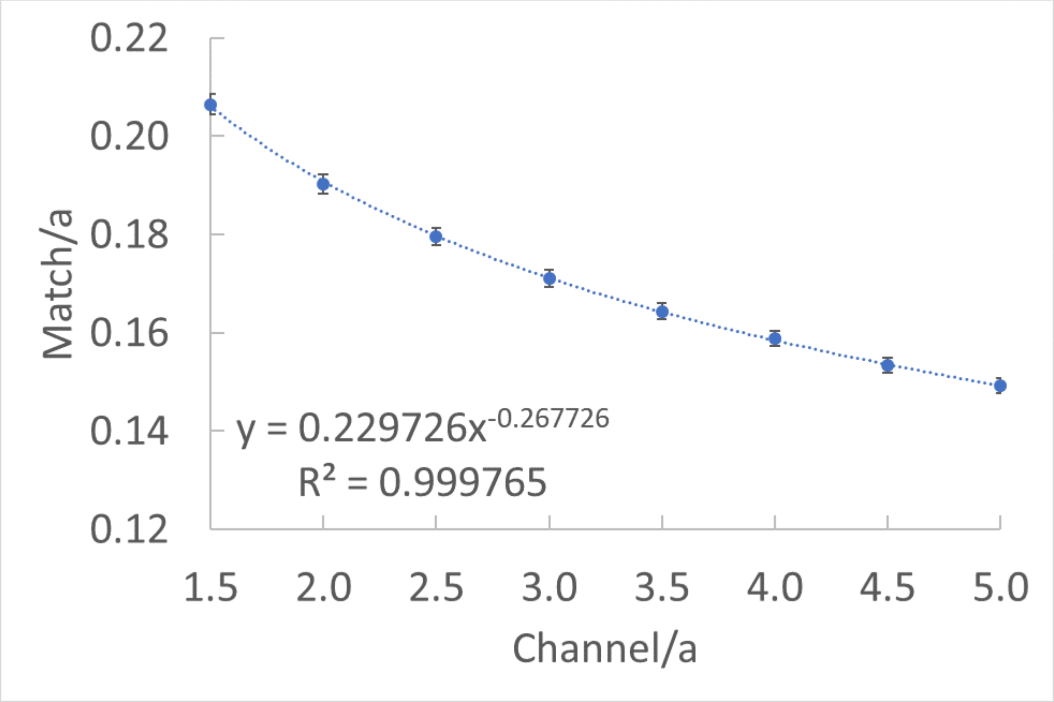

Figure 5.31: Pad layer thickness required in channel width C to produce $v_p/c = 1$ synchronism for $\omega_0$ in PBG-W structure with hole radius $r = 0.445a$.

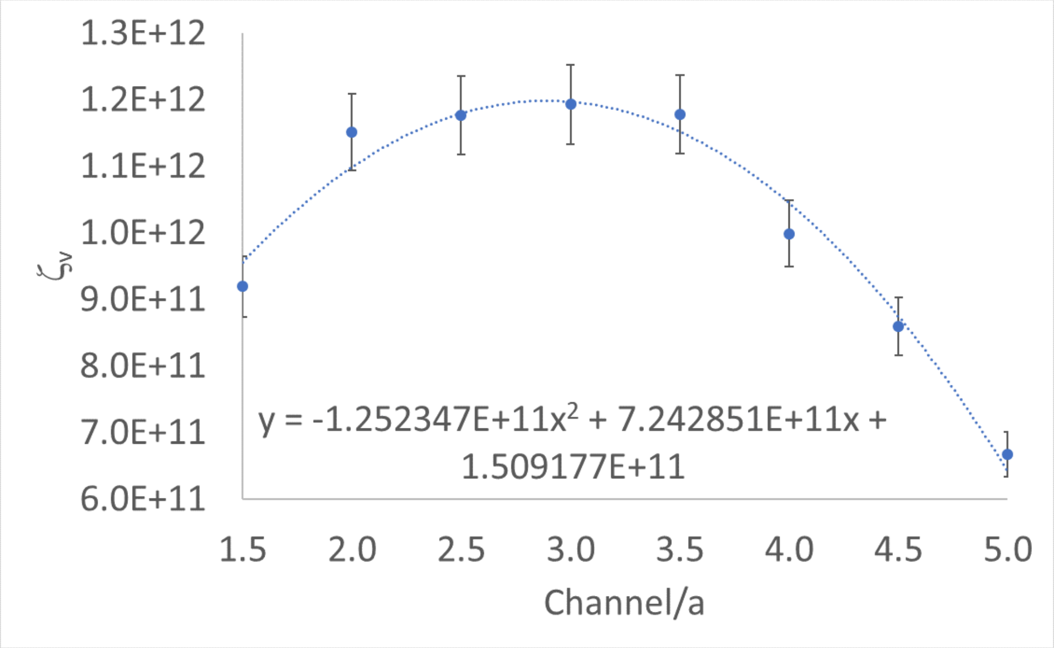

Figure 5.32: $\zeta_v$ for $v_p/c = 1$ synchronised PBG-W structures of channel width C with hole radius $r = 0.445a$.

mode in the wave vector region above interaction. Examining Fig. 5.39, for the Bragg based PBG-W—the region of the dispersion both at and above the point of interaction still had a high positive group velocity. In the triangular lattice

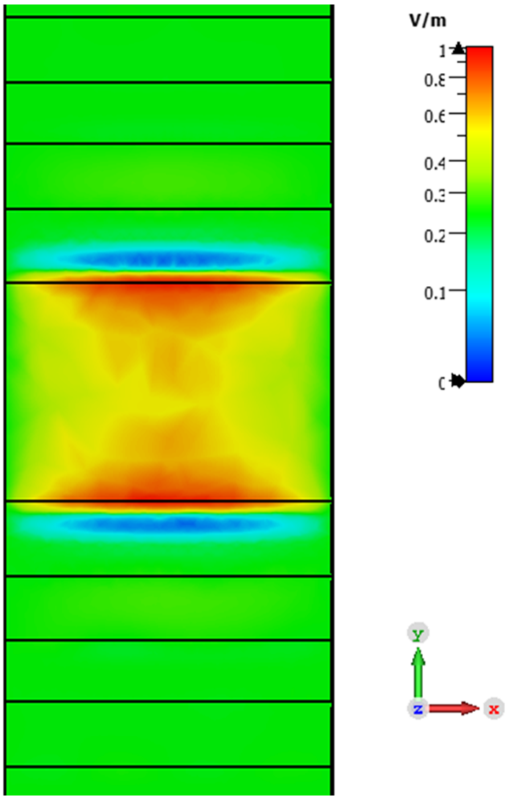

Figure 5.33: Triangular lattice based PBG-W accelerating mode longitudinal electric field.

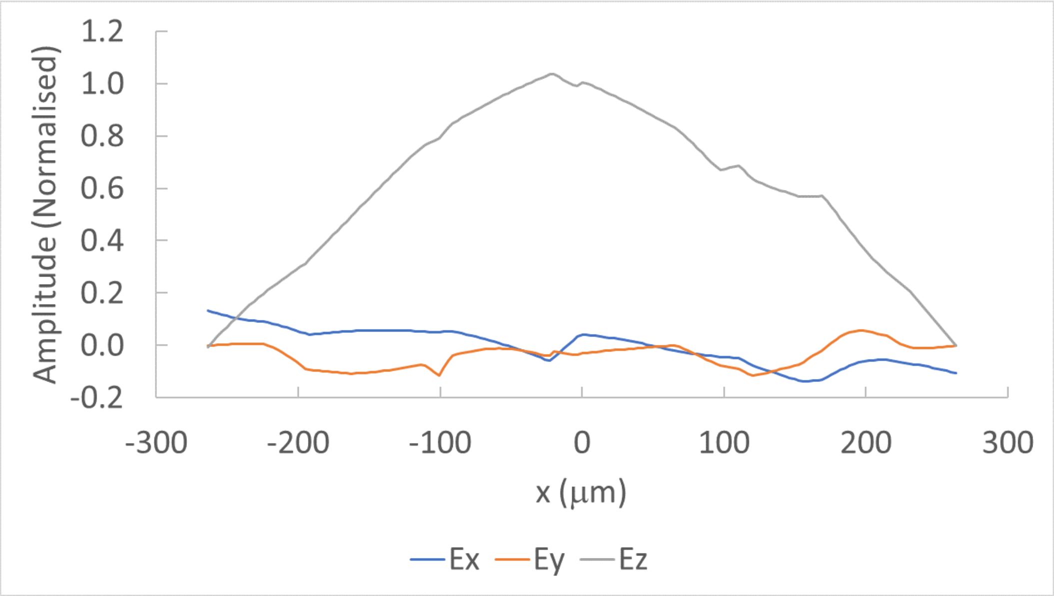

Figure 5.34: Triangular lattice based PBG-W accelerating mode electric field components along $x$-axis where $y = 0$ and $z$ when $E_z$ is maximised. Plots normalised to maximum $E_z$ when $x = y = 0$.

structure however this is either a low positive or negative group velocity region and thus contributes poorly due to low power flow—such as illustrated in Fig.

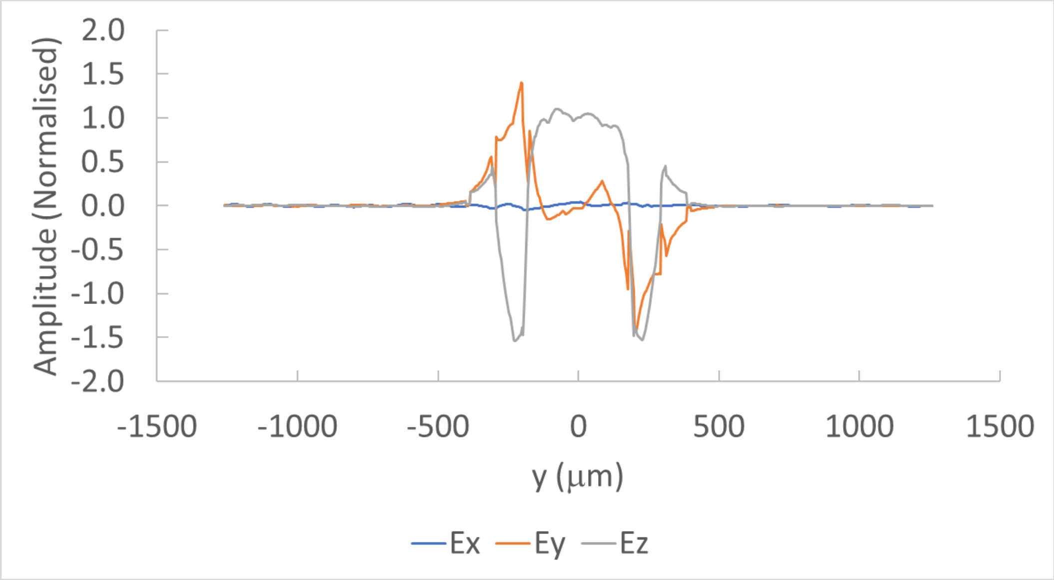

Figure 5.35: Triangular lattice based PBG-W accelerating mode electric field components along $y$-axis where $x = 0$ and $z$ when $E_z$ is maximised. Plots normalised to maximum $E_z$ when $x = y = 0$.

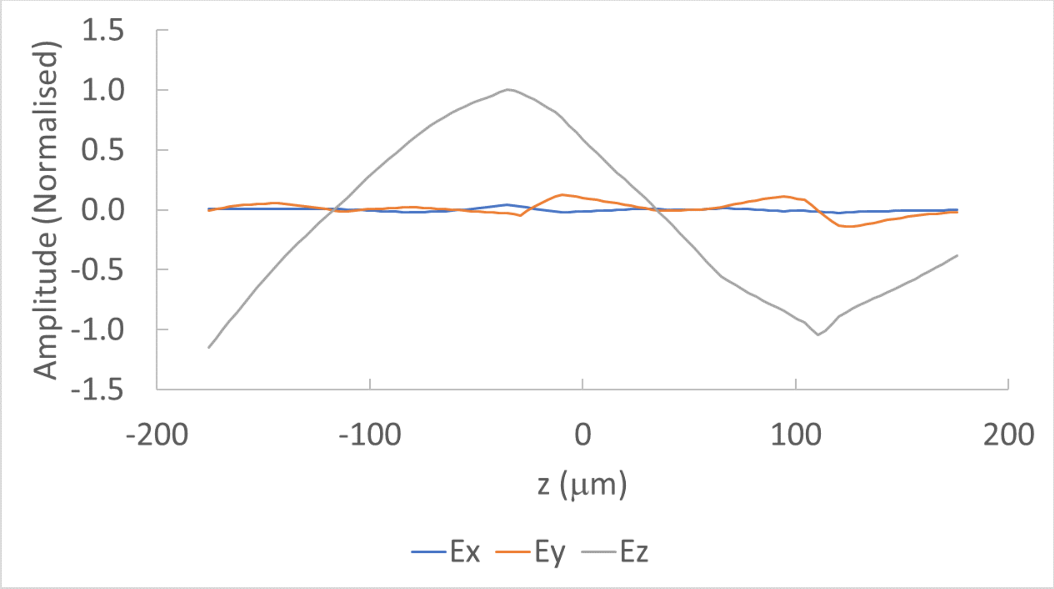

Figure 5.36: Triangular lattice based PBG-W accelerating mode electric field components along $z$-axis where $x = y = 0$. Plots normalised to maximum $E_z$ when $x = y = 0$.

5.27. To overcome this, the desire is to push the interaction into the more linear high-$v_g$ region of the dispersion. Upon examining the gap-map in Fig. 5.16, the bandgap's centre frequency can be moved down relative to the PhC "frequency" $c/a$ by reducing the hole radius. This pushes the centre-frequency into a lower wavenumber region of interaction. Choosing a radius of $r = 0.350a$ moves $\omega_0$ from

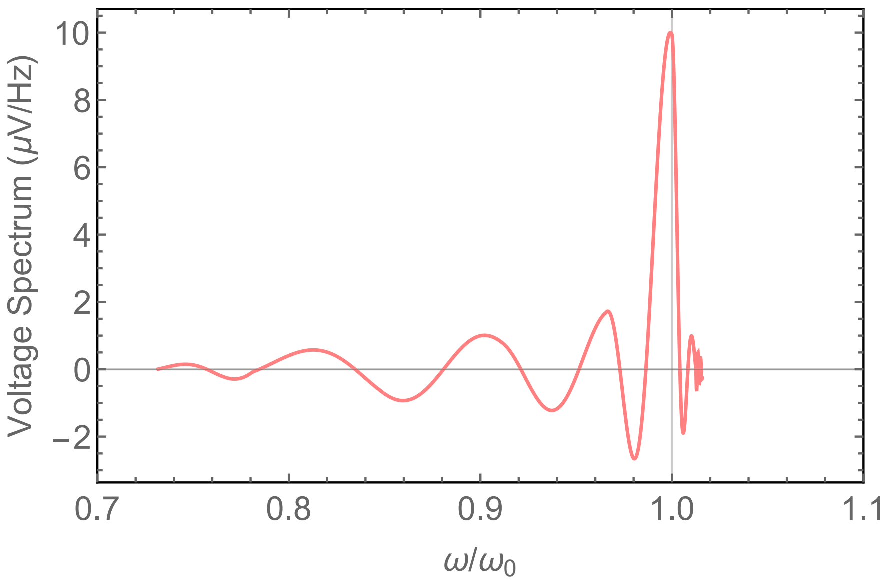

Figure 5.37: $\zeta_v$ for $v_p/c = 1$ synchronised PBG-W structures of channel width C with hole radius $r = 0.445a$.

$\omega_0 = 0.3904c/a$ to $\omega_0 = 0.2783c/a$. The resulting band diagram can be seen in Fig. 5.40.

Repeating the same process as with $r = 0.445a$—the pad-layer was tuned for

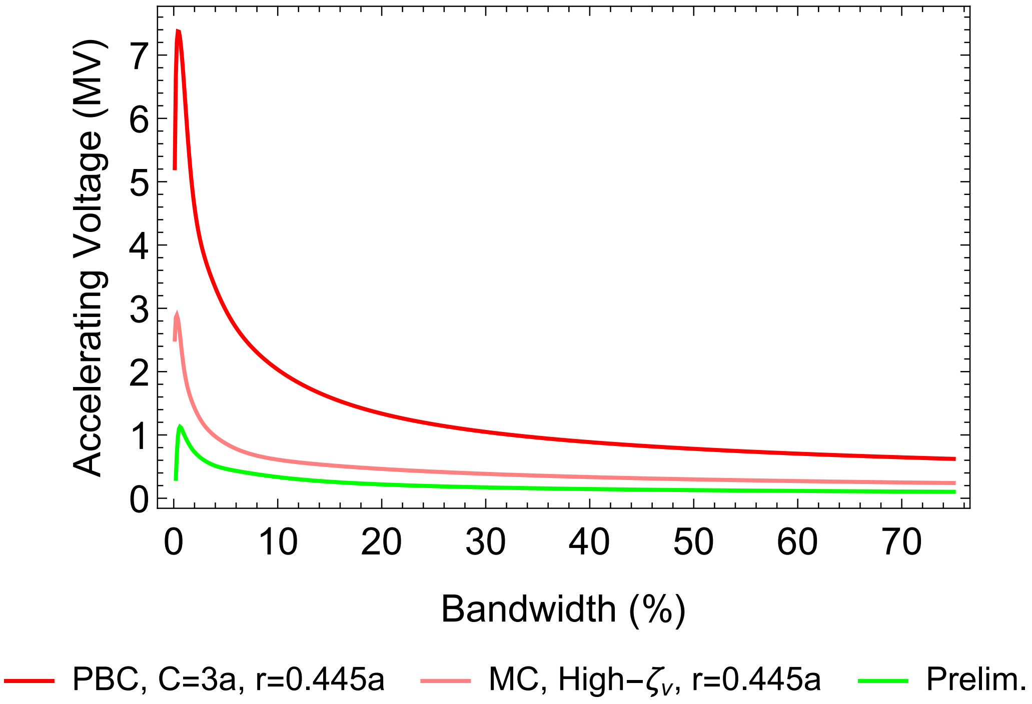

Figure 5.38: Comparison of accelerating voltage bandwidths for the PBC $r = 0.445a$, $C = 3a$ triangular lattice PBG-W with the $\zeta_v$ optimised $r = 0.445a$ metal clad structure. The preliminary design from [162] is included for comparison.

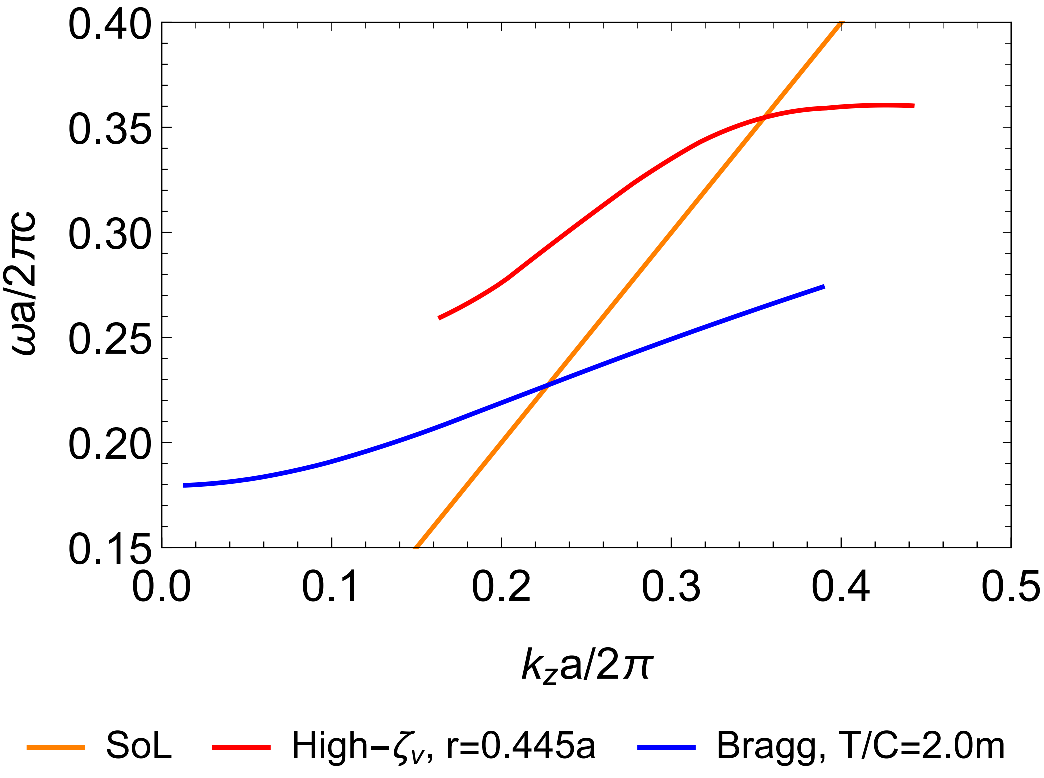

Figure 5.39: Comparison of normalised dispersion for the Bragg based, and triangular lattice based PBG-Ws

$v_p/c = 1$ at $\omega_0$ for given channel width, with curve shown in Fig. 5.41. The geometry change however produced a coupled pair of accelerating modes, with power flows shown in (a) and (b) of Fig. 5.42. These two propagating modes at $\omega/\omega_0 \approx 1$ within 1%. These are likely artefacts of the same mode coupled to the photonic crystal $a/2$ apart, with (a) coupled to the thickest region of dielectric between holes, and (b) coupled to the thinnest as these regions are where the dielectric power flow in the pad layer is highest for each mode. When scaling the structure from $C = 1.5a - 6a$, in the region of $C = 3.5a$ the two modes stop propagating and instead a single mode with power flow shown in (c) of Fig. 5.42 appears. Plotting $\zeta_v$ for channel width in Fig. 5.43 also reveals that at $C = 0.350a$, $\zeta_v$ is maximised. The disappearance of both and appearance of the third similar mode at $C = 3.5a$ indicates these are the same mode and are separated by CST due to either mathematical artefact, or physically present due to thicker pad layer required for $v_p/c = 1$ synchronism.

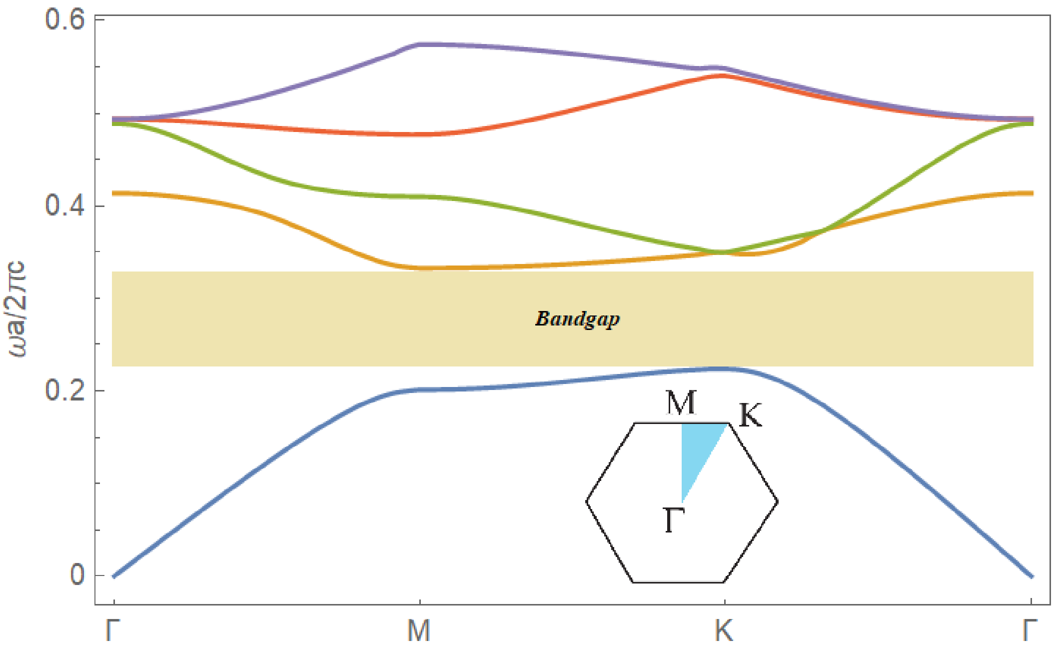

Figure 5.40: Bandgap plot of $TM_z$ modes in a $r = 0.350a$ triangular lattice photonic crystal.

In moving the interaction point down in wavenumber—the aim was to have the accelerating mode propagate with a similar shaped dispersion to the Bragg structure with good group velocity across the full dispersion, and phase velocity close to the speed of light line to ensure broadband coupling with the beam. Plotting dispersion for the $C = 3.5a, r = 0.350a$ structure, shown in Fig. 5.44, shows that while group velocity at the point of interaction was increased thus improving bandwidth, the dispersion still quickly flattens off at higher wavenumbers. While the accelerating voltage higher for the $r = 0.350a$ case than the $r = 0.445a$ case as shown in Fig. 5.45, the lack of a more symmetric dispersion around interaction still negatively affected the maximum voltage attainable. Returning to a more Bragg-like dispersion may be limited by the physical structure of this waveguide and that the propagating accelerating mode is a coupling of a dielectric mode and a vacuum mode. The properties of the dispersion indicate that mode crossing is in effect, and at higher wavenumbers the accelerating mode is taking on the properties of an undesired mode.

This chapter has so far demonstrated that optimisation for $\zeta_v$ improves ac-

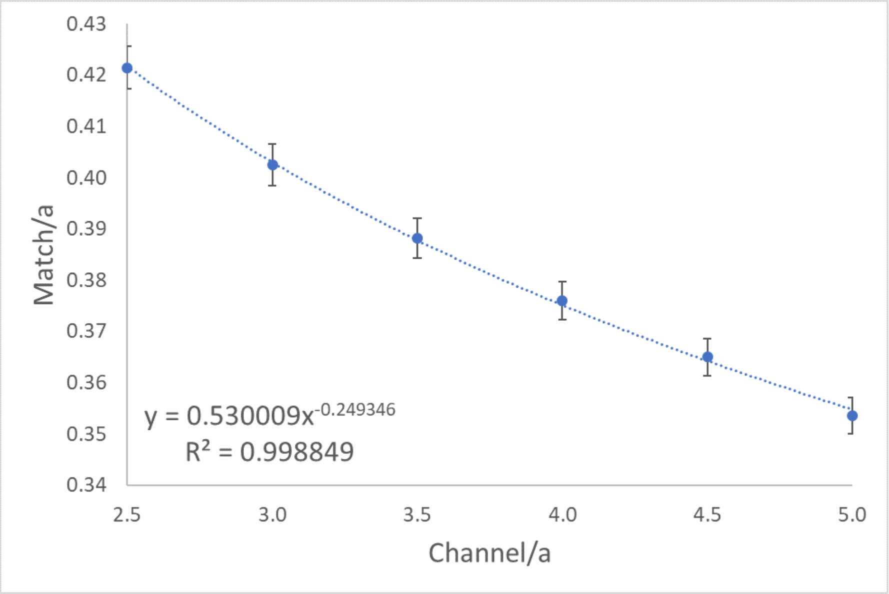

Figure 5.41: $\zeta_v$ for $v_p/c = 1$ synchronised PBG-W structures of channel width C with hole radius $r = 0.350a$.

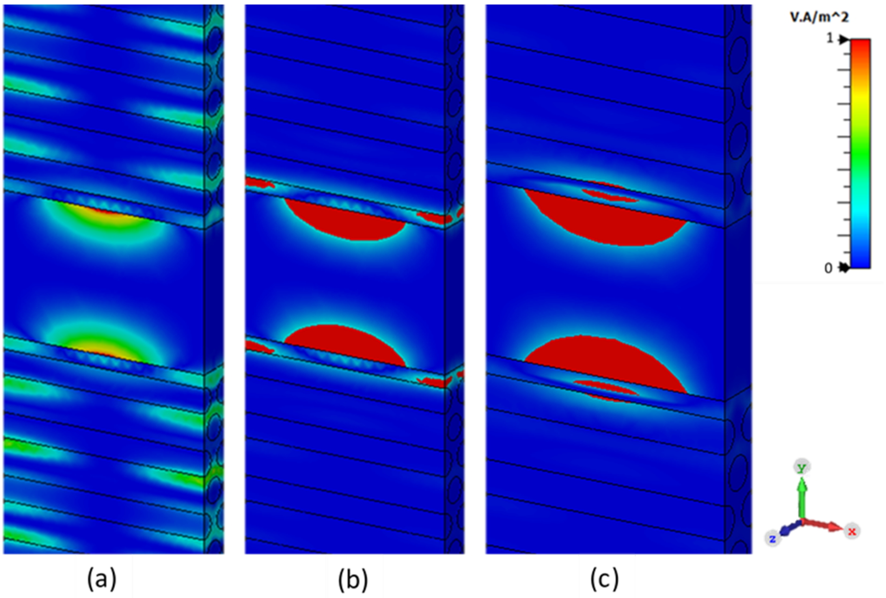

Figure 5.42: Power flow for the accelerating modes in the $r = 0.350a$ triangular lattice PBG-W based structure. (a) is the power flow for mode "A". (b) is the power flow for mode "B". (c) is the power flow for the accelerating mode in $C = 0.350a$.

celerating voltages for both narrowband and broadband excitation pulses. Work done in [162] showed that optimisation for group velocity, whilst leading to poorer voltages at the lower bandwidths, resulted in higher accelerating voltages at higher bandwidths despite having low $Z_c$. Recreating this work using a synchronous pad-layer as extrapolated from Fig. 5.41 for $C = 7.0a$ and $T/C = 1.5$, giving a pad

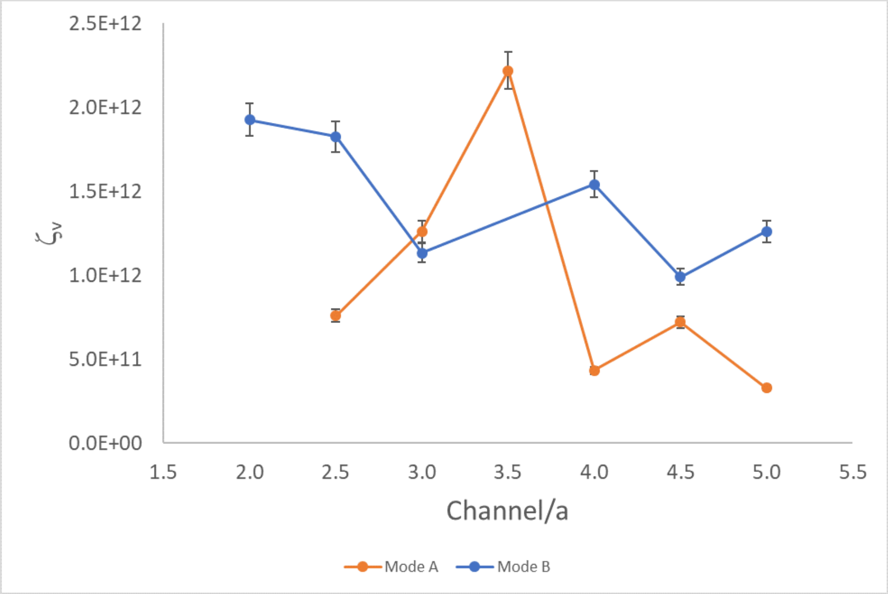

Figure 5.43: $\zeta_v$ for $v_p/c = 1$ synchronised PBG-W structures of channel width C with hole radius $r = 0.350a$.

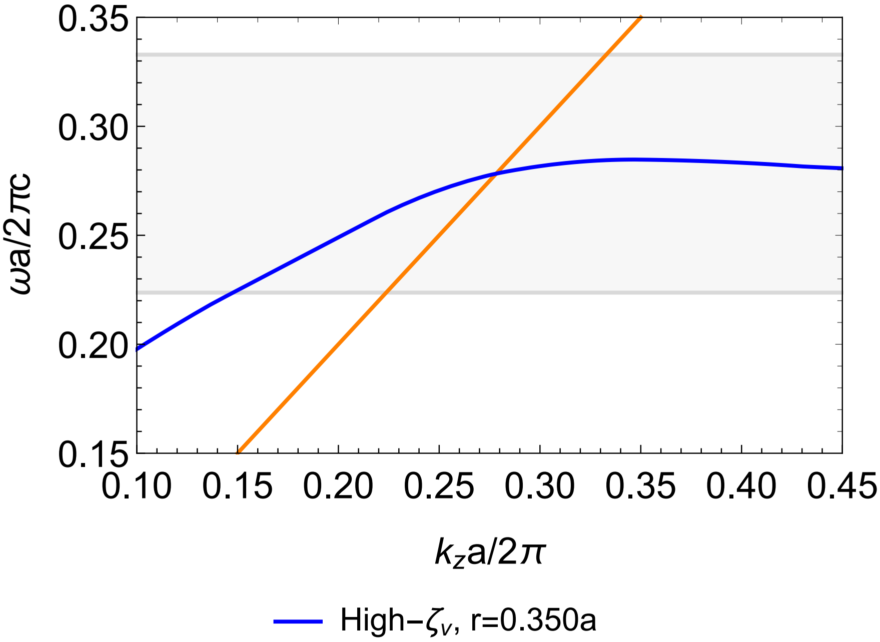

Figure 5.44: Dispersion of accelerating mode shown in Fig. 5.42 showing higher group velocity interaction and a more dramatic negative $v_g$ region compared to the $r = 0.445a$ case. Interaction is at $\omega/\omega_0 = 1$, and grey background is the photonic bandgap

layer thickness of $m = 0.3263a$, results in a structure with dispersion shown in Fig. 5.46 and the accelerating voltage bandwidth is shown in Fig. 5.47 as "MC, High-$v_g$,r=0.350a". Comparing this curve with the previously obtained high-$\zeta_v$

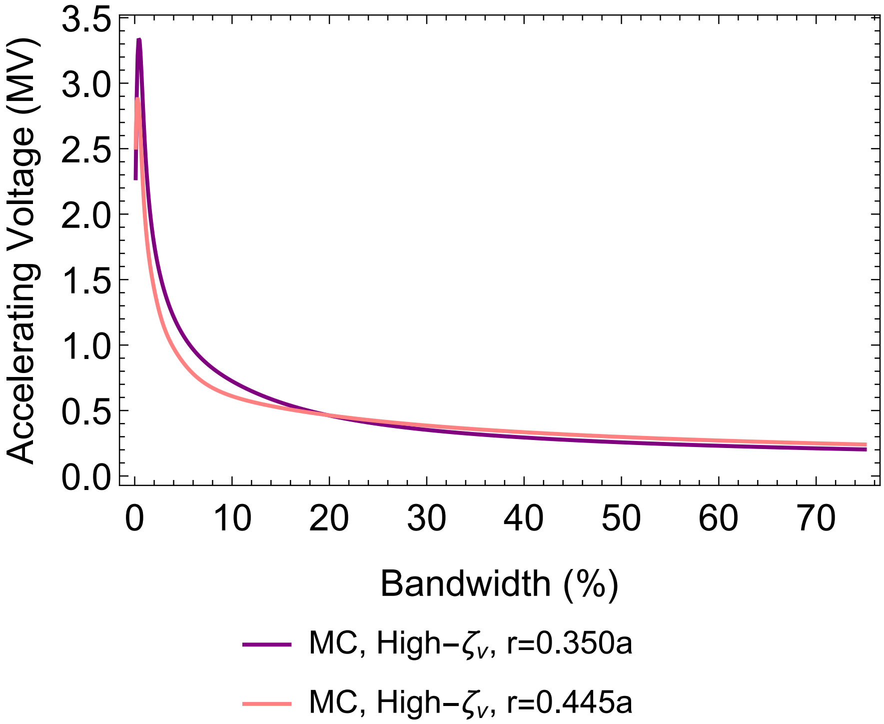

Figure 5.45: Accelerating voltage in $\zeta_v$-optimised structures with hole-radii $r = 0.350a$ and $r = 0.445a$.

and PBC accelerating PBG-Ws, it can be seen that while the peak accelerating voltage is lower—the lower peak occurs at a higher bandwidth. Above 5% bandwidth pulse, the high-$v_g$ offers double the accelerating voltage of the high $\zeta_v$ up to the maximum bandwidth investigated. At large bandwidths, the accelerating voltage is approaching the infinite structure's voltage which can be thought of as an ideal case for this structure.

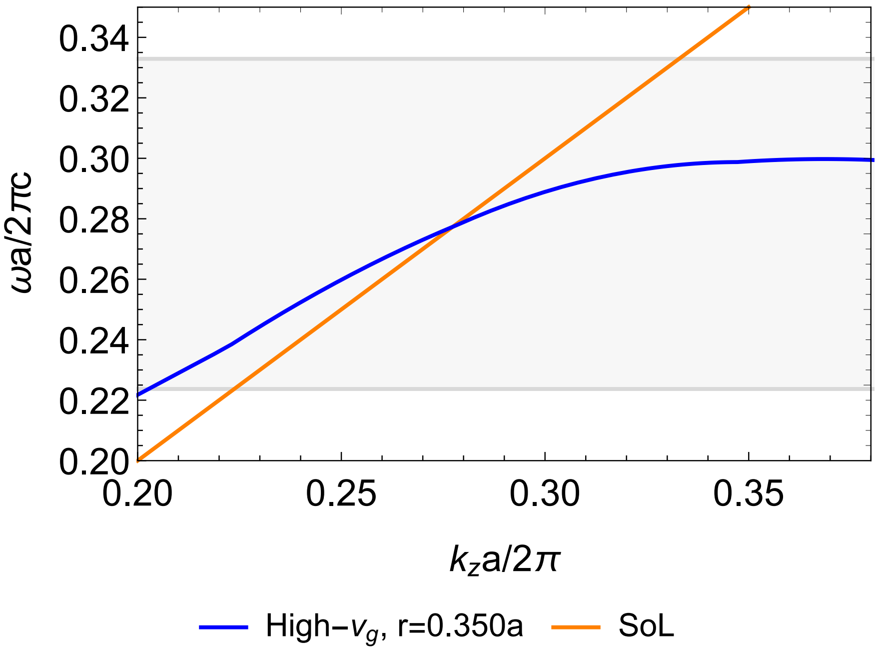

Figure 5.46: Accelerating mode Dispersion for $C = 7.0a$ triangular lattice based PBG-W, showing high group velocity in much of the region near the speed of light line. Grey background is the photonic bandgap.

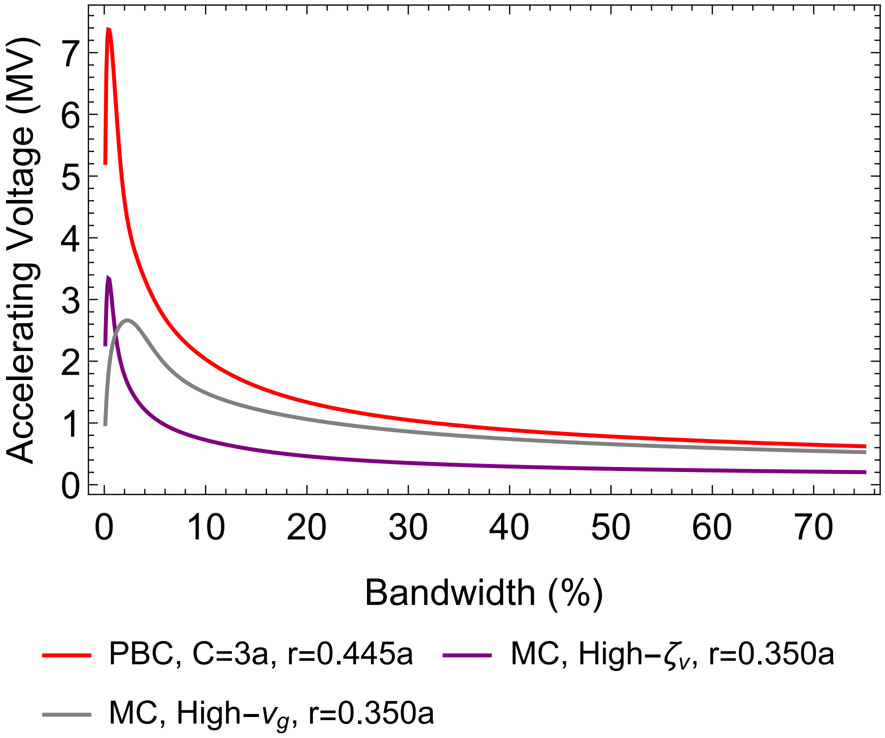

Figure 5.47: Comparing accelerating voltage bandwidth in structures optimised for $\zeta_v$ and $v_g$ with periodic boundary condition waveguide.

### 5.3.2 Comparison with DLW

To truly quantify the performance of the PBG-W in terms of actual performance, the figures of merit used in this work must also be applied to a reference counterpart waveguide as proposed in literature for THz acceleration. Due to work done in both the E-MIT group at Lancaster university, and at Cockcroft institute in the DATA group, on the dielectric lined waveguide—this was a sensible option to select for comparison. For a proper comparison with the structure, it was rescaled for $1\,THz$ operation in CST using the design parameters in [163, 87]. The waveguide height was $300\,\mu m$, width $600\,\mu m$, with a $25\,\mu m$ silica layer lining each of the major axes of the metallic waveguide. As with the PBG-Ws, the waveguide length was $5\,mm$. The schematic can be seen in Fig. 5.48.

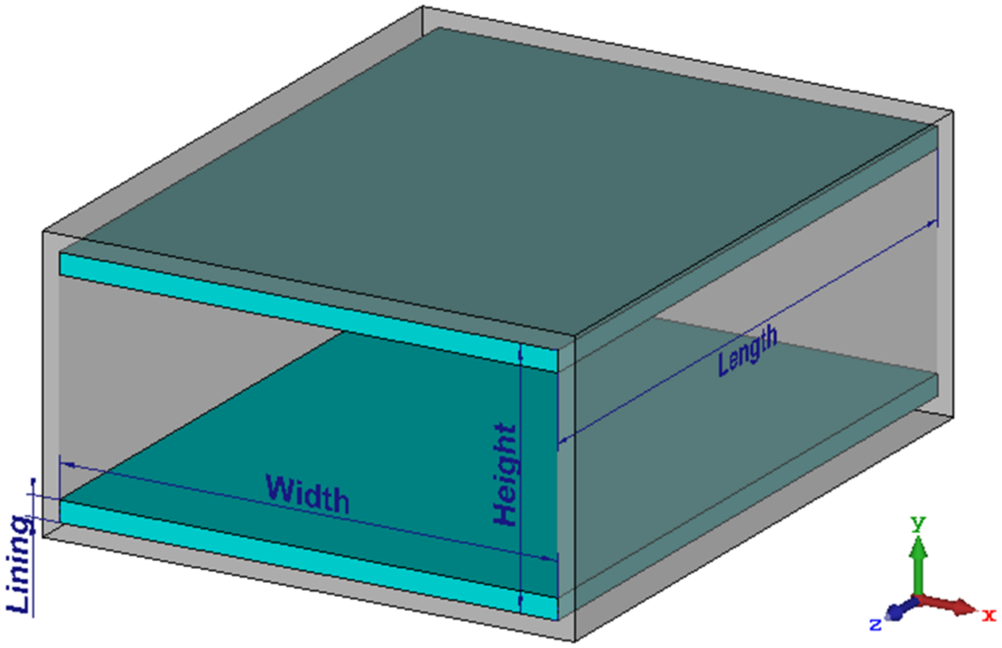

Figure 5.48: Design schematic for the DLW investigated as a comparison for PBG-Ws studied. Cyan is the dielectric lining, and transparent grey is the metal waveguide.

The accelerating mode for the DLW can be seen in Fig. 5.49, with components plotted in Figs. 5.50-5.52. The dispersion for this mode was normalised to the eigenmode unit cell length, which for continuity with PBG-Ws studied has the symbol $a$, and can be seen in Fig. 5.53. The resulting accelerating voltage in comparison with the structures studied in this thesis is shown in Fig. 5.54.

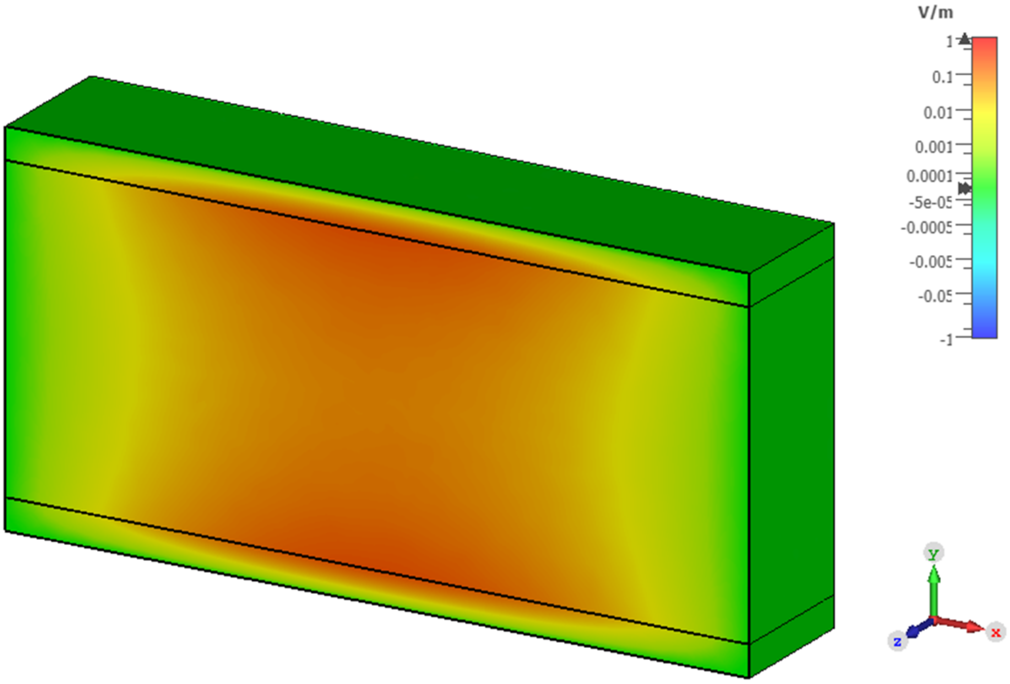

Figure 5.49: $z$-axis component of the electric field for the DLW accelerating mode.

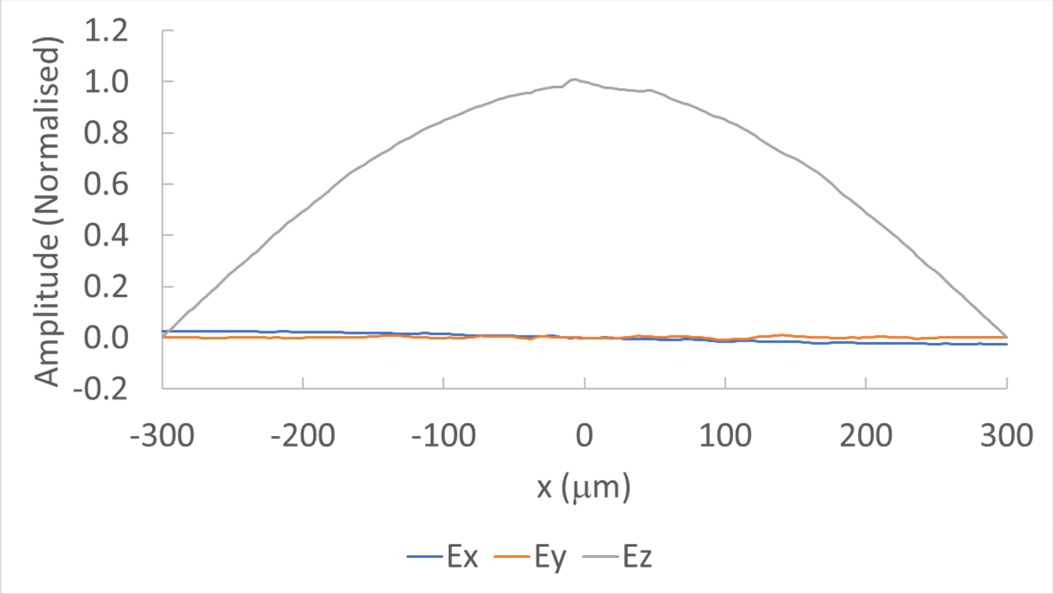

Figure 5.50: DLW accelerating mode electric field components along $x$-axis where $y = 0$ and $z$ when $E_z$ is maximised. Plots normalised to maximum $E_z$ when $x = y = 0$.

For the DLW, peak accelerating voltage to max-bandwidth is a factor of ≈ 12.5. The $\zeta_v$ optimised structure shows a peak to max-bandwidth ratio of ≈ 15 for the

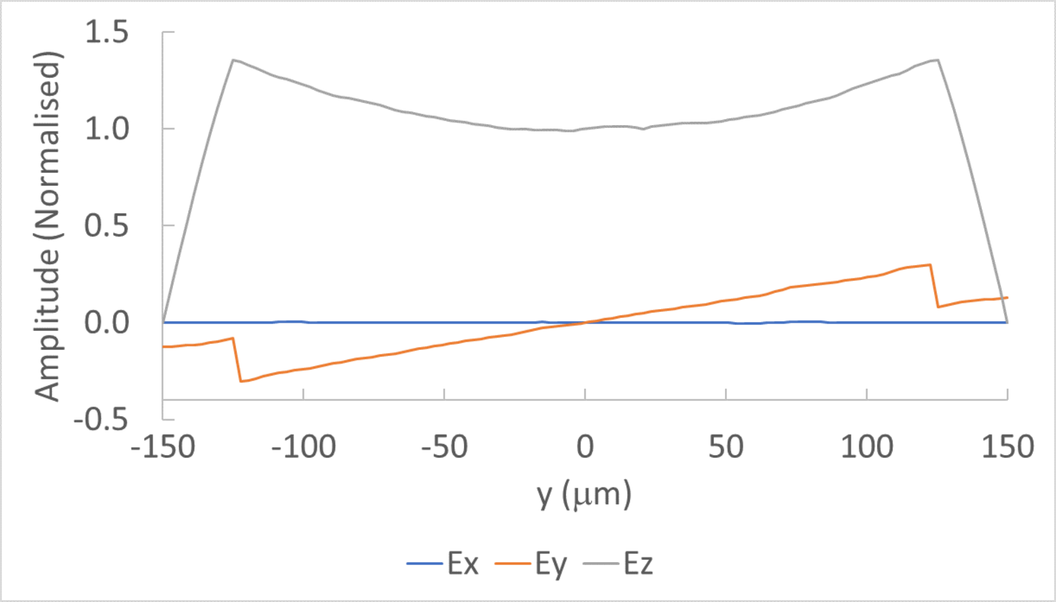

Figure 5.51: DLW accelerating mode electric field components along $y$-axis where $x = 0$ and $z$ when $E_z$ is maximised. Plots normalised to maximum $E_z$ when $x = y = 0$.

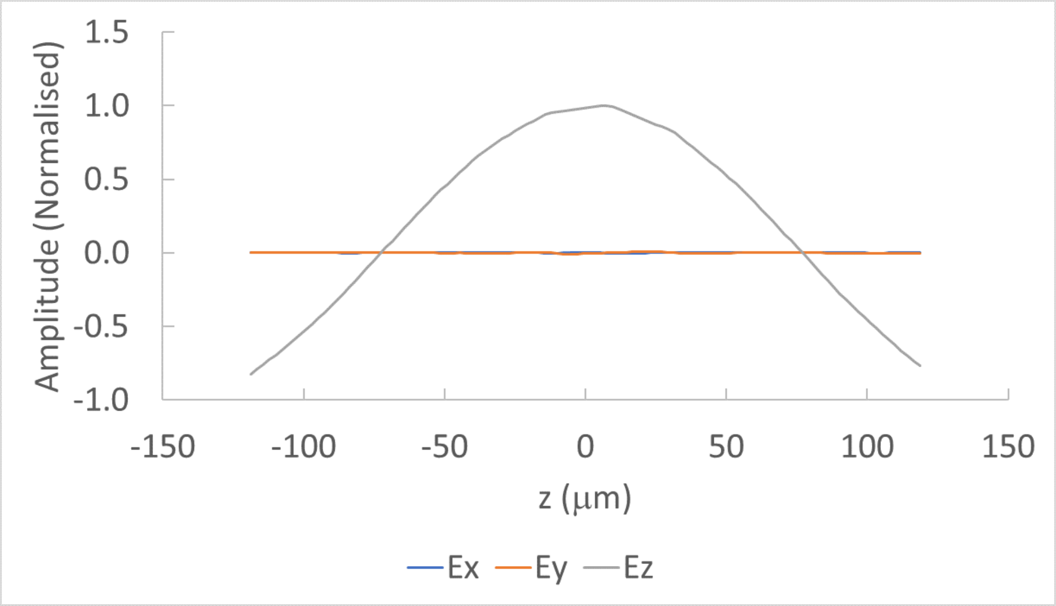

Figure 5.52: DLW accelerating mode electric field components along $z$-axis where $x = y = 0$. Plots normalised to maximum $E_z$ when $x = y = 0$.

infinite structure and $\approx 14$ for the high-$\zeta_v, r = 0.350a$ structure. The high-$v_g$ shows a $\approx 5.5$ peak to max-bandwidth ratio, with high bandwidth performance more than double the other PBG-W structures. As such, while this structure may not outperform the DLW in pure acceleration voltage, the process to optimise this structure can be applied to other structures to improve performance at the desired

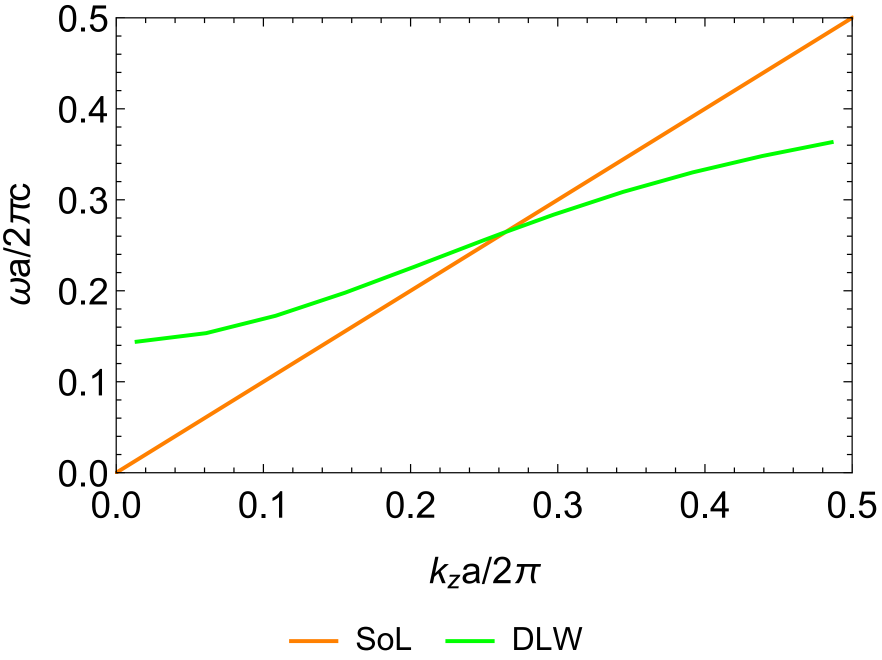

Figure 5.53: Design schematic for the DLW investigated as a comparison for PBGWs studied. Cyan is the dielectric lining, and transparent grey is the metal waveguide.

bandwidths of operation.

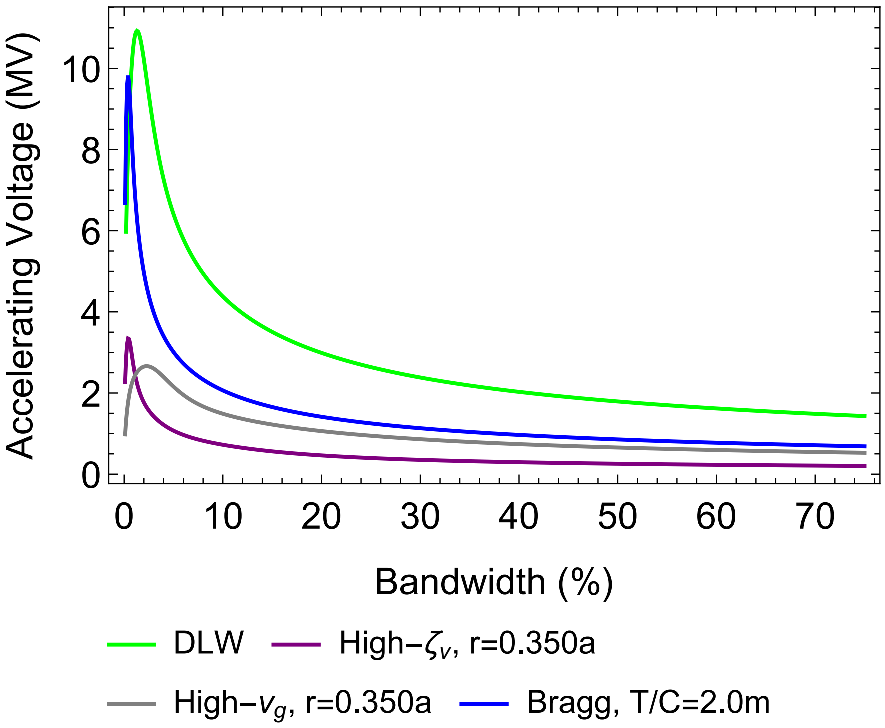

Figure 5.54: Comparison of accelerating voltages obtained for the DLW with the optimal structures investigated in this chapter.

### 5.3.3 Surface Fields

One main reason to pursue the use of PBG-Ws for acceleration is the ability to reduce both electric and magnetic fields on the metal walls compared to metal-based structures such as the DLW. Previous figures of merit have addressed the acceleration capability of PBG-Ws, and while this is an important figure of merit for comparison of performance—additional figures of merit are required to assess the field characteristics. A reduction in electric field on the metal walls for equivalent accelerating voltage will result in lower field emission. Similarly for magnetic fields—a reduction in magnetic fields will lower pulsed heating of the walls leading to less wasted energy and structural deformation. To study this property of the proposed metal-clad PBG-Ws as compared to the dielectric lined waveguide, two figures of merit will be used: $\eta_E$, and $\eta_H$, where:

$$\eta_E = \frac{E_{Wall}}{E_{acc}} \tag{5.19}$$

With $E_{Wall}$ representing the peak electric field on the metal wall in the vacuum channel, $E_{acc}$ representing the peak longitudinal field at coordinates $x = y = 0$, and:

$$\eta_H = \frac{H_{Wall}}{E_{acc}} \tag{5.20}$$

where $H_{Wall}$ representing the peak magnetic field on the metal wall in the vacuum channel. Through dimensional analysis $\eta_H$ has the units of siemens, it can be thought of as unitless like $\eta_E$ for the purposes of comparison. Whilst $\eta_E$ and $\eta_H$ are for comparing the total field at the walls with the longitudinal component, the more the longitudinal component of the field is centralised—the lower the figures will be. To obtain the field statistics it was required to run a separate eigenmode calculations. The eigenmode results presented previously in this chapter use a single photonic-crystal period for the simulated length of the structure. The wavelength of the excited mode however is longer than the

Table 5.2: Comparison of $\eta_E$ and $\eta_H$ for the investigated $v_p/c = 1$ structures.

| Structure | $\eta_E$ | $\eta_H$ |
|---|---|---|
| Bragg, T/C=1.2 | 1.567622 | 0.004885 |
| Bragg, T/C=2.0 | 0.556367 | 0.002293 |
| Max-PBG, C=3.0a | 1.147565 | 0.006063 |
| High-$\zeta_v$ | 0.546133 | 0.008349 |
| High-$v_g$ | 0.750405 | 0.006932 |
| DLW | 0.341763 | 0.002829 |

single period of the PhC. As such, an additional 3-period model was computed to obtain these results. A comparison of these results can be seen in table 5.2. It can be seen from these results that for $\eta_E$, all PBG-W designs fail to improve on this ratio compared to the DLW. For $\eta_H$, the $T/C = 2.0$ Bragg-based structure shows improved centralisation of the magnetic fields however the triangular lattice PBG-Ws do not.

One problem with these results is that as shown previously, the accelerating voltage for the PBG-Ws was lower than that of the DLW. Thus even though the metal wall fields may be reduced, the structure still had a poorer performance. The voltages however show that the best results from photonic-crystal-based waveguides occur when they have periodic boundary conditions, which is a mathematical approximation for a parallel-plate waveguide topography. Due to lack of transverse confinement however these would be unsuitable for external excitation by a source. Instead they should be driven by an internal source such as a particle beam. This is further addressed in chapter 6.

## 5.4 Coupling Structures

In order to use photonic crystal THz acceleration in an externally-driven regime, the energy from a source must be coupled into the structure. There are two options with this: direct coupling—making use of coupling structures such as horns or gratings; and indirect coupling making use of the evanescent decay of the photonic crystal. Direct coupling was the chosen method for investigation due to experience at Daresbury [18, 82] with using this method. A common method of direct energy coupling into waveguide structures is the tapered horn. While conceptually simple: compressing a plane-wave down until it enters the structure; the subtlety lies in correctly matching the output of the horn with the desired waveguide mode. For pure metal structures, a horn can simply be a tapered waveguide and it will operate effectively. For dielectric lining and photonic crystal structures, the mode matching is more complex.

### 5.4.1 Input Laser Pulse Modelling for Accelerating Mode Excitation

The accelerating mode in the photonic-crystal-based waveguide resembles that of the accelerating mode in DLW based structures. This is shown by the comparison of the $LSM_{11}$ mode in the DLW in Fig. 5.55 with that of the quasi-$LSM_{11}$ mode in the PBG-W in Fig. 5.56. Consequently, it is expected a similar excitation signal can be used to drive the PBG-W as was used to drive the DLW. Experiments at Daresbury for THz acceleration of electrons have used a quasi-$TEM_{01}$ mode created by passing a $TEM_{00}$ mode through a phase-shifting plate as shown in Fig. 5.57 [18].

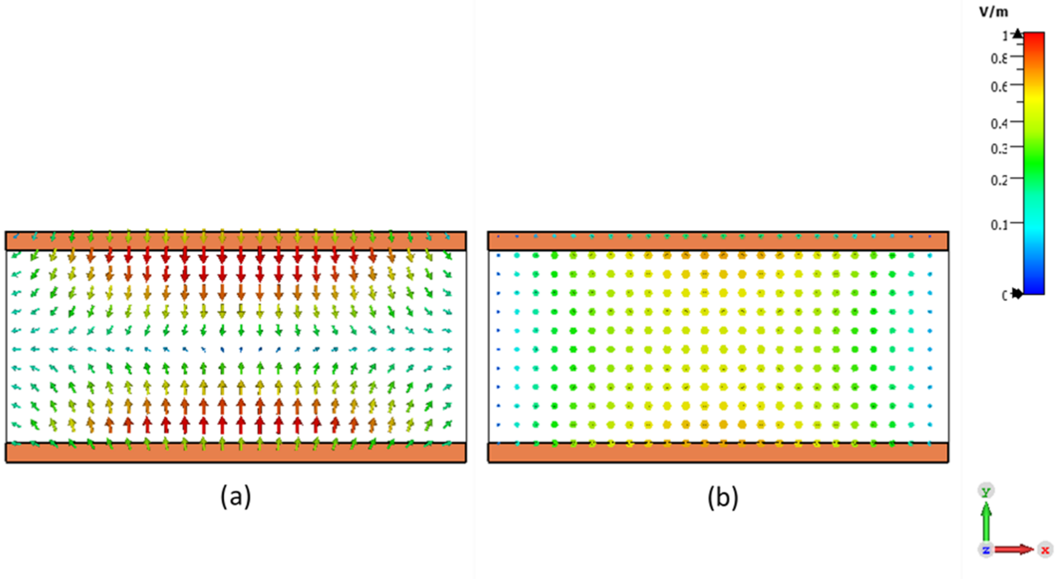

Figure 5.55: Electric field vectors in DLW at mode phase (a) 90° and (b) 180°, with typical $LSM_{11}$ behaviour.

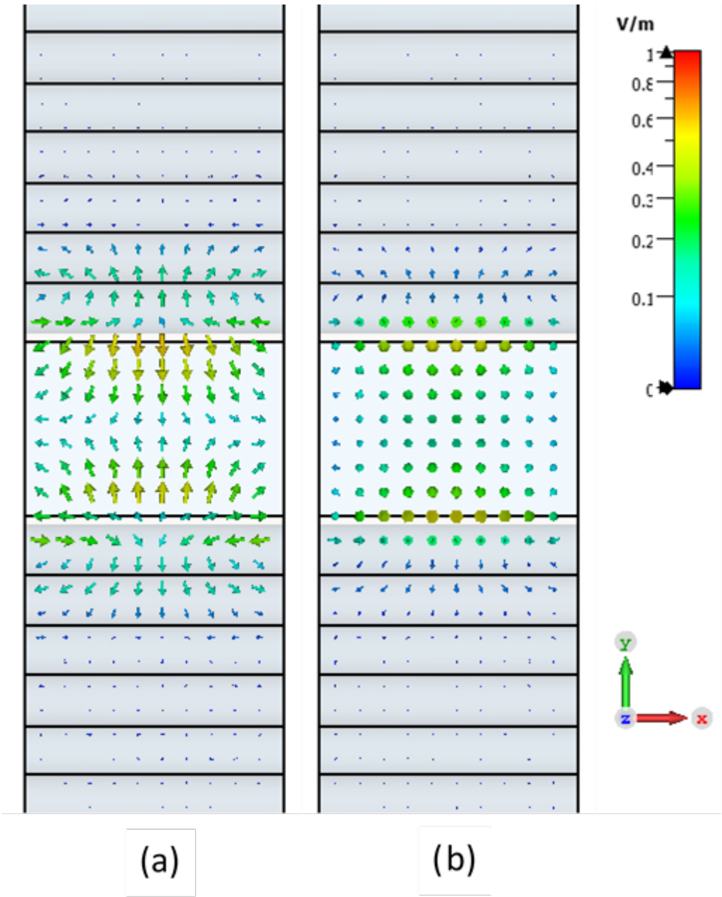

Figure 5.56: Electric field vectors in triangular lattice PBG-W at mode phase (a) 0° and (b) 60°, with quasi-$LSM_{11}$ behaviour.

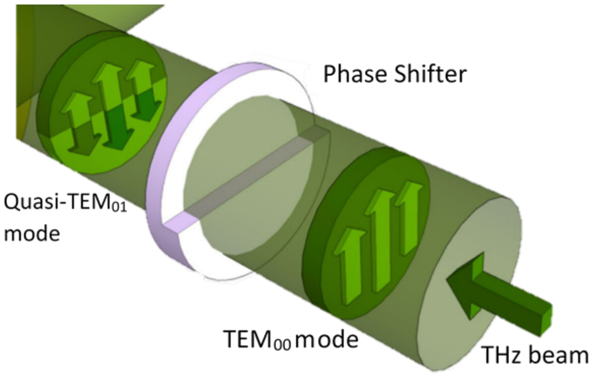

Figure 5.57: Phase shifter converting THz $TEM_{00}$ mode into quasi-$TEM_{01}$ mode as proposed in [18].

In order to model in simulation the driving pulse with quasi-$TEM_{01}$ polarisation, the method used for the horns investigated in this section use two waveguide ports driven by equal magnitude, opposite amplitude pulses in the $TE_{01}$-rectangular mode configuration as shown in Fig. 5.58. The output port of the

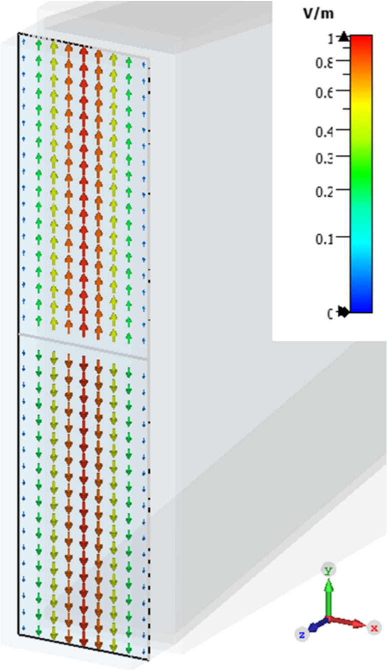

Figure 5.58: $TEM_{01}$ Mode approximation driven by two waveguide ports with equal magnitude, opposite amplitude $TE_{01}$-rectangular modes.

waveguide was implemented such that it closely resembled the DLW accelerating mode in Fig. 5.55. It used metal boundaries within the photonic crystal to generate a mode close to the expected field pattern as shown in Fig. 5.56. Due to the temporally short pulses that drive THz structures relative to the structure size, there is no energy steady state and thus the usual method of S-Parameter analysis is not applicable. This section will therefore examine frequency transmission as a function of the input pulse.

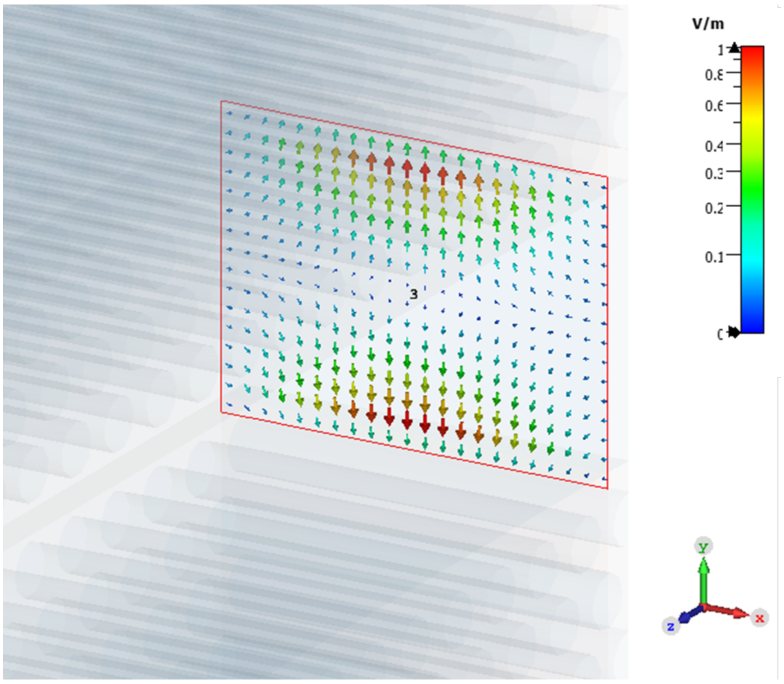

Figure 5.59: Electric field vectors for the output waveguide PBG-W port of the PBG-W accelerating mode approximation to calculate transmission.

### 5.4.2 PhC-Based Horn

The first structure investigated explored the possibility to design the horn within the same photonic crystal platform as the waveguide. This idea has the advantage to fully integrate the horn into the waveguide design, which provides advantages in fabrication and minimum reflections at the horn-waveguide interface. The design investigated uses a large slab of PBG-W as designed in this chapter, and a taper in the slab to couple between free-space and the PBG-W. The length of the horn section is $10\,mm$. The input to this horn is the two ports both driven by the ports shown in Fig. 5.58. The output waveguide port was placed $a/2$ into the PBG-W and featured metallic boundaries to ensure the correct polarisation as shown in Fig. 5.59 with total $z$-axis length of $13662\,\mu m$ between input and output ports. The schematic of this design can be seen in Fig. 5.60. The input pulse used was a 30% FWHM bandwidth pulse, with FFT shown in Fig. 5.61.

The time domain propagation is shown in Fig. 5.62. The two ports launch the correct mode into i1(2) and i2(2), 180° out of phase as shown in Fig. 5.56. Mode coupling was expected to begin after $50\,ps$ and as revealed by o3(3), there is a trivial amplitude of coupling after this time. It however remains low and rings for the remainder of the time measured, with no other mode coupling visible. This reveals that while a PhC horn may be appropriate for coupling between free space and a propagating accelerating mode, the cutaway structure presented here was not applicable for this due to generated as presented in Fig. 5.63. The circled resonances furthermore show high field concentration periodically along the surface of the cutaway and it is likely the secondary resonance this cutaway introduced has it's own photonic behaviour which interferes with the performance of the horn and thus the resonances introduced contribute to poor coupling offered by this device.

Examining Fig. 5.64, these resonances cause propagation into the photonic crystal, circled in red, which led to reflections. At each of these cutaways, the wave is attempting to couple into the photonic crystal instead of following the vacuum channel. Ultimately the photonic bandgap effect applies though and the wave is reflected, and consequently back out the horn instead of into the waveguide. The resultant poor coupling was circled in pink.

Future work could investigate other designs such as a Bragg horn into a triangular lattice based waveguide, or improving the horn surface ensuring the secondary resonances are no longer present.

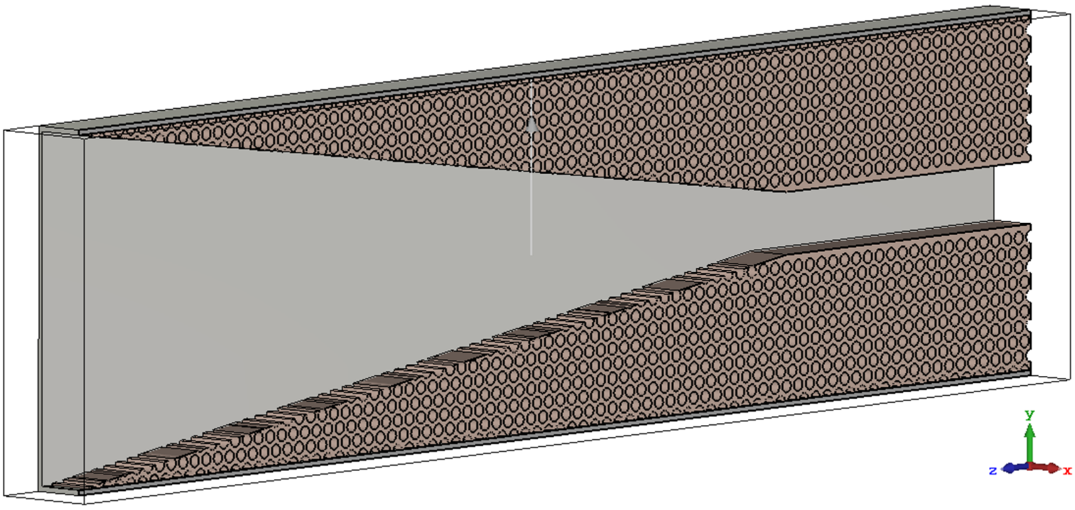

Figure 5.60: PhC cutaway horn coupler, with 10mm horn section.

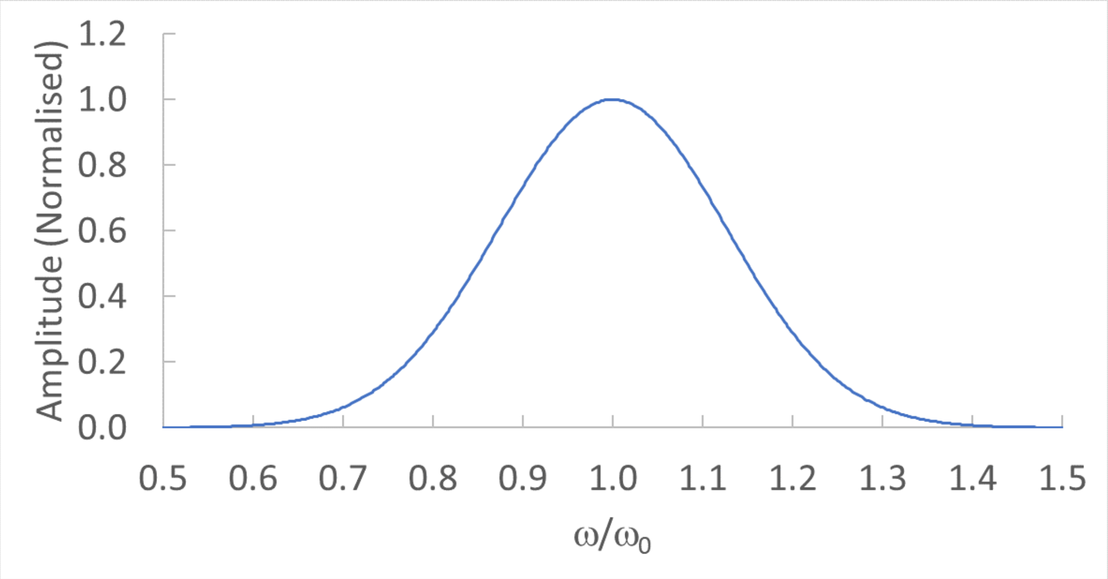

Figure 5.61: FFT of the driving pulse

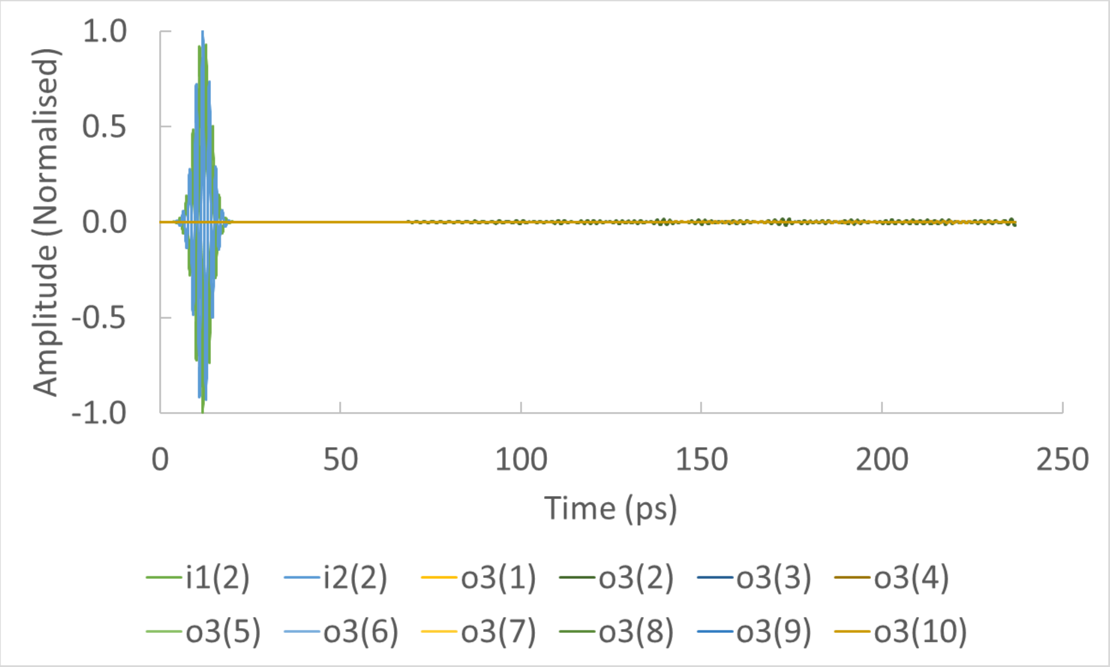

Figure 5.62: Time domain port signals for PhC-based Horn. Input signals “i” and output signals “o” to the mode number in brackets, with mode o3(3) being the accelerating mode shown in Fig. 5.59. The slight ripple on the o3(3) line after 50 *ps* shows slight coupling into the accelerating mode, but too low to be of interest, with other lines showing no coupling.

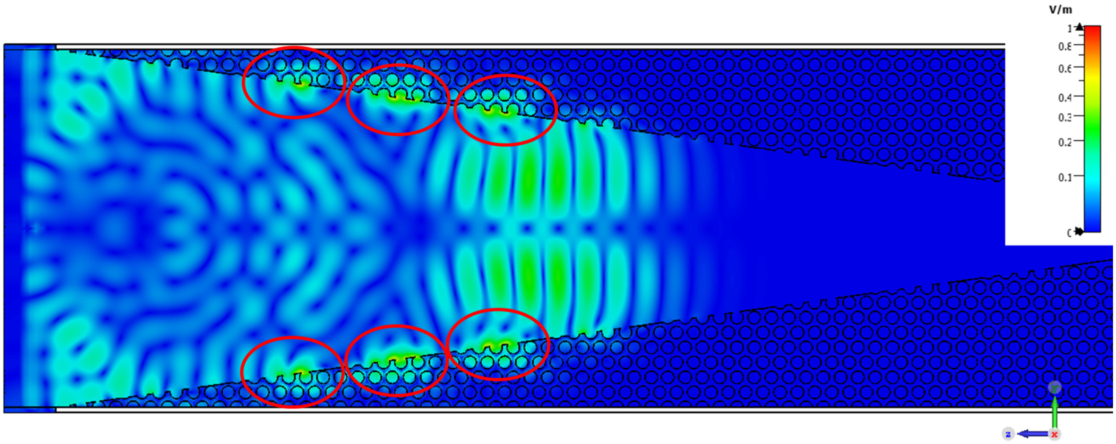

Figure 5.63: Resonances between driving pulse and PhC Horn due to slice-through of photonic crystal generating a secondary periodicity, circled in red.

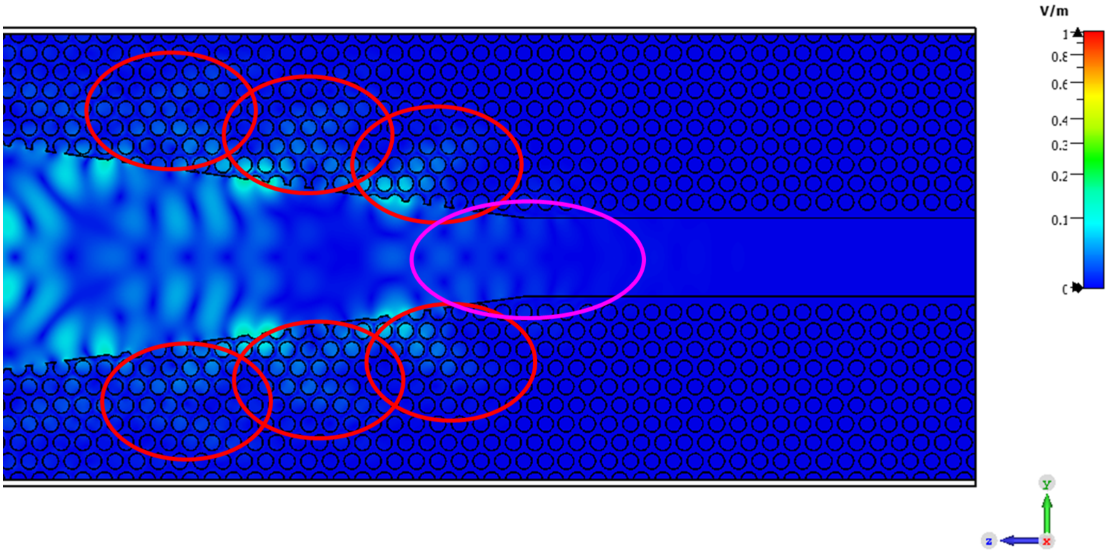

Figure 5.64: Resonances from Fig. 5.63 propagating into PhC circled in red, resulting in reflections and poor coupling, the latter circled in pink.

### 5.4.3 Dielectric Lined Metal Horn

As a cut-out in photonic crystal does not have the desired coupling effect into the structure, an alternative structure was required and as such coupling through a metal horn was considered. While multiple horn designs exist and feature designs such as parabolic curves [164] or focusing lenses [165], designs here will continue to focus on a linear taper for simplicity.

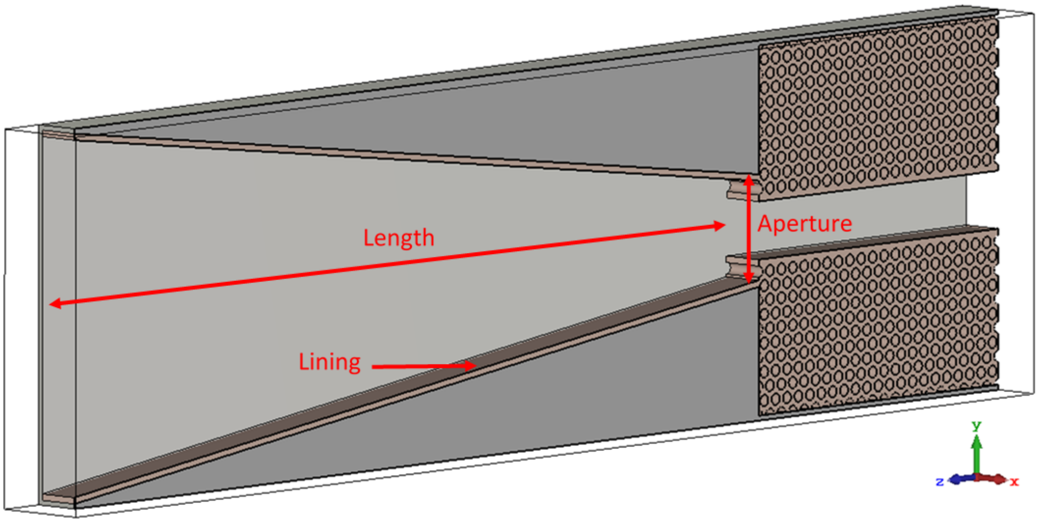

Figure 5.65: Dielectric-lined horn coupler, with Length of $10\,mm$ horn section. Dimensions investigated shown. Brown is silicon, and grey is the metal cladding.

The first attempt at coupling an accelerating mode into the PhC structure drew inspiration from work completed in [87] which used an unlined metal taper into the lined DLW section. Upon investigating this however, it was found that an unlined metal horn did not provide the mode-matching required between the PhC and the hybrid mode excited in the horn and thus the transmission was low. The accelerating mode in a PhC structure has electromagnetically “soft” boundaries which provide evanescent decay instead of “hard” boundaries where the electric field has an abrupt transition to zero. Improved matching between the two structures however was found when the horn itself has a layer of dielectric. The horn assembly, shown in Fig. 5.65, was as before driven by a quasi-$TEM_{01}$ mode via two waveguide ports outputting 180° out of phase $TE_{01}$ modes. The output waveguide port was again placed $a/2$ into the waveguide with metallic boundaries to ensure the correct mode was generated.

From these Figs. 5.66 and 5.67, it can be seen that the bare metal horn provides the poorest coupling into the accelerating mode at $\omega/\omega_0 = 1.00$. Recalling the dispersion for an accelerating mode in the $r = 0.350a$ waveguide in Fig. 5.68, there is a stop band above $\omega/\omega_0 = 1.02$. This stop-band is visible on the transmission spectra of the horn. The coupling of a higher order accelerating mode is also shown above the stop band beginning at $\omega/\omega_0 = 1.10$. Increasing the lining to $50 - 75\,\mu m$ thickness approximately doubles the coupling into the desired mode. Further increases in thickness have a negative effect. For horn designs in the rest of this section, a lining of $50\,\mu m$ will be used.

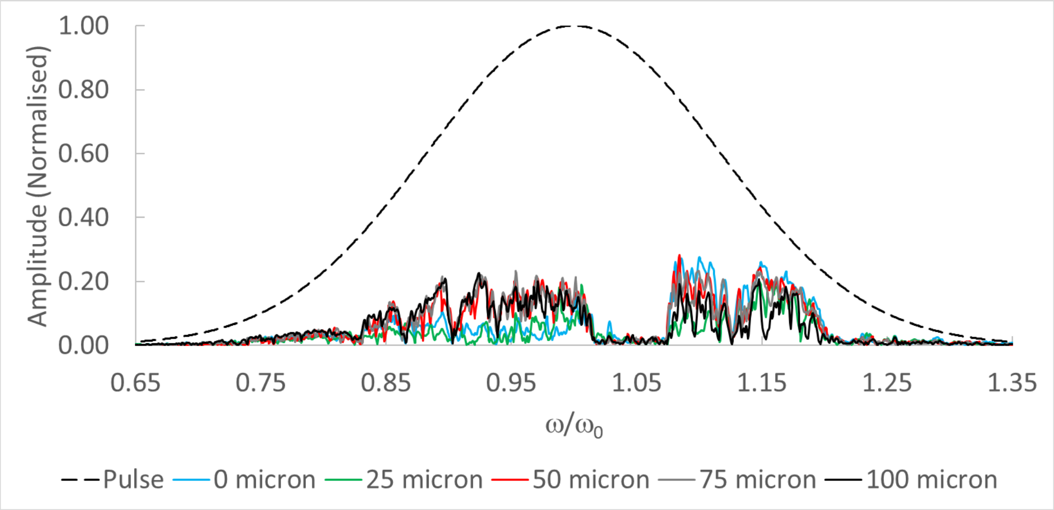

Figure 5.66: Comparison of frequency domain transmission into modes which fit the mode approximation as shown in Fig. 5.59 for horn dielectric lining thickness $0 - 100\,\mu m$, normalised to the peak amplitude of the driving pulse Fourier transform.

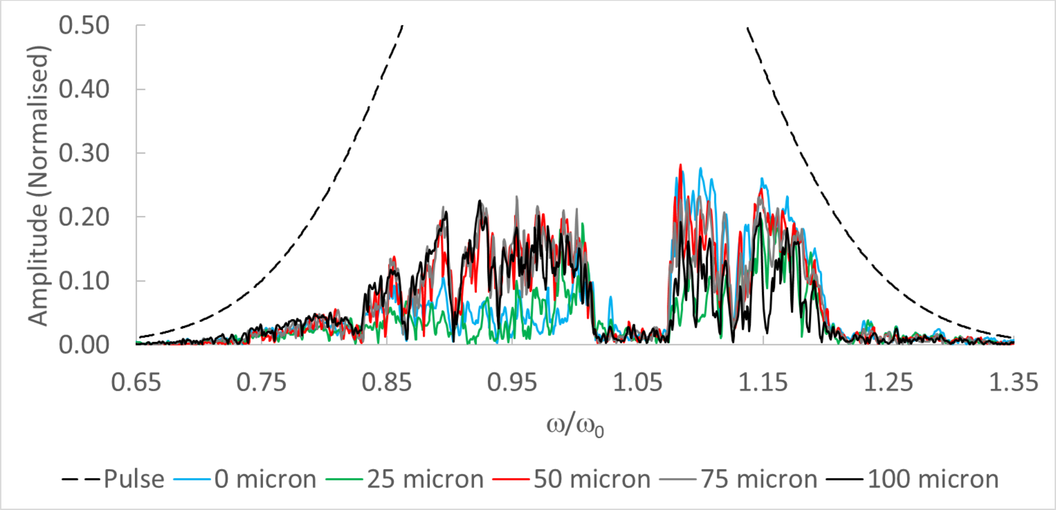

Figure 5.67: Frequency domain transmission as shown in Fig. 5.66, zoomed for clarity.

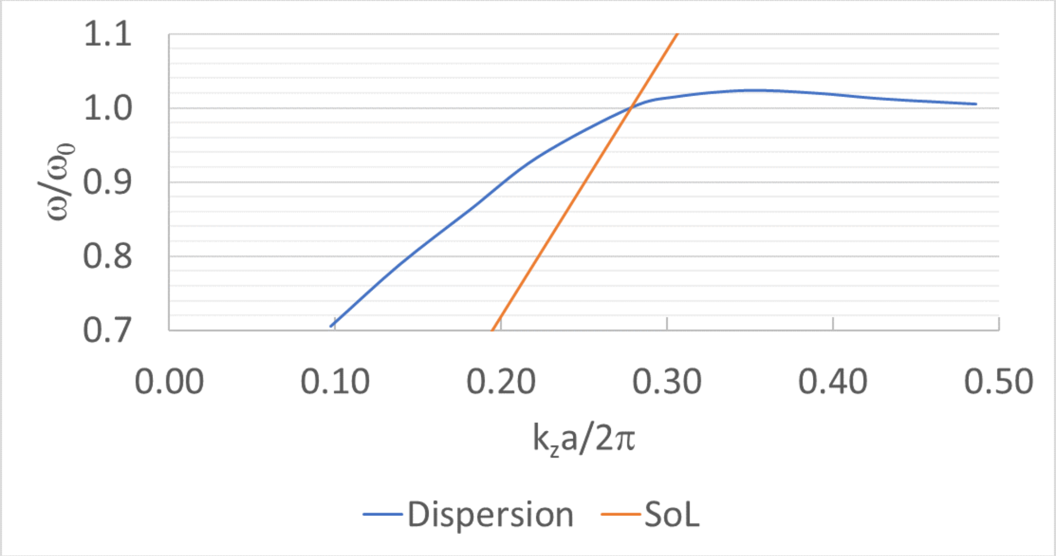

Figure 5.68: Dispersion of accelerating mode shown in (c) of 5.42 showing higher group velocity interaction and a more dramatic negative $v_g$ region compared to the $r = 0.445a$ case.

### Horn-Waveguide Coupling

With the dielectric lining chosen of $50\,\mu m$ for the horn, the modes between the horn and the PhC waveguide must be matched to minimise reflections at the horn-waveguide interface. As section 5.4.2 illustrated, using photonic crystal for the horn is not effective and thus the matching must occur between two dissimilar structures. To achieve this, the boundary between the horn and the PBG-W was varied in width between $3.5 - 6a$ in $0.5a$ steps, denoted as “Aperture” in Fig.

5.65. The plotting of the transmission signals was split across Figs. 5.69 and 5.70 for clarity. While all the time-domain port signals will not be shown due to the number of plots involved, examining transmission reveals smoother coupling in the region of $4.5a$ aperture width, whilst $5.0a - 6.0a$ show reduced transmission in the $0.8 - 1.0\,\omega/\omega_0$ region of interest. It also presented the lowest level of reflections, with input pulse and reflection shown in Fig. 5.71.

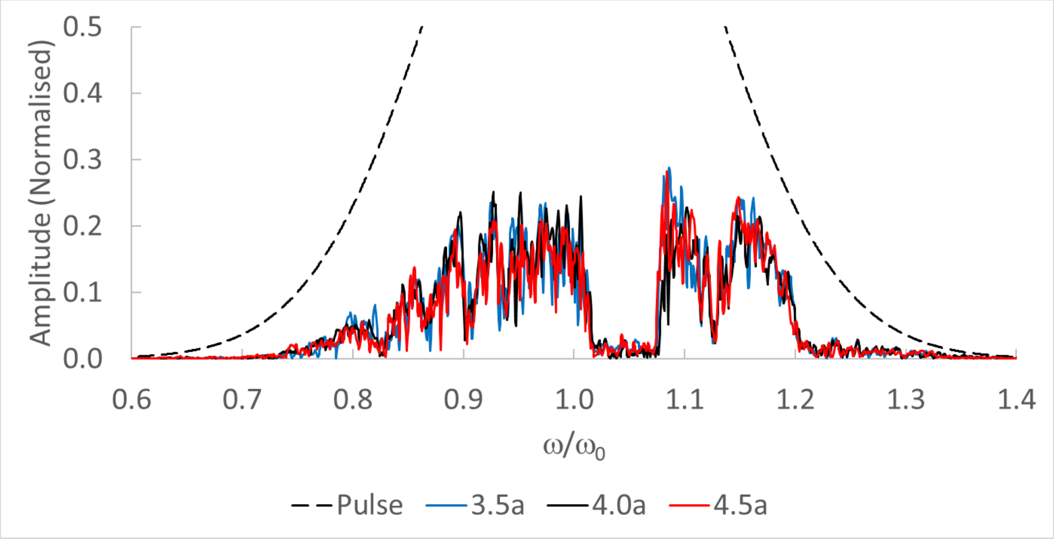

Figure 5.69: Frequency domain transmission into accelerating mode for horn aperture $3.5a - 4.5a$ with length $10\,mm$ and dielectric lining of $50\mu m$.

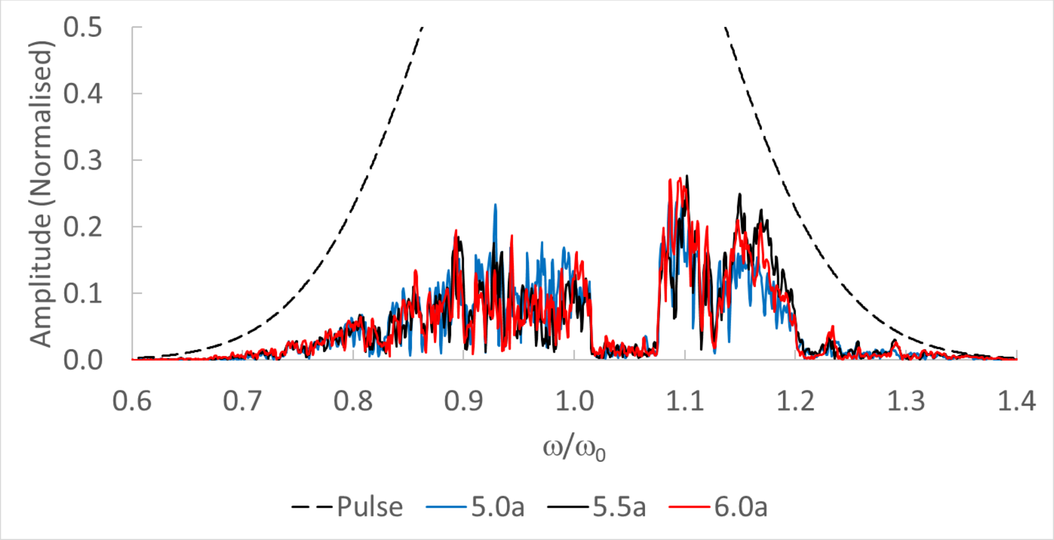

Figure 5.70: Frequency domain transmission into accelerating mode for horn aperture $5a - 6a$ with length $10\,mm$ and dielectric lining of $50\mu m$.

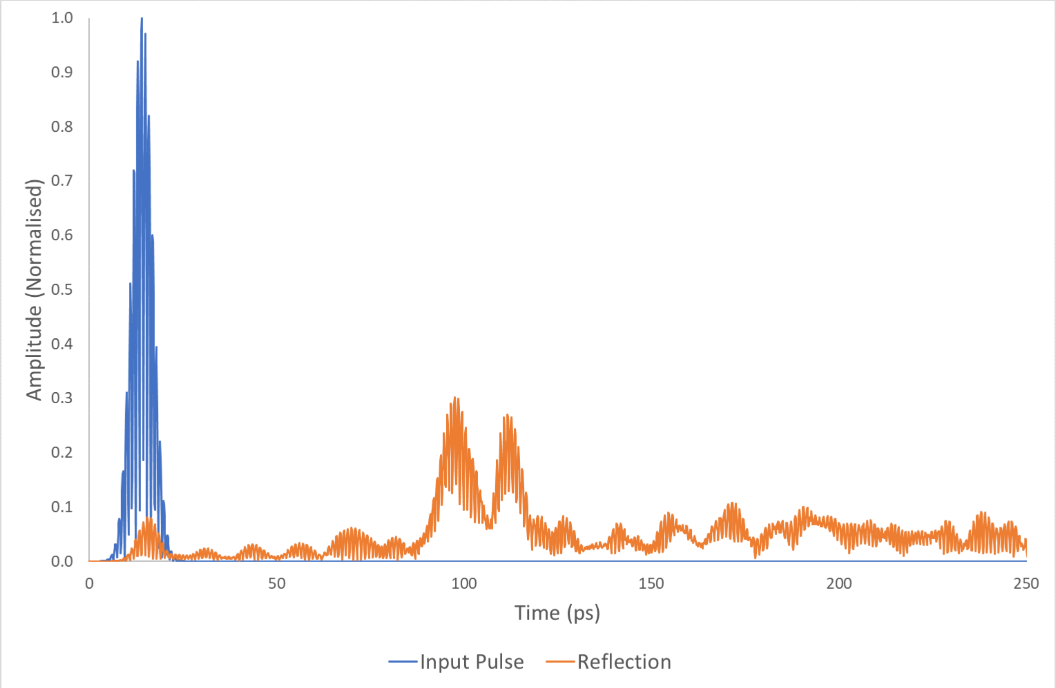

Figure 5.71: Combined time domain reflection signals from horn length $10\,mm$ with dielectric lining of $50\,\mu m$ and aperture $4.5a$.

### Length

For horn coupling, typically a longer and thus more gradual change in impedance results in better coupling as reflections are minimised. This was investigated for coupling into the photonic crystal using horn length $5-20\,mm$, with results shown in Fig. 5.72. From this it can be seen the length of the horn plays a negligible role in the coupling efficiency, with a slightly lower transmission using a $5\,mm$ horn. The $10\,mm$ and $15\,mm$ showed equivalent coupling capabilities, with slight improvement at higher frequencies for the $10\,mm$ horn, and at lower frequencies with the $15\,mm$ horn. Whilst it was expected the $20\,mm$ horn would offer the best coupling, this was not found to be the case.

Examining the reflections in the $20\,mm$ to understand the field behaviour leading to this outcome, frequency domain snapshots were taken at $\omega/\omega_0 = 0.95, 1.00, 1.05, 1.15$. These field plots, shown in Figs. 5.73–5.76 respectively, illustrate the coupling regions and stop band of the structure. Transmission in Fig. 5.73 reveals orderly coupling into the structure, with the high-field regions in the horn being the expected reason for reflection. By Fig. 5.74 the coupling has become less

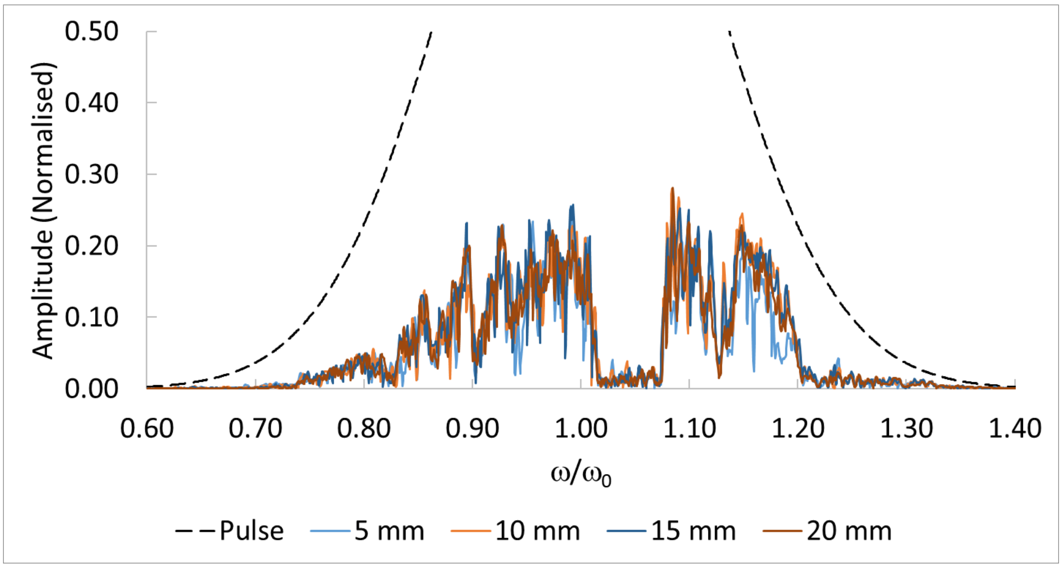

Figure 5.72: Frequency domain transmission into accelerating mode for horn length $5 - 20\,mm$ with dielectric lining of $50\,\mu m$ and aperture $4.5a$.

orderly—with backward propagating regions in the PBG-W, shown by the irregular high-field regions in the vacuum channel, likely the component indicated as in the dispersion in Fig. 5.68 as the negative group velocity region $k_z a/2\pi > 0.35$. Additionally, there are high field regions in the horn that are likely caused by the back-propagating components in the PBG-W leading to reflections. Fig. 5.75 shows the stop band, and while the horn presents the correct mode orientation to generate the accelerating mode, the dispersion reveals there is no component at this frequency and thus evanescently decays or is reflected. The plot in Fig. 5.76 shows overall improved coupling over Fig. 5.73 with reduced high field regions in the horn indicating lower reflections—it is a higher-order mode propagating in the PBG-W.

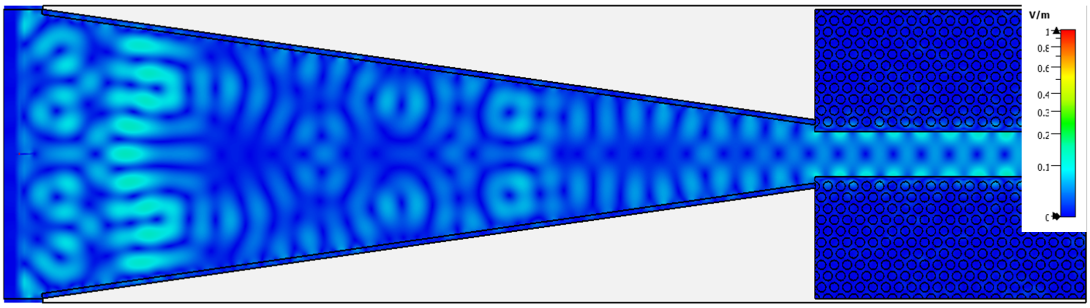

Figure 5.73: Absolute E-field value at $\omega/\omega_0 = 0.95$, below the stop band seen in earlier figures, showing coupling into the correct accelerating mode.

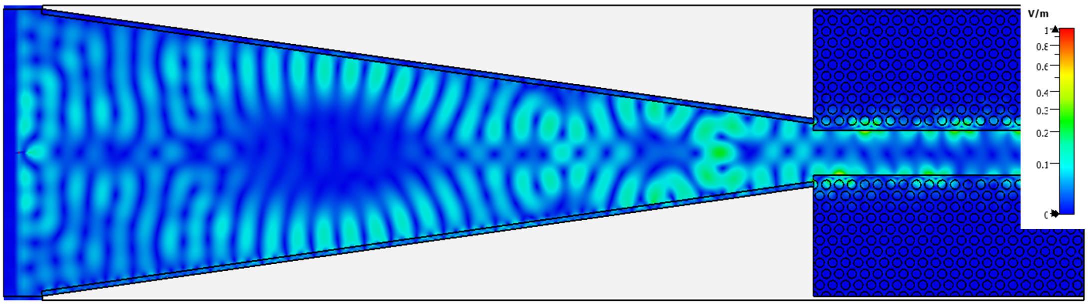

Figure 5.74: Absolute E-field value at $\omega/\omega_0 = 1.00$, below the stop band seen in earlier figures and at the accelerating frequency. Some field distortion can be seen compared to Fig. 5.73 and it is expected that a combination of meshing and structural detuning has shifted the top peak of the dispersion shown in Fig. 5.68 slightly.

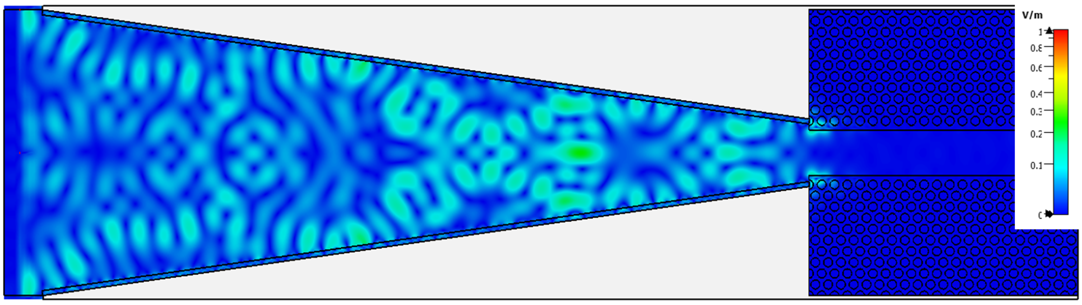

Figure 5.75: Absolute E-field value at $\omega/\omega_0 = 1.05$, in the centre of the stop band seen in earlier figures, showing no coupling into any mode.

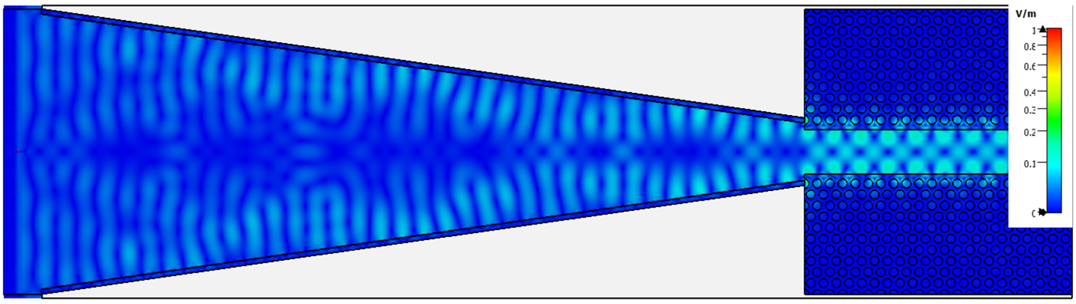

Figure 5.76: Absolute E-field value at $\omega/\omega_0 = 1.15$, above the stop band seen in earlier figures, showing coupling into an higher order mode.

### Narrowband Response

Investigation for the horn coupling structure has up until now focused on broadband excitation. The earlier sections of this chapter however reveal these structures may be effective in a narrowband regime. As can be seen from comparing the time domain plot in Fig. 5.77 with that of Fig. 5.71, for a narrowband pulse on the order of 1% bandwidth requires a much longer pulse than the short few-cycle pulses that generate the broad bandwidths. What is still visible however is the reflection from the boundary between the metallic horn and the purely dielectric photonic crystal occurring approximately $100\,ps$ after excitation similar to Fig. 5.71.

Comparing the level of coupling into the fundamental accelerating mode in the two cases, broadband and narrowband, Fig. 5.78 illustrates the coupling into the desired mode at $\omega/\omega_0 = 1$ is similar to a few percent between broadband and narrowband excitations. The narrowband excitation however does not couple into the higher order mode that can be found excited by the broadband excitation.

These transmission measurements made use two waveguide ports excited with $TE_{01}$ modes 180° out of phase. These modes were launched into a free-space gap between the ports and the entrance of the horn enclosure, the gap visible on Fig. 5.65 as the wireframe on the left, with the injection ports at the boundary of the $+z$-axis. As a confirmation this free-space gap did not negatively affect the coupling, the narrowband excitation was also repeated with metallic boundaries enclosing the gap. Examining the plots in Figs. 5.79 and 5.80, the transmission into the accelerating mode is slightly improved over the open case, but the reflections are also increased too showing they are not a function of reflection at the large opening of the horn and that discontinuity between the metal horn and the PhC structure remains the largest factor in optimisation of this device.

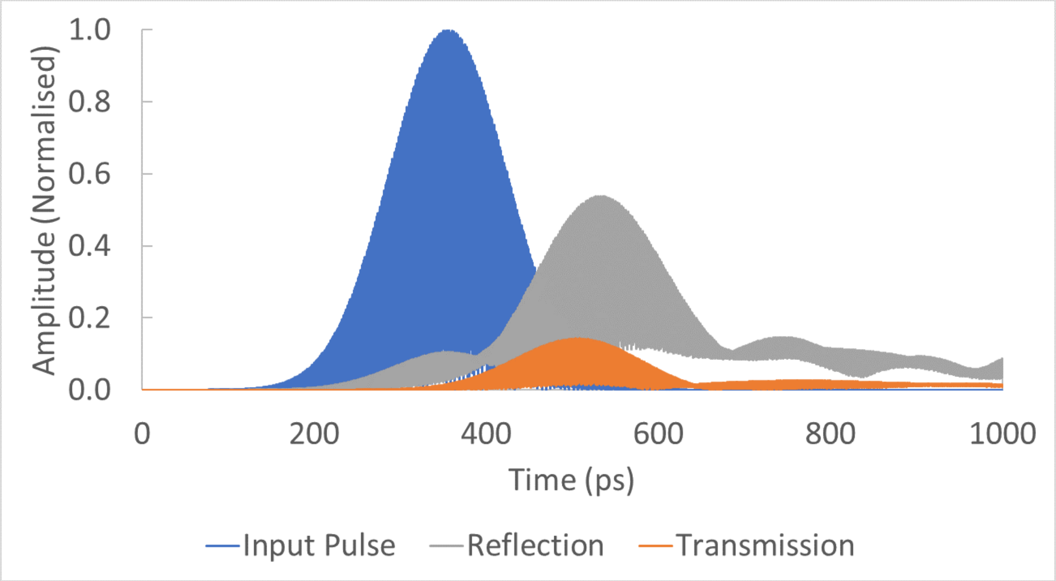

Figure 5.77: Combined time domain signals of narrowband excitation; in structure with horn length 20 $mm$ with dielectric lining of 50 $\mu m$ and aperture 4.5$a$.

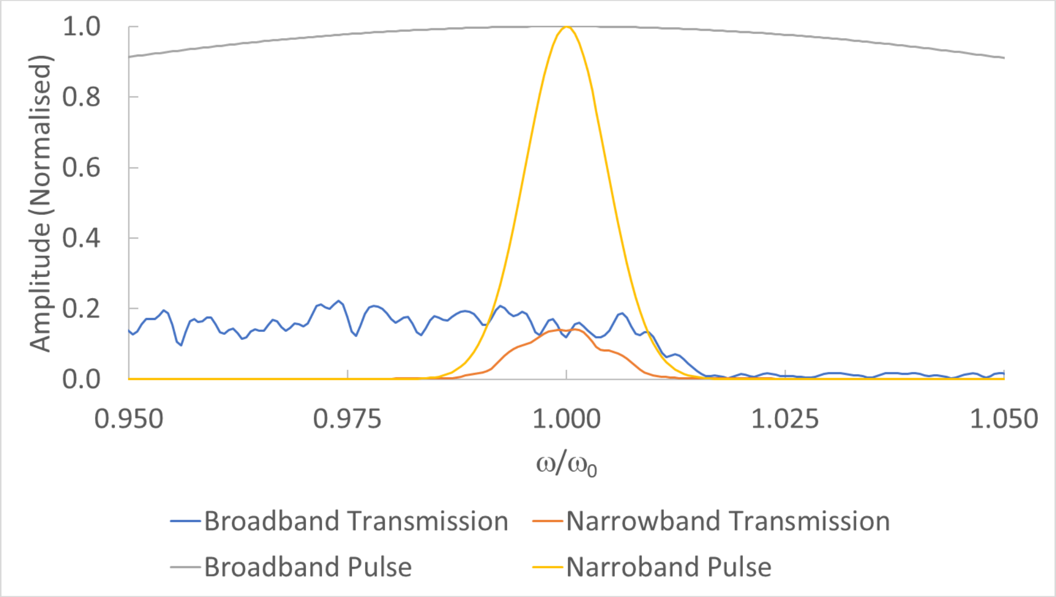

Figure 5.78: Comparison between frequency domain transmission of accelerating mode for broadband and narrowband excitation signals; in structure with horn length 20 $mm$ with dielectric lining of 50 $\mu m$ and aperture 4.5$a$.

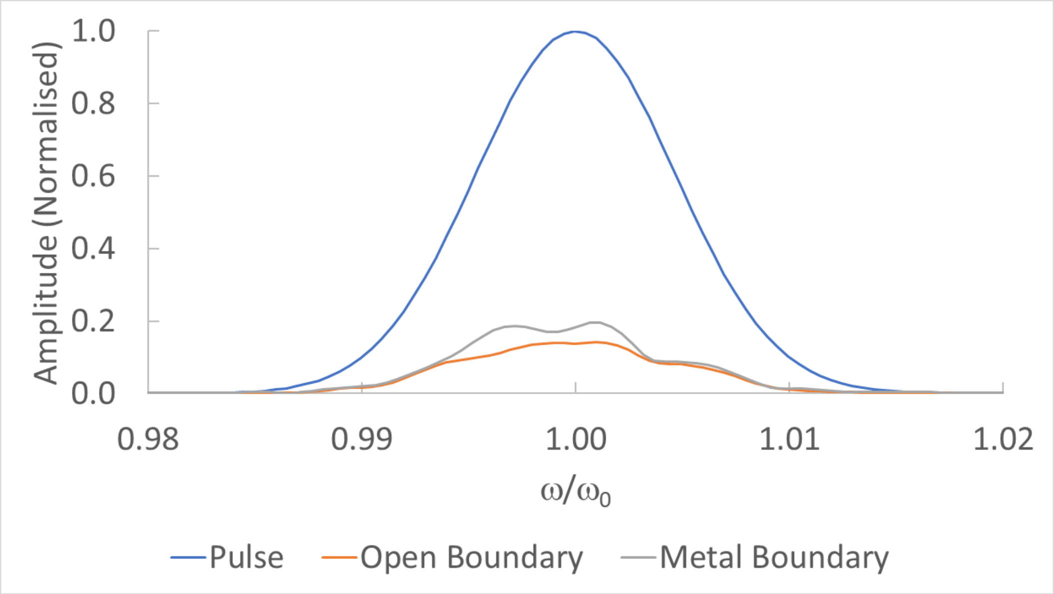

Figure 5.79: Comparison between frequency domain transmission for free-space boundary and metal boundary systems. Free-space boundary offers an open boundary between the dual waveguide ports producing the quasi-$TEM_{01}$ mode, and the metal boundary instead encloses the propagation region in metal.

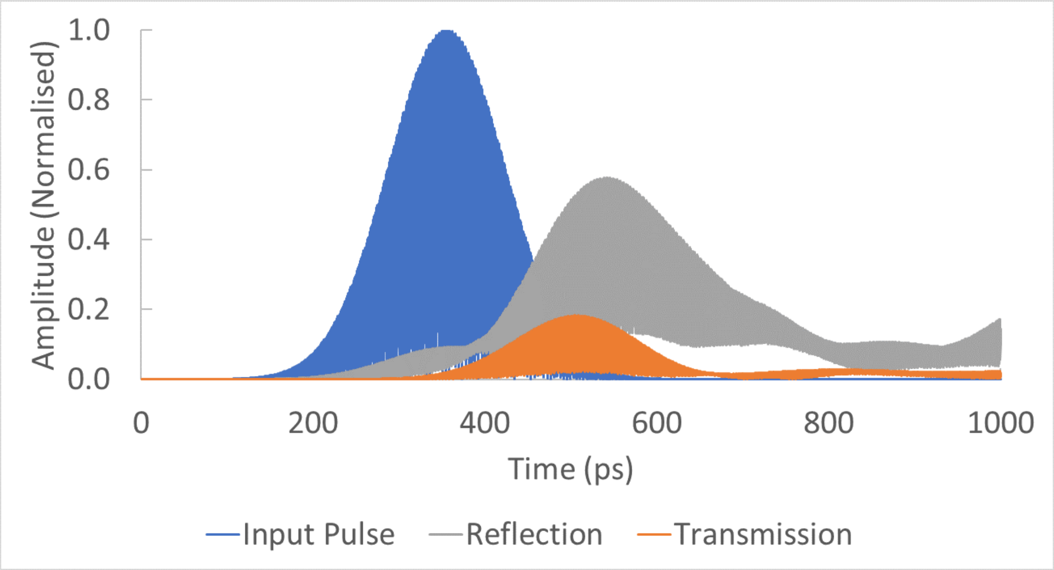

Figure 5.80: Combined time domain signals for metal boundary structure driven by narrowband excitation; in structure with horn length $20\,mm$ with dielectric lining of $50\,\mu m$ and aperture $4.5a$.

## 5.5 Mesh Analysis Study

In all computational physics there is the conflicting desire for the results to both be as accurate as possible, and the simulations to run as fast as possible. As both computing and human time is not infinite, a trade-off must be made between the two. Additionally while CST is core-unlimited in process, this comes with a real-world cost in unlocking the license to enable this—which is a common process in proprietary and closed-source software. As the simulations undertaken in this thesis often require much trial-and-error and dead-end simulation, a minimum CPU time and thus simulation time is preferable to maximise model throughput.

To this end, a mesh convergence study was undertaken to determine the error at meshing levels and the minimum acceptable mesh which could be used with a sufficient level of confidence. The computer much of the work in this thesis was undertaken on was a Dell Precision 5810 workstation featuring a 6-core/12-thread Intel Xeon E5-1650v4 CPU clocked at 3.6 GHz and 64 GiB PC4-19200E RAM; and in addition it featured a NVIDIA Tesla k40c GPGPU card for simulations such as PIC and TD which support hardware acceleration. While every effort to ensure the operating environment remained constant during the mesh study, background

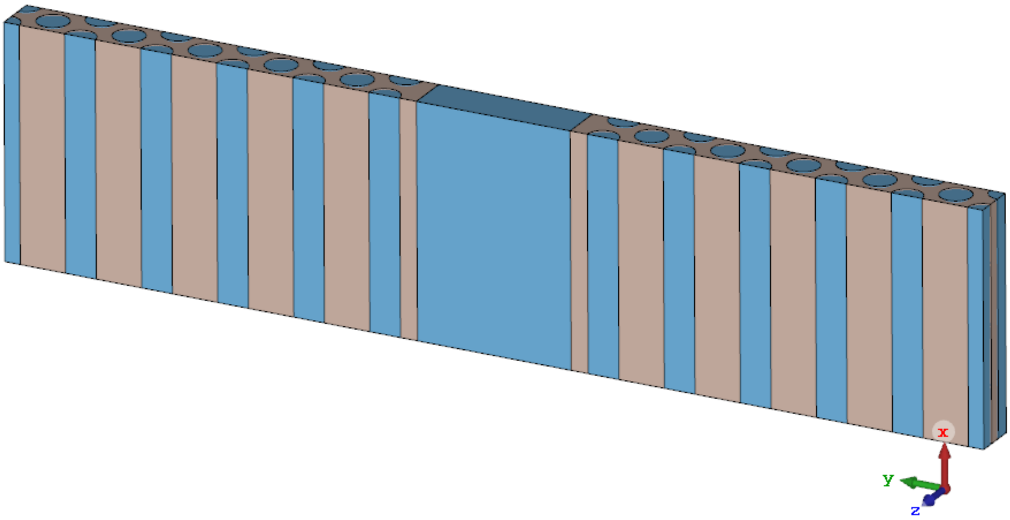

Figure 5.81: Structure analysed for mesh study, with 3.5a channel width and 10.5 layers of PhC.

operating system processes will add an error to the solver time. The absolute values for the solver time however are less important than the trend which can still be inferred as CPU time is not being measured.

The setup for this study uses the high-$\zeta_v$ structure based at $1\,THz$ centre-frequency at interaction angle 100.188° such that $v_p/c = 1$ and shown in Fig. 5.81. Losses were considered in calculation. Due to the geometric complexity required by the 2D photonic-crystal as it features arrays of circular holes, compared to a simpler structures which can be designed using orthogonally hexahedral faces such as the Bragg stack, a tetrahedral mesh was used. The solver was searching for 10 modes above the frequency of $0.998\,THz$ and solved up to second order with accuracy $10^{-6}$. Parameters featured in this mesh study are the mode frequency, the characteristic impedance $Z_c$, the solver time, and memory required. The mesh density was swept between $1 - 12\,\lambda^{-1}$ in steps of $1\,\lambda^{-1}$. Also included is CST's own auto-meshing algorithm with 1-pass and 2-pass refinement on a frequency variation of 0.001 over 10 modes. This auto method uses a more inhomogeneous meshing compared to the per-wavelength method, by concentrating mesh cells in

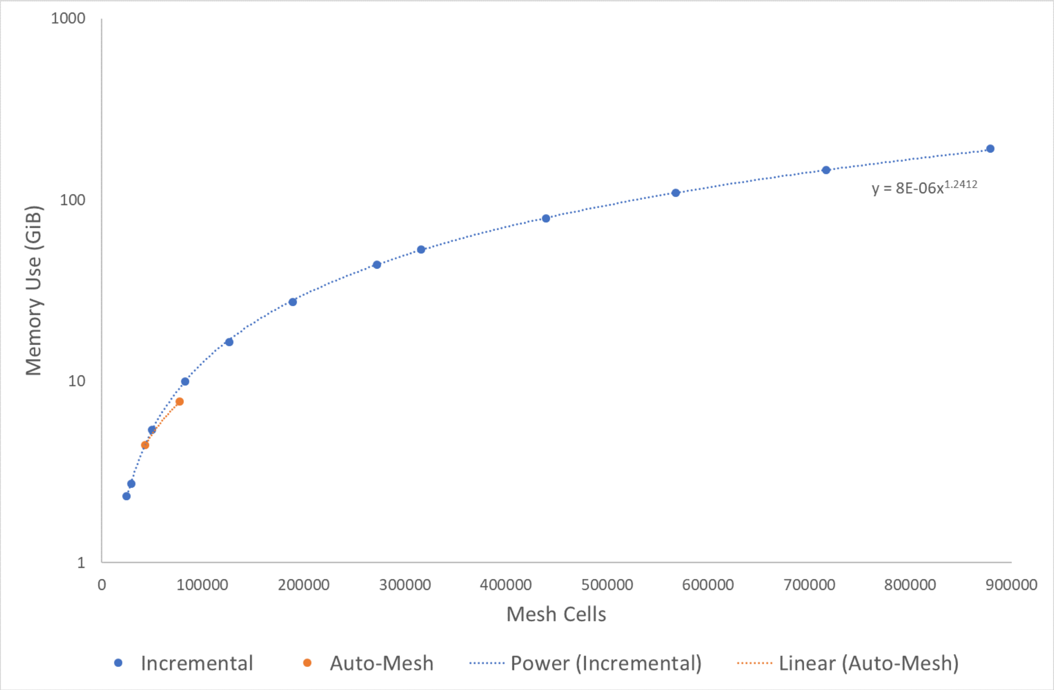

Figure 5.82: Memory use for $1-12\,\lambda^{-1}$ incremental and auto-generated tetrahedral mesh size for the test structure.

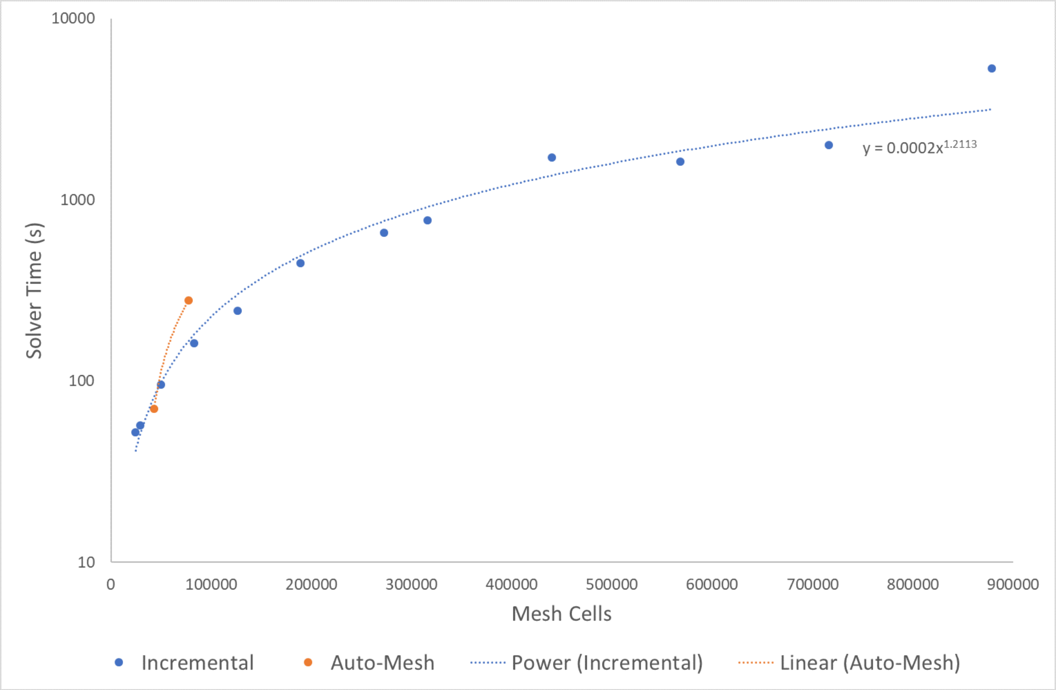

Figure 5.83: Solver time for $1 - 12\,\lambda^{-1}$ incremental and auto-generated tetrahedral mesh size for the test structure.

regions with higher field. Also investigated was a 3-pass refinement but due to the frequency variation limit being satisfied after 2-pass refinement, the solver aborted at this stage.

As can be seen by Fig. 5.82, with the used memory $g$ increasing with mesh-density $d$ by power factor $g \propto d^{1.24}$, by mesh density $8\,\lambda^{-1}$ the solver was approaching the memory limit for the machine. By $9\,\lambda^{-1}$, the limit had been reached and thus virtual memory was being used considerably slowing down the simulation and taking it out the realms of feasibility for the workstation. The larger models $d = 9 - 12\,\lambda^{-1}$ were computed on the distributed computing cluster EG-SERVER10 at Lancaster University. Relying on the cluster however brought its own issues. While solutions could be calculated faster—time was bottlenecked by both network speed to actually transfer the results to the workstation frontend, and the number of other users running simulations thus using otherwise free cores. Similarly, even with the cluster being used for the larger models, simulation time $t$ grew with mesh-density by power factor $t \propto d^{1.21}$ as seen in Fig. 5.83.

For the parametric study of the mesh convergence, the inverse of number of

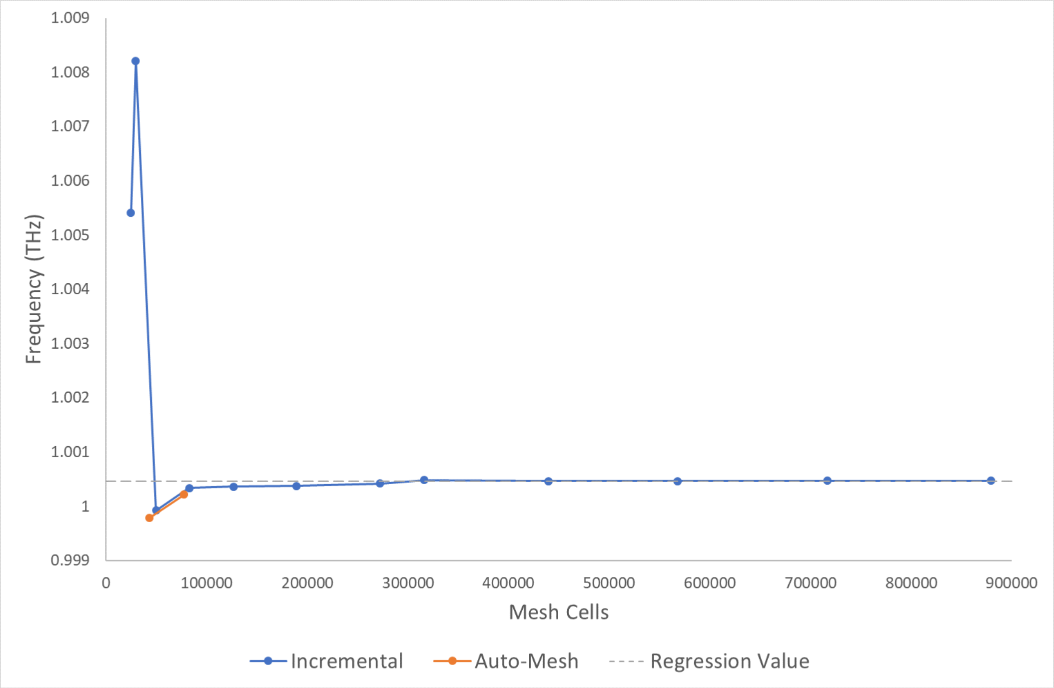

Figure 5.84: Frequency convergence for $1-12\,\lambda^{-1}$ incremental and auto-generated tetrahedral mesh size for the test structure.

mesh cells taken for each sample, and a best fit line was implemented for the linear region at high mesh cell counts. Plotting the value versus the inverse mesh cells allows an equation of best fit line to be plotted, where the standard straight-line $y = mx + c$ equation was taken. The y-intercept $c$ provided the value for "infinite" mesh cells, and was used for the regression value in the parametric plots.

The first parameter examined was the convergence in frequency with mesh. Examining Fig. 5.84 shows that $1-3\,\lambda^{-1}$ did not provide good convergence on the expected frequency. This is to be expected due to the property of Nyquist aliasing which shows a poorly sampled signal can be misinterpreted as a lower-frequency signal and thus at least $4\,\lambda^{-1}$ for the highest expected frequency is required for adequate resolution [166]. By $4\,\lambda^{-1}$ there is agreement with the regression value within around 0.01% and thus the minimum mesh size to sample the Nyquist rate is adequate for frequency resolution in these eigenmode results.

The second parameter examined was the convergence in characteristic impedance with mesh. This parameter is used extensively in post-processing and determining how effective an accelerating structure a particular design is. What can be seen from Fig. 5.85 is that while frequency converges at $4\,\lambda^{-1}$, $Z_c$ at this mesh value has error of 8.41% to the regression value, and does not converge until $5\,\lambda^{-1}$ with an error of 1.32%.

Comparison of the incremental meshing method with the auto-meshing method shows that while the auto-meshing method takes longer for an equivalent number of mesh cells, it produces a more highly converged result with fewer mesh cells, owing to the higher loading into the higher field regions compared to more background regions. While the single-pass mesh offers poor convergence, the second pass provides a frequency error of 0.02% and $Z_c$ error of 1.36% which would be appropriate for the vast majority of simulations performed. The time penalty in comparison to the $5\,\lambda^{-1}$ incremental mesh is negligible at both under 5 minutes per run and the overall memory use is lower and could even be run on low-end machines, albeit with potential time-penalties depending on hardware setup.

In all computational physics—the need to produce a result that is precise and accurate enough to answer the physics—is often at odds with the available computational ability and time. The purpose of this mesh study was to ascertain what level of meshing was appropriate so that the results could be trusted, whilst simultaneously ensuring they could be run on a desktop workstation in a reasonable length of time. The two meshing methods: iterative and auto-meshed, were compared for frequency and characteristic impedance. Both of these figures found agreement with the regression value calculated to within a tolerable error of 1.5% by $5\,\lambda^{-1}$ iterative or 2-pass auto-mesh. The auto-meshing is preferable to an homogeneous method despite the slight time penalty as it allows for fewer mesh cells and lower memory use, and provides more accurate values compared to the equivalent mesh cell count of the homogeneous mesh.

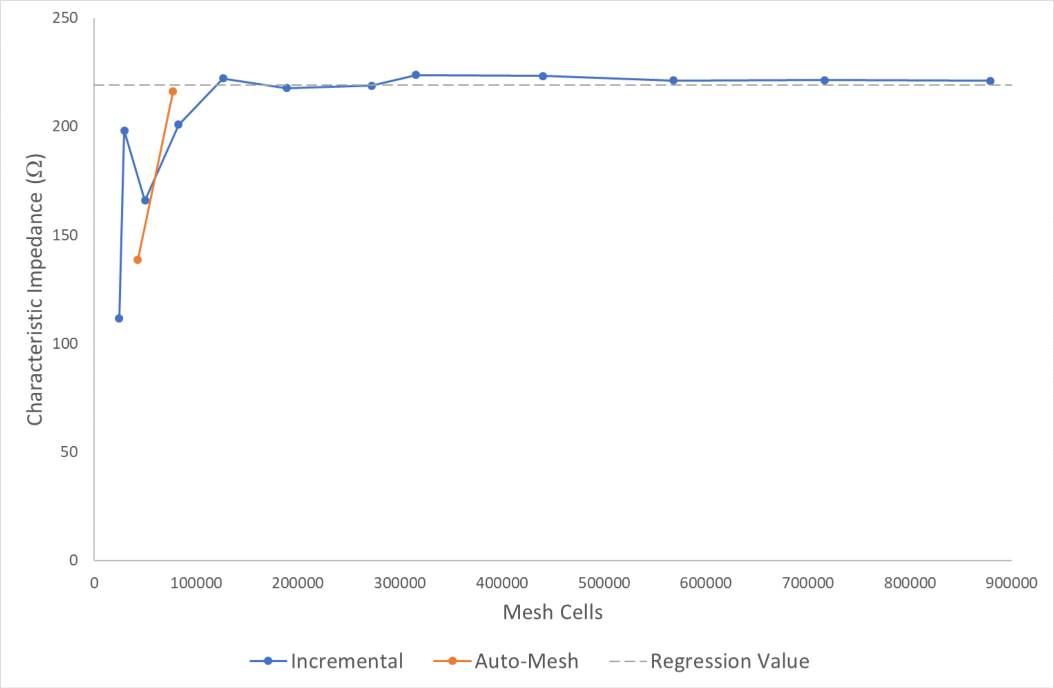

Figure 5.85: Characteristic impedance convergence for $1-12\,\lambda^{-1}$ incremental and auto-generated tetrahedral mesh size for the test structure.

## 5.6 Conclusion

This chapter explores the use of dielectric photonic crystals waveguides clad by metal plates for THz laser driven electron acceleration. Two configurations, based on the planar Bragg waveguide and a 2D photonic crystal waveguide, were investigated and compared to the dielectric lined rectangular waveguide. In particular, the 2D PhC-W was explored to reach adequate accelerating voltage for broadband THz pulses and larger waveguide aperture than required by the Bragg structure. In this pursuit, an approach for optimising waveguides for this application, applicable also to other waveguide configurations, was proposed based on the combination of the newly suggested figure of merit $\zeta_v$, and group velocity.

Results show that while 2D PBG-Ws could not match the DLW in terms of accelerating voltage, the 1D PBG-W can lead to better performance for a broadband THz pulse, approaching similar accelerating voltage compared to the DLW albeit for a smaller channel size. The 1D PBG-W in addition outperforms the DLW in terms of magnetic fields on the walls and resistive losses.

A preliminary study of the laser coupling for the 2D PBG-W was shown. The profile of both the coupling of energy, and the performance of the devices themselves, suggests that 2D PhC configurations may be more suitable to narrowband-source externally driven applications.

Important design considerations on the parameters governing optimization of the waveguide have been given.

# 6

# Wakefield Studies in Metal-Clad PBG-Ws

Work thus far in this thesis has examined photonic-bandgap waveguide structures driven with an external source. An alternative to externally driven structures is by using the resonant nature of the structure itself to excite the required acceleration mode, which can be done via wakefield excitation. This section will explore the generation of wakefields in dielectric structures and compare across different design topographies.

Waveguides, both metallic and photonic-crystal, are scalable to any wavelength and it is only external influences which dictate the absolute limits of scale—such as manufacturability, sintered grain sizes, or dielectric constant. The structures in this section are thus bound, with the limit imposed by the requirements of using a beam which is both useful and realisable. As the work presented here does not focus on beam physics, a beam which had been physically demonstrated, and had a sufficient frequency component at the design frequency of $f_0 = \omega_0/2\pi = 1\,THz$ was required. To simulate such an existing beam which could be applicable for these structures, the work at Brookhaven [81] was investigated. For simplicity, a quasi-rectangular beam was not desired, and as such was approximated with a Gaussian beam. The target beam had a bunch charge of $100\,pC$ within $300\,\mu m$. To approximate this, a Gaussian beam shape with $100\,pC$ within bunch length $2\sigma_z$ required a bunch charge of $105\,pC$. A range of Gaussian charge distributions was built, as is shown in Fig. 6.1 each being $105\,pC$ bunches, $\sigma_z$ was varied between $30 - 200\,\mu m$ and the Fourier transform of the current profile is shown in Fig.

6.2. The profiles show that for the desired $1\,THz$ to be excited adequately, a bunch smaller than $\sigma_z = 100\,\mu m$ was required. Due to the Gaussian shape of the frequency response, this additionally leads to higher frequency components of the bunch and as such $\sigma_z = 60\,\mu m$ was chosen for use in simulations. The resulting beam spectrum has a max frequency $(-20\,dB)$ of $f_{-20dB} = 1.7065\,THz$ and a bunch energy of $60\,MeV$ gives Lorentz factor of $\gamma = 116.42$.

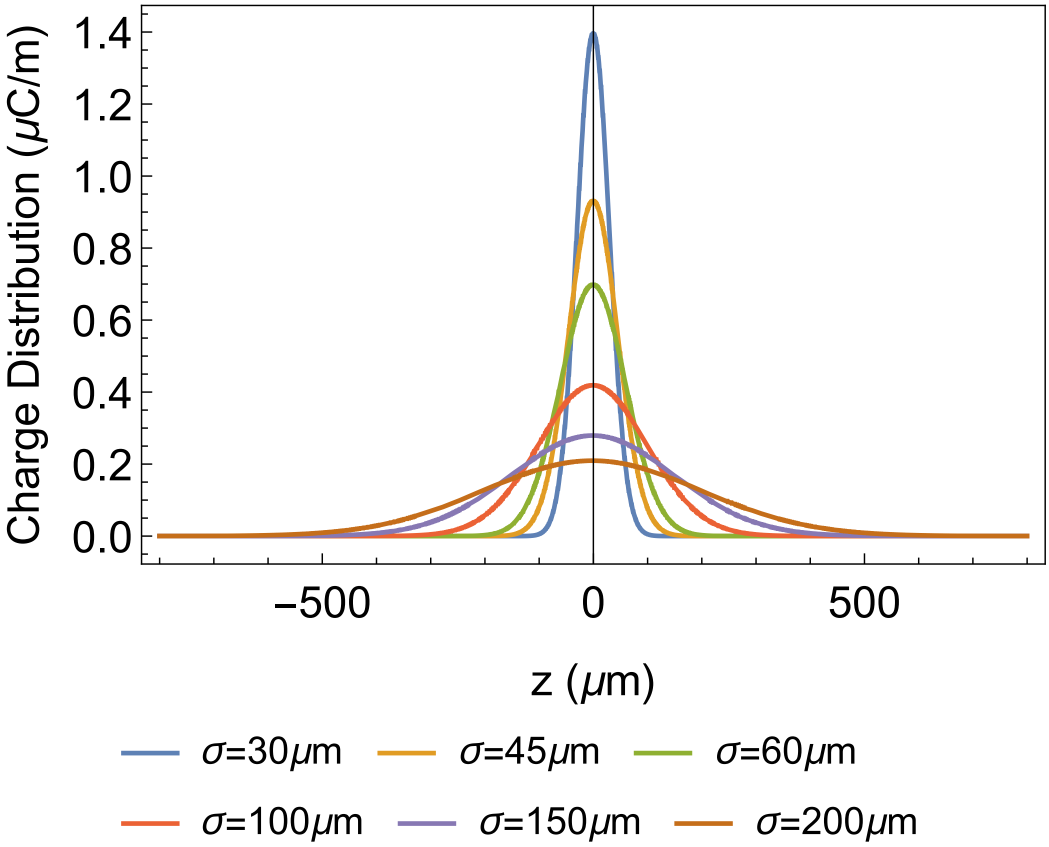

Figure 6.1: Longitudinal charge distribution in $Q = 105\,pC$ Gaussian beams for varied $\sigma$.

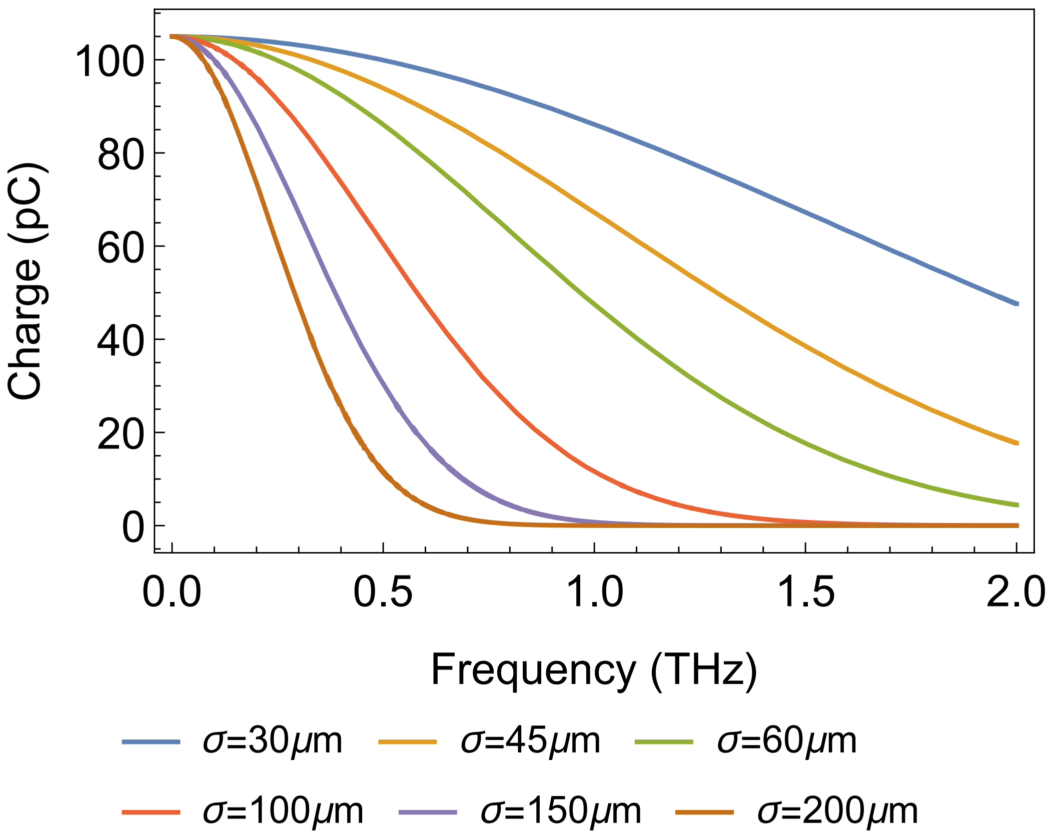

Figure 6.2: Fourier transform of the current profile for the electron bunch at a range of $\sigma$ for the $Q = 105\,pC$ bunch.

## 6.1 Wakefields in Bragg Blased PBG-Ws

### 6.1.1 Metal-Clad PBG-W Structure

Analysis began with the metal-clad 1D planar Bragg PBG-W. The design used here employs a 10-layer quarter-wave stack using materials $\varepsilon_r = 3.75$ and $\varepsilon_r = 11.66$ on the $x$-axis sides of the vacuum channel, with the first layer tuned to ensure $v_p/c = 1$ at $f_0$. For the wakefield analysis, $f_0 = 1\,THz$. The vacuum aperture is $D = 0.6\lambda_0$, which at $1\,THz$ gives $D = 179.88\,\mu m$, and the vacuum channel has aspect ratio 2:1. The length of the accelerating structure was $5\,mm$. A schematic for the waveguide design can be seen in Fig. 6.3.

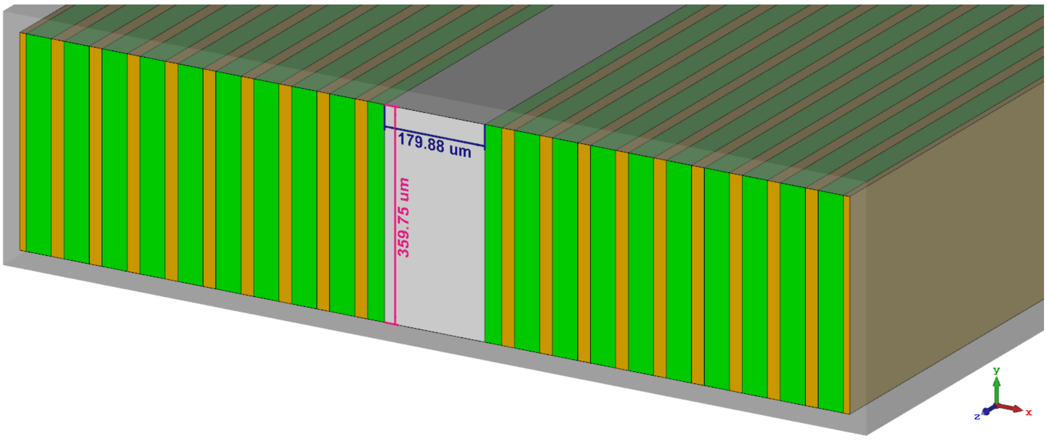

Figure 6.3: 1D-periodic Bragg waveguide designed for for $1\,THz$ operation, with $0.6\lambda_0$ separation and $1.2\lambda_0$ width. Length in $z$-axis is $5\,mm$. Transparent grey is the metallic cladding of the PBG-W in the $y$-axis; in the $x$-axis, this boundary is numerical only.

To analyse the wake impedance generated by the beam in this structure, the solver used was the wakefield solver—which as detailed in section 3.7.4, uses a thin-wire approximation of the bunch to examine the excited wake-potential in the structure. The wake impedance can then be extracted by FFT of the wake-potential. The structure was excited with the beam in four transverse positions: central to the vacuum channel; offset in $y$ by a quarter thickness; offset in $x$ by a quarter channel-width; and offset in both $x$ and $y$ by the quarter offsets. Whilst wake impedance is dependent on beam geometry as shorter beams will excite higher frequencies—CST normalises the wake impedance such that the amplitude of the wakefield impedance is independent of the beam used to excite it. The upper limit of the wakefield impedance frequency range is however limited to $f_{max}$ of the beam.

For the 1D-periodic structure, the longitudinal wake impedance in Fig. 6.4 illustrates this structure has a strong single-mode excitation; and is highly tolerant of the beam being offset towards the dielectric in $x$, with an improved impedance response likely due to the proximity of the beam to the dielectric (grey curve, Fig. 6.4). When the beam is offset in $y$ however this leads to drops of up to 50% of the impedance and an increase in the higher-order mode excitation. Combining the offset in both $x$ and $y$ led to an impedance of an undesired HOM at equivalent impedance to the main accelerating mode. Whilst undesirable, this HOM could be useful as an alignment diagnostic tool as it was only excited when the beam was off axis. Fig. 6.4 also shows a periodic resonance approximately every $50\,GHz$ and vanishes inside the photonic bandgap. This resonance is likely a Fabry-Perot resonance from the electromagnetic waves allowed to propagate within the periodic structure.

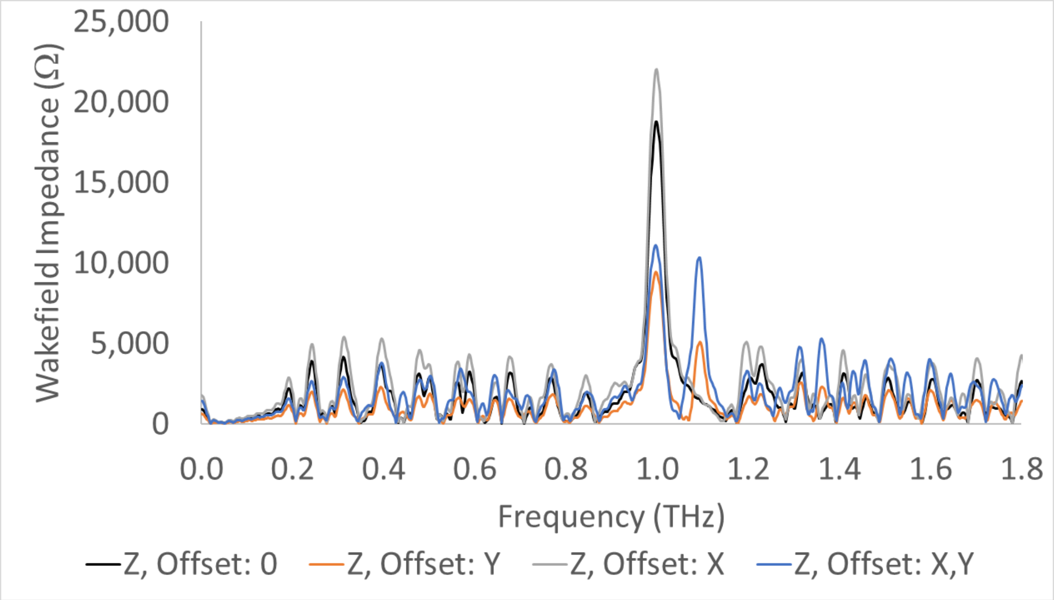

Figure 6.4: 1D-Periodic PBG-W longitudinal wakefield impedance for beam with no offset; quarter-channel offset in $x$; quarter-thickness offset in $y$; and combined offset in $x$ and $y$.

The transverse wakefield impedance generated, plotted on a log scale in Fig. 6.5 and the non-trivial impedances plotted on a linear scale in Fig. 6.6, show that except at below $200\,GHz$ which shows a large impedance, transverse modes are not excited with any non-trivial impedance until the beam is largely offset. Trivial impedances, which can be discounted without affecting conclusions, are for this work classed as less than $1\,\Omega$. The high values of impedance in the $< 200\,GHz$ region are likely due to transition/diffraction radiation.

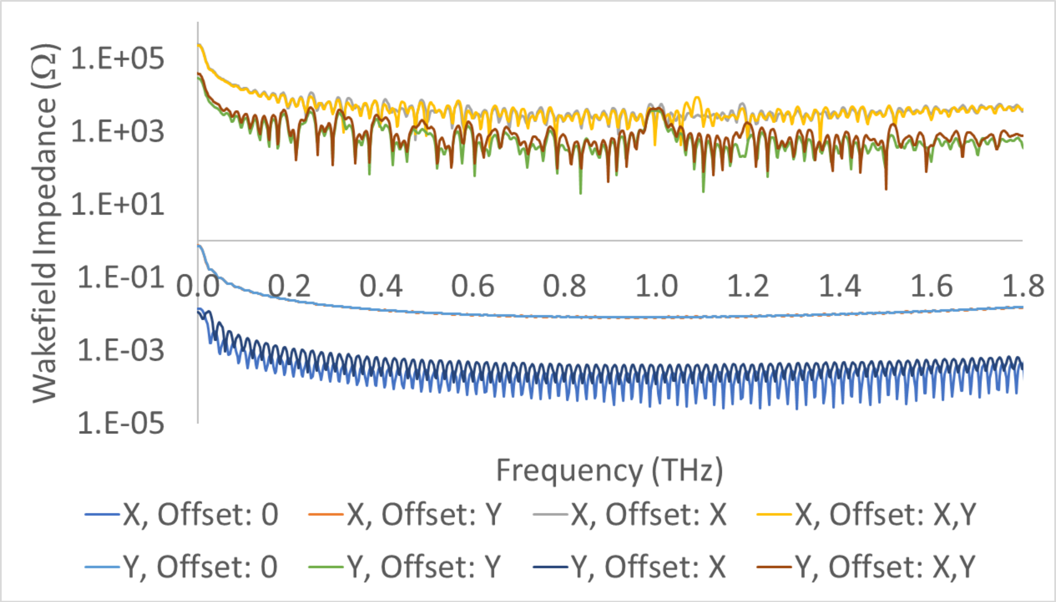

Figure 6.5: 1D-Periodic PBG-W transverse wakefield impedance for beam with no offset; quarter-channel offset in $x$; quarter-thickness offset in $y$; and combined offset in $x$ and $y$.

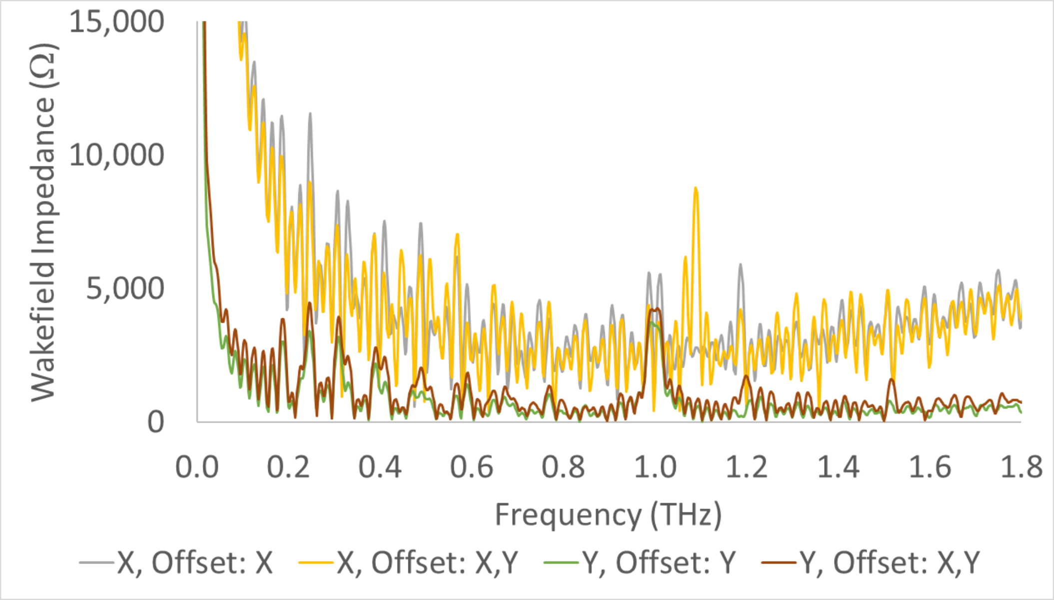

Figure 6.6: 1D-Periodic PBG-W transverse wakefield impedance linear plot for non-trivial impedances shown in Fig. 6.5.

### 6.1.2 Parallel-Plate (Open Boundary) Waveguide

An alternative waveguide geometry often investigated in literature is that of the parallel-plate waveguide topology. In this section, the PBG waveguide analogue of the parallel plate waveguide is considered. The geometry is based on the 1D PBG-W from the previous section, Fig. 6.3, where the metal plates are removed and the dimension in the $y$-axis is made large. Whilst less effective for laser excitation, it allows for simpler construction when driven by a beam. As an additional benefit it is largely tolerant of beam alignment in the open axis; as well as allowing for elliptical beams to propagate which suppress transverse mode excitation [75]. A 1D PBG-W using this topology was designed, with the first layer tuned such that $v_p/c = 1$ at $f_0 = 1\,THz$. Wakefield simulations of this geometry have only been considered for a no-offset central beam as the offset behaviour towards the dielectric in the bounded transverse dimension has already been presented in section 6.1.1, and offset in the open transverse dimension is unnecessary.

Figure 6.7 plots the longitudinal and transverse wakefield impedance for the planar Bragg waveguide showing that this geometry still provides a high impedance at the designed $1\,THz$ operation frequency with negligible transverse modes. The comparison of the longitudinal wake impedance with the metal-clad waveguide is shown in Fig. 6.8. It is found that while the impedance is decreased by 48%, the structure still provides $> 10k\,\Omega$ and reveals that the Fabry-Perot resonances are present as in the previous structure. This is expected to be present in all Bragg-based 1D-periodic PBG-W structures. The consistency and periodicity could serve as a useful "hot" diagnostic to the construction of the devices and any degradation they could experience in use and thus it may not be desirable to mitigate these, only filter it from the final output.

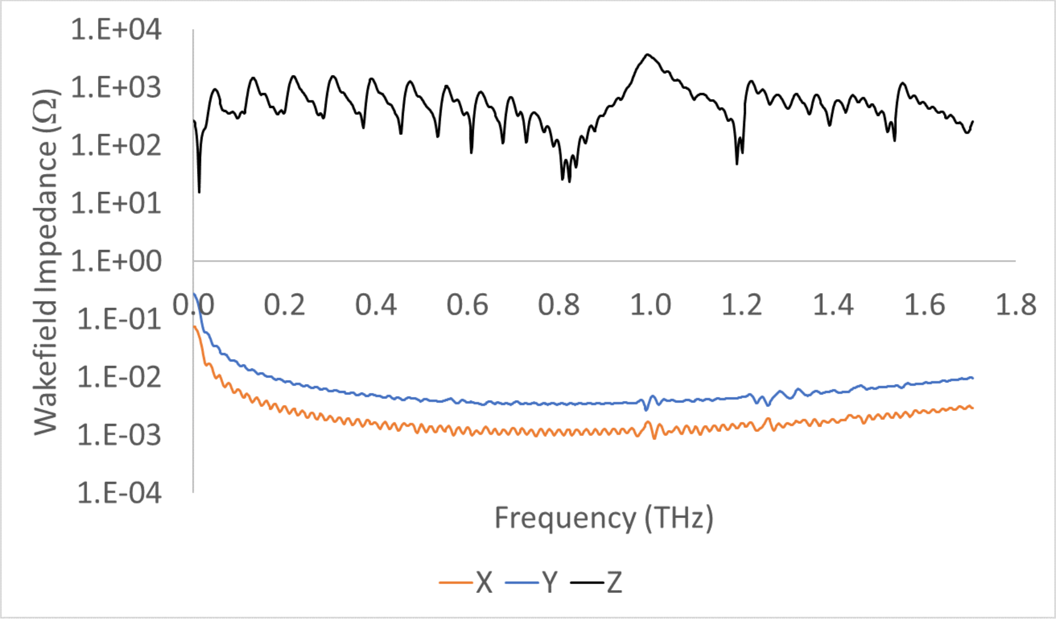

Figure 6.7: 1D-Periodic PBG-W longitudinal and transverse wakefield impedance.

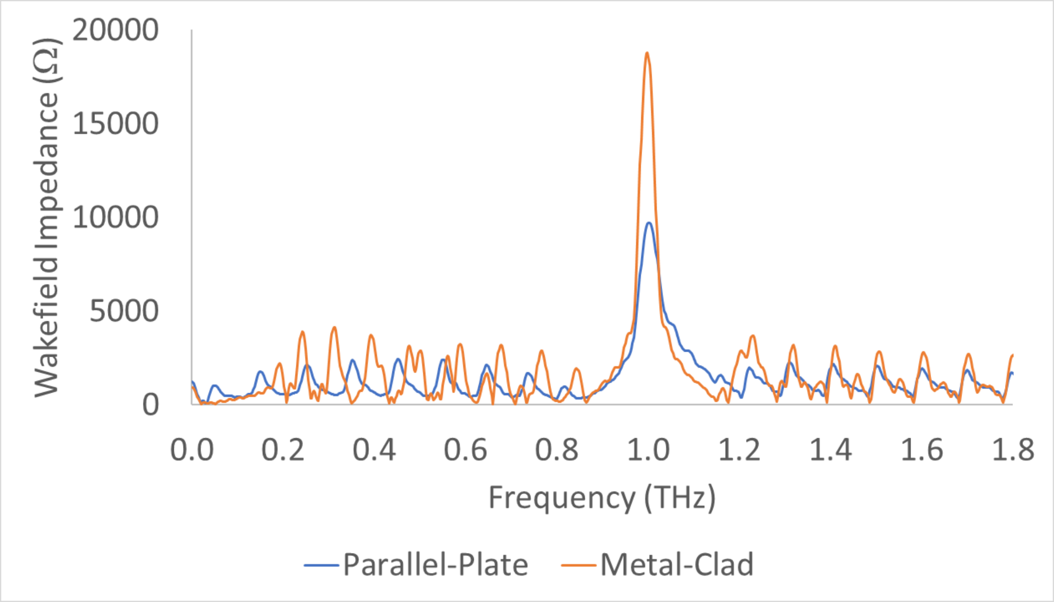

Figure 6.8: Comparison of longitudinal wakefields in parallel-plate, and metal-clad Bragg PBG-Ws.

### 6.1.3 PIC Simulations

The wakefield solver is good for examining the resultant fields from an exciting charge. It however does not provide any information related to transverse beam shape, nor any information about the beam itself. The PIC solver operates by launching defined charge-mass “macro-particles” from an emission surface with a defined energy, and solving for the Lorentz equation (Eqn. 4.1) and the equations of motion to calculate particle trajectory. Examining the behaviour of the structure using a PIC solver allows to extract some information about the beam, as well as providing a “sanity check” for the wakefield results. The same $Q = 105\,pC$, $\sigma = 60\,\mu m$ Gaussian beam was used, emitted from a $100\,\mu m$ diameter PEC surface located at $z = -300\,\mu m$. The beam energy is $60\,MeV \pm 0.1\%$. The excited **E** and **H** fields were extracted from the $x = 0$ and $y = 0$ planes at the time instant $t = 17\,ps$, the Lorentz force was calculated and normalised to the maximum decelerating force at the bunch. The force component plots obtained for the metal-clad and parallel-plate geometries in Figs. 6.9 and 6.10 respectively. From these figures, it can be noted that the trailing field is largely single-moded, and the deflecting field at the bunch is 54% of the magnitude of the decelerating force at the bunch. This result, coupled with the wakefield results, indicates the Bragg structure would be an effective narrowband radiator with less beam-breakup behaviour than conventional structures in which deflecting and decelerating forces are often found in a ratio of 1:1 (see section 6.4 for more detailed analysis on the comparative DLW structure).

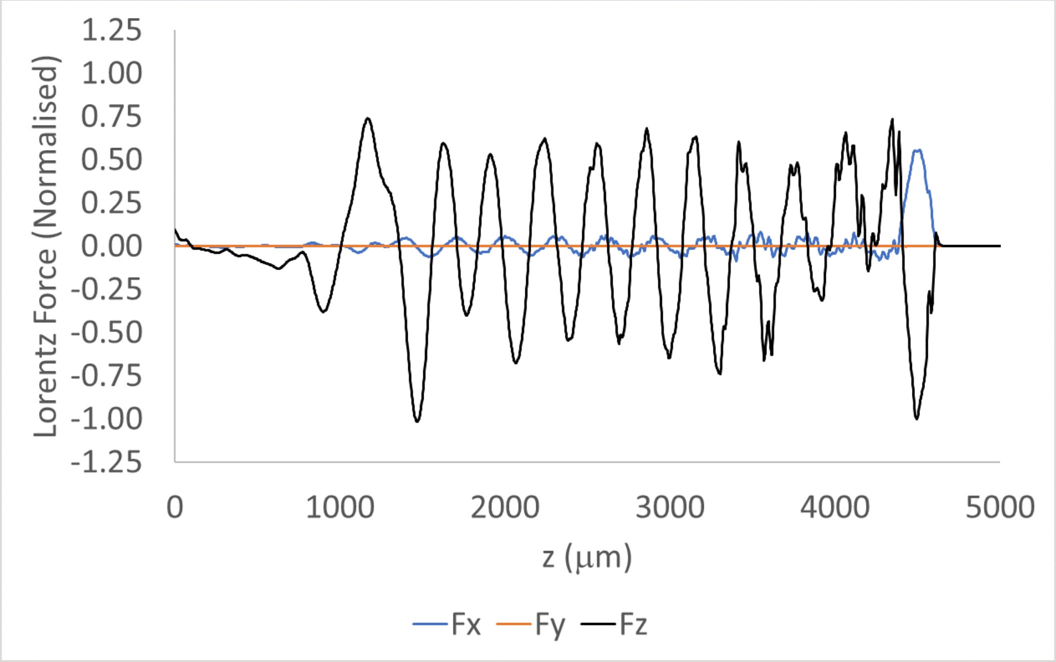

Figure 6.9: Lorentz forces in metal-clad Bragg PBG-W when driven by a $\sigma = 60\,\mu m$, $60\,MeV$, $Q = 105\,pC$ Gaussian beam.

The Bragg structure would however be less applicable in a two-bunch wakefield-acceleration regime, as at no point within the drive-bunch's wake does it offer close to the theoretical 2:1 that the metallic-based designs approach. The $F_z$ at $z \sim 1500\,\mu m$ is increased over the expected force due to reflection from the metallic boundaries and is not a function of the PhC itself, as shown in section 6.3. This result however may offer some benefit as tuning the layer-count may improve the intensity of the field at this region. The number of wavelengths trailing the drive bunch is equal to the number of layers in the Bragg design, increasing or reducing the number of Bragg layers could allow to tune for transformer ratio for beam-driven acceleration applications.

When CST creates a particle beam, this particle beam is launched with zero emittance. Studying the emittance growth of the beam through the structure

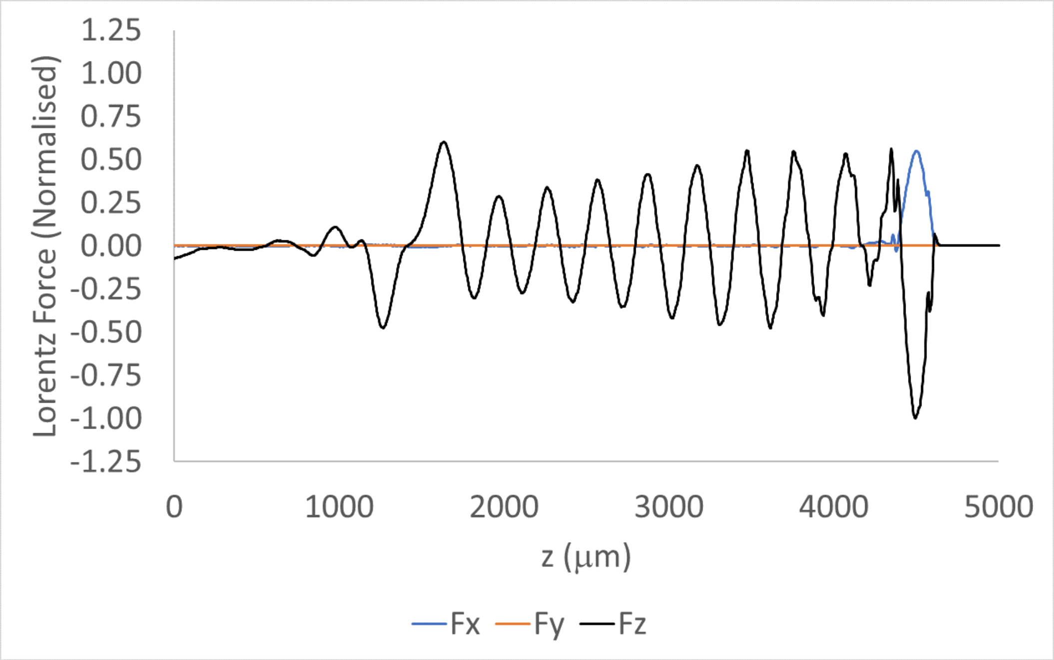

Figure 6.10: Lorentz forces in parallel-plate Bragg PBG-W when driven by a $\sigma = 60\,\mu m$, $60\,MeV$, $Q = 105\,pC$ Gaussian beam.

without prior emittance knowledge of the beam yields the expected result that the beam will diverge as it propagates, but a $\epsilon = 0$ beam is not physical. The energy profile of the bunch as it propagates through the structure is also investigated, and from this the average energy lost to the structure can be calculated. Examining the energy of the bunch in the metal-clad Bragg structure in Fig. 6.11, the bunch can be seen to lose $23.8\,keV/mm$ to the structure, or $0.12\,MeV$ in the $5\,mm$ length PBG-W.

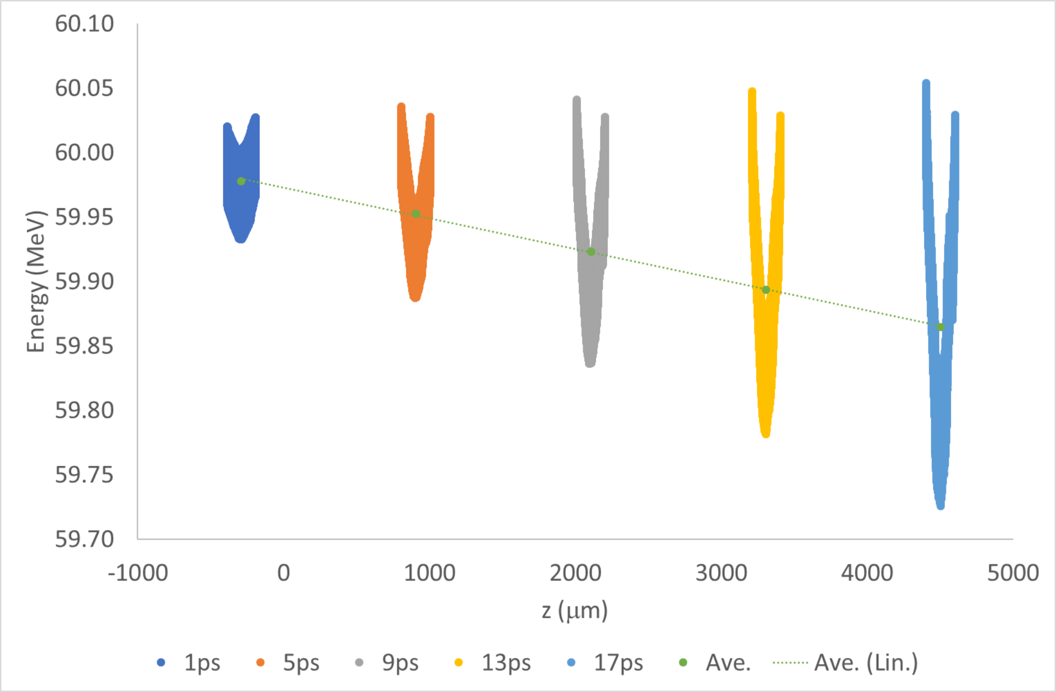

Figure 6.11: Beam energy as the bunch propagates along Bragg waveguide, showing an average energy loss of $23.8\,keV/mm$. The PBG-W being $x = 0 - 5000\,\mu m$ and the negative $x$-axis region being vacuum propagation from the emitting surface.

## 6.2 Wakefields in Triangular Lattice Based PBG-Ws

### 6.2.1 Metal-Clad PBG-W

To investigate the performance of a beam-driven triangular lattice based PBG-W, the waveguide developed in chapter 5 and shown in Fig. 6.12 served as an ideal candidate as it was already optimised for excitation of an accelerating mode—with the bandgap centred on $1\,THz$ and the pad-layer selected such that $v_p/c = 1$ thus the mode was excited by the beam.

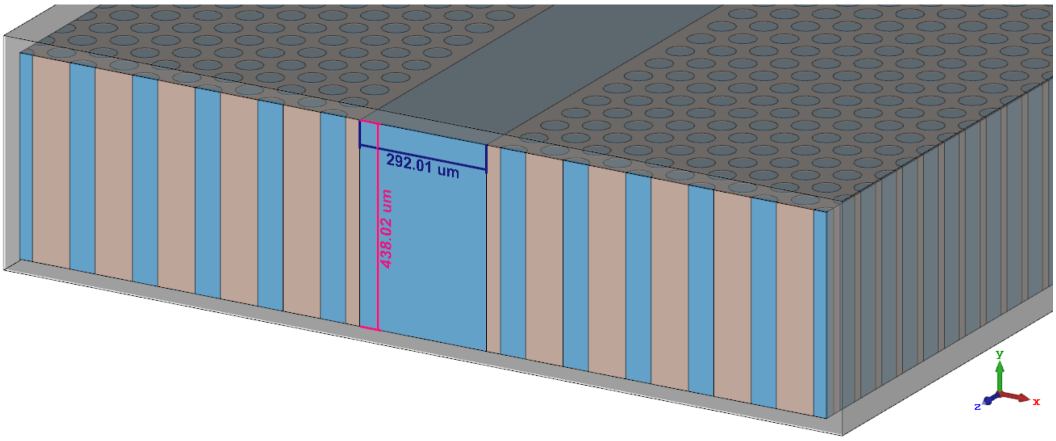

Figure 6.12: 2D-PBG waveguide designed for $1\,THz$ operation, with $3.5a$ separation and $7a$ width, where $a = 83.43\,\mu m$ and pad layer such that $v_p/c = 1$ at $1\,THz$. Length in $z$-axis is $5\,mm \pm a$ such that it is an integer number of photonic periods. Transparent grey is the metallic cladding of the PBG-W.

Examining the longitudinal wakefield results in Fig. 6.13 it can be noted that this design is not as monochromatic as the 1D Bragg structure, with additional modes excited at $\sim 1.2\,THz$ and $\sim 1.55\,THz$, the latter of which is outside the primary photonic bandgap and is likely present in a higher bandgap of the photonic crystal. Two further modes are excited between $0.2 - 0.4\,THz$ however do not belong to a photonic bandgap and are likely artefacts from the metal boundary condition imposed on the simulations in the $x$-direction; which outside the photonic-bandgap will closely resemble a dielectric-lined waveguide with thick dielectric layer.

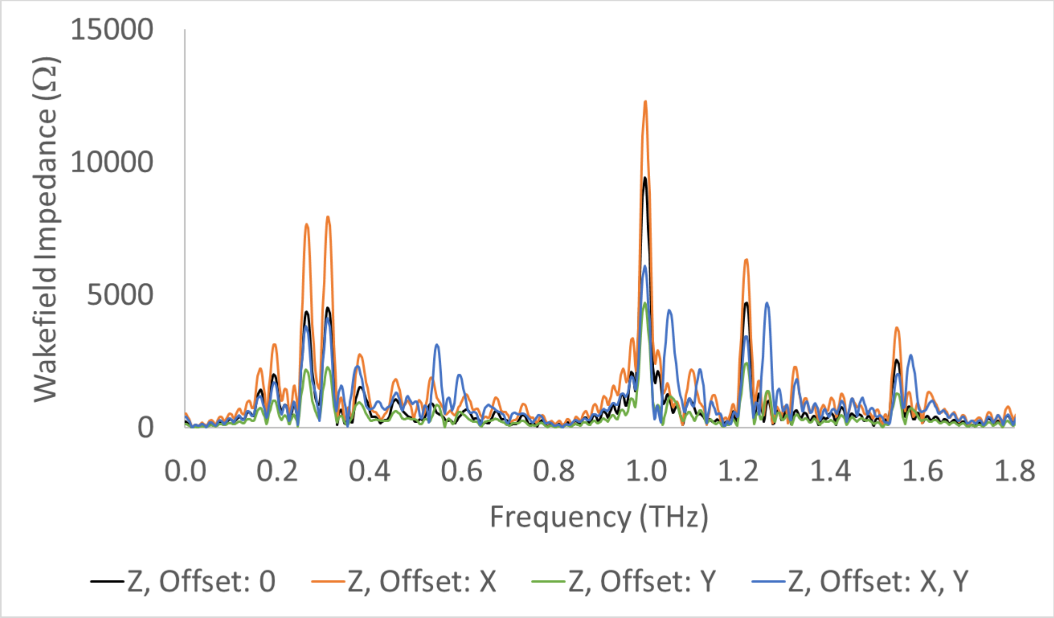

Figure 6.13: 2D-Periodic PBG-W longitudinal wakefield impedance for beam with no offset; quarter-channel offset in $x$; quarter-thickness offset in $y$; and combined offset in $x$ and $y$.

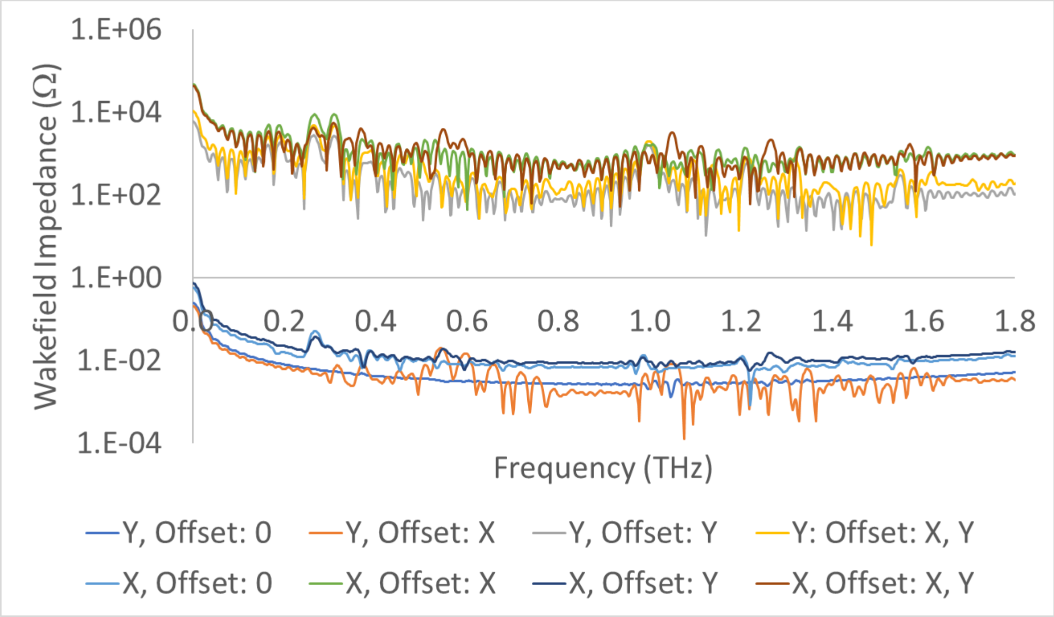

Figure 6.14: 2D-Periodic PBG-W transverse wakefield impedance for beam with no offset; quarter-channel offset in $x$; quarter-thickness offset in $y$; and combined offset in $x$ and $y$.

The transverse wakefield results shown in 6.14 show a similar response as the 1D Bragg structure as there is negligible impedance in transverse modes until the beam experiences an offset. The main two modes excited by this offset are the artefact modes between $0.2 - 0.4THz$. The only potentially undesirable mode

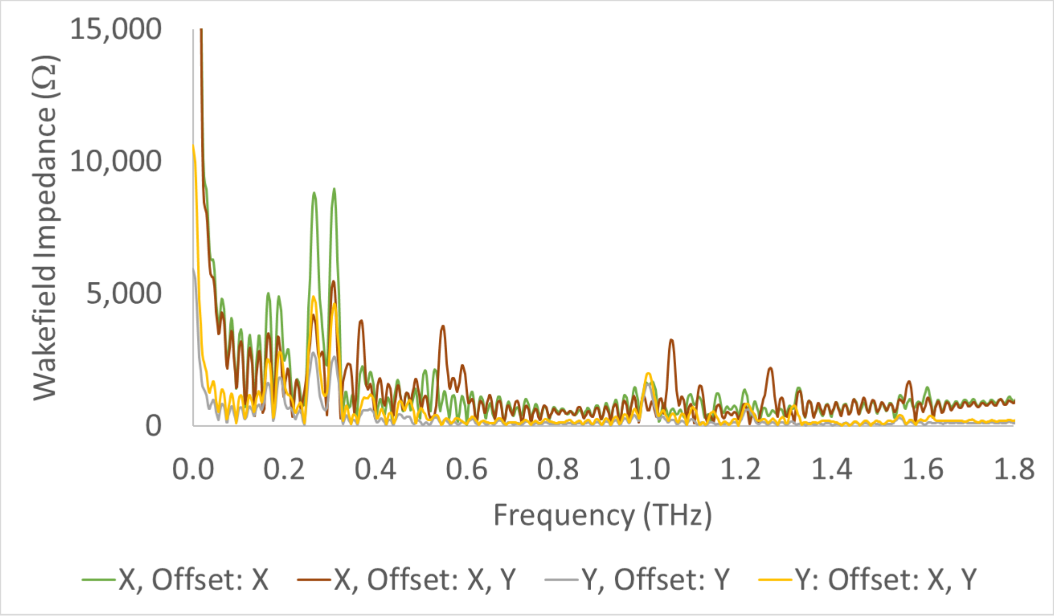

Figure 6.15: 2D-Periodic PBG-W transverse wakefield impedance linear plot for non-trivial impedances shown in Fig. 6.14.

excited transversely occurs at $\sim 1.05\,THz$, shown in Fig. 6.15, however this appears with any non-negligible impedance when the beam has a transverse offset in both axes and offers a potential diagnostic tool for determining if the beam is offset and requiring realignment.

### 6.2.2 Unclad 2D PBG Waveguide

The case of the unclad 2D PBG waveguide resembling the parallel plate waveguide configuration is discussed in this section. For this design, being large in the $y$-dimensions, the pad-layer was re-tuned so that $v_p/c = 1$ at $f_0 = 1\,THz$ as in the case in chapter 5. The longitudinal and transverse wakefield impedances can be seen in Fig. 6.16 showing negligible transverse impedances. From Fig. 6.17 it can be seen that in this 2D PBG-W, the impedance of the desired mode is found to be 38% of the impedance of the metal-clad waveguide, compared to the Bragg structure in which the open boundary had 52% impedance of the metal-clad structure at $f_0$. Furthermore, the resonance also present in metal-clad structure between $0 - 0.8\,THz$ did not experience the same attenuation seen at the desired peak at $f_0$. This ripple is likely related to the periodicity of the photonic crystal and as such will be present in all triangular-lattice 2D-periodic PBG-Ws. The lack of this resonance at the higher frequencies, combined with the lack of layers as in the 1D-periodic Bragg structure however make this unlikely to be a Fabry-Perot resonance.

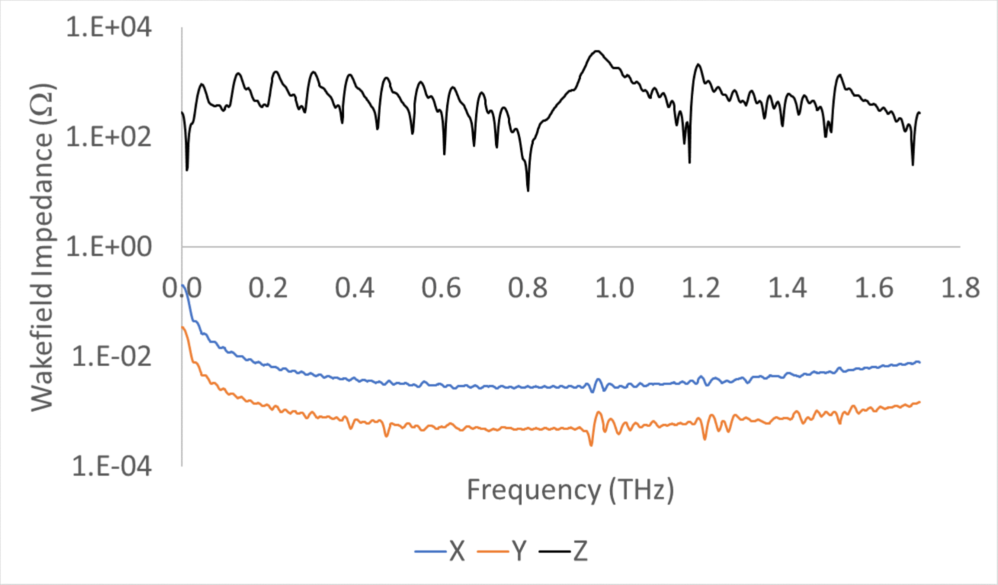

Figure 6.16: Longitudinal and transverse wakefield impedances in parallel-plate 2D-Periodic PBG-W.

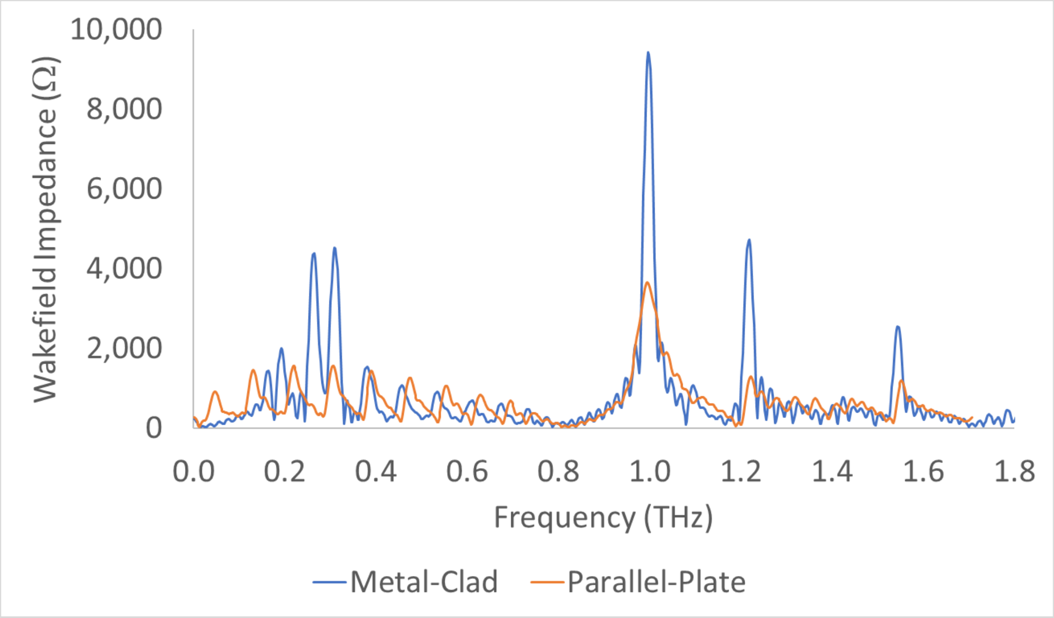

Figure 6.17: Comparison of longitudinal wakefields in unclad and metal-clad 2D PBG-Ws.

### 6.2.3 PIC Simulations

Following the same procedure as in the case of the Bragg based waveguide, PIC simulations were performed with a Gaussian beam of $Q = 105\,pC$, $\sigma = 60\,\mu m$ emitted from a $100\,\mu m$ diameter PEC surface at $z = -300\,\mu m$. The beam energy is $60\,MeV \pm 0.1\%$. The **E** and **H** fields were extracted from the $x = 0$ and $y = 0$ planes when $t = 17\,ps$, the Lorentz force was calculated via $\mathbf{F} = q(\mathbf{E} + \mathbf{v} \times \mathbf{B})$, and normalised to the maximum decelerating force at the bunch. The force component plots for the metal-clad and parallel-plate geometries are shown in Figs. 6.18 and 6.19 respectively. It can be seen that the longitudinal Lorentz force contains multiple frequencies—which is expected from the wakefield impedance plots from the previous subsections—and that the transformer ratio is less than 1:1. Examining the deflecting force generated by this structure however it can be seen that the ratio of longitudinal to deflecting force is greater than 1:1—which for acceleration and CCR source applications is typically a disadvantage. This structure could however be applicable as a wakefield streaking device [167]. These devices, often longitudinally periodic, are designed to generate transverse modes in which the profile is known such that the temporal profile of the propagating beam can be extracted. The larger deflecting force coupled with a narrowband transverse mode excitation when the beam is offset makes this structure suitable for this application, and both the metal-clad and unclad structures offer this increased longitudinal/transverse force ratio.

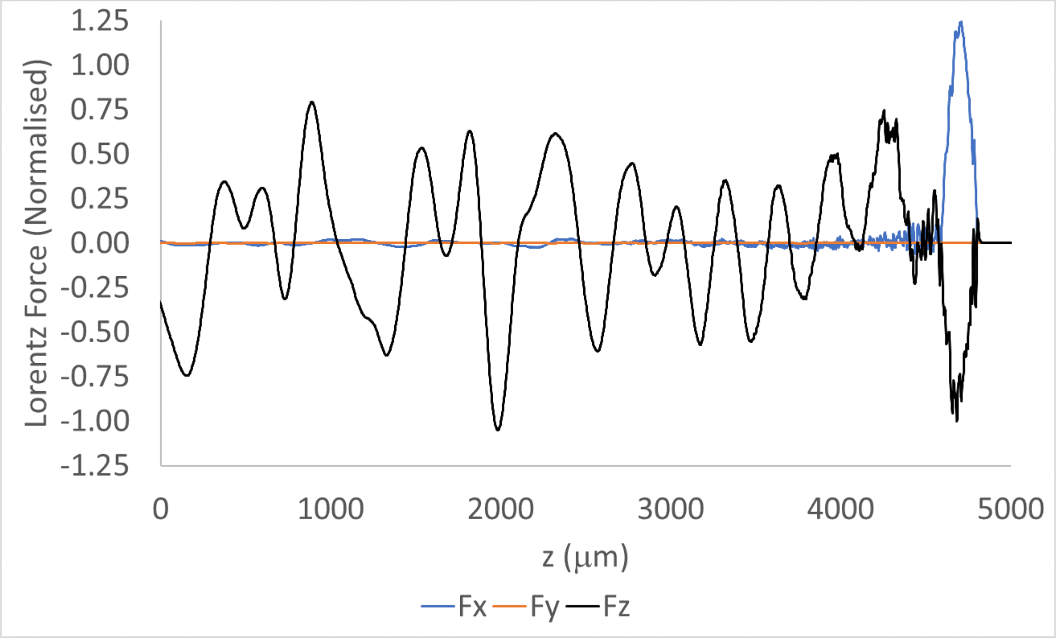

Figure 6.18: Longitudinal force in metal-clad 2D-periodic PBG-W when driven by a $\sigma = 60\,\mu m$, $60\,MeV$, $105\,pC$ Gaussian beam. Results normalised to largest decelerating force in the region of the beam.

Due to the thin-wire approximation the wakefield solver makes, the transverse forces are often $2-3$ orders of magnitude greater than what is calculated by the PIC solver. The longitudinal forces however are typically well approximated by the former. To validate these results, a comparison between the longitudinal force generated by wakefield and PIC solvers was performed. This comparison, shown in Fig. 6.20, shows the forces generated are similar in amplitude. While the PIC generates a jagged electric field which may be a mesh issue similar to that which is discussed later in section 6.2.5. Initially the trend follows that of the wakefield solver closely. Within $500\,\mu m$ however the amplitudes begin to deviate and by $2000\,\mu m$ behind the bunch the fields are entirely different. This deviation shows that both the wakefield and PIC solvers are required to obtain a full understanding of the performance of a beam-driven wakefield waveguide.

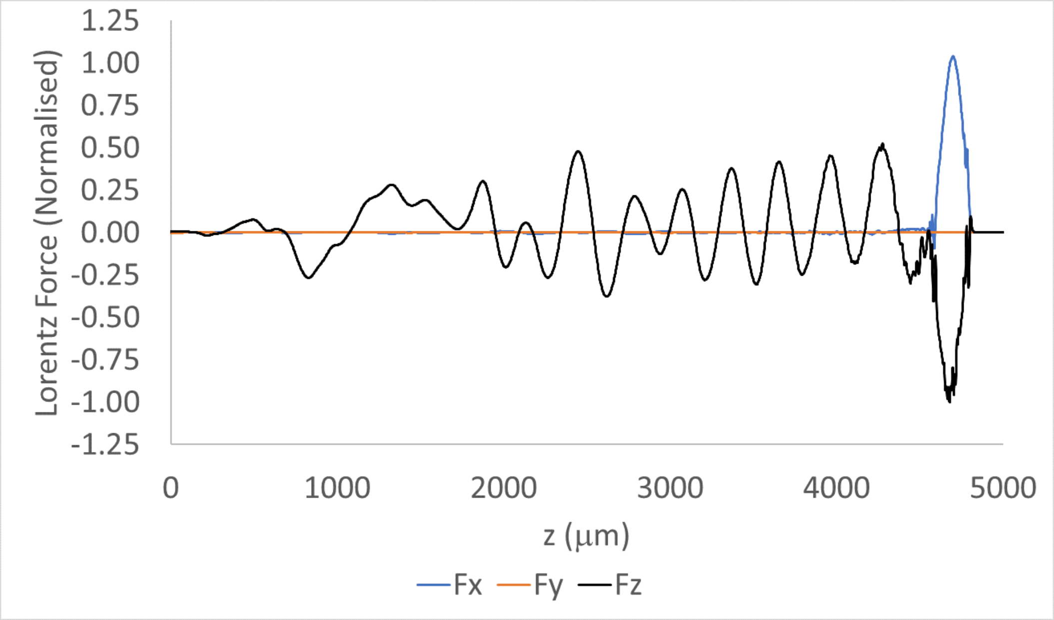

Figure 6.19: Longitudinal force in parallel-plate 2D-periodic PBG-W when driven by a $\sigma = 60\,\mu m$, $60\,MeV$, $105\,pC$ Gaussian beam. Results normalised to largest decelerating force in the region of the beam.

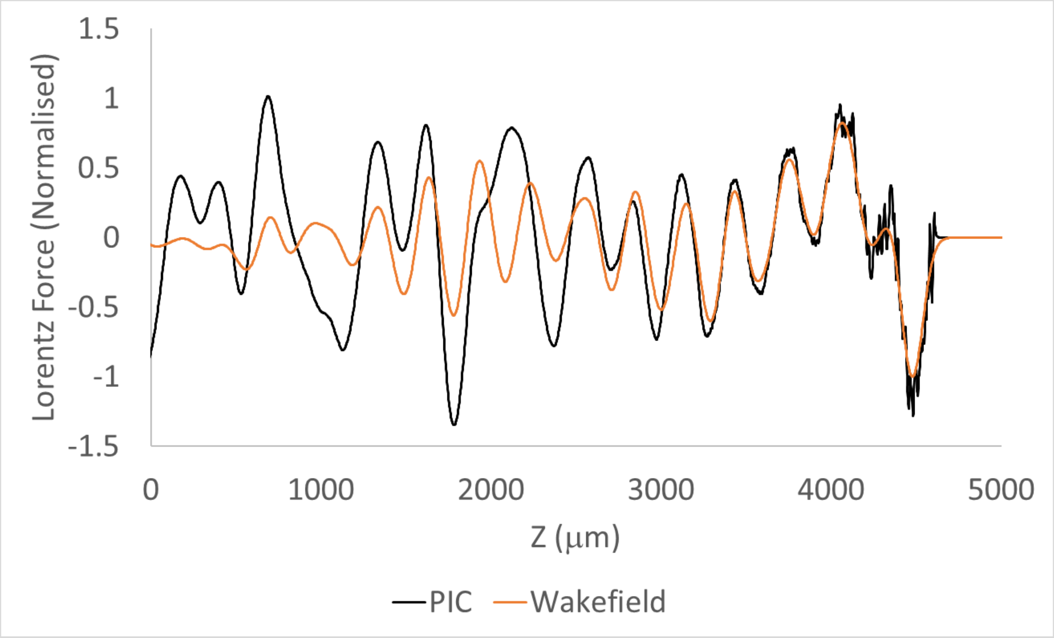

Figure 6.20: Comparison of longitudinal force in a metal-clad 2D-PBG as calculated by wakefield and PIC solvers for $\sigma = 60\,\mu m$, $60\,MeV$, $105\,pC$ Gaussian beam. Results normalised to largest decelerating force in the region of the beam for wakefield solver.

The energy of the beam was again plotted as a function of propagation along $z$ in the metal-clad 2D PBG-W, shown in Fig. 6.21. In this case, the tail of the bunch was not accelerated as in the 1D-periodic structure and the whole beam lost energy to the structure. The rate of energy loss was 12.3 $keV/mm$, or 0.06 $MeV$ in the 5 $mm$ waveguide.

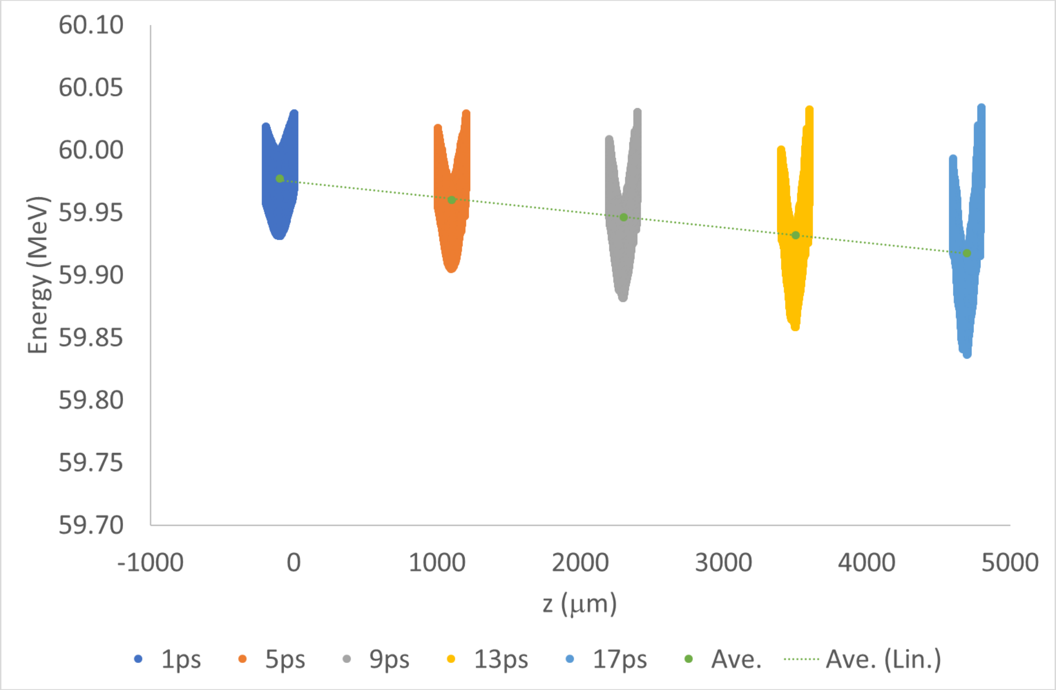

Figure 6.21: Beam energy as it propagates along 2D-periodic structure, showing an average energy loss of 12.3 $keV/mm$. The PBG-W being $x = 0 - 5000\,\mu m$ and the negative $x$-axis region being vacuum propagation from the emitting surface.

### 6.2.4 Tunability

The narrowband nature of the 2D PBG-W as demonstrated thus far makes it suitable for a narrowband CCR source. Tunability is typically a specification of these sources.

The metal-clad 2D-periodic waveguide investigated in this section has many fixed parameters that cannot be varied, such as pad-layer and slab thickness. The channel however is not as such fixed and can be varied. The channel was varied between 0.8× and 1.2× the design width in the $x$-direction and the wakefield impedance obtained. Shown in Fig. 6.22, the parametric study shows the desired frequency is tunable as are the higher order modes. The lower-frequency peaks are invariant with channel confirming they are not propagating modes of the waveguide and more likely an artefact of boundary conditions. A closer examination of the

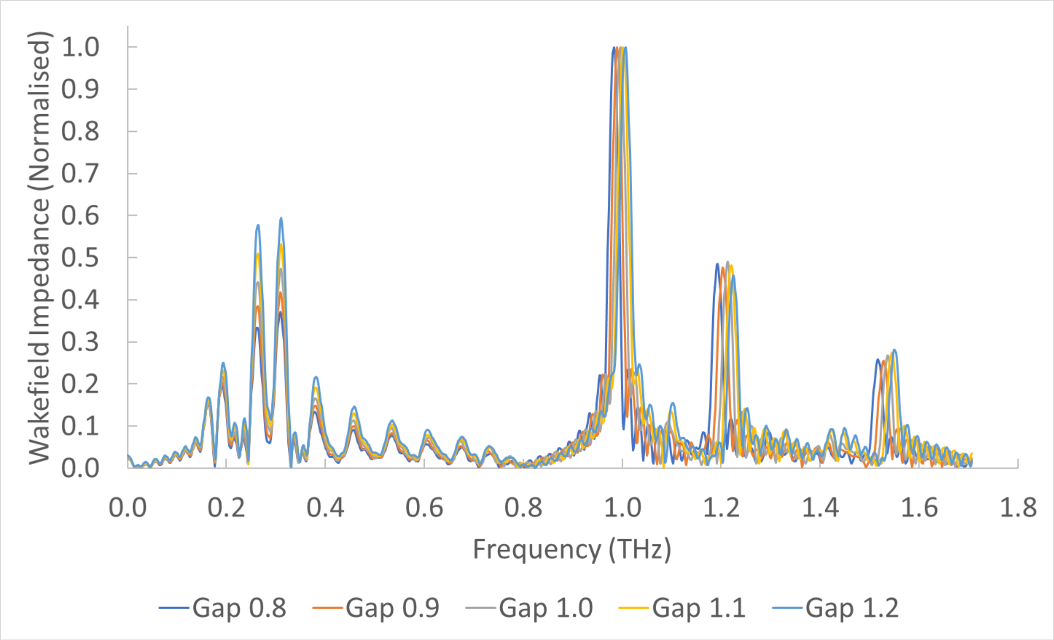

Figure 6.22: Wakefield impedance spectrum for 2D-periodic PBG-W when changing the vacuum-channel aperture between 0.8 and 1.2 design width.

operation frequency in Fig. 6.23 shows the modes have a FWHM of $30\,GHz$ and a tunable range of $40\,GHz$. The higher-order modes also showing tunability allows this structure to have a discontinuous operational range of $500\,GHz$. This structure was however not designed for tunability and a different approach to design may improve its performance.

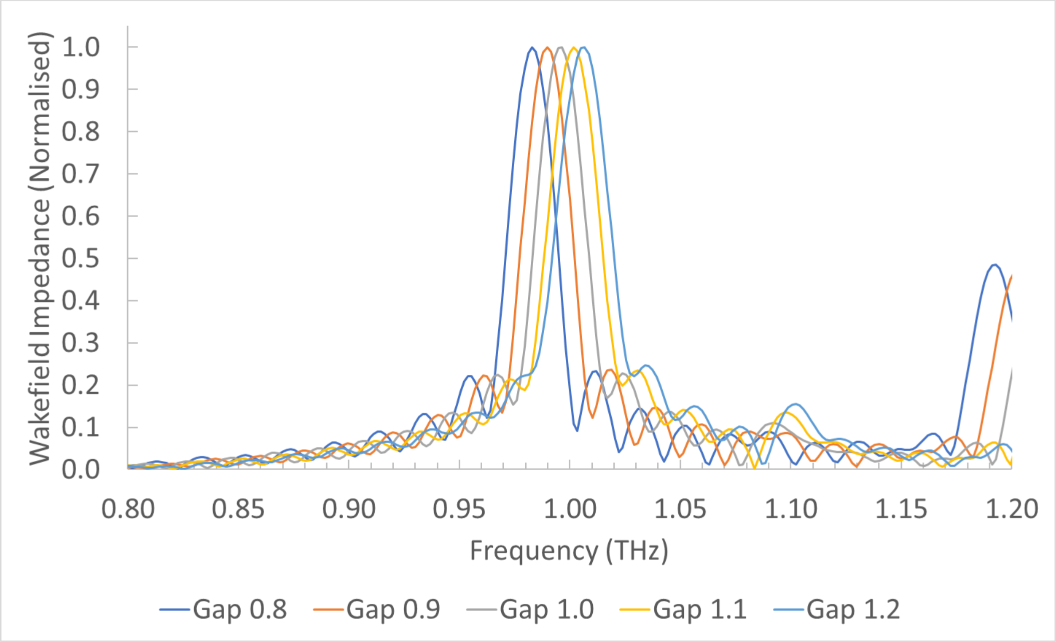

Figure 6.23: Wakefield impedance spectrum for 2D-periodic PBG-W when changing the vacuum-channel aperture between 0.8 and 1.2 times design width, with focus on $0.8 - 1.2\,THz$ region.

### 6.2.5 Anomalous Fields in Wakefield Simulations

When performing wakefield simulations in CST, it was found that standard hexahedral meshing with analytic injection caused numerical errors in the $E_z$ fields within the region of the beam self-field. An example of this can be seen in figure 6.24, with spacing between two peaks of $33\,\mu m$. As neither tetrahedral meshes nor subgridding are an option for wakefield simulations, the mesh density at any point in the structure is related to the complexity of the geometry on any axis to that point; such as a small face will generate a high mesh density in the full extent of the $x$, $y$, and $z$ axes surrounding it. This leads to inhomogeneous meshing as shown in Fig. 6.25, where the mesh density is linked to the complexity at the edge of the cylinders. The dimensions illustrated in this figure illustrate the spacings between high mesh density regions, and also the photonic crystal period. These high density regions are caused by the mesh resolving the narrow faces at the edge of the vacuum cylinders. The spacing between high mesh density regions in Fig. 6.25 can be seen to be related to the spurious peaks in Fig. 6.24.

A partial solution to this problem is to use the transmission-line method of current injection as this is more robust in the face of inhomogeneous meshes. Another approach is to use a homogeneous mesh; this approach was less preferred due to the conflict between coarse resolution of mesh at finer geometry points, or denser mesh across the full structure costing computation time. A disadvantage of the transmission-line method is it is only applicable for highly relativistic ($\beta > 0.999$) beams or the analytic injection must be used [122].

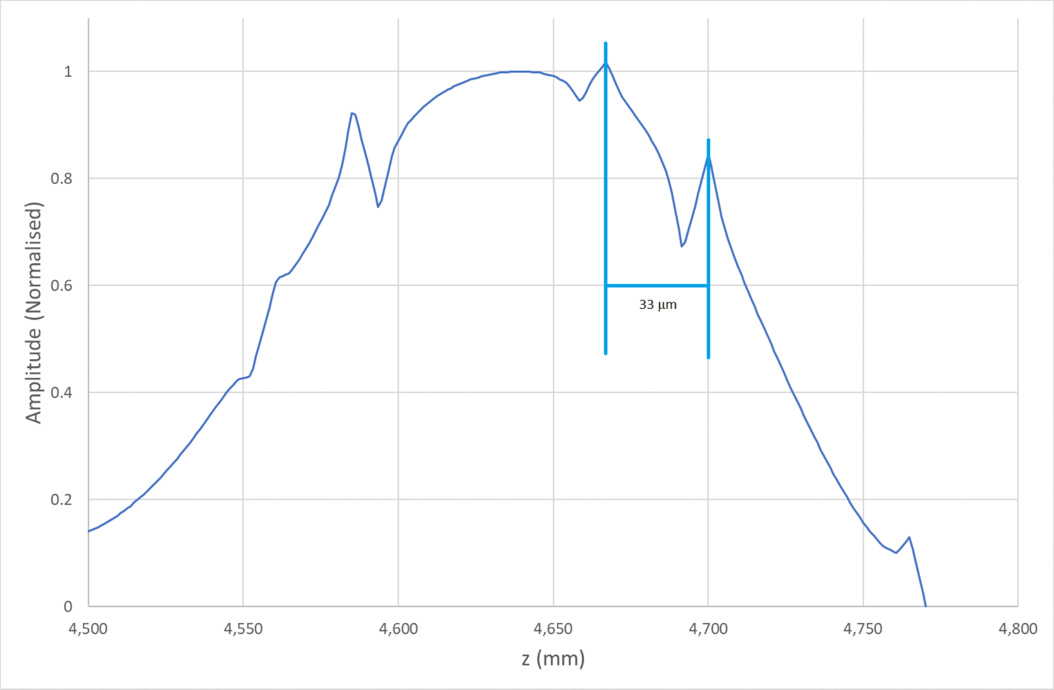

Figure 6.24: Example of anomalous fields at the driving beam in a wakefield simulation with inhomogeneous mesh using analytic beam injection.

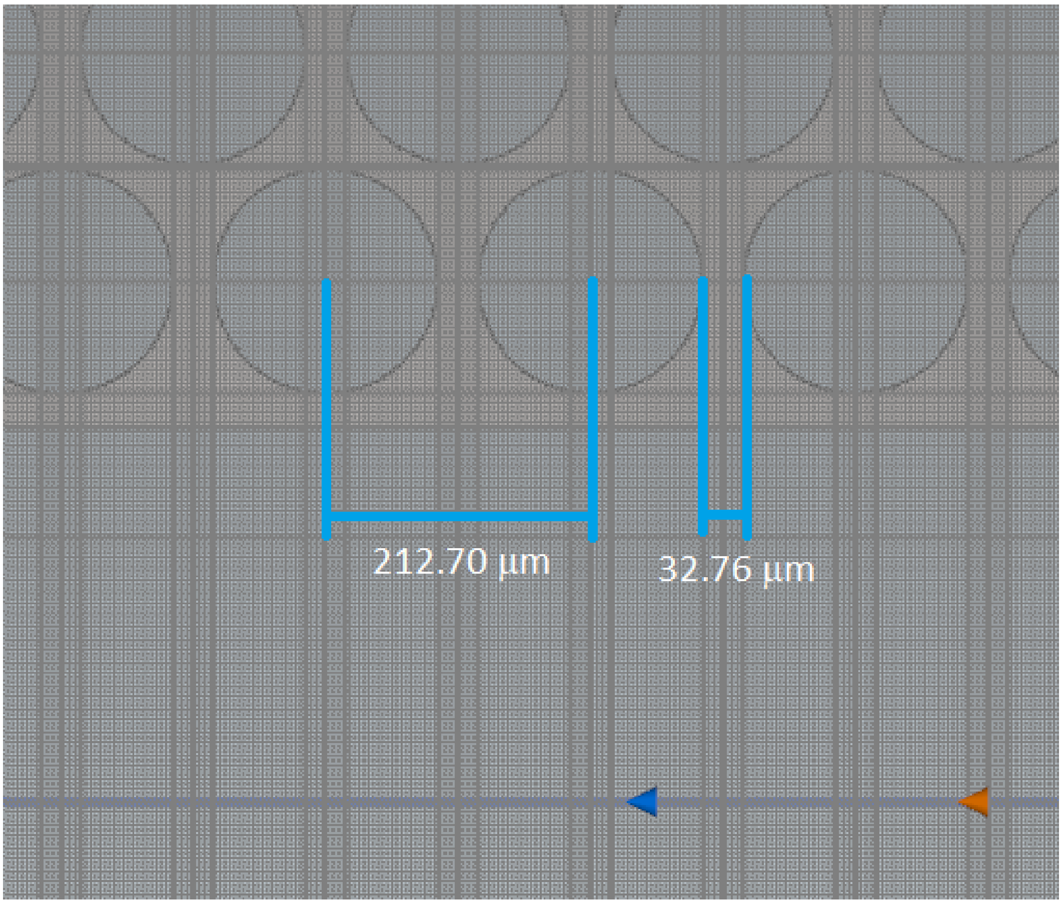

Figure 6.25: Mesh geometry which generates discontinuity.

## 6.3 Elliptical Beams

As discussed in [75], the use of a transversely elliptical beam instead of cylindrical can aid in mitigating undesired higher order modes in parallel-plate waveguide geometries. To investigate this for the PBG-Ws studied in this thesis, the models shown in sections 6.1.2 and 6.2.2 were re-simulated, where the emission surface was transformed from a cylindrical $\sigma_x/\sigma_y = 1$ surface to an elliptical one in which $\sigma_x/\sigma_y = 10$; where $\sigma_x$ and $\sigma_y$ is the transverse standard deviation of the beam in $x$ and $y$ directions respectively. Dimensions of the emitting surface are $D_x = 100\,\mu m$ and $D_y = 1000\,\mu m$, where these are the diameters of the ellipse in the $x$ and $y$ direction respectively. The other beam parameters are kept the same such that $Q = 105\,pC$, $E = 60\,MeV$. Emission points in each model were increased from approx. 1500 to approx. 4200. The structures were resolved with a mesh density of $7\,\lambda^{-1}$, with maximum simulated frequency $c/\lambda = 2\,THz$.

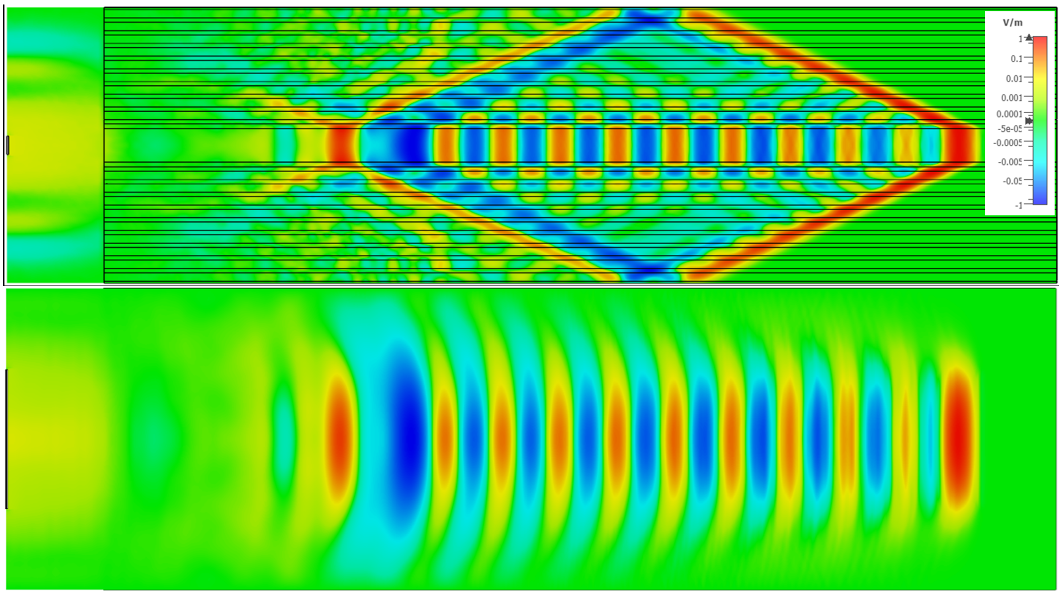

Figure 6.26: Longitudinal electric fields on $y = 0$ and $x = 0$ planes (top and bottom respectively) in the planar Bragg waveguide when excited by an elliptical $Q = 105\,pC$, $60\,MeV$ beam. Field amplitude normalised to maximum field amplitude.

We can see from Figs. 6.26 and 6.27 that the elliptical beam excites a single frequency wakefield with consistent amplitude for 9 wavelengths behind the drive bunch. The $10^{th}$ wavelength, at $z \approx 1500\,\mu m$ constructively interferes with the

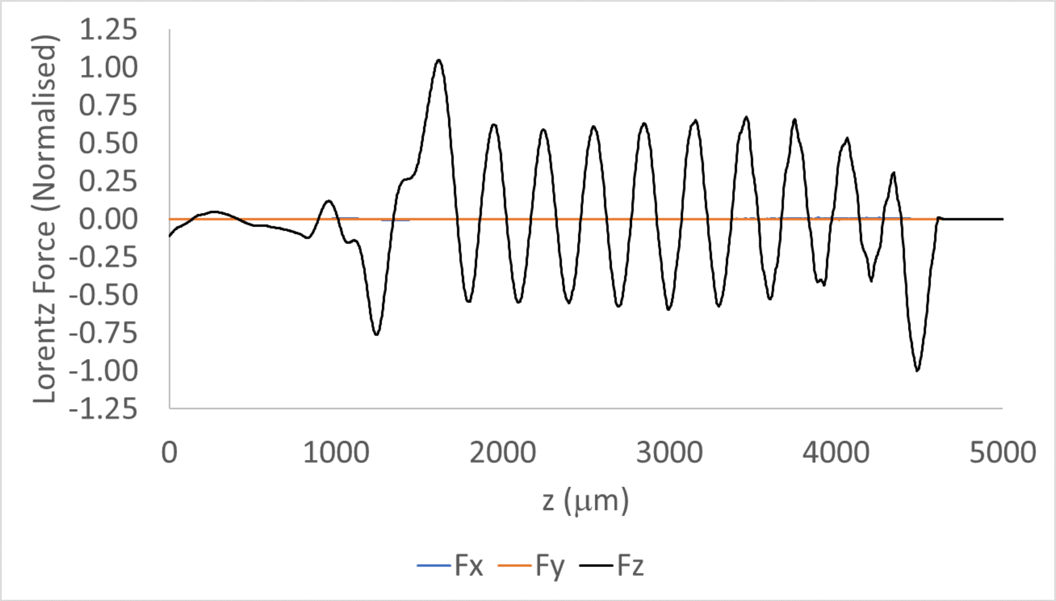

Figure 6.27: Longitudinal and transverse forces on the $x = y = 0$ axis in the planar Bragg waveguide, when excited by an elliptical $Q = 105\,pC$, $60\,MeV$ beam. Field amplitude normalised to the maximum decelerating force at the bunch.

reflection from the boundary of the simulation to produce a region in which the transformer ratio is 1:1.

As these simulations are computationally large, they are optimised to make use of the workstations Nvidia GPGPU card allowing highly parallelised calculation. This however requires the use of fully metallic boundaries to enable the calculation. Owing to the simplicity of the calculation required in the 1D PhC case compared to the 2D PhC case, an open-boundary design could be studied without the use of the GPGPU to determine the effects of the metallic boundary on the fields. The longitudinal field for the excitation in the open boundary structure, which can be seen in Fig. 6.28, shows a strong single-mode excitation similar to Fig. 6.26. The longitudinal force $F_z$ in Fig. 6.29 further illustrates this, with negligible transverse fields excited. Additionally, the higher $F_z$ region at $z \approx 1500\,\mu m$ is no longer present as the reflections from the metallic boundary have been mitigated. With this knowledge, the elliptical beam is simulated in the 2D PBG-W wrapped by metal boundaries. Figures 6.30 and 6.31 show the excited wakefield is not as single-moded as the Bragg based PBG-W, with the wakefield being a combination of 2-3 modes as expected from the study shown in Fig. 6.16. It is expected the implementation of the open boundaries along the $y$-axis would lower fields at $z \approx 1200\,\mu m$

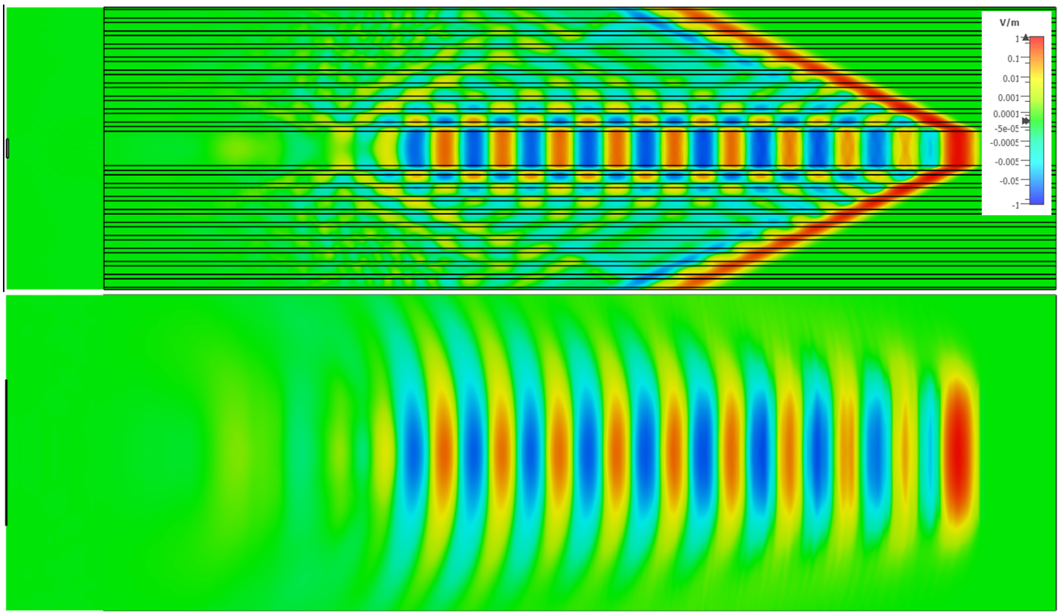

Figure 6.28: Longitudinal electric fields on $y = 0$ and $x = 0$ planes (top and bottom respectively) in planar open boundary Bragg waveguide when excited by elliptical $Q = 105\,pC$, $60\,MeV$ beam. Field amplitude normalised to maximum field amplitude.

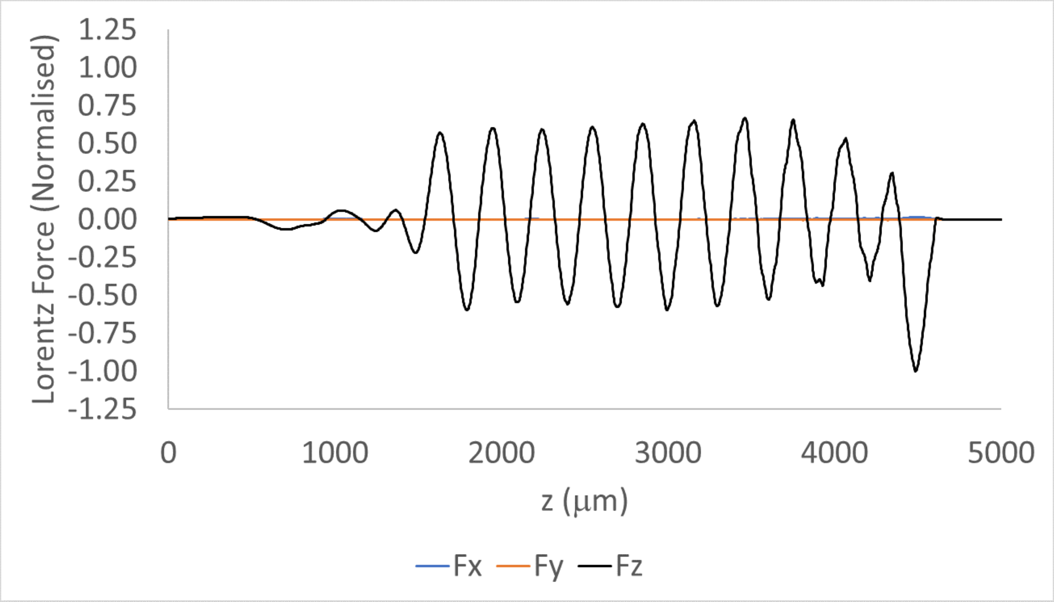

Figure 6.29: Longitudinal and transverse forces on the $x = y = 0$ axis in the open-boundary planar Bragg waveguide, when excited by an elliptical $Q = 105\,pC$, $60\,MeV$ beam. Field amplitude normalised to the maximum decelerating force at the bunch.

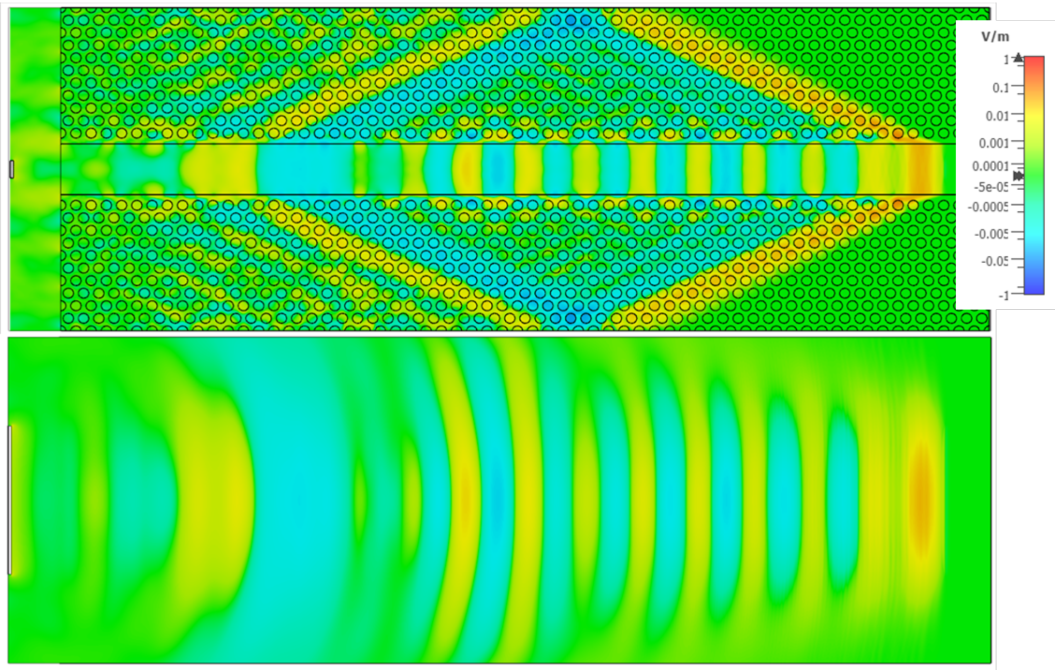

Figure 6.30: Longitudinal electric fields on $y = 0$ and $x = 0$ planes (top and bottom respectively) in the unclad triangular lattice based waveguide when excited by an elliptical $Q = 105\,pC$, $60\,MeV$ beam. Field amplitude normalised to maximum field amplitude.

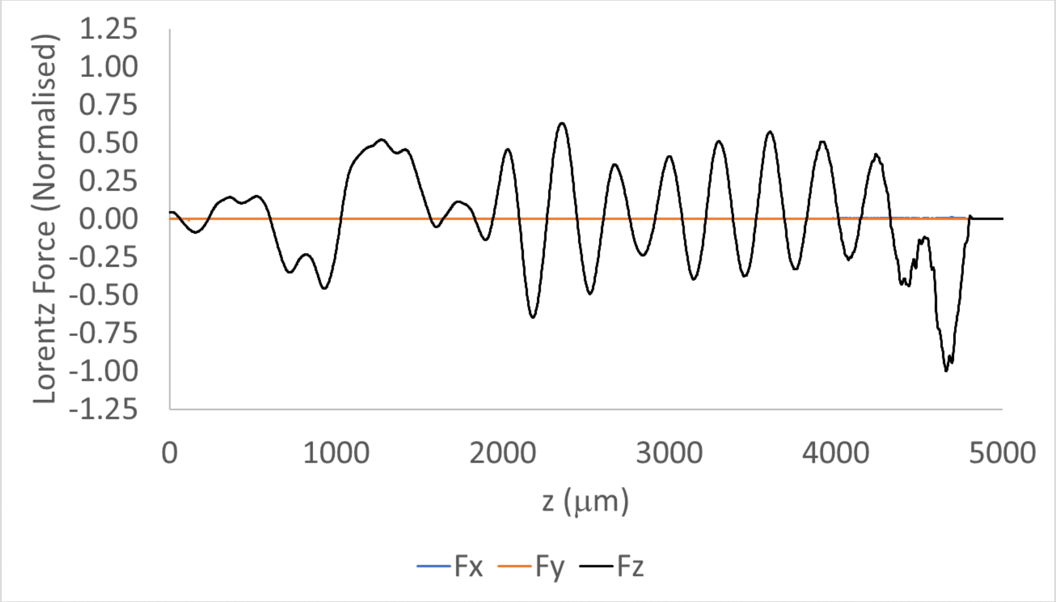

Figure 6.31: Longitudinal and transverse forces on the $x = y = 0$ axis in unclad triangular lattice based waveguide, when excited by an elliptical $Q = 105\,pC$, $60\,MeV$ beam. Field amplitude normalised to the maximum decelerating force at the bunch.

## 6.4 Comparison with Dielectric Lined Waveguide (DLW) Geometries

### 6.4.1 Wakefield studies in DLW

As in the previous chapter, the DLW is investigated for comparison with the proposed PBG-W technology. The schematic for the DLW is illustrated in Fig. 6.32. The waveguide dimensions are $300 \times 600\,\mu m$ with $25\,\mu m$ thick layers of quartz (silica) inserted to line the long edges; giving a vacuum aperture of $600 \times 250\,\mu m$. The full metal boundary DLW is analogous to the metal-clad PBG-Ws investigated. As before, a $Q = 105\,pC$, $\sigma = 60\,\mu m$, $60\,MeV$ Gaussian beam is injected in four positions: along the central axis; offset by a quarter width in $x$; offset by a quarter height in $y$; and with both $x$ and $y$ offsets.

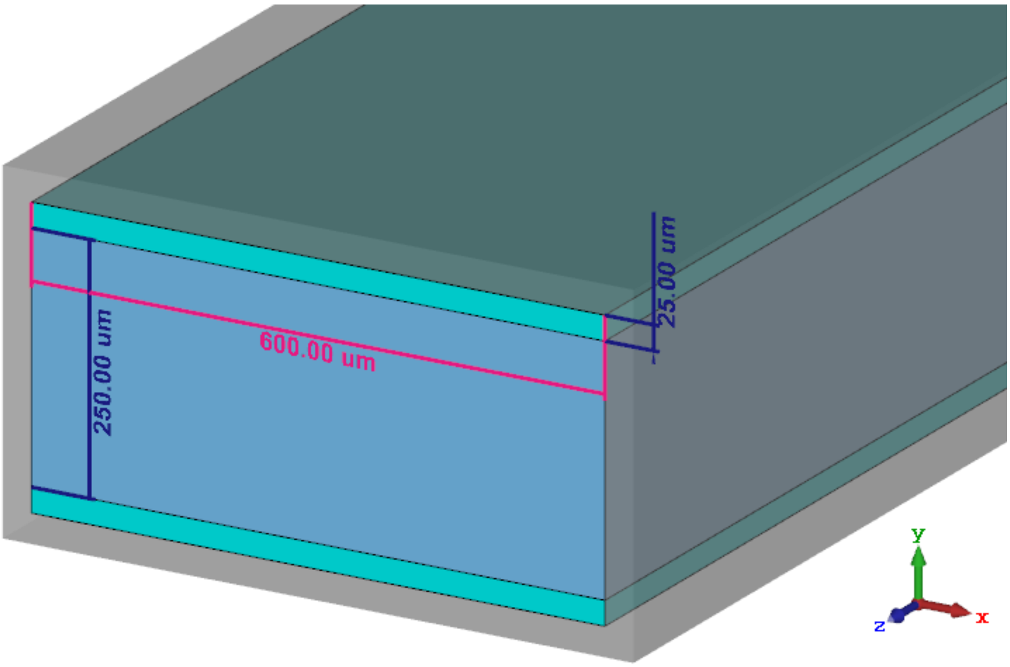

Figure 6.32: Schematic of DLW designed for $1\,THz$ operation, with $25\,\mu m$ silica lining on the major dimension of the waveguide. Length in $z$-axis is $5\,mm$. Cyan is the silica lining, blue is the vacuum, and transparent grey represents the metallic walls of the DLW.

Examining the longitudinal wakefield impedances generated by these offsets in Figs. 6.33, the no-offset beam has an impedance in similar magnitude to the 2D

PBG-W, however does not feature the sub-800 $GHz$ dielectric modes. The ripples at 1.25 $THz$ and 1.5 $THz$ are similarly present however at lower impedance to the 2D PBG-W. Offsetting the beam generates similar higher order modes at a higher impedance than the 2D-periodic structure with similar offsets.

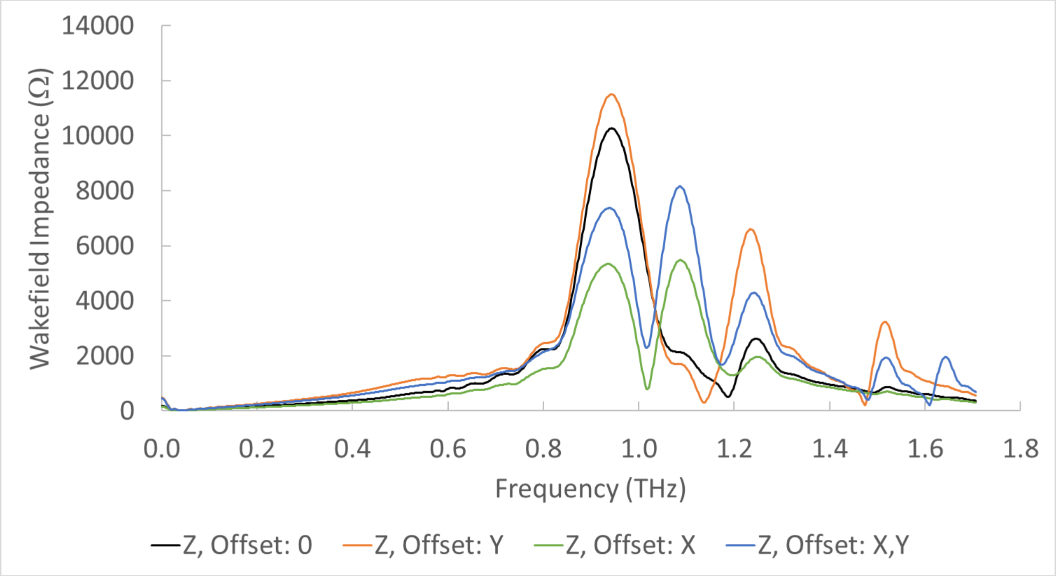

Figure 6.33: DLW longitudinal wakefield impedance for beam with no offset; quarter-channel offset in $x$; quarter-thickness offset in $y$; and combined offset in $x$ and $y$.

Similarly, the transverse impedances are shown in Figs. 6.34 and 6.35. From these figures, it can be see that a similar negligible impedance generated when the beam is centralised in the channel; additionally offsetting the beam towards the metal boundary generates little higher-order transverse modes. When the beam is offset towards the dielectric however it generates a continuous amplitude between $0.2 - 1.7\,THz$ in the range of $2\,k\Omega$, with higher impedance spikes at the same frequencies as the higher-order modes in the longitudinal spectrum.

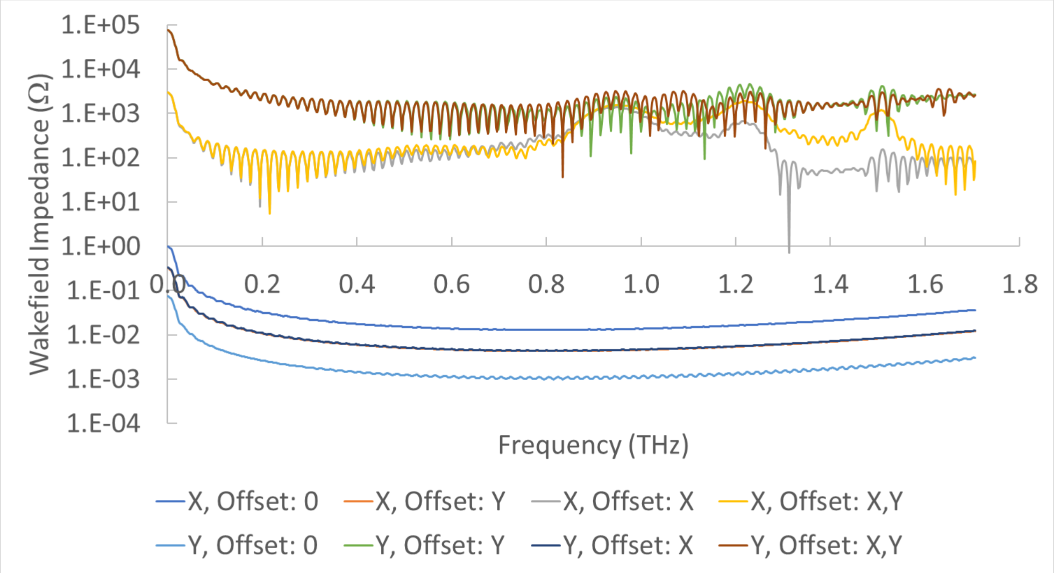

Figure 6.34: DLW transverse wakefield impedance for beam with no offset; quarter-channel offset in $x$; quarter-thickness offset in $y$; and combined offset in $x$ and $y$.

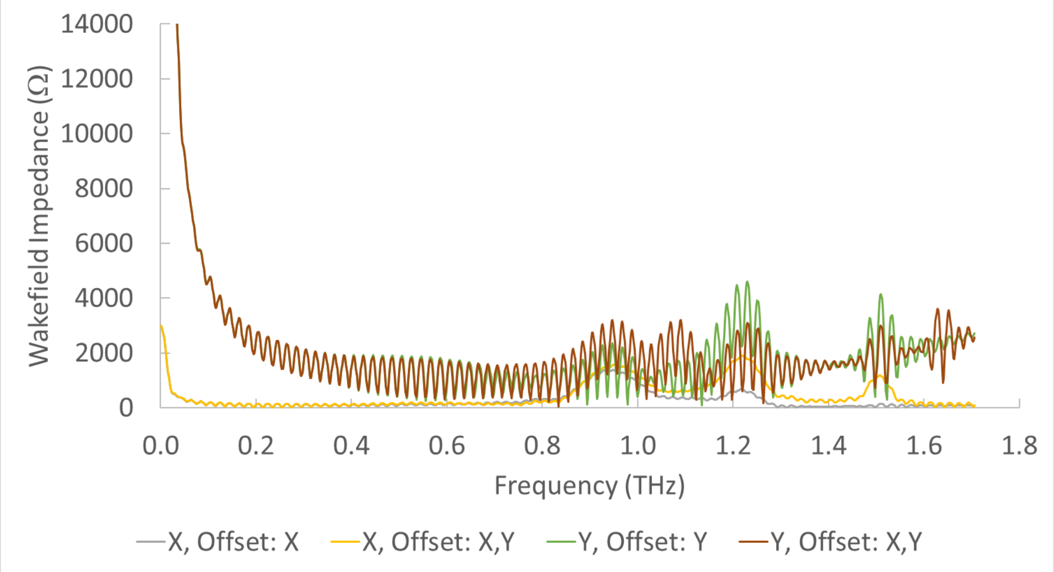

Figure 6.35: DLW transverse wakefield impedance linear plot for non-trivial impedances shown in Fig. 6.34.

### 6.4.2 Parallel-Plate DLW

The case for a parallel plate DLW is investigated in this section. The DLW was made wide, whilst preserving the parameters of the vacuum channel $C = 250\,\mu m$ and dielectric lining thickness $m = 25\,\mu m$. The longitudinal and transverse impedances for the parallel-plate DLW are shown in Fig. 6.36, and the longitudinal impedances are compared with the metal-wall case in Fig. 6.37. It can be noted that the parallel-plate design has a lower impedance as is common in all parallel-plate designs shown in this thesis—falling to 62% of the metal-clad design. It does however also detune from the desired central frequency while presenting a single-moded broadband design. Similar to the 1D Bragg based PBG-W, this could be applicable in CCR sources with the benefit of generating low levels of undesired frequencies, and this has been verified experimentally [82].

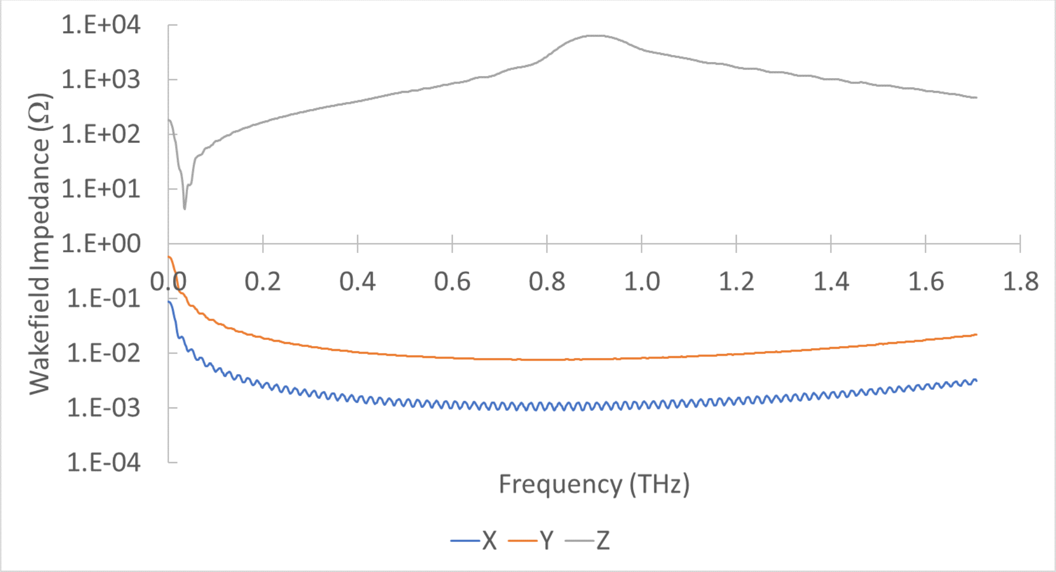

Figure 6.36: Longitudinal wakefield impedance in DLW at $x = y = 0$.

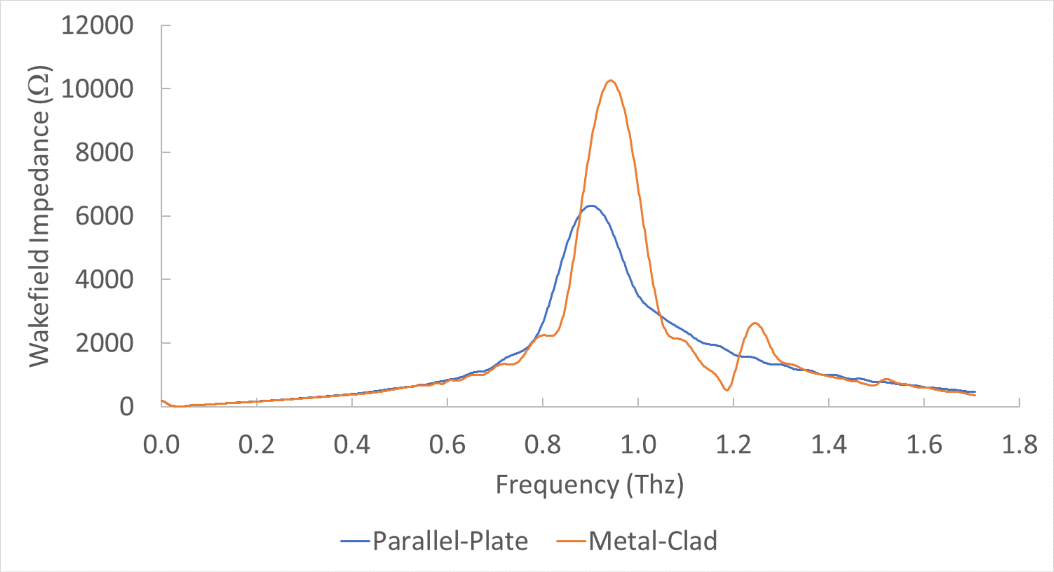

Figure 6.37: Comparison of longitudinal wakefields in parallel-plate, and metal-clad DLWs.

### 6.4.3 PIC Simulations in DLW

PIC simulations were then performed in the DLW using the $105\,pC$, $\sigma = 60\mu m$ bunch, the obtained longitudinal electric field after $17\,ps$ of propagation is shown in Fig. 6.38. The fields appear mostly single-moded with an amplitude variation indicating higher order modes, which correlates well with the wakefield models of the structure. Additionally, the normalised Lorentz forces plotted in Figs. 6.39 and 6.40 show a 1:1 ratio of longitudinal with deflecting forces at the beam. The DLW also is the only structure investigated which approaches the 2:1 transformer ratio for dual-bunch wakefield acceleration. This 1:1 force ratio coupled with the quadrupole modes excited by an offset beam has been investigated for application as a wakefield streaker [168].

Examining the energy loss by the beam to the metal boundary DLW is shown in Fig. 6.41. The evolution of the beam shows an average energy loss of $12.7\,keV$ to the structure. Additionally, the short-range wakefields in this structure serve to accelerate the tail of the bunch more than the photonic-crystal designs.

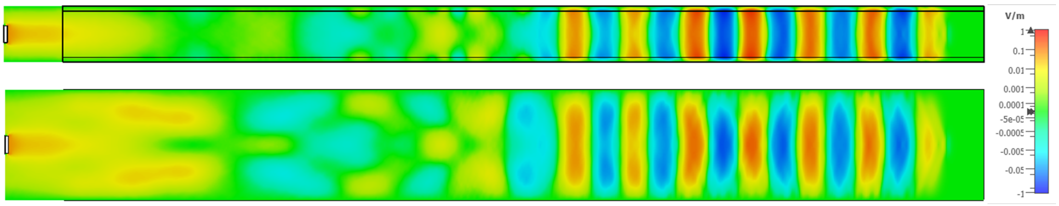

Figure 6.38: Longitudinal electric field in metal-clad DLW on $y = 0$ and $x = 0$ planes (top and bottom respectively) after 17 $ps$ beam propagation. The emission surface is on the left, with the beam propagating left to right.

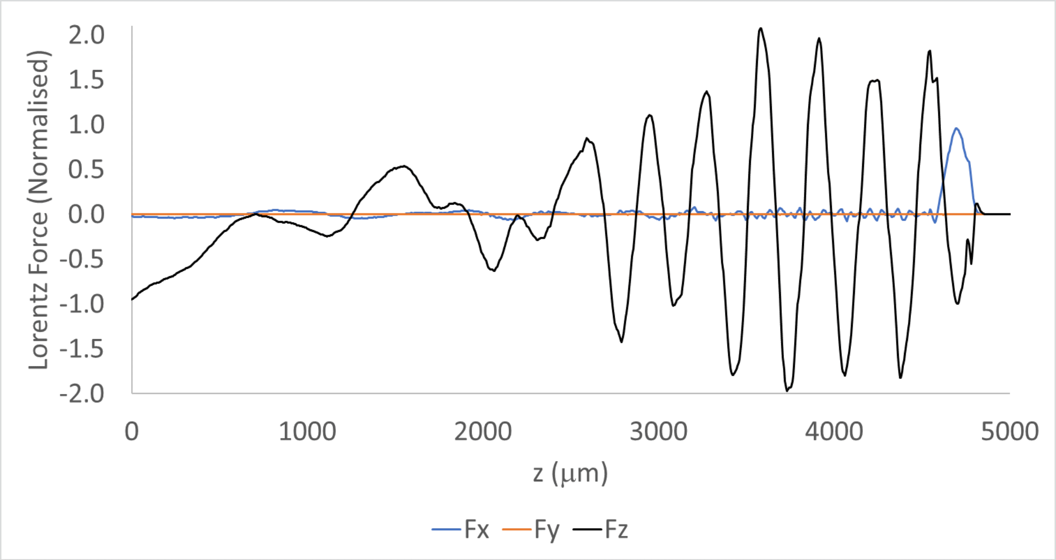

Figure 6.39: Lorentz force components in metal boundary DLW after 17 $ps$ beam propagation, normalised to absolute magnitude of longitudinal force at the beam.

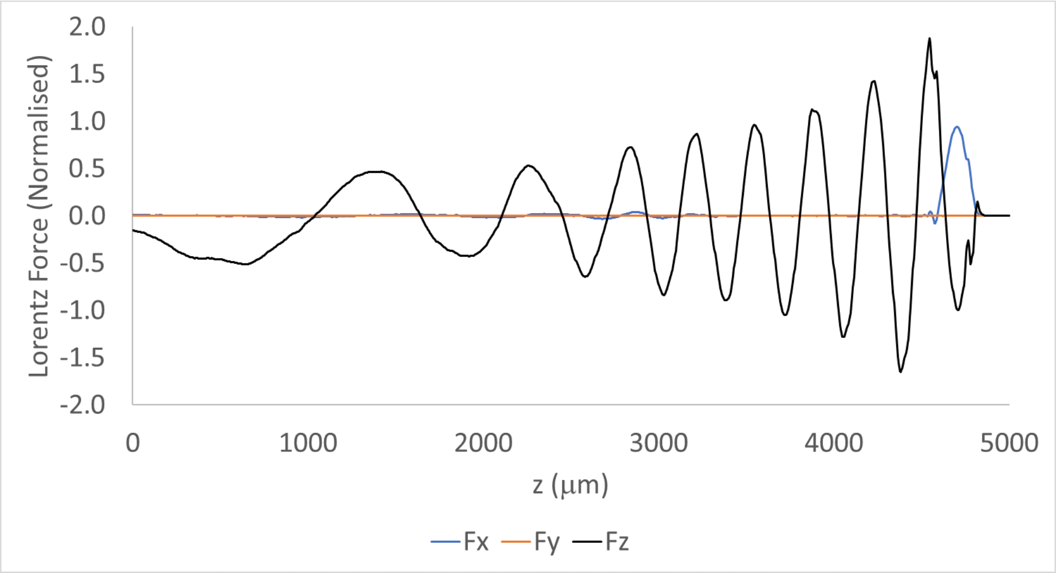

Figure 6.40: Lorentz force components in parallel-plate DLW after 17 $ps$ beam propagation, normalised to absolute magnitude of longitudinal force at the beam.

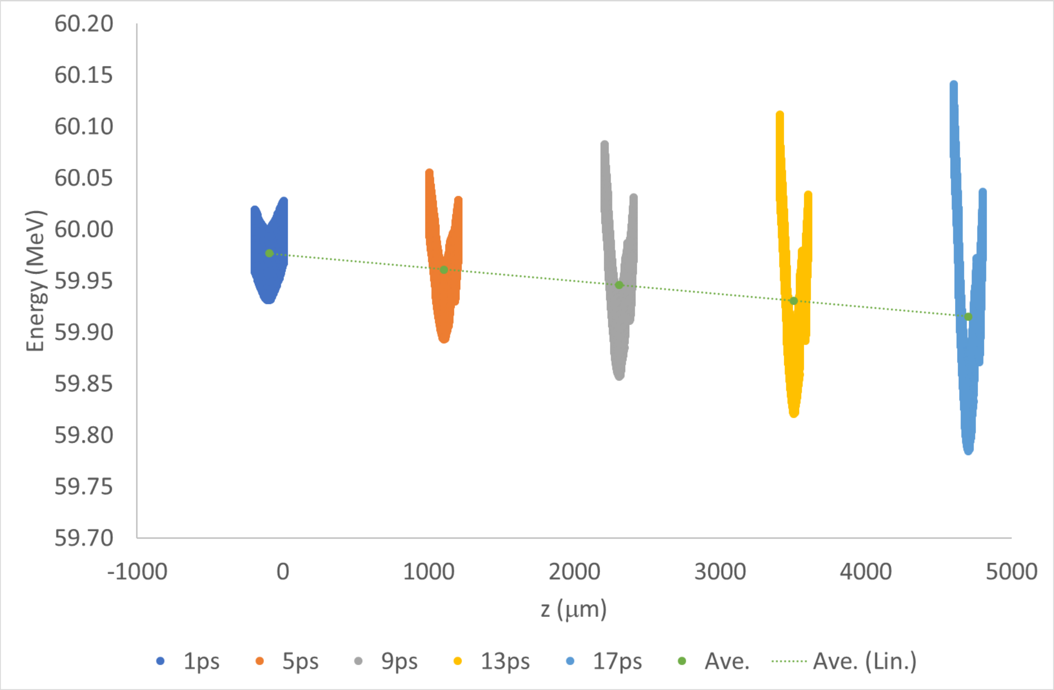

Figure 6.41: Beam energy as it propagates along DLW structure, showing an average energy loss of 12.7 $keV/mm$. The DLW being $x = 0 - 5000\,\mu m$ and the negative $x$-axis region being vacuum propagation from the emitting surface.

## 6.5 Conclusion

This chapter presented wakefield and particle-in-cell simulations of the 1D and 2D PBG-Ws. The first device discussed in this chapter was the 1D-periodic Bragg-based photonic-crystal waveguide. This is made by a 10-layer periodic structure on each side of the waveguide, with the first layer tuned such that $v_p/c = 1$, has a vacuum gap of $0.6\lambda_0$, and a vacuum channel aspect ratio of 2:1. This structure was excited with a $105\,pC$, $\sigma = 60\,\mu m$ Gaussian electron beam. The results from the wakefield simulations showed this design has a strong narrow-band single-mode response, with a 4.1% bandwidth (%-BW). There is negligible excitation of transverse and higher-order modes except when the beam is strongly off axis. Both metal-clad and parallel-plate geometries exhibited this single-mode behaviour, with the parallel-plate design having 50% impedance of the metal-clad at the frequency of interest $f_0$. The PIC results showed in addition to the single-moded nature of the device, that the beam itself experiences a 0.5:1 deflecting/decelerating force ratio, or deflection ratio (DR). The DR, coupled with the highest beam energy loss of the structures investigated at $23.8\,keV/mm$, and highest single-mode impedance of $3.8\,M\Omega/m$ indicates this device would also be favourable as a CCR source for production of THz radiation.

The second device investigated was the 2D-periodic triangular-lattice photonic-crystal waveguide. This waveguide is based on a 10-period PhC slab on each side of the central channel, with a dielectric pad-layer tuned such that $v_p/c = 1$ at the frequency of interest $f_0$. The vacuum-gap is $3.5a$ and the vacuum channel aspect ratio is 1.5:1. This structure is found to be multimoded compared to the 1D-periodic structure. In addition, it presents modes in the lower-frequency region of the impedance figure. These modes do not belong to a photonic bandgap and

Table 6.1: Summary of Beam-Driven PBG-W Geometries

| Design | %-BW | Single/Multimode | $T_R$ | DR | Impedance | Energy Loss |
|---|---|---|---|---|---|---|
| Bragg | 4.1% | Single-mode | 1 : 1 | 0.5 : 1 | $3.8\,M\Omega/m$ | $23.8\,keV/mm$ |
| 2D PBG-W | 2.5% | Multi-mode | 0.5 : 1 | 1.2 : 1 | $1.9\,M\Omega/m$ | $12.3\,keV/mm$ |
| DLW | 15.8% | Multi-Mode | 2 : 1 | 1 : 1 | $2.1\,M\Omega/m$ | $12.7\,keV/mm$ |

are instead spurious modes generated from the metallic boundary condition.

The modes excited in the 2D PBG-W are also the narrowest bandwidth of any geometry investigated, with a 2.5% FWHM bandwidth. This narrow bandwidth combined with a $1.9\,M\Omega/m$ impedance indicates this geometry would retain important characteristics for an extremely narrowband THz CCR source. The PIC results confirmed the multimode nature of the wakefield excitation, and showed the beam experiences a 1.2:1 deflecting/decelerating force ratio. This behaviour highlights potential applicability of the device as a wakefield streaker where excitation of a deflecting force is advantageous.

A comparison of the elliptical vs cylindrical beams illustrated that the higher order and transverse modes could be suppressed by the use of an elliptical beam without negative effect on the primary mode.

Tunability of the 2D PBG-W was investigated by varying the vacuum aperture between the two dielectric slabs in the metal-clad design. It was found that by varying the vacuum aperture gap by $0.8 - 1.2\times$ design width, whilst the pad layer was only tuned for one specific $f_0$, the frequency of operation could be tuned by $40\,GHz$.

The dielectric-lined waveguide was investigated as a comparison for the photonic-crystal structures. Wakefield results showed it is a multimoded structure, with the modes excited having a broad bandwidth. The impedance of the desired mode in this DLW design was slightly offset from the desired $f_0 = 1\,THz$ and the amplitude was similar to that of the 2D-periodic design indicating this design would be favourable as a CCR source. The bandwidth of the DLW however was much more broadband than the PBG-W structures investigated, at 15.5% FWHM. The PIC simulations revealed a 1:1 deflecting/decelerating force ratio and was the only structure to approach 2:1 transformer ratio to make it applicable for both wakefield acceleration and streaking applications. Its design however does not suggest a specialism in any application, and would be more applicable as a “general purpose” device as it neither offers simple fabrication at THz frequencies, narrow bandwidth for CCR sources, nor a higher than unity deflection ratio. Additionally, any higher order modes excited in the DLW are confined by the DLW unless speciality couplers are implemented whereas with PBG-W designs, this can be designed into the waveguide itself.

Bragg based designs are favourable as a CCR source due to lesser higher-order mode excitation. Additionally the mode impedance is highest in the Bragg based PBG-W compared to the other geometries investigated. The triangular lattice 2D PBG-W design is more favourable in design as a wakefield streaker as an offset beam can excite deflecting modes, and the deflecting forces relative to the longitudinal decelerating forces are the highest of all the designs investigated. A summary of the figures of merit for the structures studied can be seen in table 6.1.

# 7

# Conclusion and Future Work

The work in this thesis investigated the use of photonic bandgap based waveguides for THz driven electron acceleration. In particular, the typical properties of photonic crystals have been combined with the effectiveness of metal confinement in the form of novel and easy to realise metal/dielectric structures tailored for the THz range. The study considered both 1D and 2D photonic crystal based geometries, and compared them with the dielectric lined waveguide. Once the PhC was designed to provide a suitable photonic bandgap, the PBG-Ws were realised and optimised to synchronise a highly-relativistic electron beam with the lowest-order accelerating mode allowed within the bandgap by ensuring the speed of light synchronism $v_p/c = 1$. The mode was studied initially in the eigenmode solver with the use of periodic boundaries; the PBG-W was then clad in metal to realise 3D electromagnetic confinement and the pad-layer retuned to ensure the speed of light synchronism for varying vacuum channel aspect ratios.

It was found that when the 1D Bragg based geometry was evaluated with a periodic boundary, it offered the highest peak accelerating voltage of any structure investigated. Introducing the metal cladding reduced this peak by an approximate factor of 2 however also offers the best magnetic field ratio at the walls, and the design is single-moded so it is appropriate for THz frequency acceleration. The wakefield and PIC studies further revealed a high impedance with a single-moded operation, with 4.1% FWHM bandwidth. This result, combined with the highest energy loss figure of all geometries studied, indicates that the Bragg based geometry would also be suitable as a CCR source for narrowband THz sources.

The 2D triangular lattice based geometry was also evaluated with both periodic and metal clad boundaries. The $\zeta_v$ optimisation yielded the highest peak accelerating voltage for the 2D PBG-Ws; and the $v_g$ optimisation yielded the highest broadband accelerating voltage for 2D PBG-Ws. This geometry however yielded lower accelerating voltages than both the 1D Bragg based PBG-W and the DLW. With the maturity of DRIE manufacturing, the 2D PBG-W is the easiest of all the structures investigated to manufacture. Coupling was also investigated for the 2D PBG-W. The straight tapered horn was shown to be capable of 20% coupling at the $f_0$. The wakefield and PIC studies indicated the 2D PBG-W resulted in the most narrowband excitation of any geometry studied at 2.5% FWHM, however also resulted in non-trivial higher order and spurious mode excitation; which while present in this design, can likely be mitigated with more layers of photonic crystal and design focusing on a narrower photonic bandgap. The tunability was investigated by varying the width of the vacuum aperture. Whilst the pad layer thickness was not similarly varied to ensure the $v_p/c = 1$, the 2D PBG-W showed it could operate as a tunable CCR source with a range of $40\,GHz$. This structure additionally yielded the highest deflection forces of any geometry studied and consequently indicates this design could be favourable as a wakefield streaking device for beam characterisation.

The DLW evaluated as the main counterpart waveguide for the 1D and 2D PBG-Ws revealed that the hard confinement of the modes compared to the soft confinement offered by photonic crystals increases both the peak and broadband accelerating voltage over the PBG-Ws. This is due to the higher power flow in the vacuum channel; which itself is a function of both the mode confinement, and the dispersive characteristics of the waveguide. The wakefield and PIC simulations revealed the DLW excites lower levels of HOMs and spurious modes compared to the 2D PBG-W, but more than the Bragg geometry. The DLW however neither matched the wakefield impedance of the 1D geometry, nor the deflection capability nor narrowband excitation of the 2D design.

Comparing the 1D and 2D PBG-W results, the 1D PhC-based geometry provides more flexibility overall than the 2D PhC-based waveguide to engineer the accelerating mode dispersion and damp higher order modes. For externally driven acceleration, the former is preferable and can realistically combine the advantages of photonic crystal technology with accelerating voltages typical of the DLW. For beam-driven applications however the two geometries are both advantageous. The 1D PBG-W offers narrow-bandwidth single-mode excitation with high impedance and beam energy loss. The 2D PBG-W offers the narrowest bandwidth excitation, with comparable impedance and energy loss to the DLW, and additionally offers the capability of the simplest manufacture and in-design filtering.

Taking the work in this thesis forward, the focus should be on fabrication of the designs investigated to confirm the simulation results and allow for modification of the models where required. The 2D PBG-W was identified as being potentially favourable as a wakefield streaking device. Work should also investigate the optimal length of acceleration structure. All work in this thesis used a $5\,mm$ length PBG-W however a longer waveguide, or multiple shorter sections may offer increased performance.

The work examining coupling into the 2D PBG-W was based on illumination of a quasi-$TEM_{01}$ mode. This was assumed due to work undertaken at Daresbury however may not be either the best laser mode for driving the structure. Coupling into the 1D PBG-W is expected to have similar performance to the 2D PBG-W. Furthermore the PhC horn design which was unsuitable for 2D PBG-Ws may be suitable for the Bragg design. Coupling into the Bragg designs should be investigated using both straight taper and parabolic horns.

Silicon was used extensively in the work presented due to the maturity of silicon manufacturing technology. This may not be the best dielectric however for the designed use case. Other materials with increased hardness, breakdown resistance, radiation resistance, or high melting point, may be more suitable and should be investigated. These materials could include alumina, which meets the conditions stated; or titanates of barium or strontium which have extremely high permittivities and could lead to wide bandgaps.

One possible reason for the poorer performance of the 2D PBG-W may be due to the vacuum holes as part of the design. The Bragg based PBG-W revealed higher accelerating voltages and no low power flow region of the dispersion. Additionally as a CCR source, Cherenkov radiation is not emitted from vacuum regions, reducing the impedance. If instead the vacuum holes were replaced with a low-$\varepsilon_r$ dielectric, and the slab replaced with higher to preserve the PBG, the impedance may be improved.

Further beam work should be studied in 2D PBG-Ws. Work undertaken in this thesis investigated energy loss and wakefield impedance from short bunches. Literature has identified methods for pushing the transformer ratio beyond 2:1 with beam shaping, and this methodology may push the performance of the 2D PhC based waveguides higher.

Photonic crystal based particle acceleration is a field very much in its infancy. There are many hurdles facing a practical and efficient design incorporating numerous scientific disciplines in addition to electromagnetics—such as materials science, beam dynamics, vacuum science, microfabrication, and telemetrics. To fully understand the optimal design of a photonic crystal based accelerator, all of these factors must be understood. With the work completed in this thesis—narrow bandwidth, high impedance geometries for THz acceleration and emission have been identified. Additionally, a method for optimisation of PBG-Ws was developed that can not only be applied to the geometries studied here—but to any different waveguide geometry for THz driven acceleration.

# References

[1] Vladimir Shiltsev. On performance of high energy particle colliders and other complex scientific systems. *Modern Physics Letters A*, 26(11):761–772, 2011.

[2] Thomas L Friedman. Moore's law turns 50. *The New York Times*, 13, 2015.

[3] Wolfgang KH Panofsky. Evolution of particle accelerators. *SLAC Beam Line*, 27(1):36–44, 1997.

[4] Daniel Kleppner and Robert Kolenkow. *An introduction to mechanics*. Cambridge University Press, 2014.

[5] Klaus Wille. *The physics of particle accelerators: an introduction*. Clarendon Press, 2000.

[6] W Jones. Earnshaw's theorem and the stability of matter. *European Journal of Physics*, 1(2):85, 1980.

[7] Alexej Grudiev, S Calatroni, and W Wuensch. New local field quantity describing the high gradient limit of accelerating structures. *Physical Review Special Topics-Accelerators and Beams*, 12(10):102001, 2009.

[8] Paul Lorrain. On the design of a radiofrequency cockroft-walton accelerator. *Review of Scientific Instruments*, 20(3):216–217, 1949.

[9] Helmut Wiedemann. *Particle accelerator physics*. Springer Nature, 2015.

[10] Thomas P Wangler. *RF Linear accelerators*. John Wiley & Sons, 2008.

[11] Hywel Owen. Accelerators for proton therapy. *Presentation, Manchester University*, 2012.

[12] John M Osepchuk. The magnetron and the microwave oven: A unique and lasting relationship. In *2010 International Conference on the Origins and Evolution of the Cavity Magnetron*, pages 46–51. IEEE, 2010.

[13] Roger A Lewis. A review of terahertz sources. *Journal of Physics D: Applied Physics*, 47(37):374001, 2014.

[14] Albert Redo-Sanchez, Norman Laman, Brian Schulkin, and Thomas Tongue. Review of terahertz technology readiness assessment and applications. *Journal of Infrared, Millimeter, and Terahertz Waves*, 34(9):500–518, 2013.

[15] VL Bratman, Yu K Kalynov, and VN Manuilov. Large-orbit gyrotron operation in the terahertz frequency range. *Physical review letters*, 102(24):245101, 2009.

[16] La Agusu, T Idehara, H Mori, T Saito, I Ogawa, and S Mitsudo. Design of a cw 1 thz gyrotron (gyrotron fu cw iii) using a 20 t superconducting magnet. *International Journal of Infrared and Millimeter Waves*, 28(5):315–328, 2007.

[17] Richard J Temkin. Development of terahertz gyrotrons for spectroscopy at mit. *Terahertz Science and Technology*, 7(1):1–9, 2014.

[18] Morgan T Hibberd, Alisa L Healy, Daniel S Lake, Vasileios Georgiadis, Elliott JH Smith, Oliver J. Finlay, ..., and Steven P. Jamison. Acceleration of relativistic beams using laser-generated terahertz pulses. *arXiv preprint arXiv:1908.04055*, 2019.

[19] DA Walsh, DS Lake, EW Snedden, MJ Cliffe, DM Graham, and SP Jamison. Demonstration of sub-luminal propagation of single-cycle terahertz pulses for particle acceleration. *Nature communications*, 8(1):1–9, 2017.

[20] Gian Piero Gallerano, S Biedron, et al. Overview of terahertz radiation sources. In *Proceedings of the 2004 FEL Conference*, volume 1, pages 216–221, 2004.

[21] Zhiping Jiang and Xi-Cheng Zhang. Terahertz imaging via electrooptic effect. *IEEE Transactions on microwave theory and techniques*, 47(12):2644–2650, 1999.

[22] Frank J Duarte. *Tunable lasers handbook*. Elsevier, 1996.

[23] C Vicario, M Jazbinsek, AV Ovchinnikov, OV Chefonov, SI Ashitkov, MB Agranat, and CP Hauri. High efficiency thz generation in dstms, dast and oh1 pumped by cr: forsterite laser. *Optics express*, 23(4):4573–4580, 2015.

[24] Thomas H Pacey, Yuri Saveliev, Guoxing Xia, and Jonathan Smith. Simulation studies for dielectric wakefield programme at clara facility. *Nuclear Instruments and Methods in Physics Research Section A: Accelerators, Spectrometers, Detectors and Associated Equipment*, 909:261–265, 2018.

[25] Dongfang Zhang, Arya Fallahi, Michael Hemmer, Xiaojun Wu, Moein Fakhari, Yi Hua, Huseyin Cankaya, Anne-Laure Calendron, Luis E Zapata, Nicholas H Matlis, et al. Segmented terahertz electron accelerator and manipulator (steam). *Nature photonics*, 12(6):336–342, 2018.

[26] Dongfang Zhang, Moein Fakhari, Huseyin Cankaya, Anne-Laure Calendron, Nicholas H Matlis, and Franz X Kärtner. Cascaded multicycle terahertz-driven ultrafast electron acceleration and manipulation. *Physical Review X*, 10(1):011067, 2020.

[27] U Dorda, R Assmann, R Brinkmann, K Flöttmann, I Hartl, M Hüning, F Kärtner, A Fallahi, B Marchetti, Y Nie, et al. Sinbad—the accelerator r&d facility under construction at desy. *Nuclear Instruments and Methods in Physics Research Section A: Accelerators, Spectrometers, Detectors and Associated Equipment*, 829:233–236, 2016.

[28] Florian Burkart, Ralph Aßmann, Ulrich Dorda, Franz Kärtner, Barbara Marchetti, Nicholas Matlis, Timm Rohwer, et al. Commissioning-stages and radio-protection concept for the thz-linac based accelerator. In *10th Int. Particle Accelerator Conf.(IPAC'19), Melbourne, Australia, 19-24 May 2019*, pages 3598–3600. JACOW Publishing, Geneva, Switzerland, 2019.

[29] Emilio A Nanni, Wenqian R Huang, Kyung-Han Hong, Koustuban Ravi, Arya Fallahi, Gustavo Moriena, RJ Dwayne Miller, and Franz X Kärtner. Terahertz-driven linear electron acceleration. *Nature communications*, 6(1):1–8, 2015.

[30] Enrico Fermi. On the origin of the cosmic radiation. *Physical review*, 75(8):1169, 1949.

[31] Toshiki Tajima and John M Dawson. Laser electron accelerator. *Physical Review Letters*, 43(4):267, 1979.

[32] WP Leemans, AJ Gonsalves, H-S Mao, K Nakamura, C Benedetti, CB Schroeder, Cs Tóth, J Daniels, DE Mittelberger, SS Bulanov, et al. Multi-gev electron beams from capillary-discharge-guided subpetawatt laser pulses in the self-trapping regime. *Physical review letters*, 113(24):245002, 2014.

[33] Eric Esarey, CB Schroeder, and WP Leemans. Physics of laser-driven plasma-based electron accelerators. *Reviews of modern physics*, 81(3):1229, 2009.

[34] AJ Gonsalves, K Nakamura, J Daniels, C Benedetti, C Pieronek, TCH De Raadt, S Steinke, JH Bin, SS Bulanov, J Van Tilborg, et al. Petawatt laser guiding and electron beam acceleration to 8 gev in a laser-heated capillary discharge waveguide. *Physical review letters*, 122(8):084801, 2019.

[35] D Woodbury, L Feder, V Shumakova, C Gollner, R Schwartz, B Miao, F Salehi, A Korolov, A Pugžlys, A Baltuška, et al. Laser wakefield acceleration with mid-ir laser pulses. *Optics letters*, 43(5):1131–1134, 2018.

[36] Bernhard Hidding, Simon Hooker, Steven Jamison, Bruno Muratori, Christopher Murphy, Zulfikar Najmudin, Rajeev Pattathil, Gianluca Sarri, Matthew Streeter, Carsten Welsch, Matthew Wing, and Guoxing Xia. Plasma wakefield accelerator research 2019 - 2040: A community-driven uk roadmap compiled by the plasma wakefield accelerator steering committee (pwasc), 2019.

[37] Hyung Taek Kim, VB Pathak, Ki Hong Pae, Agustin Lifschitz, François Sylla, Jung Hun Shin, C Hojbota, Seong Ku Lee, Jae Hee Sung, Hwang Woon Lee, et al. Stable multi-gev electron accelerator driven by waveform-controlled pw laser pulses. *Scientific reports*, 7(1):1–8, 2017.

[38] Olle Lundh, J Lim, Clément Rechatin, L Ammoura, Ahmed Ben-Ismaïl, X Davoine, Guilhem Gallot, Jean-Philippe Goddet, E Lefebvre, Victor Malka, et al. Few femtosecond, few kiloampere electron bunch produced by a laser–plasma accelerator. *Nature Physics*, 7(3):219–222, 2011.

[39] Pisin Chen, JM Dawson, Robert W Huff, and Thomas Katsouleas. Acceleration of electrons by the interaction of a bunched electron beam with a plasma. *Physical review letters*, 54(7):693, 1985.

[40] M Litos, E Adli, JM Allen, W An, CI Clarke, Sébastien Corde, CE Clayton, J Frederico, SJ Gessner, SZ Green, et al. 9 gev energy gain in a beam-driven plasma wakefield accelerator. *Plasma Physics and Controlled Fusion*, 58(3):034017, 2016.

[41] M Litos, E Adli, W An, CI Clarke, CE Clayton, Sébastien Corde, JP Delahaye, RJ England, AS Fisher, J Frederico, et al. High-efficiency acceleration of an electron beam in a plasma wakefield accelerator. *Nature*, 515(7525):92–95, 2014.

[42] Ian Blumenfeld, Christopher E Clayton, Franz-Josef Decker, Mark J Hogan, Chengkun Huang, Rasmus Ischebeck, Richard Iverson, Chandrashekhar Joshi, Thomas Katsouleas, Neil Kirby, et al. Energy doubling of 42 gev electrons in a metre-scale plasma wakefield accelerator. *Nature*, 445(7129):741–744, 2007.

[43] MD Litos, R Ariniello, CE Doss, K Hunt-Stone, and JR Cary. Beam emittance preservation using gaussian density ramps in a beam-driven plasma wakefield accelerator. *Philosophical Transactions of the Royal Society A*, 377(2151):20180181, 2019.

[44] Erik Adli, Arun Ahuja, O Apsimon, Robert Apsimon, A-M Bachmann, D Barrientos, Fabian Batsch, Jeremie Bauche, VK Berglyd Olsen, M Bernardini, et al. Acceleration of electrons in the plasma wakefield of a proton bunch. *Nature*, 561(7723):363–367, 2018.

[45] Giovanni Zevi Della Porta. Recent highlights and plans of the awake experiment, 2020.

[46] MJ Hogan, TO Raubenheimer, A Seryi, P Muggli, T Katsouleas, C Huang, W Lu, W An, KA Marsh, WB Mori, et al. Plasma wakefield acceleration experiments at facet. *New Journal of Physics*, 12(5):055030, 2010.

[47] R.J. England, Noble R.J., K. Bane, D.H. Dowell, C.K. Ng, J.E. Spencer, ..., and R.B. Yoder. Dielectric laser accelerators. *Reviews of Modern Physics*, 86:1337–1389, 2014.

[48] Kenneth J Leedle, Andrew Ceballos, Huiyang Deng, Olav Solgaard, R Fabian Pease, Robert L Byer, and James S Harris. Dielectric laser acceleration of sub-100 kev electrons with silicon dual-pillar grating structures. *Optics letters*, 40(18):4344–4347, 2015.

[49] T Plettner, PP Lu, and RL Byer. Proposed few-optical cycle laser-driven particle accelerator structure. *Physical Review Special Topics-Accelerators and Beams*, 9(11):111301, 2006.

[50] EA Peralta, E Colby, RJ England, C McGuinness, B Montazeri, K Soong, Z Wu, and RL Byer. Design, fabrication, and testing of a fused-silica dual-layer grating structure for direct laser acceleration of electrons. In *AIP Conference Proceedings*, volume 1507, pages 169–177. American Institute of Physics, 2012.

[51] Yelong Wei, Guoxing Xia, Jonathan DA Smith, Kieran Hanahoe, Oznur Mete, Steve P Jamison, and Carsten P Welsch. Numerical study of a multi-stage dielectric laser-driven accelerator. *Physics Procedia*, 77:50–57, 2015.

[52] EA Peralta, K Soong, RJ England, ER Colby, Z Wu, B Montazeri, C McGuinness, J McNeur, KJ Leedle, D Walz, et al. Demonstration of electron acceleration in a laser-driven dielectric microstructure. *Nature*, 503(7474):91–94, 2013.

[53] RJ England, ER Colby, R Laouar, CM McGuinness, B Montazeri, RJ Noble, EA Peralta, K Soong, J Spencer, D Walz, et al. Manufacture and testing of optical-scale accelerator structures from silicon and silica. *Proc. IPAC, New Orleans, USA*, 2012.

[54] N Vartanian, G Travish, and E Arab. Testing of laser-driven resonant accelerating-structures possessing sub-wavelength periodic features. Proceedings of 2009 Particle Accelerator Conference, 2009.

[55] Jianyun Zhou, Joshua McNeur, Gil Travish, and Rodney Yoder. Fabrication of a prototype micro accelerator platform. In *Proceedings of 2011 Particle Accelerator Conference, IEEE*, 2011.

[56] J McNeur, G Travish, EB Sozer, K Hazra, B Matthews, RJ England, K Soong, E Peralta, Z Wu, B Montazeri, et al. Experimental search for acceleration in the micro-accelerator platform. In *IPAC Conference Proceedings*, 2013.

[57] G Travish, J McNeur, E Sozer, KS Hazra, and B Matthews. First acceleration in a resonant optical-scale laser-powered structure. *Proceedings of IPAC2015*, 2015.

[58] Josh Mcneur, EB Sozer, Gil Travish, KS Hazra, B Matthews, RB Yoder, RJ England, Ziran Wu, EA Peralta, and K Soong. Experimental results from the micro-accelerator platform, a resonant slab-symmetric dielectric laser accelerator. In *AIP Conference Proceedings*, volume 1777, page 060014. AIP Publishing LLC, 2016.

[59] Zhiyu Zhang, S Tantawi, and R Ruth. Distributed bragg coupler for optical all-dielectric electron accelerator. In *Proceedings of the 2005 Particle Accelerator Conference*, pages 2125–2127. IEEE, 2005.

[60] Zhiyu Zhang, Sami G Tantawi, and Ronald D Ruth. Distributed grating-assisted coupler for optical all-dielectric electron accelerator. *Physical Review Special Topics-Accelerators and Beams*, 8(7):071302, 2005.

[61] Iv V Konoplev, AW Cross, W He, ADR Phelps, K Ronald, GRM Robb, CG Whyte, NS Ginzburg, N Yu Peskov, and AS Sergeev. Progress of the strathclyde free electron maser experiment using a 2d bragg structure. *Nuclear Instruments and Methods in Physics Research Section A: Accelerators, Spectrometers, Detectors and Associated Equipment*, 445(1-3):236–240, 2000.

[62] IV Konoplev, P McGrane, AW Cross, K Ronald, and ADR Phelps. Wave interference and band gap control in multiconductor one-dimensional bragg structures. *Journal of Applied Physics*, 97(7):073101, 2005.

[63] NS Ginzburg, EV Ilyakov, IS Kulagin, N Yu Peskov, AS Sergeev, and V Yu Zaslavsky. Theoretical and experimental investigations of oversized ka-band surface-wave oscillator based on 2d periodical corrugated structure. In *EPJ Web of Conferences*, volume 149, page 04031. EDP Sciences, 2017.

[64] Benjamin M Cowan. Two-dimensional photonic crystal accelerator structures. *Physical Review Special Topics-Accelerators and Beams*, 6(10):101301, 2003.

[65] B Naranjo, A Valloni, S Putterman, and JB Rosenzweig. Stable charged-particle acceleration and focusing in a laser accelerator using spatial harmonics. *Physical review letters*, 109(16):164803, 2012.

[66] Thomas F Krauss, M Richard, and Stuart Brand. Two-dimensional photonic-bandgap structures operating at near-infrared wavelengths. *Nature*, 383(6602):699–702, 1996.

[67] Robert J Noble, James E Spencer, and Boris T Kuhlmey. Hollow-core photonic band gap fibers for particle acceleration. *Physical Review Special Topics-Accelerators and Beams*, 14(12):121303, 2011.

[68] C-K Ng, RJ England, L-Q Lee, R Noble, V Rawat, and J Spencer. Transmission and radiation of an accelerating mode in a photonic band-gap fiber. *Physical Review Special Topics-Accelerators and Beams*, 13(12):121301, 2010.

[69] Hernán Míguez, Cefe López, Francisco Meseguer, Álvaro Blanco Montes, Luis Vázquez, R Mayoral, Manuel Ocaña, Vicente Fornés, and A Mifsud. Photonic crystal properties of packed submicrometric sio2 spheres. 1997.

[70] Alvaro Blanco, Emmanuel Chomski, Serguei Grabtchak, Marta Ibisate, Sajeev John, Stephen W Leonard, Cefe Lopez, Francisco Meseguer, Hernan Miguez, Jessica P Mondia, et al. Large-scale synthesis of a silicon photonic crystal with a complete three-dimensional bandgap near 1.5 micrometres. *Nature*, 405(6785):437–440, 2000.

[71] Benjamin M Cowan. Three-dimensional dielectric photonic crystal structures for laser-driven acceleration. *Physical Review Special Topics-Accelerators and Beams*, 11(1):011301, 2008.

[72] Benjamin Cowan, M Javanmard, and N Wu. Photonic crystal laser-driven accelerator structures. In *AIP Conference Proceedings*, volume 737, pages 320–326. American Institute of Physics, 2004.

[73] C McGuinness, E Peralta, K Soong, RL Byer, E Colby, RJ England, R Laouar, RJ Noble, JE Spencer, Z Wu, et al. Fabrication and measurements of a silicon woodpile accelerator structure. In *Conf. Proc. C110328: 343-345, 2011*, number SLAC-PUB-16680. SLAC National Accelerator Lab., Menlo Park, CA (United States), 2016.

[74] Christopher McGuinness, E Colby, B Cowan, RJ England, J Ng, RJ Noble, E Peralta, K Soong, J Spencer, D Walz, et al. Fabrication and characterization of woodpile structures for direct laser acceleration. In *AIP Conference Proceedings*, volume 1299, pages 439–444. American Institute of Physics, 2010.

[75] PD Hoang, G Andonian, I Gadjev, B Naranjo, Y Sakai, N Sudar, O Williams, M Fedurin, K Kusche, C Swinson, et al. Experimental characterization of electron-beam-driven wakefield modes in a dielectric-woodpile cartesian symmetric structure. *Physical review letters*, 120(16):164801, 2018.

[76] Benjamin Wang, JA Rodríguez, and Mark A Cappelli. 3d woodpile structure tunable plasma photonic crystal. *Plasma Sources Science and Technology*, 28(2):02LT01, 2019.

[77] Walter Rotman. Plasma simulation by artificial dielectrics and parallel-plate media. *IRE Transactions on Antennas and Propagation*, 10(1):82–95, 1962.

[78] IS Nefedov and AJ Viianen. Wire media. In Filippo Capolino, editor, *Theory and phenomena of metamaterials*, pages 328–352. CRC press, 2017.

[79] B Hidding, JB Rosenzweig, Y Xi, B O'Shea, G Andonian, D Schiller, S Barber, O Williams, G Pretzler, T Königstein, et al. Beyond injection: Trojan horse underdense photocathode plasma wakefield acceleration. In *AIP Conference Proceedings*, volume 1507, pages 570–575. American Institute of Physics, 2012.

[80] Mukesh Kumar, Toru Miura, Yasuki Sakurai, and Fumio Koyama. Tunable hollow optical waveguide and its applications. *Frontiers in Guided Wave Optics and Optoelectronics, B. Pal, Ed*, 2010.

[81] S Antipov, SV Baryshev, R Kostin, S Baturin, J Qiu, C Jing, C Swinson, M Fedurin, and D Wang. Efficient extraction of high power thz radiation generated by an ultra-relativistic electron beam in a dielectric loaded waveguide. *Applied Physics Letters*, 109(14):142901, 2016.

[82] TH Pacey, Y Saveliev, A Healy, PG Huggard, B Alderman, P Karataev, K Fedorov, and G Xia. Continuously tunable narrow-band terahertz generation with a dielectric lined waveguide driven by short electron bunches. *Physical Review Accelerators and Beams*, 22(9):091302, 2019.

[83] Christopher MS Sears, Eric Colby, Rasmus Ischebeck, Christopher McGuinness, Janice Nelson, Robert Noble, Robert H Siemann, James Spencer, Dieter Walz, Tomas Plettner, et al. Production and characterization of attosecond electron bunch trains. *Physical Review Special Topics-Accelerators and Beams*, 11(6):061301, 2008.

[84] BD O'Shea, G Andonian, SK Barber, KL Fitzmorris, S Hakimi, J Harrison, PD Hoang, MJ Hogan, B Naranjo, OB Williams, et al. Observation of acceleration and deceleration in gigaelectron-volt-per-metre gradient dielectric wakefield accelerators. *Nature communications*, 7(1):1–7, 2016.

[85] Thomas Pacey. *Development of Novel Applications of Dielectric Wakefield Structures for Electron Accelerators.* PhD thesis, The University of Manchester (United Kingdom), 2019.

[86] AM Cook, R Tikhoplav, SY Tochitsky, G Travish, OB Williams, and JB Rosenzweig. Observation of narrow-band terahertz coherent cherenkov radiation from a cylindrical dielectric-lined waveguide. *Physical review letters*, 103(9):095003, 2009.

[87] AL Healy, Graeme Burt, and SP Jamison. Electron-terahertz interaction in dielectric-lined waveguide structures for electron manipulation. *Nuclear Instruments and Methods in Physics Research Section A: Accelerators, Spectrometers, Detectors and Associated Equipment*, 909:199–203, 2018.

[88] K Fedorov, P Karataev, A Oleinik, T Pacey, Y Saveliev, and A Potylitsyn. Experimental observation of submillimeter coherent cherenkov radiation at clara facility. In *8th Int. Beam Instrumentation Conf.(IBIC'19), Malmö, Sweden*, 2019.

[89] D Angal-Kalinin, A Bainbridge, AD Brynes, RK Buckley, SR Buckley, GC Burt, RJ Cash, HM Castaneda Cortes, D Christie, JA Clarke, et al. Design, specifications, and first beam measurements of the compact linear accelerator for research and applications front end. *Physical Review Accelerators and Beams*, 23(4):044801, 2020.

[90] S Antipov, C Jing, M Fedurin, W Gai, A Kanareykin, K Kusche, P Schoessow, V Yakimenko, and A Zholents. Experimental observation of energy modulation in electron beams passing through terahertz dielectric wakefield structures. *Physical review letters*, 108(14):144801, 2012.

[91] G Andonian, O Williams, S Barber, D Bruhwiler, P Favier, M Fedurin, K Fitzmorris, A Fukasawa, P Hoang, K Kusche, et al. Planar-dielectric-wakefield accelerator structure using bragg-reflector boundaries. *Physical Review Letters*, 113(26):264801, 2014.

[92] Adi Hanuka and Levi Schächter. Bragg accelerator optimization. *High Power Laser Science and Engineering*, 2:e24, 2014.

[93] Vadim Karagodsky, David Schieber, and Levi Schächter. Enhancing x-ray generation by electron-beam–laser interaction in an optical bragg structure. *Physical review letters*, 104(2):024801, 2010.

[94] Chiyan Luo, Mihai Ibanescu, Steven G Johnson, and JD Joannopoulos. Cerenkov radiation in photonic crystals. *science*, 299(5605):368–371, 2003.

[95] J.D. Joannopoulos, S.G. Johnson, J.N. Winn, and R.D. Meade. *Photonic Crystals*. Princeton University Press, 2nd edition, 2008.

[96] Steven G Johnson and John D Joannopoulos. Block-iterative frequency-domain methods for maxwell's equations in a planewave basis. *Optics express*, 8(3):173–190, 2001.

[97] CTM Chang, JW Dawson, and RL Kustom. A dielectric loaded slow wave structure for separation of relativistic particles. *IEEE Transactions on Nuclear Science*, 16(3):526–530, 1969.

[98] Liling Xiao, Wei Gai, and Xiang Sun. Field analysis of a dielectric-loaded rectangular waveguide accelerating structure. *Physical Review E*, 65(1):016505, 2001.

[99] Marvin Chodorow and T Wessel-Berg. A high-efficiency klystron with distributed interaction. *IRE Transactions on electron Devices*, 8(1):44–55, 1961.

[100] Yaogen Ding, Bin Shen, Shaomin Shi, and Jin Cao. S-band multibeam klystron with bandwidth of 10%. *IEEE transactions on electron devices*, 52(5):889–894, 2005.

[101] Thomas P. Wangler. *RF Linear Accelerators*. Wiley-VCH, 2 edition, 2008.

[102] Gregory TA Kovacs, Nadim I Maluf, and Kurt E Petersen. Bulk micromachining of silicon. *Proceedings of the IEEE*, 86(8):1536–1551, 1998.

[103] Kai Egashira and Katsumi Mizutani. Micro-drilling of monocrystalline silicon using a cutting tool. *Precision Engineering*, 26(3):263–268, 2002.

[104] Erno H Klaassen, Kurt Petersen, J Mark Noworolski, John Logan, Nadim I Maluf, Joe Brown, Christopher Storment, Wendell McCulley, and Gregory TA Kovacs. Silicon fusion bonding and deep reactive ion etching: a new technology for microstructures. *Sensors and Actuators A: Physical*, 52(1-3):132–139, 1996.

[105] Franz Laermer, Sami Franssila, Lauri Sainiemi, and Kai Kolari. Deep reactive ion etching. In *Handbook of silicon based MEMS materials and technologies*, pages 417–446. Elsevier, 2020.

[106] Yemin Tang, Amin Sandoughsaz, Kevin J Owen, and Khalil Najafi. Ultra deep reactive ion etching of high aspect-ratio and thick silicon using a ramped-parameter process. *Journal of Microelectromechanical Systems*, 27(4):686–697, 2018.

[107] CS Trueman and J Huddleston. Material removal by spalling during edm of ceramics. *Journal of the European ceramic society*, 20(10):1629–1635, 2000.

[108] RE Hummel and Sung-Sik Chang. Novel technique for preparing porous silicon. *Applied physics letters*, 61(16):1965–1967, 1992.

[109] T Sato, T Mizutani, and K Kawata. Electro-discharge machine for micro-hole drilling. *Natl Techn Rep*, 31:725–733, 1985.

[110] Dominiek Reynaerts, Hendrik Van Brussel, et al. Microstructuring of silicon by electro-discharge machining (edm)—part i: theory. *Sensors and Actuators A: Physical*, 60(1-3):212–218, 1997.

[111] ZY Yu, KP Rajurkar, and H Shen. High aspect ratio and complex shaped blind micro holes by micro edm. *CIRP annals*, 51(1):359–362, 2002.

[112] Sumit K Jui, Abishek B Kamaraj, and Murali M Sundaram. High aspect ratio micromachining of glass by electrochemical discharge machining (ecdm). *Journal of Manufacturing Processes*, 15(4):460–466, 2013.

[113] IW Rangelow. Reactive ion etching for high aspect ratio silicon micromachining. *Surface and Coatings Technology*, 97(1-3):140–150, 1997.

[114] MRH Knowles, G Rutterford, D Karnakis, and A Ferguson. Micro-machining of metals, ceramics and polymers using nanosecond lasers. *The International Journal of Advanced Manufacturing Technology*, 33(1-2):95–102, 2007.

[115] Zhangwei Chen, Ziyong Li, Junjie Li, Chengbo Liu, Changshi Lao, Yuelong Fu, Changyong Liu, Yang Li, Pei Wang, and Yi He. 3d printing of ceramics: A review. *Journal of the European Ceramic Society*, 39(4):661–687, 2019.

[116] EM Fayed, AS Elmesalamy, M Sobih, and Y Elshaer. Characterization of direct selective laser sintering of alumina. *The International Journal of Advanced Manufacturing Technology*, 94(5-8):2333–2341, 2018.

[117] Andrea Zocca, Pedro Lima, and Jens Günster. Lsd-based 3d printing of alumina ceramics. *Journal of Ceramic Science and Technology*, 8(1):141–148, 2017.

[118] Electroforming, additive manufacturing atom by atom. *White Paper: Veco B.V.*, 2019. Retreived: 2020-04-02.

[119] Walter Bacher, Wolfgang Menz, and Jürgen Mohr. The liga technique and its potential for microsystems-a survey. *IEEE transactions on industrial electronics*, 42(5):431–441, 1995.

[120] Marc J Madou. *Fundamentals of microfabrication: the science of miniaturization.* CRC press, 2002.

[121] CST Microwave Studio. 3ds.com/products-services/simulia/products/cst-studio-suite/. Accessed: 2021-04.

[122] Dassault Systemes. CST Documentation. CST, 2020.

[123] Youcef Saad. Overview of krylov subspace methods with applications to control problems. *NASA Ames Research Centre*, 1989.

[124] Olavi Nevanlinna. *Convergence of iterations for linear equations.* Birkhäuser, 2012.

[125] Zhengchun Du, Wei Liu, and Wanliang Fang. Calculation of rightmost eigenvalues in power systems using the jacobi–davidson method. *IEEE Transactions on Power Systems*, 21(1):234–239, 2006.

[126] Michiel E Hochstenbach and Yvan Notay. The jacobi–davidson method. *GAMM-Mitteilungen*, 29(2):368–382, 2006.

[127] Thomas Weiland. A discretization model for the solution of Maxwell's equations for six-component fields. *Archiv Elektronik und Uebertragungstechnik*, 31:116–120, 1977.

[128] Markus Clemens and Thomas Weiland. Discrete electromagnetism with the finite integration technique. *Progress In Electromagnetics Research*, 32:65–87, 2001.

[129] M Clemens, S Drobny, H Kruger, P Pinder, O Podebrad, B Schillinger, B Trapp, T Weiland, M Wilke, M Bartsch, et al. The electromagnetic simulation software package mafia 4. In *1999 International Conference on Computational Electromagnetics and its Applications. Proceedings (ICCEA'99)(IEEE Cat. No. 99EX374)*, pages 565–568. IEEE, 1999.

[130] Collin S Meierbachtol, Andrew D Greenwood, John P Verboncoeur, and Balasubramaniam Shanker. Conformal electromagnetic particle in cell: A review. *IEEE Transactions on Plasma Science*, 43(11):3778–3793, 2015.

[131] H Damerau, S Hancock, M Schokker, et al. Longitudinal performance with high-density beams for the lhc in the cern ps. *ICFA-HB2010, Mohrschach, Switzerland*, page 193, 2010.

[132] ASTRA Space Charge Tracking Algorithm. https://www.desy.de/ mpyflo/. Accessed: 2021-04.

[133] BA Shadwick and CB Schroeder. Physical fidelity in particle-in-cell modeling of small debye-length plasmas. In *AIP Conference Proceedings*, volume 1086, pages 321–327. American Institute of Physics, 2009.

[134] Ingo Hofmann and Oliver Boine-Frankenheim. Grid dependent noise and entropy growth in anisotropic 3d particle-in-cell simulation of high intensity beams. *Physical Review Special Topics-Accelerators and Beams*, 17(12):124201, 2014.

[135] Johnson SG and Joannopoulos JD. The MIT Photonic-Bands Package home page. http://ab-initio.mit.edu/mpb/. Accessed: 2021-04.

[136] OI Drivotin and DA Ovsyannikov. Stationary self-consistent distributions for a charged particle beam in the longitudinal magnetic field. *Physics of Particles and Nuclei*, 47(5):884–913, 2016.

[137] KT McDonald and DP Russell. Methods of emittance measurement. In *Frontiers of particle beams; observation, diagnosis and correction*, pages 122–132. Springer, 1989.

[138] Klaus Floettmann. Some basic features of the beam emittance. *Physical Review Special Topics-Accelerators and Beams*, 6(3):034202, 2003.

[139] Stephen Peggs and Todd Satogata. *Introduction to accelerator dynamics*. Cambridge University Press, 2017.

[140] Stephen J Dowdell, Benjamin Clasie, Nicolas Depauw, Peter Metcalfe, Anatoly B Rosenfeld, Hanne M Kooy, Jacob B Flanz, and Harald Paganetti. Monte carlo study of the potential reduction in out-of-field dose using a patient-specific aperture in pencil beam scanning proton therapy. *Physics in Medicine & Biology*, 57(10):2829, 2012.

[141] P Goldsmith and JV Jelley. Optical transition radiation from protons entering metal surfaces. *Philosophical Magazine*, 4(43):836–844, 1959.

[142] Alexander Petrovich Potylitsyn. Transition radiation and diffraction radiation. similarities and differences. *Nuclear Instruments and Methods in Physics Research Section B: Beam Interactions with Materials and Atoms*, 145(1-2):169–179, 1998.

[143] Yukio Shibata, Shigeru Hasebe, Kimihiro Ishi, Toshiharu Takahashi, Toshiaki Ohsaka, Mikihiko Ikezawa, Toshiharu Nakazato, Masayuki Oyamada, Shigekazu Urasawa, Tatsuya Yamakawa, et al. Observation of coherent diffraction radiation from bunched electrons passing through a circular aperture in the millimeter-and submillimeter-wavelength regions. *Physical Review E*, 52(6):6787, 1995.

[144] JV Jelley. Cerenkov radiation and its applications. *British Journal of Applied Physics*, 6(7):227, 1955.

[145] I Frank and I Tamm. Coherent visible radiation of fast electrons passing through matter. In *Selected Papers*, pages 29–35. Springer, 1991.

[146] G Andonian, D Stratakis, M Babzien, S Barber, M Fedurin, E Hemsing, K Kusche, P Muggli, B O'Shea, X Wei, et al. Dielectric wakefield acceleration of a relativistic electron beam in a slab-symmetric dielectric lined waveguide. *Physical review letters*, 108(24):244801, 2012.

[147] Perry B Wilson. Introduction to wakefields and wake potentials. In *AIP Conference Proceedings*, volume 184, pages 525–564. American Institute of Physics, 1989.

[148] SS Baturin, IL Sheinman, AM Altmark, and AD Kanareykin. Transverse operator method for wakefields in a rectangular dielectric loaded accelerating structure. *Physical Review Special Topics-Accelerators and Beams*, 16(5):051302, 2013.

[149] John David Jackson. *Classical Electrodynamics*. Princeton University Press, 3 edition, 1999.

[150] Karl LF Bane, Pisin Chen, and Perry B Wilson. Collinear wake field acceleration. Technical report, Stanford Linear Accelerator Center, 1985.

[151] D Mihalcea, P Piot, and P Stoltz. Three-dimensional analysis of wakefields generated by flat electron beams in planar dielectric-loaded structures. *Physical Review Special Topics-Accelerators and Beams*, 15(8):081304, 2012.

[152] SS Baturin and Alexander Zholents. Upper limit for the accelerating gradient in the collinear wakefield accelerator as a function of the transformer ratio. *Physical Review Accelerators and Beams*, 20(6):061302, 2017.

[153] WKH Panofsky and WA Wenzel. Some considerations concerning the transverse deflection of charged particles in radio-frequency fields. *Review of Scientific Instruments*, 27(11):967–967, 1956.

[154] A Tremaine, J Rosenzweig, and P Schoessow. Electromagnetic wake fields and beam stability in slab-symmetric dielectric structures. *Physical Review E*, 56(6):7204, 1997.

[155] Brian R West and Amr S Helmy. Properties of the quarter-wave bragg reflection waveguide: theory. *JOSA B*, 23(6):1207–1220, 2006.

[156] P Haring Bolivar, Martin Brucherseifer, J Gómez Rivas, Ramón Gonzalo, Iñigo Ederra, Andrew L Reynolds, M Holker, and Peter de Maagt. Measurement of the dielectric constant and loss tangent of high dielectric-constant materials at terahertz frequencies. *IEEE Transactions on Microwave Theory and Techniques*, 51(4):1062–1066, 2003.

[157] Shu Chen, Kim N Nguyen, and Mohammed N Afsar. Complex dielectric permittivity measurements of glasses at millimeter waves and terahertz frequencies. In *2006 European Microwave Conference*, pages 384–387. IEEE, 2006.

[158] Amit Mizrahi and Levi Schächter. Bragg reflection waveguides with a matching layer. *Optics Express*, 12(14):3156–3170, 2004.

[159] Jose A Hejase, Pavel R Paladhi, and Premjeet Prem Chahal. Terahertz characterization of dielectric substrates for component design and nondestructive evaluation of packages. *IEEE Transactions on Components, Packaging and Manufacturing Technology*, 1(11):1685–1694, 2011.

[160] Christopher L Davies, Jay B Patel, Chelsea Q Xia, Laura M Herz, and Michael B Johnston. Temperature-dependent refractive index of quartz at terahertz frequencies. *Journal of Infrared, Millimeter, and Terahertz Waves*, 39(12):1236–1248, 2018.

[161] Jianming Dai, Jiangquan Zhang, Weili Zhang, and Daniel Grischkowsky. Terahertz time-domain spectroscopy characterization of the far-infrared absorption and index of refraction of high-resistivity, float-zone silicon. *JOSA B*, 21(7):1379–1386, 2004.

[162] Andrew Vint, Graeme Burt, and Rosa Letizia. Optimization of pbg-waveguides for terahertz-driven electron acceleration. *IEEE Transactions on Plasma Science*, 48(4):1202–1209, 2020.

[163] Alisa Healy. Private communication. 2018.

[164] Alisha J Shutler and D Grischkowsky. Gap independent coupling into parallel plate terahertz waveguides using cylindrical horn antennas. *Journal of Applied physics*, 112(7):073102, 2012.

[165] Rajind Mendis and Daniel Grischkowsky. Undistorted guided-wave propagation of subpicosecond terahertz pulses. *Optics letters*, 26(11):846–848, 2001.

[166] Robert Oshana. *DSP software development techniques for embedded and real-time systems*. Elsevier, 2006.

[167] S Bettoni, P Craievich, AA Lutman, and M Pedrozzi. Temporal profile measurements of relativistic electron bunch based on wakefield generation. *Physical Review Accelerators and Beams*, 19(2):021304, 2016.

[168] Paolo Craievich and Alberto A Lutman. Effects of the quadrupole wakefields in a passive streaker. *Nuclear Instruments and Methods in Physics Research Section A: Accelerators, Spectrometers, Detectors and Associated Equipment*, 865:55–59, 2017.